TECHNISCHE
UNIVERSITÄT
WIEN

DISSERTATION

Efficient Physical Modeling of Bias Temperature Instability

---

zur Erlangung des akademischen Grades

Doktor der technischen Wissenschaften

eingereicht an der Technischen Universität Wien
Fakultät für Elektrotechnik und Informationstechnik
von

GERHARD RZEPA

[redacted]

Betreuer: AO.UNIV.PROF. DIPL.-ING. DR.TECHN. TIBOR GRASSER

Wien, im Juni 2018

Abstract

Efficient Physical Modeling of
Bias Temperature Instability

Metal-oxide-semiconductor (MOS) devices are a key driver of modern technologies. Of particular importance are MOS field-effect transistors (MOSFETs), which act as binary switches for electrical currents by exploiting the field effect. It is through the embedding of billions of these devices into single chips that the extensive computation that underpins modern life is made possible. A major design challenge within these technologies is to ensure maximal performance while simultaneously guaranteeing reliable behavior throughout the entire projected lifetime of the device. Of chief importance are instabilities which are sensitive to the gate bias voltage and the temperature. This phenomenon is termed bias temperature instability (BTI) and is one of several reliability issues related to charge trapping in the oxide layer of these devices.

The first reports of BTI were presented more than 50 years ago, but despite ongoing research efforts and continual economic interest, the fundamental physics is still not fully understood. From early on, diffusive processes and thermally activated reactions have been deemed responsible for BTI, and since then, the question as to which of these two processes governs the degradation kinetics remains controversial. Recent technology advancements have shed some light on these processes, and it has since been shown that many reliability phenomena can be consistently described through non-radiative multi-phonon (NMP) theory. In particular, the 4-state NMP model was successfully applied to describe degradation due to pre-existing oxide defects. In addition to these pre-existing defects, there is some evidence of a more elusive degradation mechanism, which is believed to be related to defect generation and transformation involving the relocation of hydrogen in the oxide.

In this work, the 4-state NMP model will be employed to reproduce a broad range of experimental degradation data. Starting with an analysis of pre-existing defects in simple SiO_2 oxides at negative bias temperature instability (NBTI) conditions, a unified modeling approach will be presented for such defects in devices with high-κ gate stacks at NBTI and positive bias temperature instability (PBTI) conditions.

Furthermore, it will be shown that the essential physics of these rather complex degradation mechanisms can be captured with high accuracy through a more simplified model. This condensed physical description is implemented within a new modeling framework called *Comphy*, short for "compact-physics". With this framework, the key physical properties of oxide defects in SiO_2 and HfO_2 oxides for various device processes are extracted and consistent results for both NBTI and PBTI stress are obtained. For transparency, all parameters used in the Comphy-based studies will also be listed in this work.

The detailed insights into the governing physics of pre-existing oxide defects developed here can aid future studies of the still elusive degradation mechanisms within oxides in MOS devices. Furthermore, by complementing the physical model for pre-existing oxide defects with a phenomenological description of defect generation and transformation, fast and accurate predictions of device lifetimes can be obtained. Thus, the Comphy framework presented in this thesis can contribute to the continuing improvement of MOS technology.

Kurzfassung

Effiziente physikalische Modellierung der
Bias-Temperaturinstabilität

Metal-Oxid-Halbleiter (MOS)-Bauelemente sind Schlüsselfaktoren moderner Technologien. Vor allem ihre Eigenschaft, Ströme mittels Feldeffekt ein- und auszuschalten, wird in nahezu allen elektronischen Geräten verwendet und das Zusammenspiel von Milliarden dieser MOS-Feldeffekttransistoren (MOSFETs) auf kleinen Computerchips ermöglicht die komplexen Berechnungen, die nunmehr Teil unseres Alltags sind. Eine der größten Herausforderungen dieser Technologien ist es, Geräte bei höchstmöglicher Leistung, aber zugleich auch ausreichender Zuverlässigkeit über die vorgesehene Lebensdauer hinweg zu betreiben. Besonders entscheidend sind dabei Instabilitäten die stark von der Biasspannung und der Temperatur abhängen. Dieses Phänomen wird Bias-Temperaturinstabilität (BTI) genannt und stellt eines von mehreren Zuverlässigkeitsproblemen dar, die auf das Einfangen von Ladungen in den Oxiden dieser Bauelemente zurückzuführen sind.

BTI wurde bereits vor mehr als 50 Jahren dokumentiert, aber trotz andauernder Forschung und wirtschaftlichem Interesse sind die grundlegenden physikalischen Mechanismen nicht zur Gänze geklärt. Schon früh wurden diffusive Prozesse und temperaturaktivierte Reaktionen für BTI verantwortlich gemacht, kontrovers ist jedoch, welcher dieser beiden Mechanismen den zeitlichen Verlauf der Degradation dominiert. Moderne Technologien erlauben detailliertere Studien dieser Prozesse und es wurde gezeigt, dass die Theorie der nichtstrahlenden Multiphononen (NMP) viele dieser Zuverlässigkeitsprobleme widerspruchsfrei beschreibt. Speziell mittels des 4-State-NMP-Modells konnte die Degradation aufgrund von präexistenten Defekten erfolgreich beschrieben werden. Zusätzlich zu diesen präexistenten Defekten wird ein schwerer zu erfassender Mechanismus beobachtet. Es wird vermutet, dass dieser Mechanismus mit der Defektgeneration und -transformation und einer damit einhergehenden Umverteilung von Wasserstoff in Verbindung steht.

In dieser Arbeit wird eine Vielzahl von verschiedenen experimentellen Degradationsdaten mittels des 4-State-NMP-Modells untersucht. Nach der Analyse von präexistenten Defekten in einfachen SiO_2-Oxiden unter BTI-Bedingungen mit negativer Biasspannung (NBTI) wird eine einheitliche Modellierung solcher Defekte in high-κ-Gate-Schichtstapeln bei negativen und positiven BTI-Bedingungen (PBTI) präsentiert.

Weiters wird gezeigt, dass die Essenz dieser durchaus komplexen Degradationsmechanismen mit hoher Genauigkeit und unter weitgehender Beibehaltung des physikalischen Gehalts abstrahiert werden kann. Diese auf das Wesentliche beschränkten Beschreibungen werden in einem neuen Modellierungssystem namens *Comphy*, einer Kurzform von „compact-physic", eingebettet. Mit diesem Modellierungssystem werden die grundlegenden physikalischen Eigenschaften von Defekten in SiO_2- und HfO_2-Oxiden bestimmt und konsistente NBTI- und PBTI-Simulationen für verschiedenartige Prozessierungen durchgeführt. Um diese Studien nachvollziehbar zu machen, werden alle Parameter der Comphy-Simulationen aufgelistet.

Das detaillierte Verständnis der Physik und der Eigenschaften präexistenter Oxiddefekte kann zukünftige Studien der noch ungeklärten Degradationsmechanismen von Oxiden in MOS-Bauelementen erleichtern. Darüber hinaus erlaubt die Ergänzung des physikalischen Modells für präexistente Defekte mit einem phänomenologischen Modell zur Beschreibung der Defektgeneration und -transformation eine sehr genaue und performante Berechnung der Lebensdauer von MOS-Bauteilen. Damit kann das in dieser Dissertation dargestellte Comphy-Modellierungssystem zu der Entwicklung und Verbesserung von MOS-Technologien beitragen.

Acknowledgements

PROF. TIBOR GRASSER is by far the most passionate and eager researcher I know and surely it is this passion which, at the same time, provides him the energy to maintain and encourage a large group of researchers in such a peaceful and productive way. Often I have benefited from his relentless commitment to fostering collaborations around the world and I am also truly grateful to you, Tibor, for inspiring me with your enthusiasm for research and for all that I have learned from you in the last years.

While studying at TU Wien, I have always appreciated the university's administrative efficiency, and this has remained the case even during my final days as a PhD student. DIETLINDE EGGER has helped to arrange my defense on short notice, and I am proud and thankful to have PROF. FELICE CRUPI, PROF. LUCA LARCHER and PROF. WOLFGANG GAWLIK on the examination committee.

> Certainly, my deepest gratitude goes to those whom I have befriended and with whom I share so many good memories. Unfortunately, there is not enough space to thank each of you, and even if there was, I am not sure I could find the words to adequately express my gratitude. Instead, I shall thank each of you in person and limit my acknowledgments below to the more technical aspects of this thesis' development.

I would like to thank PROF. SIEGFRIED SELBERHERR and PROF. ERASMUS LANGER, together with DIANA POP, RENATE WINKLER, EWALD HASLINGER, and MANFRED KATTERBAUER for fostering a professional, productive, and enjoyable working environment at the **Institute for Microelectronics**. The experimental studies I have conducted at this Institute would never have been possible without the equipment developed and guidance offered by MICHAEL WALTL. The basis for the development and implementation of the BTI models was provided by WOLFGANG GOES and FRANZ SCHANOVSKY, while THERESIA KNOBLOCH, MARKUS JECH, AL-MOATSAEM EL-SAYED, MISCHA THESBERG, LADO FILIPOVIC, YANNICK WIMMER and ALEXANDER GRILL always found time for helpful technical discussions and to proofread my thesis. PROF. HANS KOSINA, STANISLAV TYAGINOV, ROBERT KOSIK, BERNHARD STAMPFER, BIANKA ULLMANN, YURY ILLARIONOV, and JOHANN CERVENKA also contributed their expertise to this thesis.

My first contact with **imec and KU Leuven, Belgium** was through BEN KACZER and, from the very start, this enriching and fruitful collaboration could not have been more pleasant. During my PhD studies, I have spent more than a half year in the Device Reliability (DRE) group of imec and the exchange with the researchers there was indispensable for my work. For me DIMITRI LINTEN is the most outstanding team leader and together with GUIDO GROESENEKEN he enables the

achievements of this research group. I am deeply grateful to Ben Kaczer who broadened my technical and cultural horizons and contributed to this thesis like no other. His ideas served as the initial impetus of the Comphy framework and he coined its name. The technical comprehension of Jacopo Franco is beyond striking and he contributed extensively to this modeling framework and to my wonderful time at imec. Philippe J. Roussel and his mathematical expertise was important for the efficiency of Comphy and he is gratefully acknowledged for establishing Eq. (4.36), (4.37), (4.55), and (4.56). When it comes to the efficiency of Comphy, the refactoring of the Python code by Geert Hellings exceeded all expectations and enabled its success. I am truly grateful to my colleagues at the DRE group for the good times and their contributions to this thesis through experimental work and technical discussions. Thank you Simon Van Beek, Roman Boschke, Erik Bury, Adrian Vaisman Chasin, Shih-Hung Chen, Kent Chuang, Robin Degraeve, Myriam Janowski, Mirko Scholz, Vamsi Putcha, Marko Simicic, Alexandre Subirats, Barry O'Sullivan, Bart Vermeulen, and Pieter Weckx.

Markus Karner and Christian Kernstock welcomed me at **Global TCAD Solutions** when I was looking for a job during my master's studies, and I was pleased to find there a group of unconventional but nonetheless driven and dedicated developers and researchers, some of whom also supported me during my PhD studies. These include Ferdinand Mitterbauer, Philipp Prause, Oliver Triebl, Franz Schanovsky, Hui-Wen Karner, Klaus Schnass, Zlatan Stanojević and Oskar Baumgartner. Thank you, Markus and Christian, for this opportunity and for being truly kind supervisors.

Furthermore, I would like to thank Hans Reisinger, Wolfgang Gustin, Katja Puschkarsky, and Gunnar Rott from **Infineon, Munich** for sharing their experimental insights and providing measurement data. In the course of the European project "MoRV" I was lucky enough to collaborate with Domenik Helms and Reef Eilers from **Offis, Oldenburg**, with Roland Jancke and Kay-Uwe Giering from **Fraunhofer, Dresden**, and with Dan Alexandrescu from **IROC, Grenoble**. All of them did an outstanding job and the close collaboration within the consortium made this project such a successful and enjoyable one.

I am grateful to Martin Tomitsch, Daniela Rzepa, and Victoria Haykin for additional comments and proofreading. In large part the LaTeX template for this thesis was provided by Michael Waltl and Vel (`www.LaTeXTemplates.com`) and this research made use of the Python libraries `NumPy`, `SciPy`, and `matplotlib`. Finally, I would like to express my gratitude to those who motivated me through their interest and encouragement. It were the sincere words of Shinya Yamakawa from Sony, Runsheng Wang from Peking University, Kevin Huang from TSMC, and many other kind colleagues which spurred me to finish the work for this thesis.

Contents

Abstract iii

Kurzfassung v

Acknowledgements vi

Acronyms xiii

1 Introduction 1
- 1.1 MOS Devices and Oxide Defects . . . 1
  - 1.1.1 Random Telegraph Noise . . . 1
  - 1.1.2 Gate Leakage Currents . . . 1
  - 1.1.3 Time-Dependent Dielectric Breakdown . . . 2
  - 1.1.4 Stress-Induced Leakage Currents . . . 2
  - 1.1.5 Hot-Carrier Degradation . . . 2
  - 1.1.6 Bias Temperature Instabilities . . . 2
- 1.2 Identifying Defect Structures . . . 3
- 1.3 BTI Modeling and Controversies . . . 4
- 1.4 About this Work . . . 5
  - 1.4.1 Motivation and Outline . . . 5
  - 1.4.2 Scope . . . 6
  - 1.4.3 Structure . . . 7
  - 1.4.4 Contributions Made in this Thesis . . . 7

2 Measurement Techniques 9
- 2.1 Transfer Characteristics . . . 9
  - 2.1.1 Transconductance . . . 9
  - 2.1.2 Threshold Voltage . . . 9
  - 2.1.3 Subthreshold Swing . . . 10
  - 2.1.4 Hysteresis . . . 12
- 2.2 Measure-Stress-Measure Scheme . . . 12
  - 2.2.1 Extended MSM Technique . . . 12
  - 2.2.2 Capture-Emission Time Map Visualization . . . 12
- 2.3 On-The-Fly Measurements . . . 14
- 2.4 From Noise to Single Defects . . . 14
  - 2.4.1 Anomalous RTN . . . 15
  - 2.4.2 Temporary RTN . . . 16
  - 2.4.3 Reversal RTN . . . 16
  - 2.4.4 Correlated Drain and Gate RTN . . . 16
  - 2.4.5 Deep-Level Transient Spectroscopy on Single Defects . . . 17
  - 2.4.6 Time Dependent Defect Spectroscopy . . . 17

3 Models **19**
- 3.1 Power Law Extrapolation 19
- 3.2 Exponential-Poisson Distribution 19
- 3.3 Simple Descriptions of the Quasi-Permanent Part 22
  - 3.3.1 Brower's Simple Thermal Model 22
  - 3.3.2 Field-Dependent Thermal Transition 22
- 3.4 Non-Radiative Multi-Phonon Models 22
  - 3.4.1 Early Applications to MOS Devices 24
  - 3.4.2 4-State NMP Model 27
  - 3.4.3 Gate-Sided Hydrogen Release Model 33

4 Compact-Physics Framework: Comphy **39**
- 4.1 Electrostatics 39
  - 4.1.1 Band Gap 39
  - 4.1.2 Effective Carrier Masses 40
  - 4.1.3 Effective Density of States 41
  - 4.1.4 Carrier Concentrations at Thermal Equilibrium 41
  - 4.1.5 Electrostatics of a 1D MOS Device 43
- 4.2 Tunneling 48
  - 4.2.1 Band Edges in the Vicinity of Interfaces 49
- 4.3 2-State NMP Model 52
  - 4.3.1 Comparison of 2 and 4-State Models 52
  - 4.3.2 Modeling of Single Defects 53
  - 4.3.3 Ensembles of Defects 57
  - 4.3.4 Effective 3-State Frequency Dependence 61
- 4.4 Double-Well Model 61
- 4.5 Efficient Solution for AC Stress 63

5 Experiments and Simulations **65**
- 5.1 General Material and Simulation Settings 65
  - 5.1.1 Defect Parameter Extraction 65
  - 5.1.2 General Comphy Settings 66
- 5.2 List of Investigated Technologies 67
  - 5.2.1 Commercial 130 nm SiON Technology (*Tech. A*) 68
  - 5.2.2 Commercial 28 nm High-κ Technology (*Tech. B*) 68
  - 5.2.3 14 nm High-κ FinFET Technology (*Tech. C*) 68
  - 5.2.4 DRAM Logic Technology (*Tech. D*) 68
- 5.3 From Noise to BTI 69
- 5.4 Recoverable and Quasi-Permanent NBTI 72
  - 5.4.1 Experimental Data 72
  - 5.4.2 Modeling with TCAD 72
  - 5.4.3 Modeling with Comphy 77
- 5.5 Recoverable BTI of High-κ Devices 80
  - 5.5.1 Experimental Data 80
  - 5.5.2 Unified TCAD Simulations 81
  - 5.5.3 Contributions of Shallow HfO_2 and Deep SiO_2 Defects 84
- 5.6 Full BTI of High-κ Devices 87
  - 5.6.1 Experimental Data 87
  - 5.6.2 Parameter Extraction with Comphy 88
  - 5.6.3 Lifetime Extrapolation 88
- 5.7 Gate Stack Engineering and Anomalous BTI 92

5.7.1 Experimental Data . . . 92
5.7.2 Investigation of PBTI . . . 92
5.7.3 Investigation of NBTI . . . 93
5.7.4 Summary and Lifetime . . . 99
5.8 AC and Frequency Dependence . . . 100
5.8.1 2-State Frequency Dependence . . . 100
5.8.2 Effective 3-State Frequency Dependence . . . 101
5.9 Summary of the Results . . . 102
5.9.1 Defects Responsible for BTI . . . 102
5.9.2 Anomalous BTI . . . 103
5.9.3 Lifetime Extrapolation . . . 103
5.9.4 Thermal Budget and Anneals . . . 103
5.9.5 Diffusion of Aluminum . . . 103

6 Conclusions and Outlook **107**
6.1 Conclusions . . . 107
6.2 Outlook . . . 108
6.2.1 Extensions of the Comphy Framework . . . 108
6.2.2 Studies of Novel Materials and Structures . . . 108

Bibliography **109**

List of Publications **121**

Curriculum Vitae

Acronyms

ALD	atomic layer deposition
BTI	bias temperature instability
CC	configuration coordinate
CCDF	complementary cumulative distribution function
CDF	cumulative distribution function
CET	capture/emission time
CV	capacitance-voltage
DFT	density functional theory
DLTS	deep-level transient spectroscopy
DRAM	dynamic random-access memory
eMSM	extended measure-stress-measure
EOT	equivalent oxide thickness
ESR	electron-spin resonance
HCD	hot-carrier degradation
HDL	Harry Diamond Laboratories
HEMT	high-electron-mobility transistor
ISSG	in situ steam generated
MOS	metal-oxide-semiconductor
MOSFET	MOS field-effect transistor
MPE	lattice relaxation multiphonon emission
MSM	measure-stress-measure
NBTI	negative bias temperature instability
NCP	non self-consistent Poisson
NMP	non-radiative multi-phonon
NRA	nuclear reaction analysis
OTF	on-the-fly
PBTI	positive bias temperature instability
PDA	post deposition anneal
PDF	probability density function
PUF	physical unclonable function
R-D	reaction-diffusion
RRAM	resistive random-access memory
RTN	random-telegraph-noise
RTO	rapid thermal oxidation
SCP	self-consistent Poisson
SDL	second derivative of logarithmic drain current
SDR	spin-dependent recombination
SILC	stress-induced leakage current
SIMS	secondary ion mass spectrometry
SRH	Shockley Read Hall
STM	scanning tunneling microscopy
TAT	trap-assisted tunneling
TCAD	technology computer aided design
TDDB	time-dependent dielectric breakdown
TDDS	time dependent defect spectroscopy
TEM	transmission electron microscopy
WKB	Wentzel-Kramers-Brillouin

Chapter 1

Introduction

A deceptively simple stack of three materials has changed the world at an arguably unprecedented pace: metal-oxide-semiconductor (MOS) structures constitute the essential parts of most electronic devices which are used in everyday life. Of particular importance are MOS devices which exploit the field effect to switch currents on and off. The combination of billions of these MOS field-effect transistors (MOSFETs) on microelectronic chips is at the heart of electronic devices as it is responsible for computations. Unfortunately, the speed and the lifetime of these devices is governed by imperfections in the oxide layer. This amorphous material is prone to capture charges under operating conditions which alter the characteristics of MOS devices. This chapter outlines the corresponding degradation phenomena, the responsible mechanisms, and the related modeling attempts. Furthermore, it will be summarized how this thesis contributes to a better understanding of the above and, thus, enables improvements of the reliability and performance of MOS devices.

1.1 MOS Devices and Oxide Defects

Already a few years after the first demonstration of a point-contact transistor in 1947, the noise theory established by SCHOTTKY [1] was applied to investigate deviations from the thermal noise of these devices where an increase of the noise spectrum towards lower frequencies was observed. A review on that problem was published in 1952 where PETRITZ *et al.* summarized that this $1/f$ noise was found to be consistent with "*superimposing spectra of the* $(1/1+(\omega\tau)^2)$ *type*" and that "*a* $1/f$ *law can be approximated over a large frequency interval if a sufficiently large distribution of lifetimes is used*" [2]. Only the nature of this modulation remained speculative at that point and was eventually experimentally verified in 1985 by UREN *et al.* as "*individual carrier trapping events*" [3]. These carrier trapping events are the *common underlying source* of several reliability phenomena which will be outlined in the following.

1.1.1 Random Telegraph Noise

After the $1/f$ noise on large devices was identified as the superposition of the noise from individual carrier trapping events, much effort was put into the study of random-telegraph-noise (RTN) on devices with small gate areas. In these small devices, single carriers trapped in the interfacial region between the oxide and the channel can modulate the drain current substantially. The analysis of these discrete steps and their stochastic properties give insights on the underlying defect kinetics. Such studies were conducted within the framework of non-radiative multi-phonon (NMP) theory already in 1988 [4].

1.1.2 Gate Leakage Currents

Oxides of regular MOS devices are supposed to insulate the gate from the channel. However, not only fundamental mechanisms such as quantum mechanical tunneling and high energetic carriers can deteriorate this ideal property: The carrier trapping events discussed above can be directional, meaning that carriers are trapped from the channel and released to the gate. This will be observed as RTN *and* at the same time such defects act as tunneling centers which induce a gate leakage current [5], also referred to as trap-assisted tunneling (TAT) [6].

1.1.3 Time-Dependent Dielectric Breakdown

The leakage mechanism described in the previous subsection is stochastic but apart from that independent of time. However, it was observed that the leakage currents through dielectrics of MOS structures strongly depend on the stress time and eventually cause a breakdown of the insulator. Already in 1973, the role of defect creation was discussed as the responsible mechanism for this phenomenon but only the barrier lowering due to these charges was considered [7]. In 1995, Degraeve *et al.* proposed a model which considered both, the creation of traps and their role as tunneling centers to consistently describe time-dependent dielectric breakdown (TDDB) [8].

1.1.4 Stress-Induced Leakage Currents

While TDDB deals with tunneling currents at stress conditions, an increased tunneling current is also observed at low electric fields *after* stressing a MOS device. This phenomenon was reported in 1988 as stress-induced leakage current (SILC) and found to be *not* due to positive charge generation [9]. Experimentally, it is difficult to separate the mechanisms causing TDDB and SILC because generated defects will affect both. Accordingly, Crupi *et al.* demonstrated a correlation of SILC and defect generation in the HfO_2 layer of high-κ technologies in 2004 [10]. This finding was confirmed by later studies [11] and the subtle differences between defect generation and the transformation of pre-existing defects were discussed by Veksler *et al.* in 2014 [12]. The latter employed the NMP theory as applied to model SILC already in 2001 by Larcher *et al.* [13] and extended it by metastable states.

1.1.5 Hot-Carrier Degradation

All the abovementioned degradation phenomena related to leakage currents are due to defects in the oxide of MOS devices and are accelerated by elevated oxide fields. As opposed to that, at low oxide fields, defects in the oxide are of much less concern. However, highly energetic (“hot”) carriers can affect defects in the interfacial region of MOS structures. This hot-carrier degradation (HCD) mechanism is typically observed on MOSFETs when stress voltages are applied between the source and the drain [14, 15]. Since the work Hu in 1985, the depassivation of silicon-hydrogen bonds at the interface between the channel and the oxide have been discussed as the underlying cause [16], however, there is an ongoing controversy about the detailed mechanism [17].

1.1.6 Bias Temperature Instabilities

As discussed above, pre-existing and newly created defects in the oxide of MOS devices can capture charges, in particular at elevated oxide fields. Reports on the temperature dependence of transistors around the year 1952 [18] were followed by studies of interface state creation in 1963 [19] and of oxide vacancies in 1964 [20], all based on experimental investigations of SiO_2 under elevated bias voltage and temperature conditions. This degradation effect is now referred to as bias temperature instability (BTI).[1] Historically, this effect has become of particular importance for *negative* gates voltages and is termed negative bias temperature instability (NBTI). Several

---

[1] Further studies of this mechanism were conducted in 1966 by Miura *et al.* [21] and in 1967 by Deal *et al.* [22], the latter is often cited as the first report on bias temperature instability (BTI).

modern technologies are also considerably affected by oxide charges which accumulate at *positive* gate voltages and, thus, positive bias temperature instability (PBTI) became relevant as well. Whether and to which extend BTI and HCD act on the same defects is not fully established [23, GRJ1].

Recoverable and Quasi-Permanent BTI

Early experimental studies neglected the fast recovery of NBTI until Ershov *et al.* reported a *recoverable* and a *permanent* component in 2003 [24]. In the following years, this phenomenon was studied intensively [25], however, has remained elusive from both an experimental and a theoretical point of view: Up to date, no experimental technique is accepted to determine these components separately. Some studies suggested, that the permanent component is due to P_b centers at the Si/SiO$_2$ interface and the recoverable component is due to oxide defects [26]. While this assumption is debated as such [27], even the experimental separation of P_b centers cannot be conducted rigorously since oxide defect close to the Si/SiO$_2$ interface can have very similar properties to “real” interface states and contribute to CV measurements, DCIV measurements, etc.

A pragmatic solution to treat these two components of BTI separately is based on a pulse into accumulation which is applied after NBTI stress: It was observed that pMOS devices recover considerably during short periods of *positive* gate voltages after stress phases with negative gate voltages [28, 29]. Conveniently, the part which recovers during this pulse roughly correlates with what was considered to be the *recoverable component*. With respect to defect physics, this means that the mechanism which constitutes the recoverable component has emission time constants which are sensitive to the applied gate voltage which is not the case for the mechanism constituting the permanent component.

Note that the permanent component is to a large part not really *permanent* but recovers very slowly [GRC1] and we will refer to it as “quasi-permanent” component in this work.

Anomalous BTI

Typically, pre-existing oxide defects get positively charged during NBTI stress which induces a shift of the threshold voltage of MOS devices towards *negative* voltages. Vice versa, pre-existing oxide defects get negatively charged during PBTI stress which induces a shift of the threshold voltage towards *positive* voltages. Both of the above is a result of defects interacting with carriers in the *channel*. In contrast, if defects capture charges from the *gate*, opposite shifts of the threshold voltage are observed: *positive* shift during NBTI stress and *negative* shift during PBTI stress. This phenomenon is called *anomalous BTI* and was reported for the case of NBTI by [30] and for PBTI by [31, 32].

1.2 Identifying Defect Structures

The fact that *all* reliability phenomena listed above are consistent with *individual carrier trapping events* explains the frantic search for underlying defect structures. All kind of experimental and theoretical means have been employed to identify the culprit, a selection of which is given below.

- Electron-spin resonance (ESR) spectrometry [33] and spin-dependent recombination (SDR) technique [34] to probe paramagnetic point defects
- Resonant nuclear reaction analysis (NRA) to detect hydrogen [35]
- Transmission electron microscopy (TEM) [36] and scanning tunneling microscopy (STM) [37] to analyze the surface structure and thickness of layers

- Secondary ion mass spectrometry (SIMS) to analyze the composition of thin films [38]
- Charge pumping [39] and DCIV [40, 41] to estimate the concentration of fast interfacial states
- CV curves to profile the energy, density, and time constants of defects [42, 43]
- Density functional theory (DFT) for theoretical investigation of defect properties [44]

However, up to date, there is no consent in the literature on defect structures. Certainly, physical mechanisms have been proposed which describe some of the phenomena very well, but no model is consistent with *all* experimental observations. Even the simple case of MOS devices with a plain SiO_2 oxide and its well studied interface to the Si channel is debated: While the passivation and depassivation of Si dangling bonds with hydrogen most certainly plays a role, the details of the physical processes and the location of hydrogen before and after such a reaction are not fully established [45–47].

For defects in the SiO_2 layer of these devices, the situation is even less established, indicating that either a) a multitude of defect mechanisms or b) one rather complex defect mechanism is responsible for the degradation in this case.

A selection of defects which are discussed in the context of BTI is given below.

- P_b centers (where Si has a "*dangling bond*") are often suggested to be the dominant interface trap for both (111) and (100) Si/SiO_2 interfaces. Depending on the surface orientation, there are different types of P_b centers [48, 49].
- *Oxygen vacancies* are a defect structure in SiO_2 where two neighboring Si atoms are bonded to three instead of four oxygen atoms and were reported as a promising defect candidate, featuring multiple configurations such as the E' and E'_γ center [50].
- Also in *hydrogen bridge* defects the bond between two neighboring Si atoms in SiO_2 is distorted, but here a hydrogen atom replaces the oxygen atom [51].
- *Hydroxyl E' centers* are defects in SiO_2 where the dangling bond of a threefold-coordinated Si atom faces a hydroxyl O-H group. Similar to the oxygen vacancy and the hydrogen bridge, this defect type exhibits stable and metastable configurations in two charge states [52].

1.3 BTI Modeling and Controversies

In 1977 Jeppson and Svensson proposed a physical model for NBTI which considered two mechanisms [53]:

- *Mechanism A*: The depassivation of a Si-H defect at the Si/SiO_2 interface during stress forms a P_b center. The released hydrogen forms a hydroxyl group with a neighboring oxygen atom and diffuses away, leaving a positively charged oxygen vacancy behind.[2]
- *Mechanism B*: Holes tunnel from the valence band to defects in the oxide which, through an unknown mechanism, activate surface traps.

As most NBTI models proposed to this day are merely a modification of the above - this would be the end of this section if there was not a vivid controversy on the role of these two mechanisms, fueled by experimental studies of modern MOS technologies [54]. For many years, the model

---

[2] This was *one possible realization* proposed by the authors after a discussion of such a mechanism in general. Thus, the defect structure at the interface and the diffusing species was not claimed to be known.

of Jeppson and Svensson, usually referred to as “reaction-diffusion (R-D) model”[3], was happily accepted as the explanation for the power law dependence of the degradation and *mechanism A* was considered to be the dominant contributor [55–58]. Then, the fast recovery after NBTI stress [24] and the observations on small devices where time constants of individual defects were determined [4] shifted the attention towards *mechanism B* [59–61]. To some extent, this was accepted by the groups which used to consider *mechanism A* as the governing contributor to NBTI [62, 63], but eventually, it was heavily disputed whether, under which conditions, and to which extent NBTI is governed by a [54]

- *diffusion-limited* process (*mechanism A*) or by a
- *reaction-limited* process (*mechanism B*).

The criticism on the former is related to the unphysical parametrization which is required to describe the degradation of thin oxides as a diffusion-limited process [54]. On the other hand, some early studies of NBTI as a reaction-limited process ignored the role of interfacial states and defect creation as they relied entirely on pre-existing defects [60]. This was soon corrected [61], still, the reaction-limited description of defect creation is criticized [54]. An overview of BTI models is found in [25, 29, 54, 64, 65, GRC2].

1.4 About this Work

In this section, the central motivation which led to this thesis will be outlined. Furthermore, the scope and structure of this work will be discussed and the original contributions of this thesis will be pointed out.

1.4.1 Motivation and Outline

To this day, there are more than 10 000 publications on BTI [66] and literature research makes one feel like every degradation mechanism one could possibly think of has been already proposed. Still, the reliability community is searching for *the* defect candidate and the industry uses oversimplified power law descriptions or some R-D models of disputed physicality. Thus, a reasonable approach for “another BTI study” appears to be the following:

- *Step 1*: Connect the *right* dots: Identify and link the degradation mechanisms which are consistent with as many observations as possible.
- *Step 2*: As the above will give a very complex picture, abstract the essence to find a concise description which is useful for a broader range of applications.

In the last years, research groups at Infineon (Munich and Villach), imec (Belgium) and at the Institute for Microelectronics, TU Wien, have pursued *step 1* with considerable success: After the NMP theory was identified as an important part of the description of charge trapping in pre-existing oxide defects, the research efforts culminated in the *gate-sided hydrogen release model* [GRC3]. This model is indeed a consistent and physical one but its parametrization is very challenging and it is computationally too expensive for fast characterization of multiple technologies.

This led to *step 2* where we abstracted the gist of the complex models and created a simple and easy to use framework we call *Comphy*, short for “compact-physics”. Thereby, not only were the computational expenses reduced (see Fig. 1.1) but also the models were opened to scrutiny by others as they became fully transparent with *all* parameters listed.

---

[3] While in the original work, Jeppson and Svenson acknowledged several physical degradation mechanisms [53], the term *R-D* is often used for models which consider diffusion as the governing degradation mechanism [54].

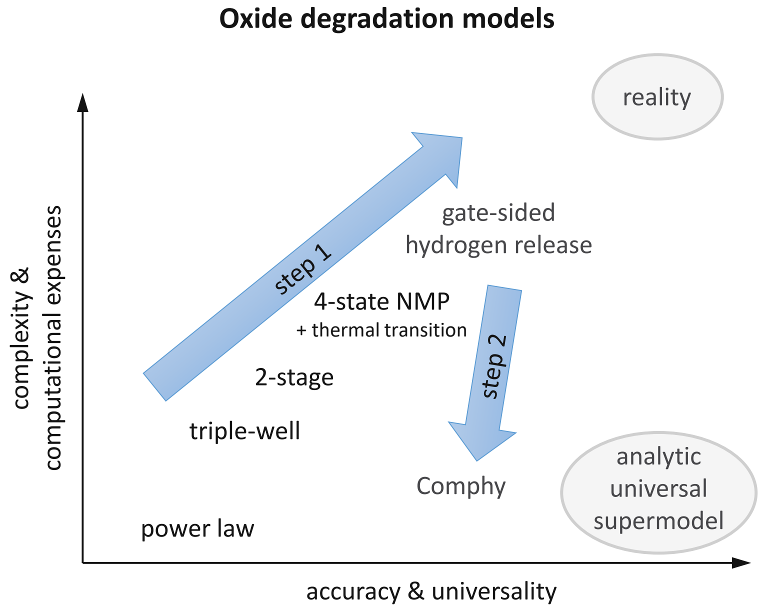

Figure 1.1: A schematic evaluation of oxide degradation models. *Step 1* indicates the efforts of Grasser *et al.* to develop an accurate and universal defect model, irrespective of computational costs. This started with the *triple-well model* [60], followed by the *2-stage model* [61], the *4-state NMP model* [67], and culminated in the *gate-sided hydrogen release model* [GRC3]. *Step 2* indicates the abstraction of the complex mechanisms in the concise but still physical framework *Comphy* [GRJ2]. The existence of an *analytic universal supermodel* is questioned and the complexities of *reality* are acknowledged.

1.4.2 Scope

The models presented in this work describe *reaction-limited* processes since diffusion of relevant species in thin oxides was found to be too fast to determine transfer rates [54]. Furthermore, only those models and experimental techniques are discussed which are of direct consequence for the presented results and their interpretation.

While it is tempting to apply a theory to the most advanced techniques, an in-depth understanding of the basic mechanisms has to be established first. This is done in this work by starting the analysis of BTI on simple planar MOS devices with plain SiO_2 oxides. After resolving that, we will increase the complexity step by step towards high-κ FinFETs and different multi-layer gate stacks. We have already demonstrated the applicability of the models to more advanced technologies such as

- SiGe devices [GRC4, GRJ3, GRJ4]
- GaN/AlGaN high-electron-mobility transistors (HEMTs) [GRC5]
- InGaAs MOS devices [GRC6]
- Nanowires [GRC7–GRC9]
- Junctionless devices [GRC10]
- 2D channel devices with black phosphorus (BP) [GRJ5, GRJ6], molybdenum disulfide (MoS_2) [GRT1, GRJ7, GRJ8, GRC11, GRC12], and graphene [GRJ5]

However, in this work we want to establish the fundamental properties of oxide defects. Most sensibly, such studies are conducted on well characterized and understood MOS devices with Si channels and, thus, limited to those.

The device-to-device variability is inherent to BTI models which describe the charge transfers of single defects [GRC13, GRJ9]. We will study this variability and its time-dependence, but we will not cover across-wafer variability.

1.4.3 Structure

After this introduction, an overview is given of *experimental techniques* (Chapter 2) and *models* (Chapter 3) for BTI on which this work will build upon. In Chapter 4, the fundamental theory of 1D MOS devices which is required for physical modeling is presented, followed by a description of the BTI models we have implemented in the *Comphy* framework. The results of exemplary technologies are presented in Chapter 5 where we will demonstrate for both, technology computer aided design (TCAD) simulations and Comphy simulations, that a profound understanding of BTI is established. Finally, the work is summarized in Chapter 6.

1.4.4 Contributions Made in this Thesis

The first three chapters of this work are a summary of the state of the art and literature research on BTI. This serves as a basis for the Comphy framework presented in Chapter 4 and for the results presented in Chapter 5, both established through this PhD research.

The main work in Chapter 4 was to find a description which relies on established physics but is efficient to model BTI with all key mechanisms included:

- Section 4.1: A summary of selected semiconductor physics and how they can be employed to model a 1D MOS device with oxide charges. The latter is original work and was outlined in [GRJ2].
- Section 4.2: While the Wentzel-Kramers-Brillouin (WKB) approximation is well established to compute tunneling probabilities in oxides, general formulas are presented here, which, to the best of our knowledge, were not previously published.
- Section 4.3: The basic physics of defects with two states in the framework of the NMP theory have been well established for many years. The contribution of this work is how these physics can be described sufficiently accurate for BTI modeling. In particular, an advanced approximation for the interaction with Fermi-Dirac distributed carriers is presented as previously outlined in [GRJ2]. The part on the effective 3-state frequency dependence is taken from the literature.
- Section 4.4: A simple double-well model is presented which is a slightly modified version of previously published models to better capture the experimental evidence. This model was outlined in [GRJ2].
- Section 4.5: An efficient way to compute degradation for AC signals is reviewed. The formula for analytic evaluation of digital AC stress was not published before.

In Chapter 5, a broad range of experimental data and simulations with TCAD and Comphy are presented. For this, we implemented the 4-state NMP model in a commercial TCAD software. Our implementation of this BTI model can handle arbitrary device geometries and considers the interaction of oxide defects with carriers in the gate and in the channel [GRC14]. Comphy was implemented in a Python framework [GRJ2].

- Section 5.1: General simulations procedure, parameters, and settings for the simulations.
- Section 5.2: A summary of the technologies investigated in this chapter.
- Section 5.3: A TCAD study linking noise to BTI, originally presented in [GRC14].

- Section 5.4: Previously published data is reproduced with TCAD simulations [GRC15] and Comphy simulations [GRJ2] to demonstrate recoverable and quasi-permanent NBTI.
- Section 5.5: Experiments conducted through this PhD research are reproduced with TCAD simulations to extract the properties of defects which are responsible for recoverable BTI of high-κ devices [GRC16]. This study is complemented by previously unpublished experimental data on the variability of small devices.
- Section 5.6: Experimental data is reproduced with Comphy simulations to investigate the lifetime of commercial high-κ technologies [GRJ2].
- Section 5.7: The impact of process engineering on the BTI behavior is analyzed by applying Comphy simulations to a broad set of experimental data [GRJ2].
- Section 5.8: A brief discussion on AC modeling with Comphy and the frequency dependence is presented based on experimental data and simulations, originally outlined in [GRJ2] and complemented by frequency dependent data which was not published previously.
- Section 5.9: The key findings are summarized and all Comphy parameters are listed. The parameters were originally published in [GRJ2].

Chapter 2

Measurement Techniques

In this chapter, we will summarize the most fundamental measurement techniques to quantify BTI and to analyze the properties of single defects.

2.1 Transfer Characteristics

The drain current I_D of a MOSFET as a function of the gate voltage V_G at a given drain voltage V_D is typically referred to as "transfer characteristics", "$I_\mathrm{D}V_\mathrm{G}$ curve", or simply "IV curve". This curve is subject to charges in the oxide and, as such, often used to quantify BTI. Measuring I_D while sweeping V_G at a small V_D might appear straightforward, however, the timing is crucial since defects with short time constants can charge or discharge during the measurement. This effect can be employed in dedicated experiments such as hysteresis measurements [68], but usually, $I_\mathrm{D}V_\mathrm{G}$ curves are intended to give a *snapshot* of the transistor properties. To minimize the impact of charge capture and emission during V_G sweeps, very fast measurements are desirable [69]. In this section, common transistor parameters such as the transconductance g_m, the threshold voltage V_th, the subthreshold swing SS, and the hysteresis width will be outlined on the basis of $I_\mathrm{D}V_\mathrm{G}$ curves.

2.1.1 Transconductance

The transconductance g_m stands for "transfer conductance" and is the small-signal conductance for input gate voltage and output drain current as a function of V_G at constant V_D:

$$g_\mathrm{m} = \frac{\mathrm{d}I_\mathrm{D}}{\mathrm{d}V_\mathrm{G}} \tag{2.1}$$

Charges close to the interface of the channel affect carriers due to Coulomb scattering and reduces their mobility [70]. Furthermore, it was shown that the mobility degradation due to interface-states can be determined by the mobility at the point of maximum transconductance $g_\mathrm{m,max}$ [71] and that the transconductance is proportional to the mobility [72]. Therefore, the degradation of $g_\mathrm{m,max}$ indicates an increase in the concentration of defects in the near-interfacial region which makes it an important parameter for characterization of oxide degradation.

2.1.2 Threshold Voltage

Naturally, the gate voltage above which a significant drain current is observed in MOSFETs is an important device parameter. However, when it comes to the definition of this threshold voltage V_th, it does not seem to be that natural anymore: There are several theoretical definitions [73] and many different experimental extraction methods [74, 75]. Common experimental methods will be outlined below. The most popular theoretical definition is that V_th is the gate voltage at which the surface potential of the channel equals two times the Fermi potential in the bulk. For quantification of BTI, the *shift* ΔV_th of the threshold voltage is often used since it represents the impact of all charges in the oxide and at the interface on the transistor performance. However, the extraction of ΔV_{th} at low gate voltages implies that very fast states in the near-interfacial region are usually lost in the measurement, depending on their defect level. It was experimentally shown that even 1 ns after NBTI stress, V_{th} has partially recovered [76]. For this reason, ΔV_{th} is commonly considered to describe a rigid shift of the $I_{\mathrm{D}}V_{\mathrm{G}}$ curve while the fast transient features have to be captured with dedicated techniques.

Constant Current Method

In the simple *constant current* method, the threshold voltage is identified as the gate voltage where

$$I_{\mathrm{D}}\frac{L}{W} = I_{\mathrm{ref}} \tag{2.2}$$

holds with W being the channel width and L the channel length as shown in Fig. 2.1. I_{ref} is the normalized current criterion which is typically 1 nA but may vary between technologies. This method enables continuous measurement of V_{th} by tracking V_{G} with a feedback loop to maintain a constant I_{D} [69].

Linear Extrapolation Method

If full $I_{\mathrm{D}}V_{\mathrm{G}}$ curves are available, the *linear extrapolation* method is most frequently used to determine V_{th}: From the $I_{\mathrm{D}}V_{\mathrm{G}}$ curve, g_{m} is computed to obtain the gate voltage of $g_{\mathrm{m,max}}$. At this voltage, the $I_{\mathrm{D}}V_{\mathrm{G}}$ curve is extrapolated linearly to zero drain current. Subtracting $V_{\mathrm{D}}/2$ from this gate voltages gives V_{th} [77] as shown in Fig. 2.2.

Second Derivative of Logarithmic Drain Current Method

The *SDL method* [78] addresses the shortcoming of the linear extrapolation method which is its deviation of the extracted V_{th} from the theoretical value used in compact models. Furthermore, the SDL method is suitable for both low and high drain voltages. In this method, V_{th} is defined as the gate voltage at which the second derivative of the logarithm of the drain current has its minimum, see Fig. 2.3.

2.1.3 Subthreshold Swing

The *shubthreshold swing SS* is defined as the inverse of the *subthreshold slope* of the $\log(I_{\mathrm{D}})V_{\mathrm{G}}$ curve [79]:

$$\begin{aligned} SS &= \frac{\mathrm{d}V_{\mathrm{G}}}{\mathrm{d}\log\left(I_{\mathrm{D}}\right)} && (2.3)\\ &= \ln(10)\frac{\mathrm{d}V_{\mathrm{G}}}{\mathrm{d}\ln\left(I_{\mathrm{D}}\right)} && (2.4)\\ &= \ln(10)\frac{\mathrm{d}V_{\mathrm{G}}}{\mathrm{d}\ln\left(\beta\psi_{\mathrm{S}}\right)} && (2.5)\\ &= \ln(10)\frac{k_{\mathrm{B}}T}{q}\frac{C_{\mathrm{ox}}+C_{\mathrm{D}}+C_{\mathrm{it}}}{C_{\mathrm{ox}}} && (2.6) \end{aligned}$$

Here, C_{D} is the depletion capacitance, C_{ox} is the oxide capacitance, and C_{it} is the capacitance associated with the interface state density N_{it} [80]. While the effect of fast near-interfacial defects

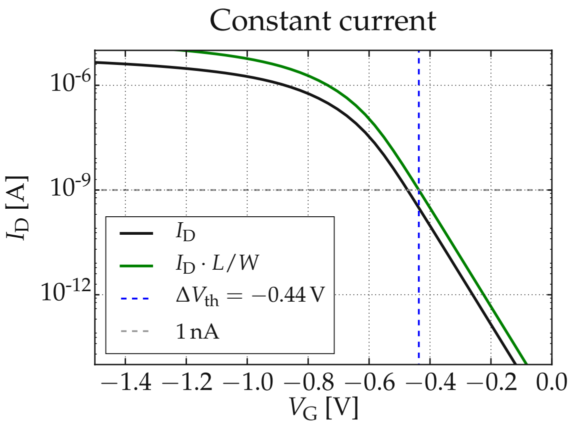

FIGURE 2.1: An $I_D V_G$ curve (black) of a pMOSFET from TCAD simulation with the channel width $W = 20$ nm and the length $L = 65$ nm. In the *constant current* method, V_{th} is extracted at $I_D L/W = I_{ref}$. The reference current I_{ref} is assumed to be 1 nA here.

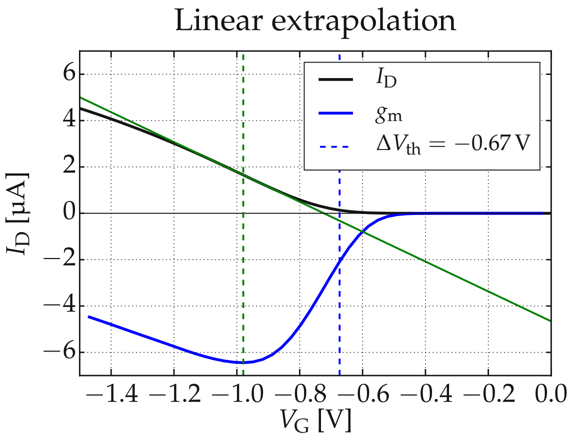

FIGURE 2.2: For the extraction of V_{th} with the *linear extrapolation method*, first the V_G which corresponds to $g_{m,max}$ has to be determined. In this point, the $I_D V_G$ curve is extrapolated to zero drain current and from this gate voltage $V_D/2$ is subtracted to obtain V_{th} [77].

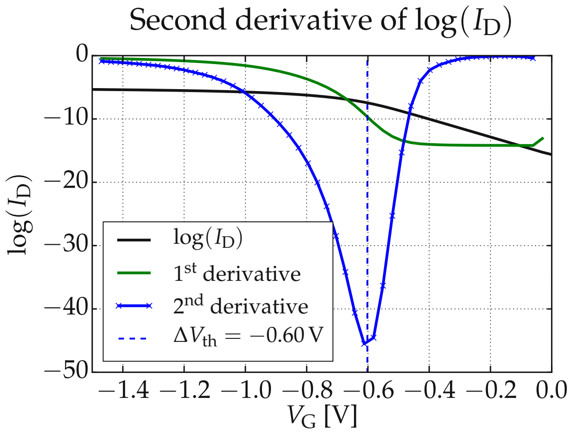

FIGURE 2.3: The second derivative of logarithmic drain current (SDL) method is based on the second derivative (blue) of the logarithm of the drain current (black). The threshold voltage V_{th} is then defined as the gate voltage at which the second derivative has its minimum [78].

is typically not monitored in V_{th} measurements, it can be observed as a degradation of SS, accordingly. In the ideal case with $C_{\mathrm{D}} = C_{\mathrm{it}} = 0\,\mathrm{F}$ the subthreshold swing evaluates to $\ln(10)k_{\mathrm{B}}T/q$ which gives the well known lower limit of $SS \approx 60\,\mathrm{mV/dec}$ for room temperature.

2.1.4 Hysteresis

Ideal $I_{\mathrm{D}}V_{\mathrm{G}}$ curves which are not affected by transient charge trapping give the same reproducible result for a given sweep range, slew rate, and measurement temperature. However, in reality, such measurements are affected by charge trapping and, accordingly, a hysteresis between consecutive up and down-sweeps of V_{G} will be observed in I_{D} of MOSFETs. While this effect is usually negligible in silicon technologies, it can be pronounced for example in less stable 2D technologies where this technique is employed to investigate charge trapping [GRJ5, 81, GRC17]. Similarly, also in more stable high-κ technologies [82] as well as in Ge-based [83] and SiC-based technologies [68], this effect is investigated.

2.2 Measure-Stress-Measure Scheme

Since the shift of the threshold voltage was accepted as an important measure of BTI, the idea of the measure-stress-measure (MSM) scheme is very obvious: Measure the initial threshold voltage $V_{\mathrm{th,0}}$ of a MOSFET, apply stress at elevated V_{G} and temperature for some time, and measure V_{th} again afterwards to characterize the degradation as $\Delta V_{\mathrm{th}} = V_{\mathrm{th}} - V_{\mathrm{th,0}}$. The problem with this naive approach was already identified by Breed in 1975: "*a considerable part of the trapped charge disappears as soon as the voltage bias is removed from the sample*" [84], meaning that the measurement delay t_{D} between the stress phase and the subsequent measurement is crucial. While apparently this fact was of no concern for many years, the problem resurfaced in 2003 when BTI research gained traction and Ershov reported "*an unusual effect - a significant dynamic recovery relaxation of NBTI degradation after removal of stress voltage*" [85]. This triggered experimental efforts to reduce t_{D} in order to minimize a loss of information about the actual degradation during stress: While Ershov measured with $t_{\mathrm{D}} = 0.4\,\mathrm{s}$ [85], later in 2003 Rangan reported data with $t_{\mathrm{D}} = 1\,\mathrm{ms}$ [86], followed by Reisinger in 2006 with $t_{\mathrm{D}} = 1\,\mu\mathrm{s}$ [69], and finally in 2018 Yu reported an experimental setup with $t_{\mathrm{D}} = 1\,\mathrm{ns}$ which is still not fast enough to measure V_{th} without recovery effects [76].

2.2.1 Extended MSM Technique

On the one hand, the fast recovery after stress poses difficulties for characterization of BTI, while on the other hand this recovery comprises valuable information about the defect kinetics, a fact employed by the *extended measure-stress-measure (eMSM) technique* [87]: Instead of recording V_{th} for a short period after stress and then applying stress conditions again, the recovery period is extended to record the recovery behavior of V_{th} for a long time. After this *recovery trace* is recorded, the same stress conditions are applied again with incremental stress times for subsequent stress phases. Conveniently, the subsequent phases are typically not affected by the extended measurement phases if the stress times are increased exponentially with a factor of about 10 [69] as shown for a measurement in Fig. 2.4.

2.2.2 Capture-Emission Time Map Visualization

The eMSM technique with a recovery trace after each subsequent stress phase contains detailed information on the defects and their time constants which are active at the given stress and recovery conditions [87]. A way to *visualize* these time constants and the related degradation intuitively are capture/emission time (CET) maps [89, 90]. These map represent the density g as

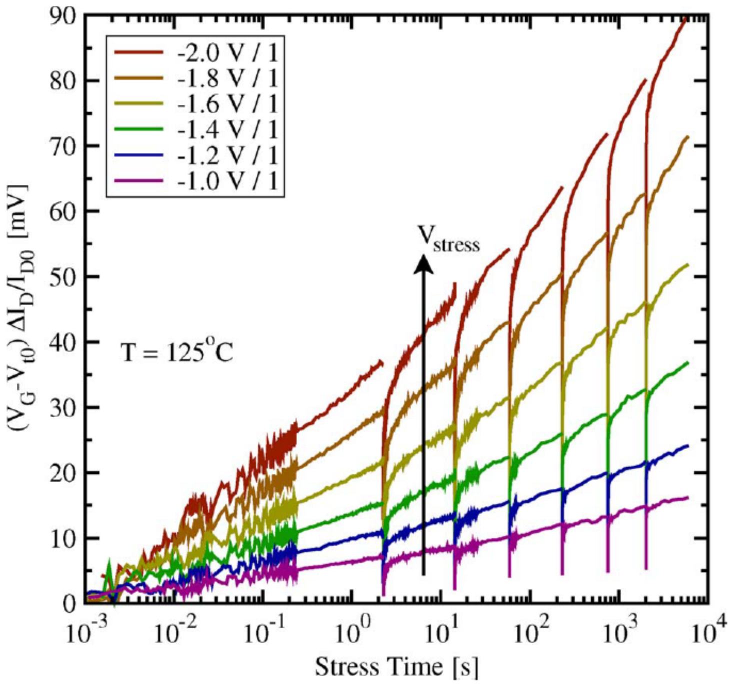

FIGURE 2.4: The degradation of a pMOSFET subject to NBTI stress recorded following the eMSM scheme: The stress is interrupted periodically on a logarithmic time scale to record intermediate recovery traces (not shown). After each recovery measurement, stress is applied again and the degradation quickly follows the same trend as prior to the interruption. After [88].

a function of the capture time constant τ_c at stress conditions and the emission time constant τ_e at recovery conditions and is obtained from the mixed partial derivative of a set of ΔV_{th} recovery traces [67]:

$$g(\tau_c, \tau_e) \approx -\frac{\partial^2 \Delta V_{th}(\tau_c, \tau_e)}{\partial \tau_c \partial \tau_e} \tag{2.7}$$

Vice versa, the degradation ΔV_{th} can be computed from g as [67]

$$\Delta V_{th}(t_s, t_r) \approx \int_0^{t_s} d\tau_c \int_{t_r}^{\infty} d\tau_e g(\tau_c, \tau_e). \tag{2.8}$$

As such, the density g of CET maps represents the time constants of the defects weighted by their impact on V_{th}, and ΔV_{th} can be obtained from these maps for any stress time t_s and recovery time t_r by integrating g from 0 s to t_s and from t_r to ∞. Note that this scheme represents data with constant stress and recovery conditions at one temperature and it is only strictly applicable to visualize first order reactions. Usually, data from large area devices where many defects contribute to ΔV_{th} is shown in CET maps to obtain a picture of the mean degradation of a technology at certain stress conditions, see Fig. 2.5.

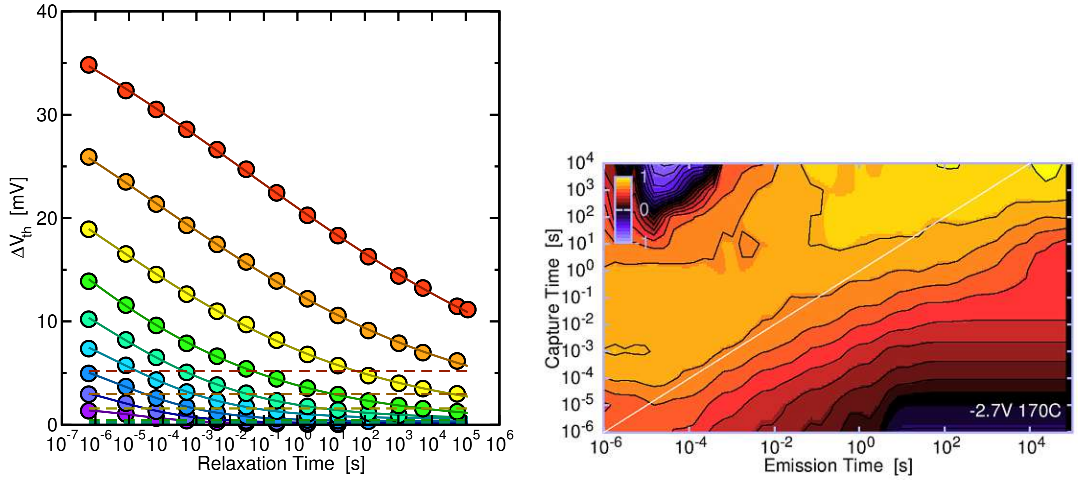

Figure 2.5: The data from an eMSM experiment (left) is visualized in a CET map (right). Both representations are equivalent and the original data (circles in the left figure) can be reproduced from the density g again (lines in the left figure). The CET map allows for direct evaluation of the time constants of defects and their impact on V_{th}. After [67].

2.3 On-The-Fly Measurements

In order to overcome the limitation of MSM techniques imposed by the measurement delay after stress, the *on-the-fly (OTF) measurement* was proposed [91]. In these measurements, the drain current is monitored during stress conditions and the corresponding degradation is determined without any interrupts. A simple but imprecise scheme allows a mapping of I_{D} in the linear regime to V_{th} based on a reference drain current $I_{\mathrm{D},0}$ and threshold voltage $V_{\mathrm{th},0}$ [92]:

$$\Delta V_{\mathrm{th}} \approx \frac{I_{\mathrm{D}} - I_{\mathrm{D0}}}{I_{\mathrm{D0}}}(V_{\mathrm{G}} - V_{\mathrm{th0}}) \tag{2.9}$$

In a more elaborate OTF scheme, a small modulation of the gate voltage around the stress value is employed to measure the transconductance continuously at stress conditions and deduce V_{th} from that [91]. While the issue with the measurement delay *after* stress is resolved by OTF measurements, the drawback of this method compared to MSM schemes is the measurement delay *at the beginning* of the stress which poses a lower bound for measurable stress times. Furthermore, such experiments are typically conducted at accelerated stress conditions and at these stress voltages fast interfacial defects could be charged which would not contribute at use conditions and do not affect V_{th} measured with MSM techniques.

2.4 From Noise to Single Defects

The theory of noise in semiconductors due to charge trapping with distributed transition rates for capture and emission processes and the implications for the noise spectrum was already established in the early 1950s [2, 93] and modeled by McWhorter [94] in 1957. Still, the debate on the origin of the $1/f$ noise spectral density observed on large area MOS devices was settled much later: In 1985, Uren *et al.* linked the $1/f$ noise to the RTN observed on devices with small active gate area [3]. An example is shown in Fig. 2.7. Thus, analysis of degradation due to defects based on the noise spectra was established and since the noise power scales with the inverse of the gate area [95], much attention was put into the analysis of RTN of scaled technologies. The time constants as a function of temperature, gate voltage, and drain voltage were studied in the following and the defect levels and the interface distance of defects were deduced [96–98]. These simple models were extended later to account for NMP processes for a more reliable extraction of defect parameters based on the capture and emission time constants determined by RTN experiments [12, 99, 100].

2.4.1 Anomalous RTN

MOSFET technologies with small effective gate areas led to an important observation in 1988: Uren *et al.* analyzed RTN signals and found that some of them show "*rapidly switching RTS modulated by an envelope of the same amplitude*" [4]. In their study, they ruled out possible mechanisms for this *anomalous RTN* such as a) two traps in the same percolation channel, b) Coulomb interactions between pairs of traps in close proximity and suggested that this observation manifests c) "*a single defect with two reconstruction modes (metastable states) available for the filled trap.*". In this early work Uren *et al.* already put forward a corresponding configuration coordinate (CC) diagram of such a defect featuring three states [3] which became the base of BTI models featuring metastable states described within the NMP theory [101]. An example for a measured anomalous RTN trace is shown in Fig. 2.6, left, together with a model with three states.

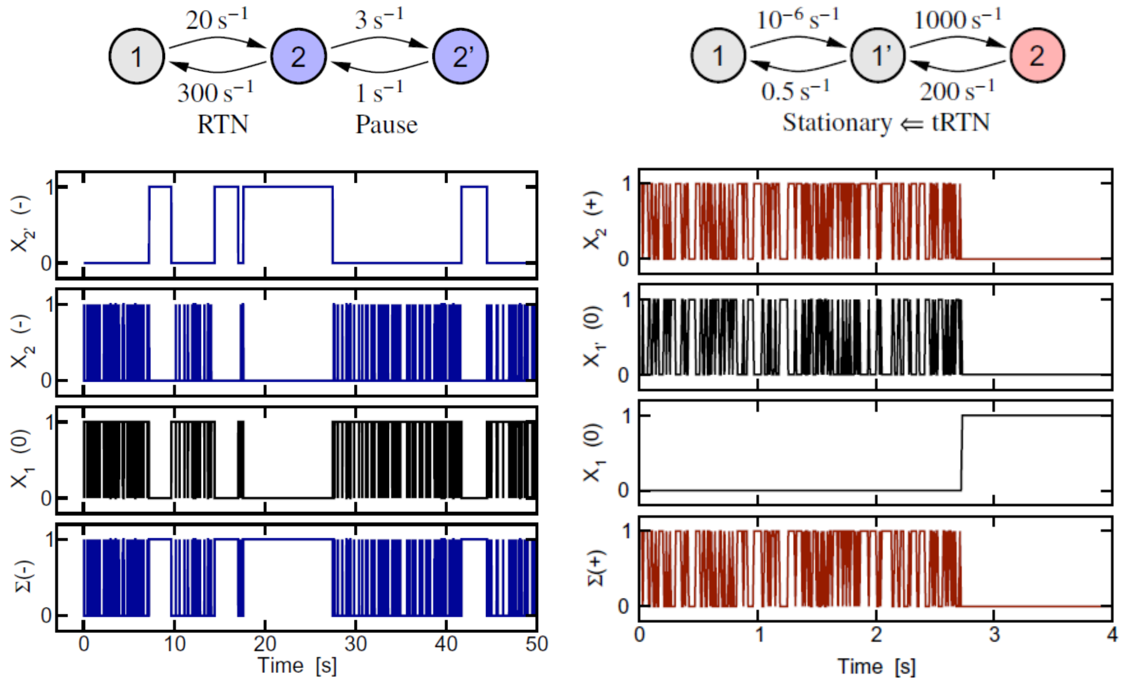

Figure 2.6: Both, *anomalous RTN* (left) and *temporary RTN* (right) is consistent with a three-state defect which exhibits RTN while switching between two charge states. Additionally, a metastable state is involved which can interrupt the RTN for some time (anomalous RTN) or end the RTN (temporary RTN). In the latter case, the defect can be forced into its less stable configuration again by applying stress conditions. Top: the three states in negative (blue), neutral (gray), and positive (red) charge states and the time constants for the transitions between the states for this example. Bottom: Simulated occupancies of the states and the sum of the negative states (last row left) and positive states (last row right) as they would be recorded experimentally. After [67].

2.4.2 Temporary RTN

In *temporary RTN*, a regular RTN signal disappears, but in contrast to anomalous RTN, the signal does not reappear at constant bias conditions [67]. Accordingly, temporary RTN has to be triggered and consistent with the interpretation based on three states, it disappears once the defect relaxes in a more stable configuration as shown in Fig. 2.6, right.

2.4.3 Reversal RTN

The measurement of RTN traces for long times at high sampling rates revealed a phenomenon called "*reversal RTN*" [102]: For some period of time, a signal with two levels exhibits much faster emission time constants compared to the capture time constants, followed by a period of time where the reverse situation is observed (faster capture time constants compared to emission time constants). These two "zones" alternate even at constant bias and Guo *et al.* suggested that this manifests a trapping mechanism with four states, two of which are metastable [102].

2.4.4 Correlated Drain and Gate RTN

In 1988 Olivo *et al.* investigated SILC and concluded that it "*originates from localized defect-related weak spots where the insulator has experienced significant deterioration from electrical stress*" [9]. Similarly, an increase in RTN was understood to manifest defect-related degradation in the oxide during stress. As such, it was speculated that these two phenomena originate from the same mechanism and a correlation of the respective degradation parameters was expected [10, 11]. Indeed, in 2011 Chen *et al.* demonstrated direct simultaneous measurements of the drain and gate current and found correlated capture and emission events in the respective RTN traces [103]: Carrier capture events in the oxide not only affect the drain current but can also open and close tunneling paths through the oxide as they alter the configuration of oxide defects, see Fig 2.7.

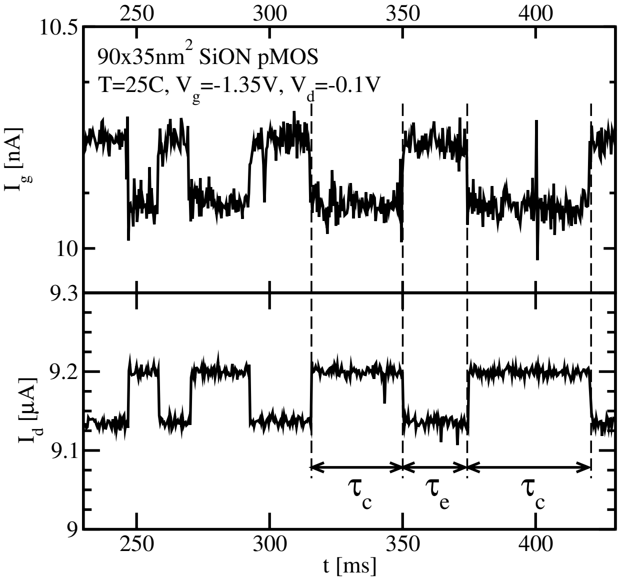

Figure 2.7: An RTN measurement where the fluctuations in the gate (upper panel) and drain current (lower panel) were monitored simultaneously. After a capture time τ_c, a hole is trapped in the oxide which reduces the drain current and at the same time increases the gate current as the defect now constitutes a tunneling path. After an emission time τ_e, the hole is emitted again and the defect structure restores to its initial configuration where it no longer acts as a tunneling center. After [104].

2.4.5 Deep-Level Transient Spectroscopy on Single Defects

The analysis of RTN enabled the study of the time constants of single defects in MOSFETs [96]. This approach, however, is limited to defects which exhibit RTN at the respective bias conditions, meaning that their capture and emission time constants have to be on the same order of magnitude. As such, this approach is not suitable to investigate the full spectrum of defects which constitute BTI. In order to determine the *emission time constants* in a more general fashion, KARWATH and SCHULZ extended the deep-level transient spectroscopy (DLTS) proposed by LANG in 1974 [105] to small-area MOSFETs in 1988 [106]. The *DLTS on single defects* assumes that a) "*the distribution of the* (emission time) *steps for a specific trap is exponential*" and that b) "*the step height differs for each trap*" [106]. Therefore, a repeated stress/recovery experiment and the statistical analysis of the discrete steps in the recovery traces gives the average emission time constant of single defects. Already in 1988, this technique was applied to analyze defects at different temperatures to derive their activation energy which was linked to NMP processes [106].

2.4.6 Time Dependent Defect Spectroscopy

In 2010 the DLTS on single defects was extended to the *time dependent defect spectroscopy (TDDS)* which not only determines the *emission time constants* but also the *capture time constants* of single defects in MOSFETs at stress conditions [89, 107]. While originally in the DLTS on single defects it was assumed that all defects are charged after switching to stress conditions without paying much attention to stress times and defects with larger capture time constants, it was later understood that the occupation probability p of defect at the stress conditions are important for such experiments: Assuming the defect to follow first order reaction kinetics, one obtains the occupation probabilities for equilibrium conditions during stress $p_\mathrm{H}(t \rightarrow \infty)$ and recovery conditions $p_\mathrm{L}(t \rightarrow \infty)$ as

$$p_\mathrm{H}(t \rightarrow \infty) = \frac{\tau_\mathrm{e,H}}{\tau_\mathrm{e,H} + \tau_\mathrm{e,H}}, \tag{2.10}$$

$$p_\mathrm{L}(t \rightarrow \infty) = \frac{\tau_\mathrm{e,L}}{\tau_\mathrm{e,L} + \tau_\mathrm{e,L}}, \tag{2.11}$$

with the capture time constant τ_c and the emission time constants τ_e at stress (denoted with a superscript "H" for *high*) and recovery (superscript "L" for *low*), to determine the transient occupation probability of a defect which was at $p_\mathrm{L}(t \rightarrow \infty)$ prior stress to be

$$p(t_\mathrm{s}) = p_\mathrm{L}(t \rightarrow \infty) + \left(p_\mathrm{H}(t \rightarrow \infty) - p_\mathrm{L}(t \rightarrow \infty)\right)\left(1 - \mathrm{e}^{-t_\mathrm{s}/\tau_\mathrm{c,H}}\right) \tag{2.12}$$

after the stress time t_s. The TDDS employs this relation by applying the *DLTS on single defects* multiple times with varying stress times, typically by increasing t_s subsequently by a factor of 10. For each of these stress times, $p(t_\mathrm{s})$ is deduced from the number of recovery events $N_\mathrm{e}(t_\mathrm{s})$ of a defect and the number of traces $N(t_\mathrm{s})$ as

$$p(t_\mathrm{s}) = \frac{N_\mathrm{e}(t_\mathrm{s})}{N(t_\mathrm{s})}. \tag{2.13}$$

Typically, this gives p close to zero for very small t_s and p close to unity for very large t_s and the capture time constant of this defect can be computed by fitting the data to Eq. (2.12). For convenient visualization of such experimental data, *spectral maps* were suggested [107]. These maps depict the emission events for multiple recovery experiments and a given stress time as a function of the step heights of these events, see Fig. 2.8.

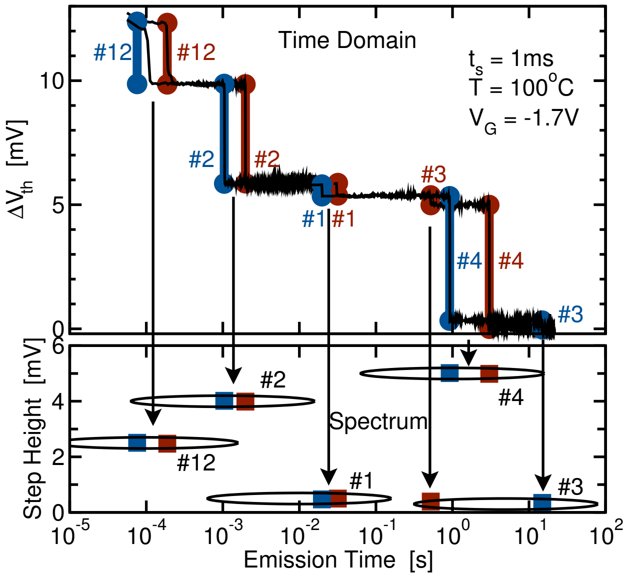

Figure 2.8: Discrete events of two recovery traces (black lines in top panel) recorded after identical stress on the same device, are mapped according to their emission times and step heights to a *spectral map* (bottom panel). These events (squares) form clusters of active defects in such spectral maps if multiple traces are analyzed. After [107].

Chapter 3

Models

In this chapter, those models related to BTI which are essential for the discussions in this thesis will be outlined. After a brief presentation of the power law description, the exponential-Poisson model, and thermal transitions in the context of BTI, we will review the history of charge trapping in the framework of the NMP theory and discuss selected models.

3.1 Power Law Extrapolation

The simple power law in the form of

$$x = Ay^k \tag{3.1}$$

was already used in 1978 to describe BTI, quantified by the shift of the flatband voltage ΔV_{fb} as a function of stress time t_{s} and stress voltage V_{G} by SINHA *et al.* as [108]

$$\Delta V_{\mathrm{fb}} \approx A\,\mathrm{abs}(V_{\mathrm{G}})^{\gamma} t^{n} \mathrm{e}^{-E_{\mathrm{a}}/(k_{\mathrm{B}}T)}. \tag{3.2}$$

Here, γ is the voltage acceleration, n the power law time dependence (0.2 in the original work), A defines the offset of ΔV_{fb}, and E_{a} is the activation energy. Since then, the power law description was applied to BTI extensively to obtain simple and often reasonably accurate estimations of the degradation. Note that the simple power law can be written as

$$\log y = k \log x + \log A. \tag{3.3}$$

Thus, a power law function appears as a straight line on a log-log plot.

3.2 Exponential-Poisson Distribution

The *exponential-Poisson distribution*, also referred to as *defect-centric* description, was introduced by KACZER *et al.* in 2010 [109] where “*NBTI stress is argued to be a convolution of exponential distributions of uncorrelated individual charged defects Poisson-distributed in number*” [110].

The impact Δv_{th} (denoted with a lowercase “v”, referred to as *step height*) of an individual defect on the threshold voltage of a device V_{th} depends on the position of the defect in the oxide. Assuming a continuous doping in the channel and a single layer oxide, Δv_{th} scales linearly with the interface distance [111], weighted by a bell function depending on the lateral position between the source and the drain [112]. Experimentally, much wider distributions of Δv_{th} are observed which was found to be due to percolation paths in the channel [96], caused by discrete dopants [113], see Fig. 3.1. Whether the resulting distribution is better described by a log-normal distribution [114–116] or an exponential distribution, is another controversial issue [GRC18]. Any way, the analysis of discrete steps after NBTI stress was found to be described

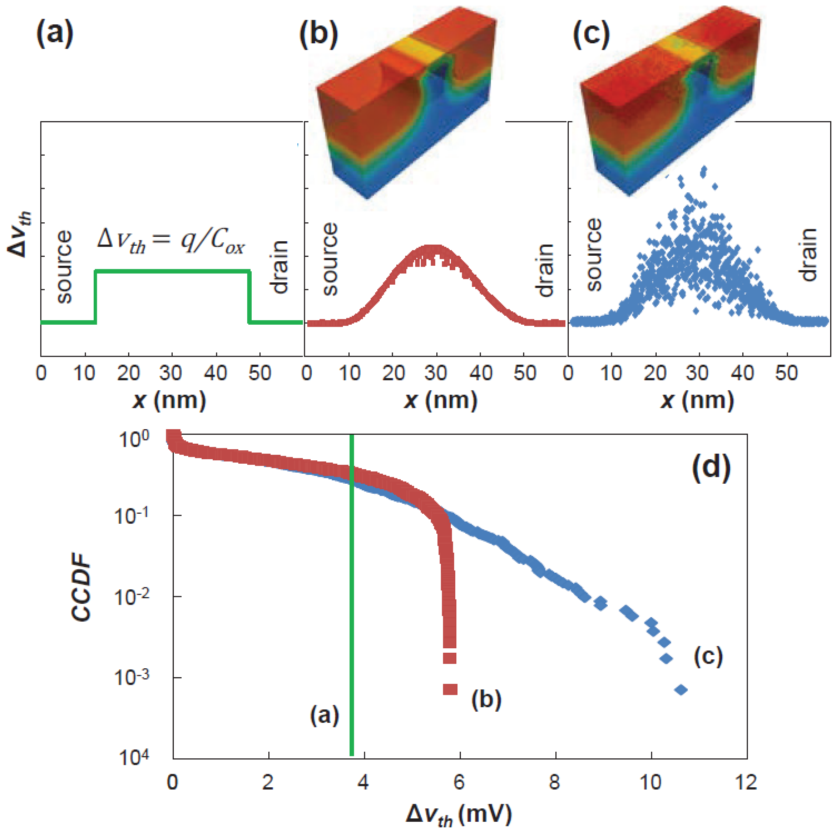

FIGURE 3.1: The distribution of the step heights Δv_{th} of individual defects located at the interface of the oxide is constant in the simple charge sheet approximation (a) [111]. Considering device electrostatics with a continuous doping profile, a bell shape is obtained for the impact of single charges between source and drain (b) [112]. Experimentally, much wider distributions are observed which is because of percolation paths due to the discrete dopants (c) [113]. The simulated complementary cumulative distribution function (CCDF) considering random dopant fluctuations features the roughly exponential tail observed experimentally [109] (d). After [GRC18].

well with exponential distributions as shown in Fig. 3.2. The corresponding probability density function (PDF) f_1 and cumulative distribution function (CDF) F_1 of the individual step heights read [109]

$$f_1(\Delta v_{\mathrm{th}}, \eta) = \frac{1}{\eta} \mathrm{e}^{-\Delta v_{\mathrm{th}}/\eta}, \tag{3.4}$$

$$F_1(\Delta v_{\mathrm{th}}, \eta) = 1 - \mathrm{e}^{-\Delta v_{\mathrm{th}}/\eta}, \tag{3.5}$$

with the mean step height η of a single charged defect. Now, for devices with n defects, the PDF f_n and CDF F_n of the distributon of ΔV_{th} evaluates to [109]

$$f_n(\Delta V_{\mathrm{th}}, \eta, n) = \frac{1}{\eta^n} \mathrm{e}^{-\Delta V_{\mathrm{th}}/\eta} \frac{\Delta V_{\mathrm{th}}{}^{n-1}}{(n-1)!}, \tag{3.6}$$

$$F_n(\Delta V_{\mathrm{th}}, \eta, n) = 1 - \frac{\Gamma(n, \Delta V_{\mathrm{th}}/\eta)}{(n-1)!} \tag{3.7}$$

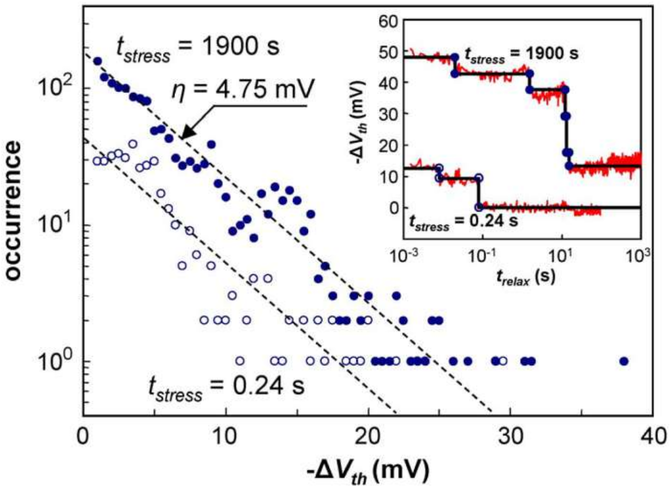

FIGURE 3.2: The histogram of step heights Δv_{th} of a technology of which 72 pMOSFETs were subject to NBTI stress for 0.24 s (empty circles) and 1900 s (filled circles), both following an exponential distribution. Inset: Δv_{th} was obtained from discrete steps in recovery traces after NBTI stress. After [109].

with the gamma function Γ. Now, the number of defects n is typically assumed to be Poisson distributed with the probability [110, 117]:

$$P_N(n) = \frac{\mathrm{e}^{-N} N^n}{n!} \tag{3.8}$$

with the mean number of defects $N = WLN_{\mathrm{OT}}$ depending on the effective gate width W and length L as well as on the defect concentration N_{OT} projected to the interface. To obtain the PDF f_{N} and the CDF F_{N} of the ΔV_{th} distribution assuming such a Poisson distributed number of defects, the distributions F_n have to be weighted by P_n to obtain [109]

$$f_{\mathrm{N}}(\Delta V_{\mathrm{th}}, \eta) = \mathrm{e}^{-\mathrm{N}} \left(\delta(\Delta V_{\mathrm{th}}) + \frac{N}{\eta} \mathrm{e}^{-\Delta V_{\mathrm{th}}/\eta} \, {}_0\mathcal{F}_1 \left(2; N \frac{\Delta V_{\mathrm{th}}}{\eta} \right) \right), \tag{3.9}$$

$$F_{\mathrm{N}}(\Delta V_{\mathrm{th}}, \eta) = \sum_{n=1}^{\infty} \frac{\mathrm{e}^{-N} N^n}{n!} F_n(\Delta V_{\mathrm{th}}, \eta, n), \tag{3.10}$$

with the hypergeometric function ${}_0\mathcal{F}_1$ and the Dirac function δ. Important properties of this distribution are the mean $\langle \Delta V_{\mathrm{th}} \rangle$ and the variance $\sigma_{\Delta V_{\mathrm{th}}}$ [109]

$$\langle \Delta V_{\mathrm{th}} \rangle = N\eta, \tag{3.11}$$

$$\sigma_{\Delta V_{\mathrm{th}}} = 2N\eta^2, \tag{3.12}$$

which conveniently allow to determine the mean step height η and the number of active defects N from the distribution of ΔV_{th} as

$$\eta = \frac{\sigma^2_{\Delta V_{\mathrm{th}}}}{2\langle \Delta V_{\mathrm{th}} \rangle}, \tag{3.13}$$

$$N = \frac{2\langle \Delta V_{\mathrm{th}} \rangle^2}{\sigma^2_{\Delta V_{\mathrm{th}}}}. \tag{3.14}$$

3.3 Simple Descriptions of the Quasi-Permanent Part

The quasi-permanent component of BTI is commonly ascribed to the passivation and depassivation of interface states. Models which are based on the idea of simple thermal activation for these processes are outlined in the following.

3.3.1 Brower's Simple Thermal Model

As summarized by STESMANS [46], the *simple thermal* model introduced by BROWER in 1988 [118–121] considers rate limited reactions for passivation and depassivation of P_b centers. The rate equations for the passivation of reactive sites $[P_\mathrm{b}]$ and for the depassivation of reactive sites $[HP_\mathrm{b}]$ read

$$\frac{\mathrm{d}[P_\mathrm{b}]}{\mathrm{d}t} = -k_\mathrm{f}[H_2][P_\mathrm{b}], \tag{3.15}$$

$$\frac{\mathrm{d}[HP_\mathrm{b}]}{\mathrm{d}t} = -k_\mathrm{d}[HP_\mathrm{b}], \tag{3.16}$$

with the transition rates for passivation k_f and depassivation k_d following the Arrhenius equation as

$$k_\mathrm{f} = k_{\mathrm{f0}}\mathrm{e}^{-E_\mathrm{f}/(k_\mathrm{B}T)}, \tag{3.17}$$

$$k_\mathrm{d} = k_{\mathrm{d0}}\mathrm{e}^{-E_\mathrm{d}/(k_\mathrm{B}T)}, \tag{3.18}$$

where E_f is the activation energy for passivation and E_d is the activation energy for depassivation. In this model, the molecular hydrogen $[H_2]$ was assumed to react with the P_b center without preliminary cracking. Furthermore, the activation energies where assumed to be single valued in [119, 121]

$$E_\mathrm{d} \approx 2.56\,\mathrm{eV}, \tag{3.19}$$

$$E_\mathrm{f} \approx 1.66\,\mathrm{eV}, \tag{3.20}$$

an approximation which was refined by STESMANS in the *generalized simple thermal* model [46].

3.3.2 Field-Dependent Thermal Transition

GRASSER *et al.* introduced a phenomenologic field dependence to BROWER's simple thermal model in 2009 to describe the coupling of the stages in the two-stage model [61]. While the rate equations remained the same, both the passivation and depassivation barrier were modified as

$$E_\mathrm{d}(F) = E_\mathrm{d}(F=0) - \gamma F, \tag{3.21}$$

$$E_\mathrm{f}(F) = E_\mathrm{f}(F=0) + \gamma F, \tag{3.22}$$

with the electric field F and the field dependence γ as depicted in Fig. 3.3. Thus, the activation energies of depassivation are reduced at stress conditions whereas the opposite is the case for the activation energy of passivation.

3.4 Non-Radiative Multi-Phonon Models

Charges trapped in oxide defects affect the surrounding electrons and nuclei. As a consequence, the exchange of an electron between an oxide defect and a carrier reservoir such as the channel of a MOSFET not only comprises a) the tunneling of the carrier under b) conservation of energy

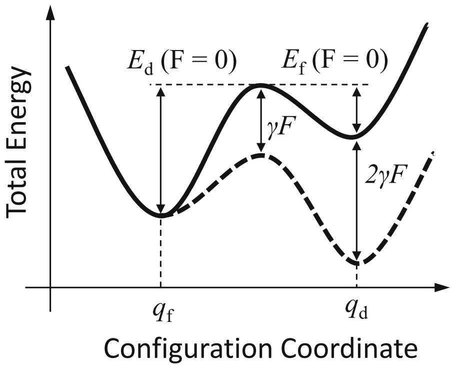

Figure 3.3: The field-dependent thermal transition considers two states which describe the passivated (f) and the depassivated (d) state of a P_b center in the two-stage model [61]. The activation energy for depassivation E_d is reduced by γF while the passivation energy is increased by γF.

but also c) the deformation of the defect site and d) relaxation towards the equilibrium position of the system [122]. Without the latter, the process would be elastic which would imply:

- that the time constants of the carrier exchange would be governed by elastic tunneling which is in contradiction with measurements on devices with thin oxides [123]
- a distinctively weak temperature dependence of the time constants whereas experimentally an Arrhenius-like activation is observed [124]
- that defects closer to the reservoir will be charged faster, which results in a correlation of the stress time and step heights, which is not observed experimentally [100, GRC19]
- a roughly linear bias dependence of the time constants while single defect studies show peculiar bias dependence [107]

All of the above underlines that *the deformation of the defect site and the relaxation towards the equilibrium position of the system* is indispensable for an accurate description of charge exchange with oxide defects. The physics of this deformation are governed by *electron-phonon coupling*: while the distribution of the electrons is determined by the vibration of the atoms, the vibration of the atoms themselves are affected by the number and distributions of the electrons. This problem can be described by considering the coupling between the wave functions of the two systems which, however, is practically impossible for amorphous oxides.

Conveniently, electronic motion is typically much faster compared to nuclear motion which allows for them to be treated separately in the Born-Oppenheimer approximation [125]. The electronic wave function can then be solved for fixed nuclei positions and the energy of the system which includes all Coulomb and kinetic energies is obtained for this configuration. This gives the energy as a function of the atomic configuration which is a $3N$-dimensional surface for a system with N atoms called *potential energy surface*. For defect structures of amorphous oxides, this is a highly complex multidimensional surface which computation is barely feasible. However, transitions between states of a potential energy surface are governed by the transitions path with the lowest energy barrier. This allows reducing the $3N$-dimensional surface to an effective CC diagram which describes the energy along this dominant transition path. In order to enable an analytic treatment of problems based on CC diagrams, approximations for potential energy surfaces are desirable. Conveniently, approximating the potential energy surfaces with parabolas results in quantum harmonic oscillators where the energy of the system E_i in state i evaluates to

$$E_i = E_{i,\mathrm{min}} + c_i\,(q - q_i)^2 \tag{3.23}$$

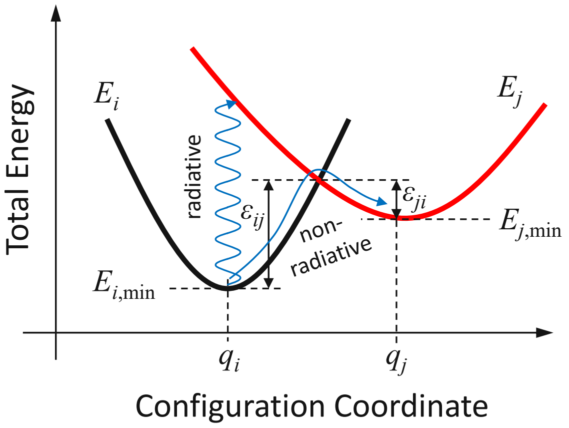

FIGURE 3.4: A schematic CC diagram of a system with a neutral state i (thick black line) and a positive charge state j (thick red line). Transitions can be radiative for example by photon excitation or non-radiative due to phonon interaction. For the latter, the relaxation energy ε_{ij} from state i to state j and ε_{ji} from state j to state i are depicted.

with the curvature c_i and the equilibrium position at q_i and the energy minimum $E_{i,\min}$ as depicted in Fig. 3.4. This approximation is only accurate for sufficiently small displacements from the equilibrium position and appears crude to describe transitions between charge states of oxide defects, still it is widely used and gives reasonable results [67]. The excitation and relaxation of defect structures in MOS devices can be radiative for example in measurements where defects are excited using photons. However, in conventional applications, the excitations and relaxations are due to phonon interaction which is described by the NMP theory [122, 126, 127].

In the harmonic approximation both the electronic and the nuclear wave functions can be computed, allowing for a rigorous evaluation of the transition rate k_{ij} from state i to state j as

$$k_{ij} = A_{ij} f_{ij} \tag{3.24}$$

where A_{ij} is the electronic matrix element and f_{ij} the lineshape function. While the former accounts for the tunneling of electrons which is independent of the vibrational state, the latter is the average of all initial vibrational states α of the sum of all final vibrational states β of the Franck-Condon factor $f_{i\alpha j\beta}$ [126, 128]:

$$f_{ij} = \underset{\alpha}{\text{ave}} \sum_{\beta} f_{i\alpha j\beta} \tag{3.25}$$

The Franck-Condon factor accounts for the overlap of the nuclear wave functions which are obtained from the molecular Schrödinger equation as discussed in [GRJ10]. In MOS devices, defects interact with reservoirs such as semiconductors or metals. In general, the total transition rate can then be obtained based on the density of states D and the carrier distribution function f as

$$k_{ij}(E) = \int_{-\infty}^{\infty} D(E) f(E) A_{ij}(E) f_{ij}(E) \mathrm{d}E. \tag{3.26}$$

3.4.1 Early Applications to MOS Devices

The foundations for NMP models were established in 1950 [126] but it was a long way untill they were applied to model BTI. In the 1970s, first applications on semiconductors revealed properties of single defects [122, 129–131] followed by a consistent understanding of $1/f$ noise and RTN based on the NMP theory in the 1980s [3, 132–134]. Finally, in the 1990s the work of Kirton and Uren on noise due to single defects in the framework of NMP theory [127] was applied to model the threshold voltage shift of MOSFETs by Tewksbury [135, 136]. This pioneering work was barely adopted for several years and most groups studied multi-phonon processes in the only context of trap-assisted tunneling [6, 13, 137–139] while BTI was continued to be modeled as a diffusion-limited process [55, 56].

Tewksbury's Lattice Relaxation Multiphonon Emission Model

In the following, the lattice relaxation multiphonon emission (MPE) model is outlined as presented by Tewksbury in [135]. The discussion will focus on the NMP physics of this model while other aspects such as tunneling factors and density of states will be omitted. Tewksbury starts the discussion of the MPE model with the total energy E_j of a system with an empty defect in the oxide and an electron at the conduction band edge at the interface with the energy E_C. Using the notation introduced in Eq. (3.23) the total energy of the system is

$$E_j = E_\mathrm{C} + c_j q^2 \tag{3.27}$$

with the definition of $q_j = 0$. When the electron is captured by the defect, the deformation of the lattice is approximated to modulate the electron energy E_e as

$$\delta E_\mathrm{e} = -Bq \tag{3.28}$$

with the deformation potential $B = -\partial E_\mathrm{e}/\partial q$. This gives the total energy E_i of the system for the trapped electron with the new energy minimum at $q_i = B/(2c_i)$ and $c_i = c_j$ as

$$\begin{aligned} E_i &= c_i q^2 - Bq, \qquad (3.29)\\ &= -c_i q_i^2 + c_i\,(q - q_i)^2\,. \qquad (3.30) \end{aligned}$$

Thereby, both parabolas and, hence, the relaxation energies are defined (see Fig. 3.4). In order for the electron to be emitted again from the defect, the system must acquire the energy

$$\varepsilon_{ij} = E_{\mathrm{min},j} - E_{\mathrm{min},i} + \varepsilon_{ji}. \tag{3.31}$$

The probability p_{ij} to acquire this energy is given by the normalized Boltzmann distribution:

$$p_{ij} = \frac{1}{k_\mathrm{B}T}\mathrm{e}^{-(E_{\mathrm{min},j} - E_{\mathrm{min},i} + \varepsilon_{ji})/(k_\mathrm{B}T)}. \tag{3.32}$$

For the reverse process the probability is:

$$p_{ji} = \frac{1}{k_\mathrm{B}T}\mathrm{e}^{-\varepsilon_{ij}/(k_\mathrm{B}T)}. \tag{3.33}$$

Based on these probabilities Tewksbury derived capture and emission time constants which also consider the densities of states and forward and backward transition probabilities maintaining detailed balance. This gives the "*rather formidable integral*" (3.23) in [135] for the electron capture time constant τ_c which is interesting from NMP perspective because it gives the proportionality of the rate k_c for electron capture as

$$\frac{1}{\tau_\mathrm{c}} = k_\mathrm{c} \propto \mathrm{e}^{-(E_\mathrm{F} - E_\mathrm{T} - \varepsilon_{ji})/(k_\mathrm{B}T)} \tag{3.34}$$

where E_F is the Fermi level at the channel and E_T is the trap level. In [136] the shift of E_T due to the applied oxide electric field F is given as

$$E_T(F) = E_T(F=0) - qFx \tag{3.35}$$

with the elementary charge q and the distance from the channel interface x. This is the foundation of NMP modeling in the context of BTI which Tewksbury systematically applied to obtain time constants of defects and to simulate how these defects affect the threshold voltage shift of MOSFETs during stress and recovery [136]. Still, most groups continued working with some R-D models and it took another 15 years until the NMP theory was adopted for BTI simulations by a broader community, spearheaded by Grasser's *two-stage model* in 2009 [61, 101].

Grasser's Two-Stage Model

The two-stage model was inspired by E' centers (stage one) as described by the Harry Diamond Laboratories (HDL) model [140, 141] and extended by an activation mechanism of P_b centers (stage two), see Fig. 3.5. In *stage one*, hole trapping of near-interfacial E' centers with two neutral and one positive states is modeled within the NMP theory with the same proportionality in Eq. (8) of [101] as in Eq. (3.34) (note that electron emission corresponds to hole capture of the defect). In *stage two*, the depassivation of a P_b center is only possible with a positive E' center as a precursor which supplies an atomic hydrogen. This processes modeled with a thermal activation over a field-dependent barrier as described in Subsection 3.3.2. The charge of depassivated P_b centers is determined using the Shockley Read Hall (SRH) mechanism.

This two-stage model was the first attempt to model both the permanent and the recoverable component of NBTI consistently based on hydrogen relocation while accounting for NMP transitions. These ideas were refined subsequently: First, the *4-state NMP model* was presented in

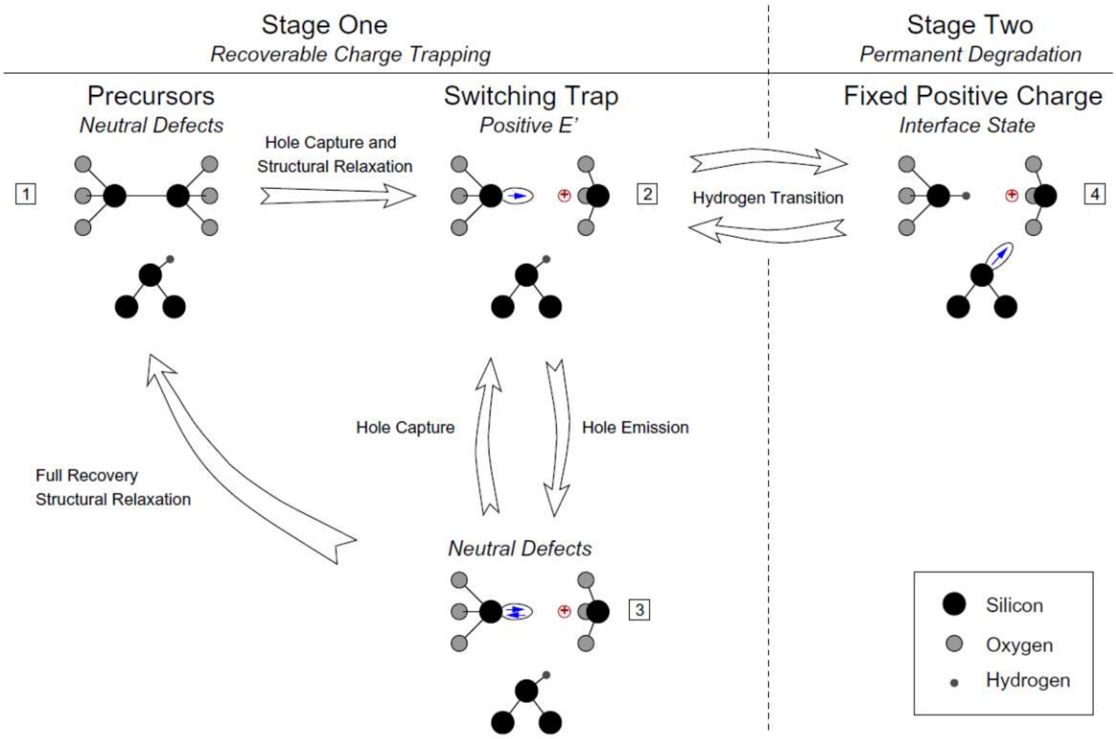

Figure 3.5: In the two-stage model a P_b center is depassivated by a hydrogen atom supplied from a E' center in the near-interfacial region. This E' center features three states which are modeled with NMP transitions. After [61].

2010 [107] which focused on the details of the recoverable component considering metastable states as described in Subsection 3.4.2. Later in 2015 the role of hydrogen was revisited and modeled in detail in the *gate-sided hydrogen release model* [GRC20], see Subsection 3.4.3.

3.4.2 4-State NMP Model

In the following, we will outline the 4-state NMP model, starting with the discussion of *switching traps* as they have initiated this model. We will then present the description of single defects within the 4-state NMP model, followed by the sampling of an ensemble of such defects to describe the recoverable component of BTI.

Evidence for a 4th State: Switching Traps

The introduction of the 4-state NMP model was motivated by observations at single defect level and is closely related to the TDDS (see Subsection 2.4.6): While the two-stage model was able to explain several phenomena related to NBTI, the time constants of *switching traps* remained puzzling [107]. As opposed to *fixed positive charge traps* which feature constant emission time constants towards low gate voltages, the switching traps show a pronounced drop of the emission time constant at low gate voltages, see Fig. 3.6.

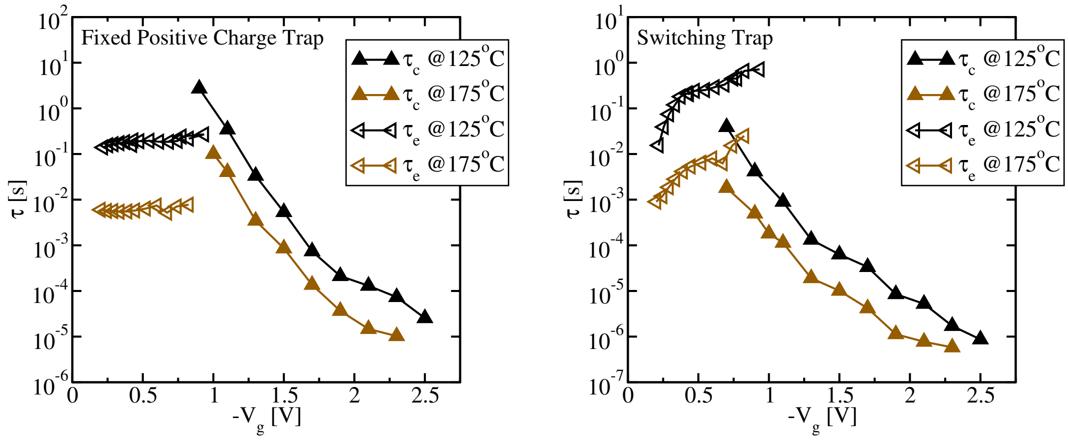

FIGURE 3.6: Studies on the time constants revealed two distinct type of oxide defects: *Fixed positive charge traps* have constant emission time constants at low gate voltages (left), while *switching traps* feature a drop of the emission time constants towards low gate voltages (right) [107]. After [GRT2].

An explanation which is consistent with other observations on single defect level such as anomalous RTN (see Subsection 2.4.1) and an inherent frequency dependence [142] is given by the 4-state NMP model: A positively charged E' center (in state 2) can be discharged via its *metastable positive state* $2'$ as introduced in the two-stage model already. Additionally, the 4-state NMP model accounts for a discharge via an alternative path via the *metastable neutral state* $1'$. This is consistent with the physics of the E' center as a structural relaxation follows a charge exchange in both charge states [143] as shown in Fig. 3.7. Since every defect is different due to its surrounding configuration in amorphous oxides, the activation energies for both discharge paths will differ as well. Defects with high energy barriers via state $1'$ will have constant emission time constants governed by the gate bias independent energy barrier between states 2 and $2'$ as they can only emit via state $2'$. These defects are called "fixed positive charge traps" as their emission time constants do not depend on the gate voltage, hence, they cannot be forced to discharge (see Fig. 3.8). On the other hand, the discharge of defects with lower energy barriers via path $1'$ is governed by the gate voltage dependent energy barrier via the state $1'$ and are called "switching traps" as they can be forced to discharge by applying low gate voltages as shown in Fig. 3.9.

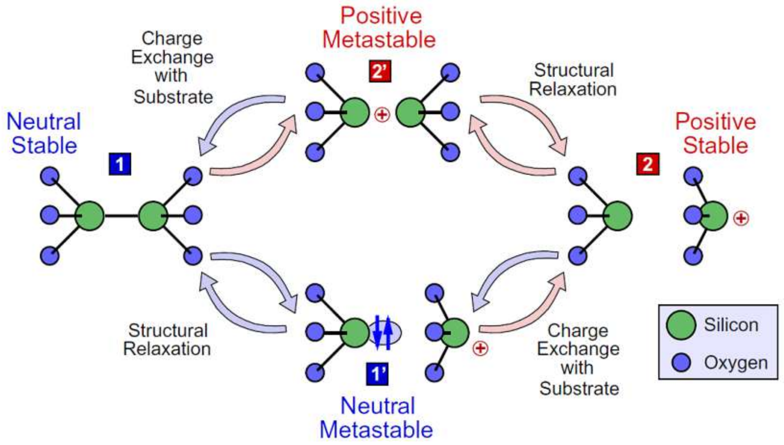

FIGURE 3.7: Defects described by the 4-state NMP model depicted for the example of the E' center with its two metastable states $1'$ and $2'$ and its two stable states 1 and 2. The ball-and-stick model shows the structural relaxation of the metastable states to its more stable configuration with the silicon moving through the plane spanned by its three neighboring oxygen atoms. This opens two paths for discharging a positive defect in state 2: The bias independent path via $2'$ is favored by *fixed positive charge traps* (see Fig. 3.8), while the strongly bias dependent path via $1'$ governs the emission of *switching traps* (see Fig. 3.9). After [67].

Single Defect Model

The transition rates which describe a charge exchange in the 4-state NMP model are treated according to the NMP theory as presented in Eq. (3.26). For applications of this model above room temperature [GRJ10] the lineshape function can be approximated to only contribute at the intersection points of the parabolas. Thus, with the energy barrier ε_{ij} from state i to state j in the Boltzmann factor, the transition rate reads:

$$k_{ij}(E) = \int_{-\infty}^{\infty} D(E) f(E) A_{ij}(E) \mathrm{e}^{-\varepsilon_{ij}(E)/(k_\mathrm{B}T)} \mathrm{d}E. \tag{3.36}$$

Here, $D(E)$ is the density of states, $f(E)$ is the distribution function, and $A_{ij}(E)$ is the electronic matrix element. In the following we will discuss the energy barrier ε_{ij}. The 4-state NMP model follows the commonly used approximation of the potential energy surfaces with quantum harmonic oscillators as introduced in Eq. (3.23). The intersection point of the parabolas of the states i and j gives the energy barrier in the classical limit:

$$\varepsilon_{ij} = \frac{c_i(q_j - q_i)^2}{\left(\frac{c_i}{c_j} - 1\right)^2} \left(1 \pm \sqrt{\frac{c_i}{c_j} + \frac{(E_{j,\mathrm{min}} - E_{i,\mathrm{min}})\left(\frac{c_i}{c_j} - 1\right)}{c_j(q_j - q_i)^2}} \right)^2 . \tag{3.37}$$

Transitions are governed by the path with the lowest energy barrier, hence, the solution of this equation with "+" for "±" can be neglected. Furthermore, the above equation can be rewritten using the definitions of the relaxation energy S_{ij}, the curvature relation R_{ij}, and the energy

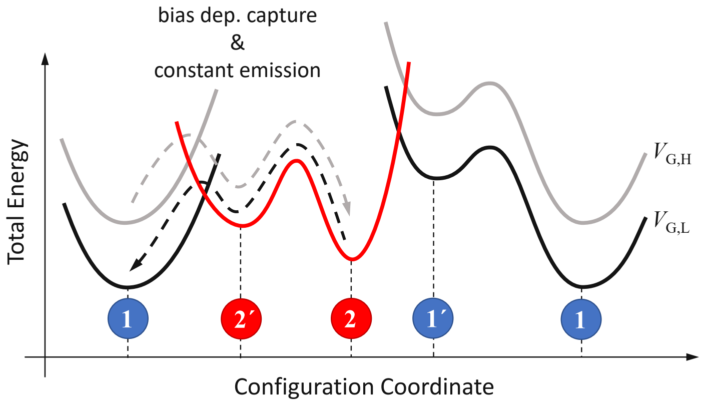

FIGURE 3.8: *Fixed positive charge traps* capture holes during stress ($V_{G,H}$) via the metastable state 2′. Also at low gate voltages ($V_{G,L}$), transitions via the state 2′ are favored because of the high energy barriers for transitions via the state 1′. Therefore, the emission time constants of these defects are governed by the barrier $\varepsilon_{22'}$, hence, they are roughly independent of gate bias.

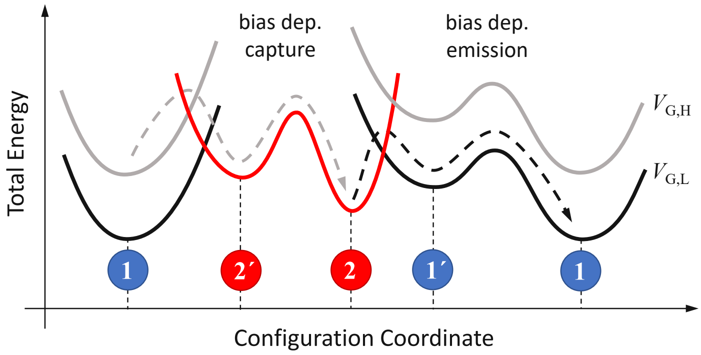

FIGURE 3.9: *Switching traps* capture holes holes during stress ($V_{G,H}$) via the metastable state 2′ just like fixed positive charge traps. However, at low gate voltages ($V_{G,L}$), transitions via the state 1′ are favored because of the low energy barriers of these defects for transitions via the state 1′. Since the barrier of the NMP transition between state 2 and 1′ depends on the gate bias, these defects feature a drop in the emission time constants towards low gate voltages.

difference ΔE_{ij} as

$$S_{ij} = \mathcal{S}_{ij}\hbar\omega = c_i\,(q_j - q_i)^2\,, \tag{3.38}$$

$$R_{ij}^2 = \frac{c_i}{c_j}, \tag{3.39}$$

$$\Delta E_{ij} = E_{j,\mathrm{min}} - E_{i_{,\mathrm{min}}}, \tag{3.40}$$

where $\mathcal{S}_{ij}$ is the Huang-Rhys factor [126], to obtain

$$\varepsilon_{ij} = \frac{S_{ij}}{(R_{ij}^2-1)^2}\left(1 - R_{ij}\sqrt{\frac{S_{ij} + \Delta E_{ji}(R_{ij}^2-1)}{S_{ij}}}\right)^2, \tag{3.41}$$

with the removable singularity for $R_{ij} = 1$

$$\varepsilon_{ij} = \frac{(S_{ij} + \Delta E_{ji})^2}{4S_{ij}}. \tag{3.42}$$

Note that the energy barrier ε_{ij} depends on the electric field F because of the field-dependence of ΔE_{ij}. Similar to Eg. (3.35), the approximation of a constant electric field in the oxide gives

$$\Delta E_{ji}(F) = \Delta E_{ji}(F=0) - qxF. \tag{3.43}$$

In addition to *NMP transitions* between states which involve charge exchange, the 4-state NMP model also accounts for structural relaxation which corresponds to *pure thermal transitions* between states *without* a charge exchange. The energy barriers for the latter correspond to activation energies in the Arrhenius equation and result in the transition rate

$$k_{ij} = \nu_0 \mathrm{e}^{-\varepsilon_{ij}/(k_\mathrm{B}T)} \tag{3.44}$$

between the states i and j and with the attempt frequency ν_0 and the energy barrier ε_{ij} from state i to state j. As opposed to the energy barrier in NMP transitions, the energy barrier here is approximated to be constant and does not depend on the electric field. The full CC diagram for a 4-state NMP defect with two NMP transitions and two pure thermal transitions can be described with the parameters listed in Table 3.1 and is depicted in Fig. 3.10 together with all energy barriers.

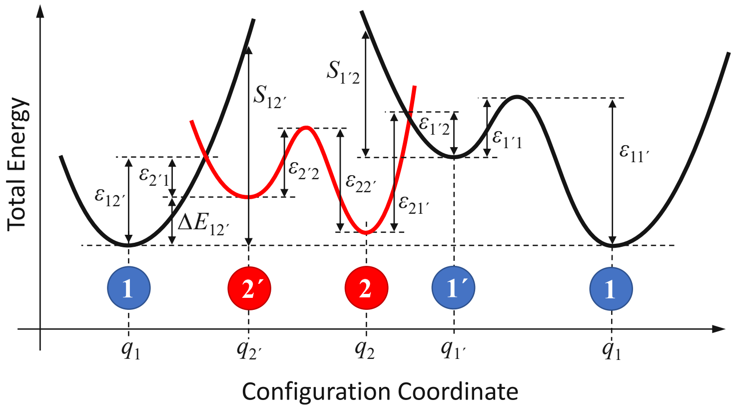

FIGURE 3.10: A schematic CC diagram of a 4-state NMP defect with the NMP transitions between the states 1 ↔ 2′ and 1′ ↔ 2 and the pure thermal transitions between the states 1 ↔ 1′ and 2 ↔ 2′. All energy barriers ε_{ij}, the difference between the energy minima $\Delta E_{12'} = E_{2',\mathrm{min}} - E_{1,\mathrm{min}}$, and the relaxation energies S_{ij} are depicted.

TABLE 3.1: Parameters of a single defect in the *4-state NMP model*. The trap level in the positive stable state E_2 is chosen as reference level in this description.

parameter	description
E_1	trap level in the neutral stable state 1
$E_{1'}$	trap level in the neural metastable state 1′
$E_{2'}$	trap level in the neural metastable state 2′
$R_{12'}$	square of the curvature ratio of state 1 and 2′
$R_{1'2}$	square of the curvature ratio of state 1′ and 2
$S_{12'}$	relaxation energy from state 2′ to 1
$S_{1'2}$	relaxation energy from state 2 and 1′
$\varepsilon_{11'}$	activation energy from state 1 to 1′
$\varepsilon_{22'}$	activation energy from state 2 to 2′

With these energy barriers, the full set of rates reads

$$k_{12'} = \int_{-\infty}^{\infty} D(E) f(E) A_{12'}(E) \mathrm{e}^{-\varepsilon_{12'}(E)/(k_\mathrm{B}T)} \mathrm{d}E, \tag{3.45}$$

$$k_{2'1} = \int_{-\infty}^{\infty} D(E) f(E) A_{2'1}(E) \mathrm{e}^{-\varepsilon_{2'1}(E)/(k_\mathrm{B}T)} \mathrm{d}E, \tag{3.46}$$

$$k_{21'} = \int_{-\infty}^{\infty} D(E) f(E) A_{21'}(E) \mathrm{e}^{-\varepsilon_{21'}(E)/(k_\mathrm{B}T)} \mathrm{d}E, \tag{3.47}$$

$$k_{1'2} = \int_{-\infty}^{\infty} D(E) f(E) A_{1'2}(E) \mathrm{e}^{-\varepsilon_{1'2}(E)/(k_\mathrm{B}T)} \mathrm{d}E, \tag{3.48}$$

$$k_{11'} = \nu_0 \mathrm{e}^{-\varepsilon_{11'}/(k_\mathrm{B}T)}, \tag{3.49}$$

$$k_{1'1} = \nu_0 \mathrm{e}^{-\varepsilon_{1'1}/(k_\mathrm{B}T)}, \tag{3.50}$$

$$k_{22'} = \nu_0 \mathrm{e}^{-\varepsilon_{22'}/(k_\mathrm{B}T)}, \tag{3.51}$$

$$k_{2'2} = \nu_0 \mathrm{e}^{-\varepsilon_{2'2}/(k_\mathrm{B}T)}. \tag{3.52}$$

The probability p_i of the defect to be in state i is obtained from the master equation of this first-order Markov chain as [67]

$$\frac{\mathrm{d}p_1(t)}{\mathrm{d}t} = k_{1'1} p_{1'}(t) + k_{2'1} p_{2'}(t) - k_{11'} p_1(t) - k_{12'} p_1(t), \tag{3.53}$$

$$\frac{\mathrm{d}p_{1'}(t)}{\mathrm{d}t} = k_{11'} p_1(t) + k_{21'} p_2(t) - k_{1'1} p_{1'}(t) - k_{1'2} p_{1'}(t), \tag{3.54}$$

$$\frac{\mathrm{d}p_2(t)}{\mathrm{d}t} = k_{2'2} p_{2'}(t) + k_{1'2} p_{1'}(t) - k_{22'} p_2(t) - k_{21'} p_2(t), \tag{3.55}$$

$$\frac{\mathrm{d}p_{2'}(t)}{\mathrm{d}t} = k_{12'} p_1(t) + k_{22'} p_2(t) - k_{2'1} p_{2'}(t) - k_{2'2} p_{2'}(t). \tag{3.56}$$

With these rates, the time constants for the transitions via state $1'$ and $2'$ can be computed as [67]

$$\tau_\mathrm{c}^{1'} = \frac{k_{11'} + k_{1'1} + k_{1'2}}{k_{11'} k_{1'2}}, \tag{3.57}$$

$$\tau_\mathrm{c}^{2'} = \frac{k_{12'} + k_{2'1} + k_{2'2}}{k_{12'} k_{2'2}}, \tag{3.58}$$

$$\tau_\mathrm{e}^{1'} = \frac{k_{1'1} + k_{1'2} + k_{21'}}{k_{1'1} k_{21'}}, \tag{3.59}$$

$$\tau_\mathrm{e}^{2'} = \frac{k_{2'1} + k_{2'2} + k_{22'}}{k_{2'1} k_{22'}}, \tag{3.60}$$

to obtain the total capture and emission time constants

$$\tau_\mathrm{c} = \left(\frac{1}{\tau_\mathrm{c}^{1'}} + \frac{1}{\tau_\mathrm{c}^{2'}} \right)^{-1}, \tag{3.61}$$

$$\tau_\mathrm{e} = \left(\frac{1}{\tau_\mathrm{e}^{1'}} + \frac{1}{\tau_\mathrm{e}^{2'}} \right)^{-1}. \tag{3.62}$$

Simulations with this model correctly reproduce all features observed experimentally for fixed positive charge traps and switching oxide traps as shown in Fig. 3.11.

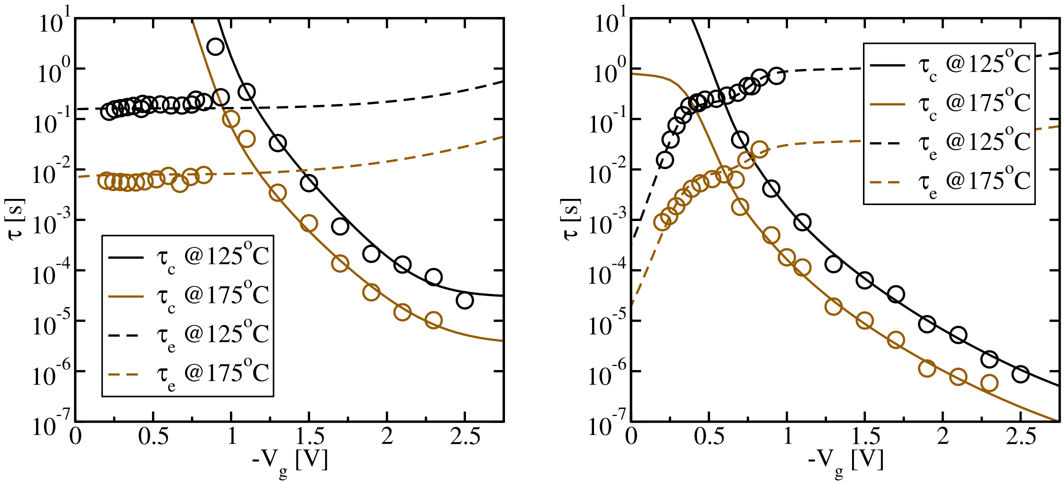

FIGURE 3.11: The calculated time constants with the 4-state NMP model (lines) correctly reproduces all experimental features (circles) obtained for *fixed positive charge traps* (left) and *switching traps* (right). After [GRT2].

Modeling the Recoverable Component of BTI: Ensemble of Defects

With this accurate model for single defects, the total degradation of MOS devices due to preexisting defects can be simulated in a straightforward manner by Monte Carlo sampling: Assuming a constant defect concentration N_{OT} in the oxide within the width W, length L, and thickness x, the average number of defects is $N = WLxN_{\mathrm{ot}}$. It is commonly assumed that the random fluctuations of number of defects n follow a Poisson distribution [110, 117]:

$$P_N(n) = \frac{\mathrm{e}^{-N}N^n}{n!} \tag{3.63}$$

Each of these defects in the amorphous oxide has a unique configuration resulting in slightly different CC diagrams as mentioned in the previous subsection. The actual distributions and possible correlations of the parameters describing the CC diagrams cannot be determined directly, and first-principles simulations and experimental studies can only give vague ideas [GRC21]. The naive assumption commonly used for the 4-state NMP model are *independent and normally distributed* parameters [GRC15]. As an example, a distribution of defects and their CC diagrams is shown in Fig. 3.12. Following the model outlined above, each of these defects has distinct capture and emission time constants as a function of the gate voltage (see Fig. 3.13).

The charges q_{T} stored in each of these defects can be computed based on the occupation probabilities as

$$q_{\mathrm{T}} = q\left(p_2 + p_{2'}\right). \tag{3.64}$$

There are several options how to compute the impact V_{traps} of these charges on the threshold voltage of MOS. In the simple *charge sheet approximation* for an oxide with the thickness t_{ox}, the width W, the length L, the relative permittivity ε_{r}, the vaccum permittivity ε_0, and the number of defects N_{T}, the impact evaluates to [111, 136]

$$V_{\mathrm{traps}} = \epsilon_0\epsilon_{\mathrm{r}}WL\sum_{n}^{N_{\mathrm{T}}} -q_{\mathrm{T},n}t_{\mathrm{ox}}\left(1 - \frac{x_{\mathrm{T}}}{t_{\mathrm{ox}}}\right). \tag{3.65}$$

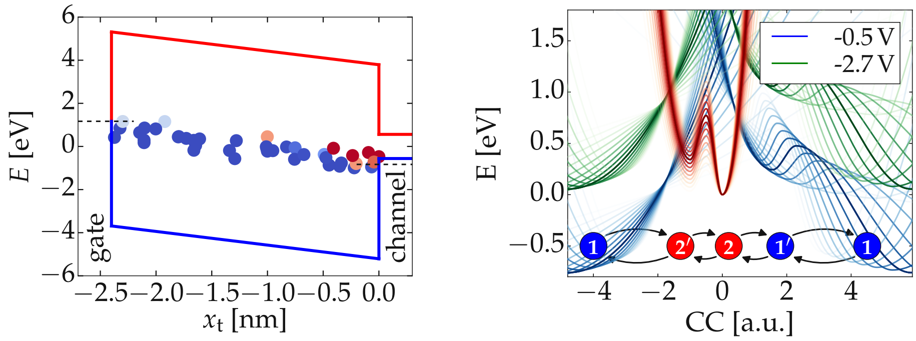

FIGURE 3.12: Left: A band diagram of a SiO_2 pMOSFET with a random distribution of oxide defects in positive (red circles) and neutral states (blue circles). Right: The schematic distribution of CC diagrams of such a device for two different gate voltages. After [GRC2].

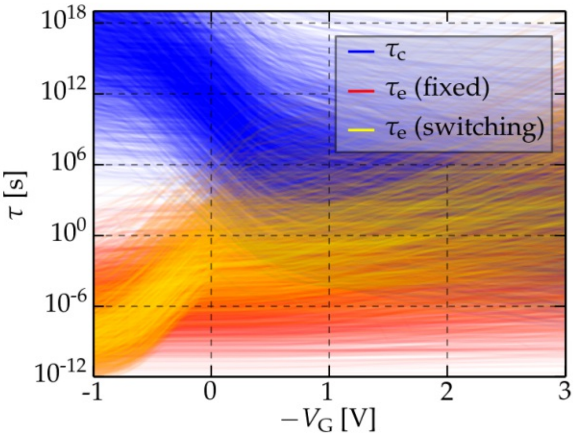

FIGURE 3.13: The capture and emission time constants of an ensemble of defects computed with the 4-state NMP model. The characteristic features of the fixed positive oxide charges (red) and the switching traps (yellow) are visible around $V_G = 0.5$ V. After [GRC13].

Towards Hydrogen Release: The Quasi-Permanent Part

The discussion above was limited to pre-existing oxide defects in the 4-state NMP model, hence, covered the *recoverable* component of BTI. While the *quasi-permanent* component was coupled directly to the recoverable part in the two-stage model, they are treated separately in the 4-state NMP model. Thus, in order to describe the full degradation at BTI conditions, the 4-state NMP model has to be complemented by a description of the quasi-permanent part. The field-dependent thermal transition model was used for this purpose previously [GRC15], see Subsection 3.3.2. While the 4-state NMP model describes single defect level in considerable detail, the decoupling from the quasi-permanent component is unsatisfying given the number of studies which indicate a mechanism coupled via hydrogen relocation [35, 144, 145]. This motivated further research which led to the development of the *gate-sided hydrogen release model* [GRC20] as presented in the following.

3.4.3 Gate-Sided Hydrogen Release Model

The gate-sided hydrogen release model [GRC20] is an evolution of the 4-state NMP model which considers the role of hydrogen as a link between the recoverable and the quasi-permanent component of BTI. In the following, evidence for hydrogen being involved in BTI will be presented and the implementation of hydrogen mechanisms in the gate-sided hydrogen release model will be discussed.

Motivation for the Model

Hydrogen has long been suspected of activating, creating or altering defects or interface states at NBTI conditions. Studies (listed chronologically) have suggested that

- Degradation induced by vacuum-ultraviolet irradiation does not recover if the sample is subjected to large negative gate bias. However, at zero gate bias and positive gate bias, the sample does recover, and, deduced from deactivation of boron "*the experiments unambiguously show that H is released during the decay of donor states and not when annealing is inhibited*" [144].
- The exposure of a Si/SiO$_2$ sample with atomic hydrogen from a remote plasma induces a much larger interface state density (determined by electrical measurements) compared to the increase in silicon bond density (measured with ESR) [146]. Experiments with hot-electron stress indicate the same [147].
- Temperature treatment at 400°C increases the number of precursors for fast interfacial states while it does not affect the number of oxide traps which cause a shift of the threshold voltage. This effect is pronounced for temperature treatments in forming gas anneal. The defects induced by this treatment are found to differ from the original defects as they can be annealed without supplying hydrogen and saturate after moderate stress times [145].
- NBTI stress induces an increase of interface states in general, accompanied by an increase of P_b density in SiO$_2$ based pMOSFETs [148].
- The hydrogen concentration in the near-interfacial region increases during NBTI stress [35].
- After NBTI stress, followed by one week of recovery, the ratio of the total threshold voltage shift to the threshold voltage shift deduced from charge pumping is roughly 1:1 [149].
- P_b centers are *generated* on hydrogen-passivated Si/SiO$_2$ interfaces during NBTI stress while they are *reduced* on hydrogen-free Si/SiO$_2$ interfaces [150].
- Defects which capture holes at NBTI conditions can become inactive for an extended period of time. This *volatility* was suggested to be due to the relocation of hydrogen atoms [151].

Mechanisms Considered in the Model

In the search for a physical mechanism which is consistent with these observations and with the studies on the two-stage model and the 4-state NMP model, Grasser *et al.* conducted long-term measurements (up to 90 days) during which the quasi-permanent component was constantly monitored [GRC20]. These measurements employed a pragmatic definition for the quasi-permanent component which relies on $I_\mathrm{D}V_\mathrm{G}$ sweeps removing most of the recoverable component [GRC20]. The experiments revealed that during recovery at zero gate bias and 350°C additional defects are created, see Fig. 3.14. In the model, these defects are described as activated precursors due to additional hydrogen which is released from a *gate-sided* reservoir at elevated temperatures [GRC20].

In addition to this mechanism, the gate-sided hydrogen release model accounts for a redistribution of hydrogen within the oxide: In this model, hydrogen at a defect site can only be released

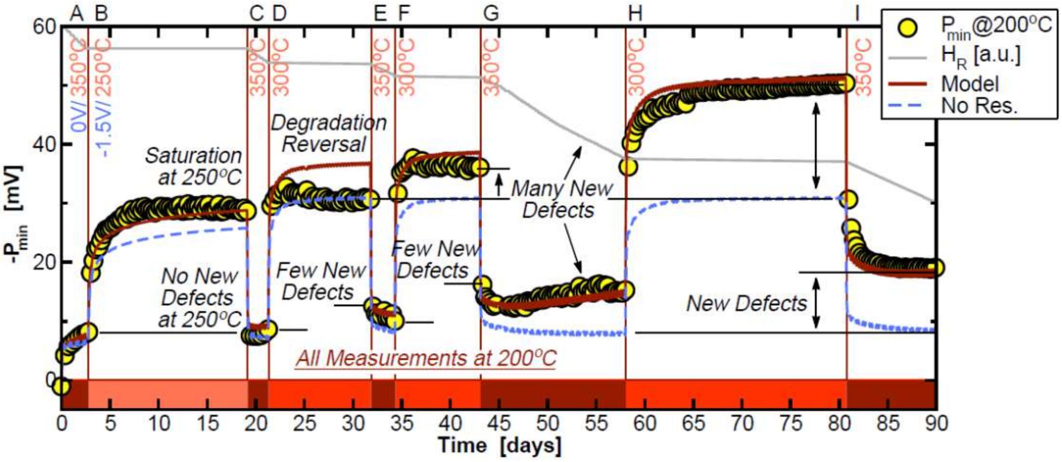

FIGURE 3.14: The measurement of the quasi-permanent component P_{min} (circles) saturates in the stress phases B, D, F, and H with $V_{\mathrm{G}} = 1.5\,\mathrm{V}$. All other phases have zero gate bias, still there are new defects created during phase G with 350°C for a long time. These defects are suggested to be created due to hydrogen released from a *gate-sided* reservoir [GRC20]. In the model, the hydrogen concentration (gray line) increases accordingly and as opposed to the model without the reservoir (dashed blue), the full gate-sided hydrogen release model (red line) is in agreement with the experimental data. After [GRC1].

in the neutral stable defect configuration which corresponds to state 1 in the 4-state NMP description. As a consequence, defects which are neutralized during stress can release atomic hydrogen. This hydrogen redistributes quickly in the oxide [152] to find a precursor with which he can transform into a positive defect. Thus, defects which are favorably charged positively at stress conditions will more likely bind a hydrogen [GRC20]. For the case of NBTI, this causes a deactivation of defects close to the gate during stress followed by an increase of active defects and hydrogen in the near-interfacial region as depicted in Fig. 3.15.

The gate-sided hydrogen release model was subsequently extended to also account for the creation of P_{b} centers. This is a natural extension for this model as the atomic hydrogen which redistributes after stress can easily depassivate SiH bonds to create P_{b} centers [120]. With the full gate-sided hydrogen release model as depicted schematically in Fig. 3.16, all of the findings listed above can be understood consistently which enables unified modeling of various aspects of BTI [GRC3].

Concise Mathematical Description

Mathematically, the gate-sided hydrogen release model builds on top of the 4-state NMP model with the occupation probabilities p_1, $p_{1'}$, p_2, and $p_{2'}$ of its states, see Eq. (3.53) - (3.56). For numerical convenience, “oxide sites” are defined as a local collection of hydrogen trapping sites which can trap $H_{\mathrm{T,max}}$ hydrogen atoms via exchange with the hydrogen reservoir from state 1. For each oxide site i the trapped number of hydrogen atoms $H_{\mathrm{T},i}$ gives its total positive charge

$$q_{\mathrm{T},i} = q\left(p_{2,i} + p_{2',i}\right) H_{\mathrm{T},i}. \tag{3.66}$$

With the rates of hydrogen capture k_{01} and hydrogen release k_{10}, the rate equation reads

$$\frac{\mathrm{d}H_{\mathrm{T},i}}{\mathrm{d}t} = -k_{10,i}p_{1,i}H_{\mathrm{T},i} + k_{01,i}H^0\left(H_{\mathrm{T,max}} - H_{\mathrm{T},i}\right) \tag{3.67}$$

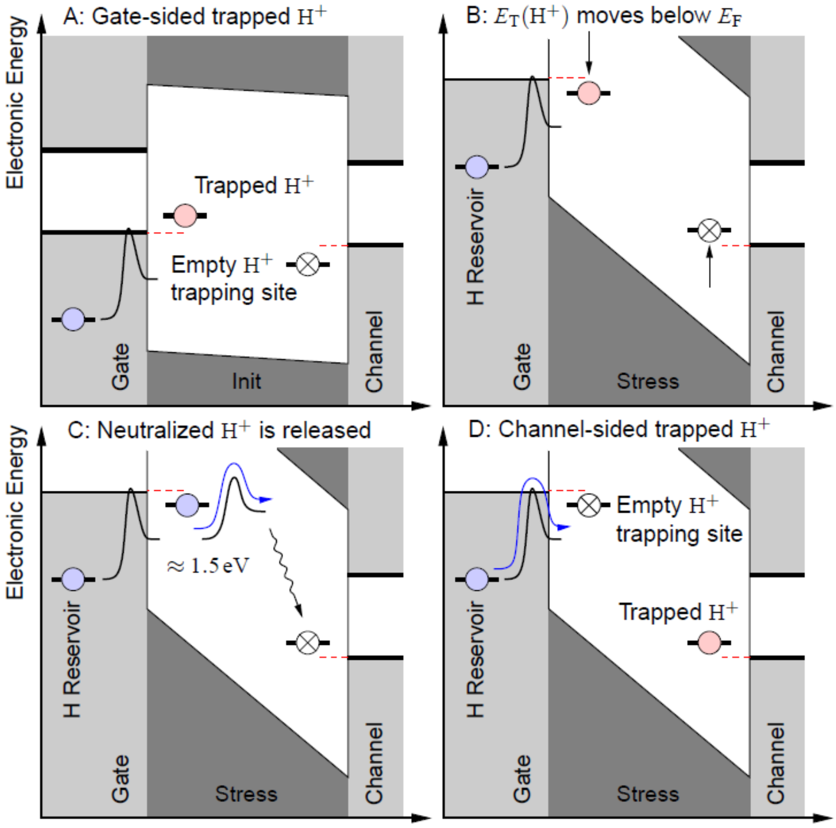

FIGURE 3.15: The gate-sided hydrogen release model extends the 4-state NMP model by two mechanisms: I) The total hydrogen concentration in the oxide is controlled by a *gate-sided* reservoir which is thermally activated (bottom right). II) Atomic hydrogen can be released from defects in the neutral configuration (bottom left) to redistribute subsequently and activate an energetically more favorable precursor (bottom right). After [GRC1].

where H^0 is the number of interstitial hydrogen atoms. This interstitial hydrogen is coupled to the gate-sided hydrogen reservoir H_R as

$$\frac{\mathrm{d}H_\mathrm{R}}{\mathrm{d}t} = -k_{\mathrm{R}0}H_\mathrm{R} + k_{0\mathrm{R}}H^0 \tag{3.68}$$

with the rates for hydrogen being released from the reservoir $k_{\mathrm{R}0}$ and captured in the reservoir $k_{0\mathrm{R}}$. The total number of hydrogen atoms H_tot must stay constant:

$$H_\mathrm{tot} = H^0 + H_\mathrm{R} + \sum_i H_{\mathrm{T},i}. \tag{3.69}$$

Finally, the depassivation of P_b centers can be described following a reaction-limited model [29]. With the above, a coupled system of defect generation and charging is described. Its rates are governed by activation energies as the diffusion of hydrogen is found to be too fast to affect the degradation of thin oxides above room temperature [152].

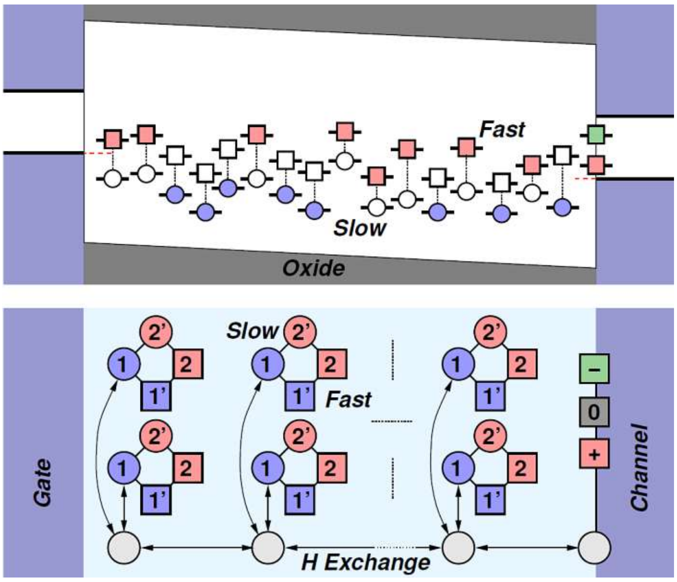

FIGURE 3.16: The schematic band diagram for the full gate-sided hydrogen release model indicating the more stable primary configurations (circles) compared to the metastable states with higher trap levels (squares). Atomic hydrogen can activate 4-state NMP precursors and can be released again in the neutral stable configuration (state 1). Additionally, the atomic hydrogen can depassivate P_b centers (squares at the channel interface) which then can be positive (red), neutral (gray), or negative (green), depending on the Fermi level. After [GRC3].

Chapter 4

Compact-Physics Framework: Comphy

Very detailed BTI models were presented in the last chapter which can describe various reliability phenomena related to oxide degradation. However, these models are rather complex and the extraction of the model parameters is a tedious task which requires in-depth knowledge of the underlying physics and considerable computational power. Still, these models are very useful to investigate the essential mechanisms of oxide degradation. Step by step we developed concise physical models which accurately describe the mean degradation due to BTI. In this chapter, we will present this framework called *Comphy*, short for "compact-physics".

4.1 Electrostatics

The description of the electrostatics is vital for every *physical* degradation model. In this section, we will first review the basics of semiconductor modeling which will then be employed to solve the electrostatics of a 1D MOS device.

4.1.1 Band Gap

A review of analytic expressions for the temperature dependence of the silicon band gap is found in the work of GREEN [153]. BLUDAU's experimental work on the band gap of silicon was captured well with a 2nd degree polynomial model $E_\mathrm{G} = A + BT + CT^2$ with the coefficients for the temperature range of 0 to 190 K as [154]

$$\begin{aligned} A &= 1.17\,\mathrm{eV}, \\ B &= 1.059 \times 10^{-5}\,\mathrm{eV/K}, \\ C &= -6.05 \times 10^{-7}\,\mathrm{eV/K^2}, \end{aligned}$$

and in the range of 150 K to 300 K as [154]

$$\begin{aligned} A &= 1.1785\,\mathrm{eV}, \\ B &= -9.025 \times 10^{-5}\,\mathrm{eV/K}, \\ C &= -3.05 \times 10^{-7}\,\mathrm{eV/K^2}. \end{aligned}$$

For temperatures above 250 K, GREEN suggested the expression below, adopted from MACFARLANE *et al.* [155]:

$$E_\mathrm{G} = 1.206 - 2.73 \times 10^{-4}\,\mathrm{eV} \times T \tag{4.1}$$

The latter approximation gives good results for elevated temperatures which are typically used in accelerated BTI studies. A comparison of the approximations together with the experimental data is shown in Fig. 4.1.

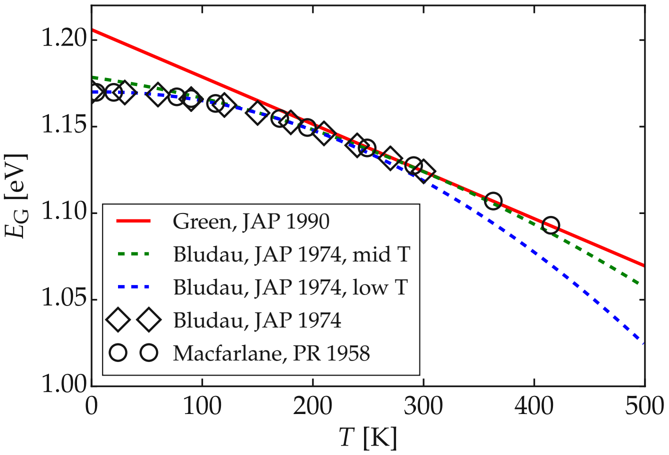

FIGURE 4.1: The temperature dependence of the band gap of silicon was measured in 1958 by MACFARLANE *et al.* [155]. This data is shown here (circles) corrected by the excitation binding energy of 0.014 eV [156]. BLUDAU *et al.* obtained similar values (diamonds) and suggested a model for low temperatures (dashed blue) and moderate temperatures (dashed green) [154]. Based on that, GREEN suggested a first-order approximation (red) which is valid for higher temperatures [153].

4.1.2 Effective Carrier Masses

The effective mass calculations of BARBER in 1967 [157] were improved later in 1981 by MADARASZ *et al.* [158]. Based on this work, LANG *et al.* gave the following polynomial fitted expression for the effective mass of the valence band of silicon $m_{p,\mathrm{eff}}$ [159]:

$$\frac{m_{p,\mathrm{eff}}(T)}{m_0} = \left(\frac{A + BT + CT^2 + DT^3 + ET^4}{1 + FT + GT^2 + HT^3 + IT^4}\right)^{2/3} \tag{4.2}$$

The corresponding coefficients are [159]:

$$\begin{aligned} A &= 0.443\,587\,0 & B &= 0.360\,952\,8 \times 10^{-2}\,\mathrm{K}^{-1} \\ C &= 0.117\,351\,5 \times 10^{-3}\,\mathrm{K}^{-2} & D &= 0.126\,321\,8 \times 10^{-5}\,\mathrm{K}^{-3} \\ E &= 0.302\,558\,1 \times 10^{-8}\,\mathrm{K}^{-4} & F &= 0.468\,338\,2 \times 10^{-2}\,\mathrm{K}^{-1} \\ G &= 0.228\,689\,5 \times 10^{-3}\,\mathrm{K}^{-2} & H &= 0.746\,927\,1 \times 10^{-6}\,\mathrm{K}^{-3} \\ I &= 0.172\,748\,1 \times 10^{-8}\,\mathrm{K}^{-4} \end{aligned}$$

For the effective mass of the conduction band $m_{n,\mathrm{eff}}$ GREEN proposed a refinement of the work of BARBER to account for the temperature dependence as [153]

$$\frac{m_{n,\mathrm{eff}}(T)}{m_0} = \left(\left(0.1905\frac{E_\mathrm{G}(T = 0\,\mathrm{K})}{E_\mathrm{G}(T)}\right)^2 0.9163\right)^{1/3}. \tag{4.3}$$

Here we use Eq. (4.1) to compute $E_\mathrm{G}(T)$. The effective masses as a function of the temperature are shown in Fig. 4.2.

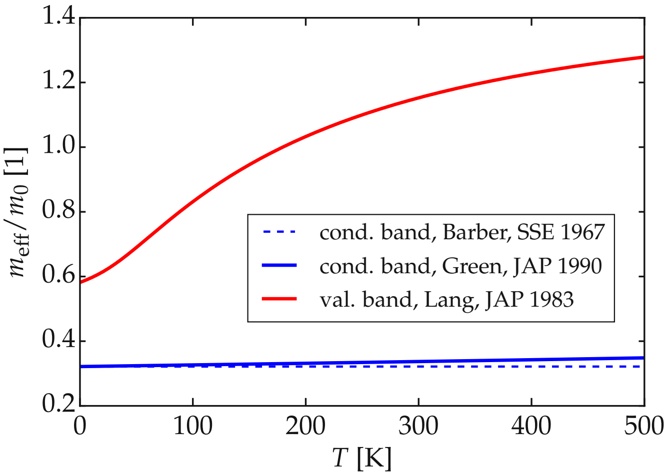

FIGURE 4.2: The temperature dependence of the effective mass for the valence band (red) is computed following LANG *et al.* [159], compare Eq. (4.2). The temperature independent effective mass for the conduction band (dashed blue) following the work of BARBER [157] is shown together with the temperature dependent refinement (solid blue) proposed by LANG *et al.* [159], compare Eq. (4.3).

4.1.3 Effective Density of States

The effective density of states of the conduction band N_C and of the valence band N_V are given by [79]:

$$N_C = 2(2\pi m_{n,\text{eff}} k_B T / h^2)^{3/2} M_C, \tag{4.4}$$

$$N_V = 2(2\pi m_{p,\text{eff}} k_B T / h^2)^{3/2}, \tag{4.5}$$

with the number of equivalent conduction band minima $M_C = 6$ for silicon.

4.1.4 Carrier Concentrations at Thermal Equilibrium

While the intrinsic carrier concentration of a semiconductor n_i is simply [79]

$$n_i = \sqrt{N_C N_V} e^{-E_G/(2k_B T)} \tag{4.6}$$

the electron concentration n is given by the density of states $\mathcal{N}_C(E)$ and their occupation probability function $f(E)$:

$$n = \int_{E_C}^{\infty} \mathcal{N}_C(E) f(E) dE \tag{4.7}$$

Fermi-Dirac Distribution

With the Fermi-Dirac distribution function $f_F(E)$ as

$$f_F(E) = \frac{1}{1 + e^{(E-E_F)/(k_B T)}} \tag{4.8}$$

and a parabolic density of states with the *effective* density of states of the conduction band N_C, the electron concentration for thermal equilibrium conditions n_0 evaluates to [79]

$$n_0 = N_\mathrm{C} \frac{2}{\sqrt{\pi}} \int_{E_\mathrm{C}}^{\infty} \frac{\sqrt{(E - E_\mathrm{C}) \,/\, (k_\mathrm{B} T)}}{1 + \mathrm{e}^{(E - E_\mathrm{F})/(k_\mathrm{B} T)}} \frac{\mathrm{d}E}{k_\mathrm{B} T} \tag{4.9}$$

with the conduction band edge E_C. Since this integral cannot be evaluated analytically, there are several approximations, two of which are discussed in the following.

Boltzmann Approximation

For non-degenerated semiconductors with $E_\mathrm{C} - E_\mathrm{F} \gg k_\mathrm{B} T$ and $E_\mathrm{F} - E_\mathrm{V} \gg k_\mathrm{B} T$ the Fermi-Dirac distribution approaches the Boltzmann distribution and the carrier concentration of electrons n_0 and holes p_0 for thermal equilibrium conditions can be approximated by

$$n_0 \approx N_\mathrm{C} \mathrm{e}^{-(E_\mathrm{C} - E_\mathrm{F})/(k_\mathrm{B} T)}, \tag{4.10}$$

$$p_0 \approx N_\mathrm{V} \mathrm{e}^{-(E_\mathrm{F} - E_\mathrm{V})/(k_\mathrm{B} T)}. \tag{4.11}$$

Joyce-Dixon Approximation

In 1977 Joyce and Dixon extended the Boltzman approximation with a polynomial term [160] as

$$-\frac{E_\mathrm{C} - E_\mathrm{F}}{k_\mathrm{B} T} \approx \ln \frac{n_0}{N_\mathrm{C}} + \sum_{m=1}^{4} A_m \left(\frac{n_0}{N_\mathrm{C}} \right)^m, \tag{4.12}$$

$$-\frac{E_\mathrm{F} - E_\mathrm{V}}{k_\mathrm{B} T} \approx \ln \frac{p_0}{N_\mathrm{V}} + \sum_{m=1}^{4} A_m \left(\frac{p_0}{N_\mathrm{V}} \right)^m, \tag{4.13}$$

with following coefficients [160]:

$$A_1 = 3.535\,53 \times 10^{-1} \qquad A_2 = -4.950\,09 \times 10^{-3}$$

$$A_3 = 1.483\,86 \times 10^{-4} \qquad A_4 = -4.425\,63 \times 10^{-6}$$

With these four coefficients, this approximation is valid for a much wider range of degeneracy up to $E_\mathrm{F} - E_\mathrm{C} \approx 8 k_\mathrm{B} T$.

Fermi Level at Thermal Equilibrium

The Fermi level in the channel of a doped MOS device for thermal equilibrium ($E_{\mathrm{F},0}$) can be obtained as follows. Assuming that all dopants in the semiconductor are ionized, charge neutrality prevails if

$$n_0 + N_\mathrm{A} = p_0 + N_\mathrm{D} \tag{4.14}$$

holds, where N_A is the concentration of acceptors and N_D the concentration of donors. For non-degenerated semiconductors in thermal equilibrium with $n_\mathrm{i}{}^2 = n_0 p_0$ this gives for n-type semiconductors ($N_\mathrm{D} > N_\mathrm{A}$) [79]

$$n_0 = \frac{N_\mathrm{D} - N_\mathrm{A}}{2} + \sqrt{\left(\frac{N_\mathrm{D} - N_\mathrm{A}}{2}\right)^2 + {n_\mathrm{i}}^2}, \tag{4.15}$$

$$p_0 = \frac{{n_\mathrm{i}}^2}{n_0}, \tag{4.16}$$

$$N_\mathrm{D} - N_\mathrm{A} = n_\mathrm{i}\mathrm{e}^{(E_{\mathrm{F},0} - E_\mathrm{i})/(k_\mathrm{B}T)}, \tag{4.17}$$

and analogously for p-type semiconductors ($N_\mathrm{A} > N_\mathrm{D}$)

$$n_0 = \frac{{n_\mathrm{i}}^2}{p_0}, \tag{4.18}$$

$$p_0 = \frac{N_\mathrm{A} - N_\mathrm{D}}{2} + \sqrt{\left(\frac{N_\mathrm{A} - N_\mathrm{D}}{2}\right)^2 + {n_\mathrm{i}}^2}, \tag{4.19}$$

$$N_\mathrm{A} - N_\mathrm{D} = n_\mathrm{i}\mathrm{e}^{(E_{\mathrm{F},0} - E_\mathrm{i})/(k_\mathrm{B}T)}. \tag{4.20}$$

Thus, $E_{\mathrm{F},0}$ can be evaluated given the intrinsic Fermi level E_i as [79]

$$E_\mathrm{i} = \frac{E_\mathrm{C} + E_\mathrm{V}}{2} + \frac{k_\mathrm{B}T}{2}\ln\left(\frac{N_\mathrm{V}}{N_\mathrm{C}}\right). \tag{4.21}$$

4.1.5 Electrostatics of a 1D MOS Device

With the basic semiconductor equations outlined above, we now can compute the electrostatics of 1D MOS devices. First, this will be shown for an ideal, defect-free, MOS device. Afterward, we will discuss three options of different accuracy to consider oxide charges. Finally, we will show a simplified approach to obtain the electrostatics which requires the surface potential as an input quantity.

Charge-Free Oxide

In order to compute the surface potential φ_S at the interface between the channel and the oxide of a 1D MOS device without oxide charges, we employ an iterative solver following the scheme presented in Fig. 4.3 with the input quantities listed in Table 4.1 and the computed quantities listed in Table 4.2.

The total space charge Q_S (per unit area) in the channel as a function of the surface potential can be written as [79]

$$Q_\mathrm{S} = \pm\frac{\sqrt{2}k_\mathrm{B}T}{qL_\mathrm{D}}\left(\left(\mathrm{e}^{-\varphi_\mathrm{S}/(k_\mathrm{B}T)} + \varphi_\mathrm{S}\left(k_\mathrm{B}T\right) - 1\right) + \frac{n_0}{p_0}\left(\mathrm{e}^{\varphi_\mathrm{S}/(k_\mathrm{B}T)} - \varphi_\mathrm{S}\left(k_\mathrm{B}T\right) - 1\right)\right)^{1/2} \tag{4.22}$$

with positive sign for $\varphi_\mathrm{S} > 0$ and negative sign for $\varphi_\mathrm{S} < 0$ and the Debye length for holes L_D given as

$$L_\mathrm{D} = \sqrt{\frac{k_\mathrm{B}T\varepsilon_0\varepsilon_{\mathrm{r,chan}}}{p_0q^2}}. \tag{4.23}$$

TABLE 4.1: *Input quantities* for electrostatics in Comphy.

quantity	description
N_A	concentration of acceptor doping of the channel
N_D	concentration of donor doping of the channel
$\Delta E_\mathrm{W,0}$	intrinsic work function difference, see Eq. (4.28) and Fig. 4.5
V_G	gate voltage
$\varepsilon_\mathrm{r,chan}$	relative permittivity of the channel
$\varepsilon_\mathrm{r,ox}$	relative permittivity of the oxide
x_ox	thickness of the oxide

TABLE 4.2: *Computed quantities* in Comphy.

quantity	description	equation
$E_\mathrm{G,chan}$	band gap of the channel	Eq. (4.1)
$m_{n,\mathrm{eff}}$	effective carrier concentration of the conduction band	Eq. (4.3)
$m_{p,\mathrm{eff}}$	effective carrier concentration of the valence band	Eq. (4.2)
N_C	effective density of states of the conduction band	Eq. (4.4)
N_V	effective density of states of the valence band	Eq. (4.5)
$E_\mathrm{F,0}$	Fermi level in the channel at thermal equilibrium[2]	Eq. (4.17) & (4.20)
n_0	electron concentration at thermal equilibrium	Eq. (4.15) & (4.18)
p_0	hole concentration at thermal equilibrium	Eq. (4.16) & (4.19)
Q_S	total space charge obeying the Poisson equation	Eq. (4.22)
φ_S	surface potential obeying the Poisson equation	Eq. (4.29)
E_F	Fermi level of the channel at the interface to the oxide	Eq. (4.32)
n	electron concentration of the channel at the interface	Eq. (4.12)
p	hole concentration of the channel at the interface	Eq. (4.13)
E_ox	electric field at the interface	Eq. (4.30)
φ	electrostatic potential across the oxide	Eq. (4.31)

Furthermore, with the effective[1] gate width W and length L, the capacitance of the oxide C_ox is

$$C_\mathrm{ox} = \frac{\varepsilon_0 \varepsilon_\mathrm{r,ox} WL}{x_\mathrm{ox}} \tag{4.24}$$

and simple electrostatics give (see Fig. 4.4)

$$V_\mathrm{ox}(\varphi_\mathrm{S}) + \varphi_\mathrm{S} - V_\mathrm{G} + \Delta E_\mathrm{W}/q = 0. \tag{4.25}$$

With

$$V_\mathrm{ox}(\varphi_\mathrm{S}) = \frac{Q_\mathrm{S}(\varphi_\mathrm{S}) WL}{C_\mathrm{ox}} \tag{4.26}$$

---

[1] The nominal gate dimensions of a technology are not necessarily what defines the oxide capacitance. For example the height of the fin has to be considered for FinFETs.

[2] The intrinsic Fermi level E_i is approximated to be at mid-gap in the simulations.

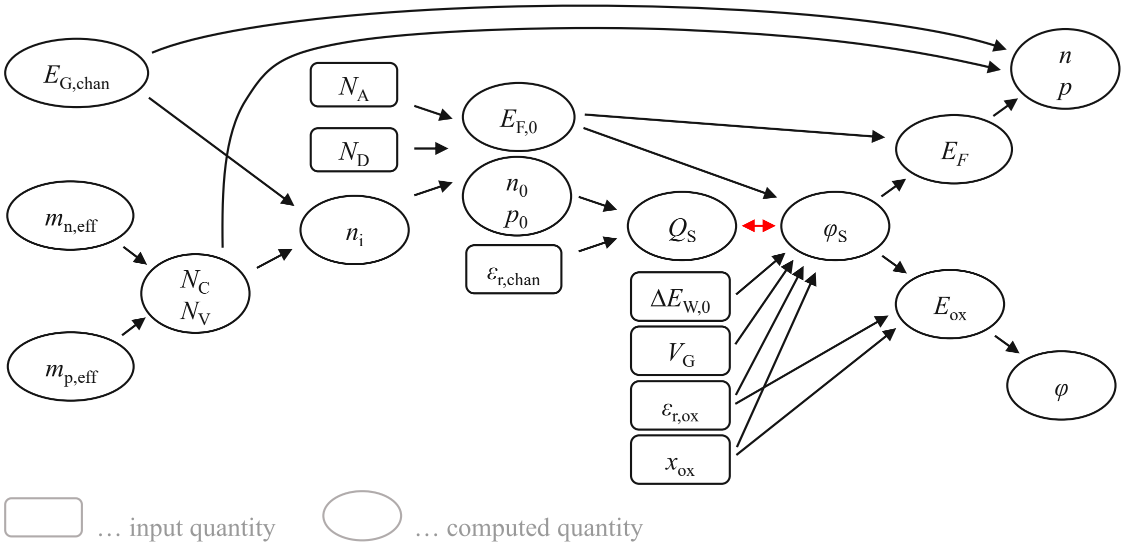

FIGURE 4.3: In order to compute the carrier concentrations n and p at the interface of the channel of a 1D MOS device and the electrostatic potential φ across the oxide, the surface potential φ_S has to be calculated. As depicted here schematically, this can be done following the approximation of the total space charge Q_S based on the Poisson equation derived in [79] in an iterative scheme with the input quantities listed in Table 4.1 and the computed quantities listed in Table 4.2.

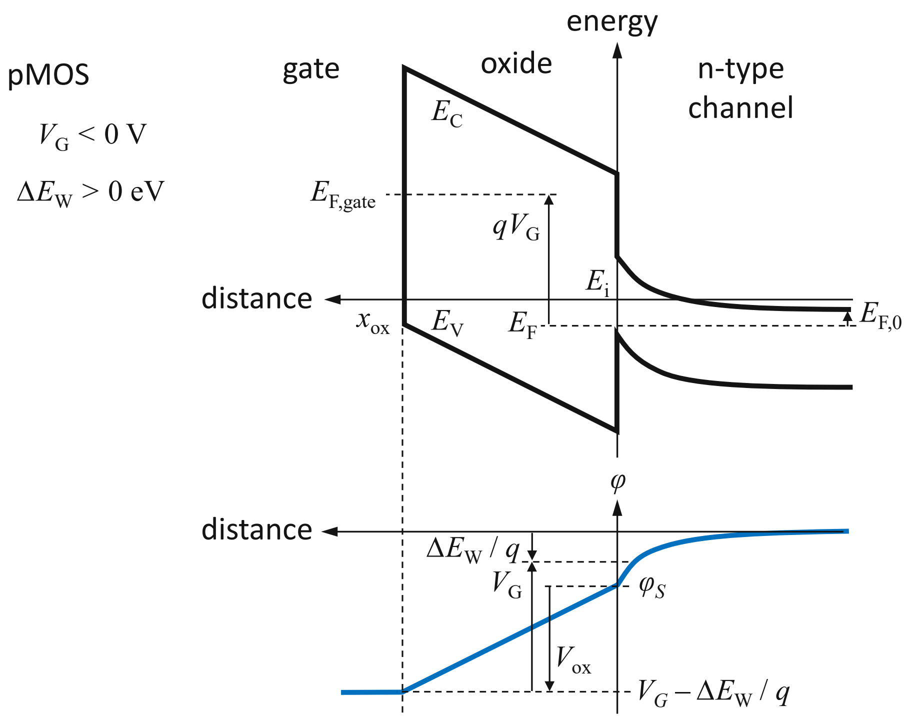

FIGURE 4.4: A schematic band diagram of a pMOSFET with $V_G < 0$ V (top) and the corresponding electrostatic potential (bottom). With the voltage drop across the oxide $V_{\text{ox}} = Q_S WL / C_{\text{ox}}$, the surface potential φ_S can be computed following Eq. (4.29) and the oxide field E_{ox} as given in Eq. (4.30).

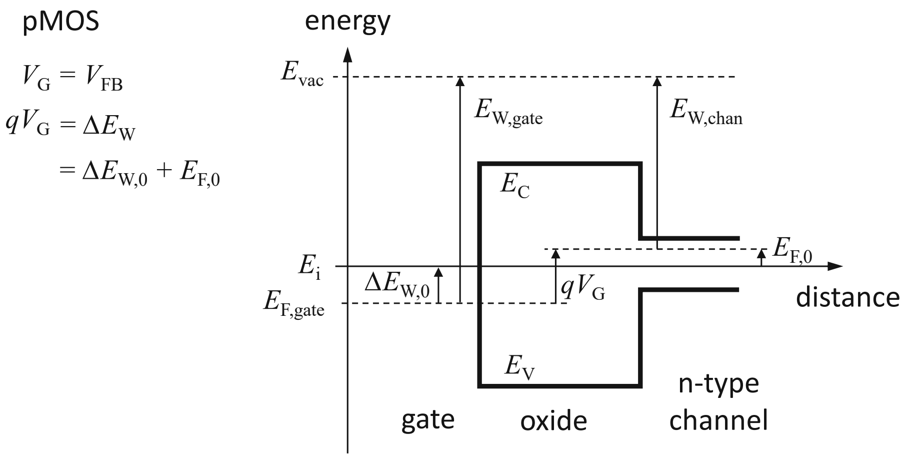

FIGURE 4.5: A schematic band diagram of a pMOSFET with V_G equals the flat band voltage V_{FB}. The work functions $E_{W,gate}$ and $E_{W,chan}$ are defined as the difference of the vacuum energy E_{vac} and the respective Fermi levels and constitute the work function difference $\Delta E_W = E_{W,gate} - E_{W,chan}$. However, as simulation input, it can be advantageous to specify the *intrinsic work function difference* $\Delta E_{W,0} = \Delta E_W - E_{F,0}$.

and the work function difference ΔE_W defined as

$$\Delta E_W = E_{W,gate} - E_{W,chan} \tag{4.27}$$

Eq. (4.25) can be evaluated in an iterative scheme to obtain φ_S. However, ΔE_W is an input quantity in this approach but, at the same time, is a function of $E_{W,chan}$ which is readily defined by the doping concentrations[3] which are input quantities as well. Thus, we employ the *intrinsic work function difference* $\Delta E_{W,0}$ given by (see Fig. 4.5)

$$\Delta E_{W,0} = \Delta E_W - E_{F,0} \tag{4.28}$$

to obtain φ_S from solving the following equation an iterative scheme:

$$\frac{Q_S(\varphi_S)WL}{C_{ox}} + \varphi_S - V_G + \Delta E_{W,0}/q + E_{F,0}/q = 0 \tag{4.29}$$

Based on the surface potential φ_S, the electric field E_{ox} of the charge free oxide can be computed in a straightforward manner (see Fig. 4.4) as

$$E_{ox} = \frac{V_G - \Delta E_W/q - \varphi_S}{x_{ox}} \tag{4.30}$$

and the electrostatic potential across the oxide is given by

$$E_{ox} = -\nabla\varphi. \tag{4.31}$$

Note that this scheme can be extended for oxide stacks with multiple layers of arbitrary permittivities and thicknesses but is presented here for a single layer oxide for clarity. Since E_F can be determined by φ_S as

$$E_F = E_{F,0} + q\varphi_S \tag{4.32}$$

---

[3] The work function $E_{W,chan}$ depends on the Fermi level at thermal equilibrium $E_{F,0}$ (see Fig. 4.5) which, in turn, is a function of the doping, see Eq. (4.17) & (4.20).

the carrier concentrations of holes p and electrons n at the interface of the channel can now be evaluated using the Joyce-Dixon approximation given in Eq. (4.13) & (4.12).

Oxide Charges Decoupled from Poisson Equation

As discussed above, the scheme presented in Fig. 4.3 applies to oxides without any charges as they do not enter the approximation of the surface potential given by Sze in [79]. A simple and computationally efficient way to estimate the impact of charges in the oxide on the threshold voltage of the MOS device is given by the *charge sheet approximation*, see Eq. (3.65). This approximation is valid for low net concentrations of charges in the oxide as they are computed fully decoupled from the Poisson equation in a postprocessing step. This method is particularly efficient because it is robust for arbitrary sparse sampling in the time domain.

Non Self-Consistent Poisson Scheme

In the *non self-consistent Poisson (NCP)* scheme, the oxide charges are neglected in the first time step $[i = 0]$ but for all following time steps i the impact of the oxide charges V_traps obtained from the charge sheet approximation, enters the Poisson equation via an *effective* gate voltage $V_\mathrm{G,eff}$ as

$$V_\mathrm{G,eff}[i] = V_\mathrm{G}[i] - V_\mathrm{traps}[i-1] + V_\mathrm{traps}[i=0]. \tag{4.33}$$

This scheme requires a reasonably fine sampling in the time domain, but the reduction of the electric field due to charges in the oxide is well approximated, in particular if the net concentration of oxide charges is low in the first time step. Note that a qualitative comparison between these schemes is difficult because the accuracy strongly depends on the device and defect properties as well as on the stress conditions.

Self-Consistent Poisson Scheme

The most accurate way to consider charges in the oxide is to account for them in the Poisson equation in a self-consistent manner. In this *self-consistent Poisson (SCP)* mode, the scheme presented in Fig. 4.3 is extended to consider oxide charges in the iterative computation of φ_S and this scheme is put into an outer iteration loop to correct the charges of the oxide defects according to the updated electrostatics self-consistently. For this, the electrostatic impact of the oxide charges has to be considered in Eq. (4.29) to determine the surface potential as

$$\frac{Q_\mathrm{S}(\varphi_\mathrm{S})WL}{C_\mathrm{ox}} + \varphi_\mathrm{S} - V_\mathrm{G} + \Delta E_\mathrm{W,0}/q + E_\mathrm{F,0}/q + V_\mathrm{traps} = 0 \tag{4.34}$$

where V_traps is the sum of the electrostatic impact of the oxide charges projected to the gate according to the Poisson equation. Once the above equation has converged, the resulting φ_S is used to compute the electrostatic potential $\varphi(x)$ across the device, again under consideration of the oxide charges following the Poisson equation. This updated potential may affect the charge state of oxide defects which have to be updated accordingly. Solving the above equation again with the updated charges gives a difference in the surface potentials which has to be smaller than the criterion for the time step to converge.

Surface Potential as an Input Quantity

Alternatively to calculating the surface potential φ_S following the scheme given in Fig. 4.3, $\varphi_\mathrm{S}(V_\mathrm{G})$ can also be supplied as an external function to obtain the carrier concentrations and the electrostatic potential of the 1D MOS device. This can be useful since the surface potential can be roughly deduced from experimental capacitance-voltage (CV) curves directly [161] or from other device simulators. In this case, the input quantities N_A, N_D, $\varepsilon_\mathrm{r,chan}$, and $\Delta E_\mathrm{W,0}$ are not used and instead $E_\mathrm{F,0}$ has to be supplied. The evaluation of the electrostatics is straightforward then as it does not require an iterative solver anymore, however, note that the SCP scheme cannot be applied anymore, since φ_S is a fixed function of the gate voltage.

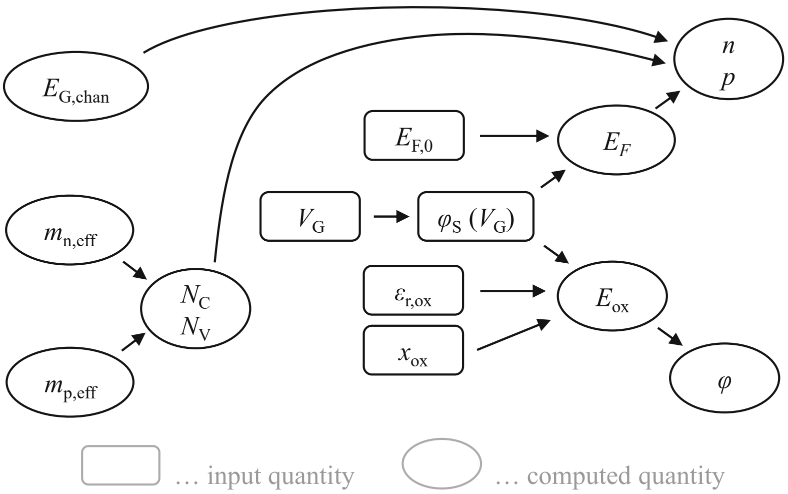

FIGURE 4.6: Alternatively to the scheme presented in Fig. 4.3, the carrier concentrations n and p at the interface of the channel of a 1D MOS device and the electrostatic potential φ across the oxide can be computed based on a given surface potential $\varphi_\mathrm{S}(V_\mathrm{G})$. The remaining quantities here are still computed as listed in Table 4.2 based on the quantities given in Table 4.1, except that $E_\mathrm{F,0}$ and φ_S are now treated as input quantities.

4.2 Tunneling

At BTI conditions, charge trapping is typically determined by quantum-mechanical tunneling. The wavefunction of carriers in the gate and the channel penetrates into the oxide to defect sites resulting in a finite tunneling probability T which can be determined by solving the Schrödinger equation. A frequently employed approach to obtain T for various barrier shapes is based on the WKB approximation [162] which reads [79]

$$T \approx \exp\left(-\frac{2}{\hbar}\sqrt{2m_\mathrm{t}} \int_{x_1}^{x_2} \left(U(x) - E_0\right) \mathrm{d}x \right) \tag{4.35}$$

with the effective tunneling mass m_t, the potential of the barrier $U(x)$, the energy of the carrier E_0 and the barrier width $x_\mathrm{T} = x_2 - x_1$. The tunneling probability between a carrier reservoir and a defect in the oxide at the distance x_T can be obtained from the product of the tunneling probabilities of the segments along this distance with the band edge approximated to be linear within each segment. Thus, T has to be solved for arbitrary *linear* energy barriers which can be obtained from the integral above, distinguishing two cases: *direct tunneling* with a trapezoidal energy barrier shape and *Fowler-Nordheim* tunneling [163] with a triangular energy barrier shape. With the energies depicted in Fig. 4.7, the equation for direct tunneling reads

$$T = \exp\left(-\frac{2}{\hbar}\sqrt{2m_\mathrm{t}} x_\mathrm{T} \frac{2}{3} \left(\sqrt{E_2 - E_0} + \frac{E_1 - E_0}{\sqrt{E_1 - E_0} + \sqrt{E_2 - E_0}} \right) \right) \tag{4.36}$$

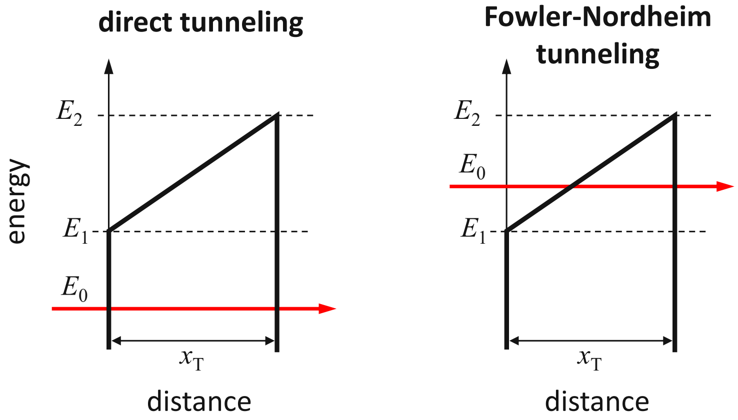

FIGURE 4.7: Schematic band diagram showing a carrier with the energy E_0 tunneling through an energy barrier with the width x_T in the regime of *direct tunneling* ($E_1 > E_0$ and $E_2 > E_0$) and in the regime of *Fowler-Nordheim tunneling* ($E_2 > E_0 > E_1$).

and is valid for all values within the regime of direct tunneling, defined by $E_1 > E_0$ and $E_2 > E_0$. In the regime of Fowler-Nordheim tunneling defined by $E_2 > E_0 > E_1$, the equation reads

$$T = \exp\left(-\frac{2}{\hbar} \sqrt{2m_t} x_T \frac{2}{3} (E_2 - E_0)^{3/2} \frac{1}{E_2 - E_1} \right). \tag{4.37}$$

4.2.1 Band Edges in the Vicinity of Interfaces

Usually, the band edges of stacked materials are approximated by the respective bulk values with abrupt transitions at the interfaces. This is a good approximation for layers where bulk properties can establish and the transition region between the materials is small compared to the layer thicknesses. However, in aggressively scaled high-κ technologies below the 14 nm node, the interfacial SiO_2 layers are merely a few Ångström thick and the properties of these thin layers are affected by the adjacent material and imperfections of the interface. A first-principles simulation result is given for the Si/SiO_2 interface in Fig. 4.8. A transition from silicon to the amorphous oxide is visible in this DFT simulation where the silicon lattice is distorted because of compensating forces induced by the amorphous structure on top. While the concept of band edges itself can be questioned in such small structures, we argue that the *tunneling probability* T is underestimated if abrupt transitions of the band edges to the respective bulk values are applied. To improve this we suggest approximating the band edges for the evaluation of the tunneling probability by ramps in the transitional region. This is in line with calculations of other groups [164–167] as shown in Fig. 4.9.

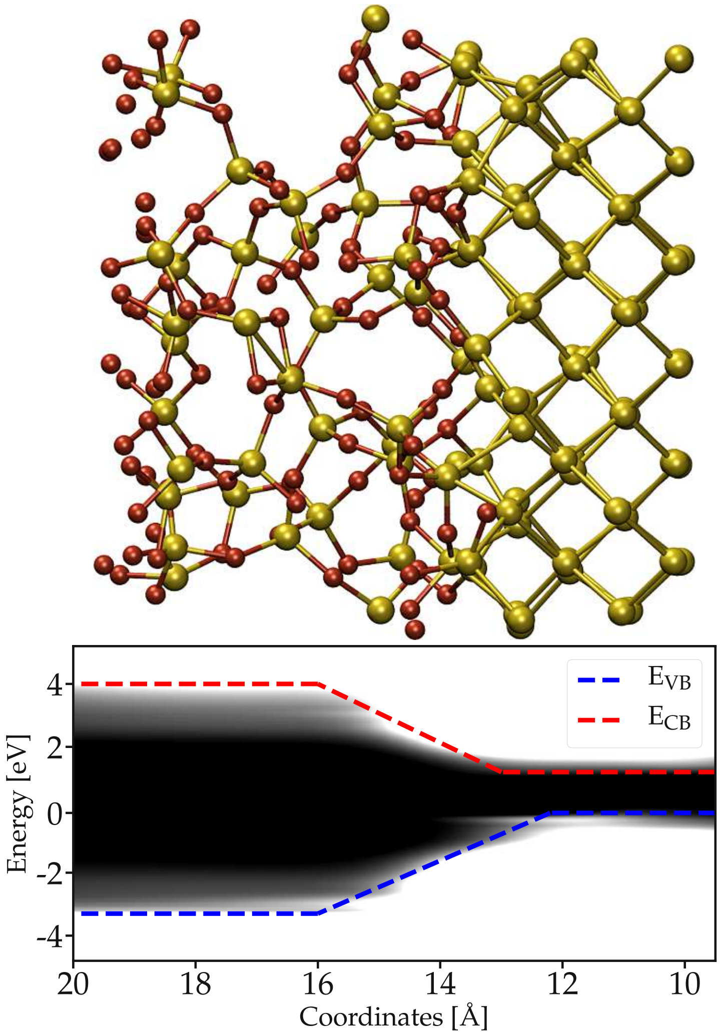

FIGURE 4.8: A 0.6 nm thick amorphous SiO_2 layer on top of crystalline silicon was created following the approach introduced in [168] and simulated using DFT. The ball-and-stick model (top) shows the oxygen atoms (red spheres) and silicon atoms (yellow spheres) accordingly. The distortion of the silicon lattice is visible close to the interface and also the oxide is affected which manifests in a gradual change of the *density of states* (white density) in the vicinity of the nominal interface of this structure (bottom). Approximated band edges are indicated for the conduction band (red line) and for the valence band (blue line). After [GRJ2].

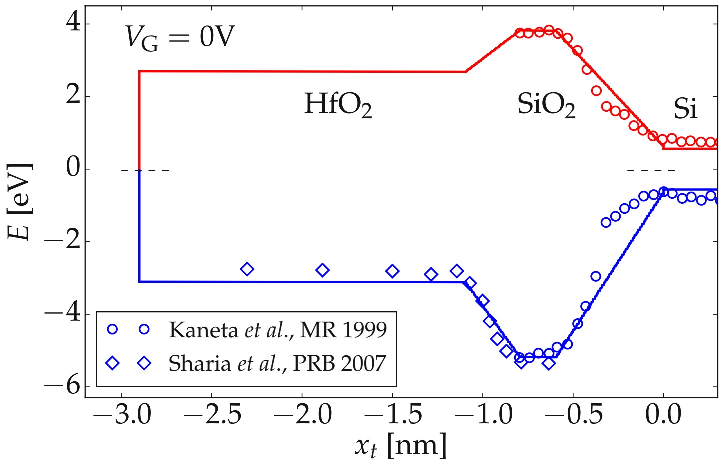

FIGURE 4.9: A band diagram of a high-κ device to motivate the approximation of the band edges around the interfaces of aggressively scaled technologies. Abrupt transitions of the band edges at the interface to the respective bulk values lead to an underestimation of the tunneling probabilities of such structures. More accurate values are obtained when ramps at these interfaces are considered for the computation of the tunneling probabilities. Comparison with values from literature indicates a transitional region at the Si/SiO$_2$ interface [164, 165, 167] and the SiO$_2$/HfO$_2$ interface [166] of about 0.6 nm and 0.3 nm, respectively. As a reference, the results from DFT studies are shown for the Si/SiO$_2$ interface (circles: scaled in energy to fit the SiO$_2$ band gap) [164] and for the SiO$_2$/HfO$_2$ interface (diamonds) [166]. After [GRJ2].

4.3 2-State NMP Model

As we have established the device electrostatics above, the charge trapping kinetics of pre-existing oxide defects can be evaluated now. For this, we employ a 2-state NMP model which we will briefly outline and compare to existing NMP models in the first subsection. After that, we will discuss the modeling details of individual 2-state NMP defects and how the properties of these defects are distributed to describe BTI degradation. Finally, we will review an approach to consider the frequency dependence due to metastable states using effective 2-state models.

4.3.1 Comparison of 2 and 4-State Models

Tewksbury's MPE model was the first model which employed the NMP theory to describe BTI during stress and recovery successfully [135, 136]. This model featured a 2-state NMP transition which was later refined to four states by GRASSER *et al.* as discussed in Subsection 3.4.1. In particular the *4-state NMP model* was successfully applied to model various features related to BTI in a unified fashion [GRJ5, GRC14–GRC16]. However, based on the results of the 4-state NMP model it was later shown that the essential features of the *mean degradation* at BTI conditions can be captured reasonably well with two states already [GRC2].

As shown in Subsection 3.4.2, a single defect is described in the 4-state NMP model with nine parameters (see Table 3.1). A simple *2-state NMP* defect which does not consider any metastable states can be described with three instead of nine parameters, see Table 4.3. An example of CC diagrams of single defects for both models are shown in Fig. 4.10.

TABLE 4.3: Parameters of a single defect in the *2-state NMP model*.

parameter	description	equation
E_T	trap level	
R	square of the curvature ratio of state 1 and 2	Eq. (3.39)
S	relaxation energy from state 2 to 1	Eq. (3.38)

Typically, all nine parameters of the 4-state NMP model are assumed to be independent and normally distributed while the defects are assumed to be distributed uniformly in space [GRC15]. Similarly, in the 2-state NMP model, we assume normal distributions of E_T and S and uniform distributions in space, however, in exemplary studies the distribution of R was found to be narrow, hence, R is approximated to be constant [GRC2]. This leaves three distributed parameters for a defect band described with the 2-state NMP model. The corresponding distributions are depicted in CC diagrams in Fig. 4.11.

While there are certainly differences in the description of the 2-state and the 4-state NMP model *at the single defect level*, it is important to verify that the *mean degradation* of ΔV_th at BTI conditions can be captured by the 2-state NMP model. Furthermore, for a reliable lifetime extrapolation it must be ensured that simulations with the 2-state NMP model still capture the gist of the degradation in a *physical* manner. To evaluate this, we have simulated an exemplary BTI multi-state stress pattern on a 2.4 nm thick $\mathrm{SiO_2}$ device with the full 4-state NMP model implemented in a TCAD simulator [169] and compared the result to the 2-state NMP model implemented in the device simulator described in Section 4.1.5. For this comparison we have used the 4-state NMP model parameters previously extracted for $\mathrm{SiO_2}$ oxides [GRC16] and used the *same values* for E_T and N_OT in the 2-state NMP model, while R and S were optimized to obtain a match with the results from the 4-state NMP model, see Fig. 4.12. These simulations indicate that E_T and N_OT retain their physical meaning while the parameters R and S are effective quantities which abstract the physics from all four states [GRC2].

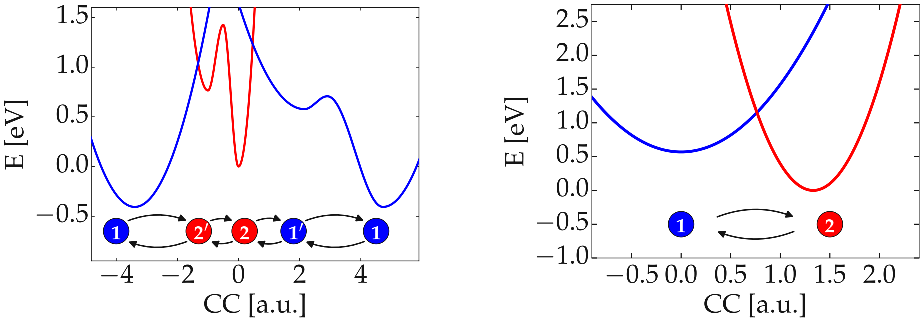

FIGURE 4.10: CC diagrams of a single defect described by the *4-state NMP model* (left) and by the *2-state NMP model* (right). The corresponding parameters are listed in Tables 3.1 and 4.3 for the 4-state and 2-state NMP model, respectively. After [GRC2].

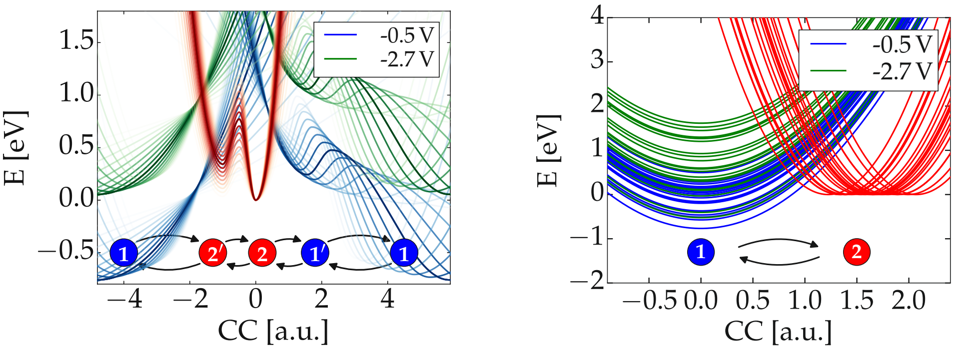

FIGURE 4.11: CC diagrams of a 4-state NMP (left) and a 2-state NMP defect band (right). While the former is based on nine normally distributed parameters, the latter is described with the two distributed parameters E_T and S. R is approximated to be constant for defect bands described with the 2-state NMP model. For both models, the defects are assumed to be uniformly distributed in space. After [GRC2].

4.3.2 Modeling of Single Defects

In Subsection 4.1.5 three schemes to evaluate the impact of oxide charges on V_th were discussed:

- Simple charge sheet approximation: Oxide charges are neglected in the Poisson equation.
- Non self-consistent Poisson (NCP) equation: Oxide charges enter the Poisson equation via an effective V_G.
- Self-consistent Poisson (SCP) equation: Oxide charges are considered in the Poisson equation in a self-consistent manner.

All three schemes rely on the net charge $q_\mathrm{T}(t)$ of single defects. To obtain this charge for 2-state NMP defects, the occupation probabilities p_1 of state 1 and p_2 of state 2 have to be computed and multiplied with the charge of the respective state. For *donor-like* defects with a neutral state 1 and a positive state 2 this gives

$$q_\mathrm{T}(t) = q p_2(t) \tag{4.38}$$

and for *acceptor-like* defects with a negative state 1 and a neutral state 2 this gives

$$q_\mathrm{T}(t) = -q p_1(t). \tag{4.39}$$

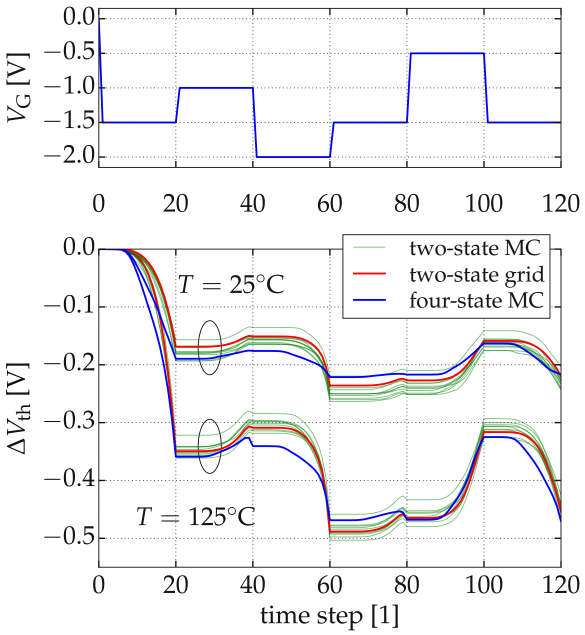

FIGURE 4.12: For verification of the abstraction of the 4-state NMP model with the 2-state NMP model, we simulate the degradation of a 2.4 nm thick SiO_2 device with 4-state NMP parameters extracted previously [GRC16] and optimize R and S of the 2-state NMP model while using the *same values* for E_T and N_{OT} as in the 4-state NMP model [GRC2]. For a multi-level stress pattern (top) the mean degradation ΔV_{th} is simulated at two different temperatures (bottom) with the 4-state NMP model and the 2-state NMP model (with Monte Carlo sampling with 20 k defects and sampling on a grid as described in Subsection 4.3.3). The stress times of each phase are 100 s and the results are shown on separate logarithmic scales with 20 samples each, starting 1 ps after the previous phase to bring out all features of the degradation. After [GRC2].

In both cases, the Master equation for the occupation probabilities reads

$$\frac{\mathrm{d}p_1(t)}{\mathrm{d}t} = -p_1 \sum_{r=1}^{N_R} k_{12,r} + p_2 \sum_{r=1}^{N_R} k_{21,r}, \tag{4.40}$$

$$\frac{\mathrm{d}p_2(t)}{\mathrm{d}t} = +p_1 \sum_{r=1}^{N_R} k_{12,r} - p_2 \sum_{r=1}^{N_R} k_{21,r}, \tag{4.41}$$

and $p_1 + p_2 = 1$ must hold. In the above equations, $k_{12,r}$ is the *electron emission* and $k_{21,r}$ the *electron capture* rate of the defect interacting with the carrier reservoir r. The total rates k_{12} and k_{21} of a defect are the sum of the rates of all N_R carrier reservoirs. In Comphy, the carrier reservoirs are

- the valence band of the channel,
- the conduction band of the channel, and
- the metal gate.

The solution of the above differential equation then reads

$$p_2(t) = \frac{k_{12}}{k_{12}+k_{21}} + \left(p_2(0) - \frac{k_{12}}{k_{12}+k_{21}}\right)\mathrm{e}^{-t(k_{12}+k_{21})}. \tag{4.42}$$

Below we will discuss the rates k_{12}^{CB} and k_{21}^{CB} for the conduction band of the channel. The rates for the other carrier reservoirs are obtained analogously. Based on Eq. (3.26) and Fermi-Dirac distributions we get [GRT2]

$$k_{12}^{\mathrm{CB}} = n v_{\mathrm{th},n} \sigma_{0,n} T_n \mathrm{e}^{-\beta(\varepsilon_{21}^{\mathrm{CB}} - E_{\mathrm{T}} + E_{\mathrm{F}})}, \tag{4.43}$$

$$k_{21}^{\mathrm{CB}} = n v_{\mathrm{th},n} \sigma_{0,n} T_n \mathrm{e}^{-\beta \varepsilon_{21}^{\mathrm{CB}}}, \tag{4.44}$$

where

- n is the electron concentration at the interface following Eq. (4.12),
- $v_{\mathrm{th},n} = \sqrt{8 k_{\mathrm{B}} T / (\pi m_{n,\mathrm{eff}})}$ is the thermal velocity,
- $\sigma_{0,n}$ is the capture cross section of electrons,
- T_n is the tunneling probability for electrons following Eq. (4.35),
- $\beta = (k_{\mathrm{B}} T)^{-1}$ is the thermodynamic beta,
- E_{T} is the trap level of the defect,
- E_{F} is the Fermi level at the interface following Eq. (4.32), and
- $\varepsilon_{21}^{\mathrm{CB}}$ is the energy barrier from state 2 to 1 following Eq. (3.41) and (3.42).

Hence, a 2-state NMP defect can be described with the three parameters listed in Table 4.3. The corresponding schematic CC diagram is shown in Fig. 4.13. Note that the capture time constants τ_{c} and the emission time constants τ_{e} of a 2-state NMP defect are simply the inverse of the corresponding total rates. If not stated otherwise, "capture" refers to a hole being captured by the defect.

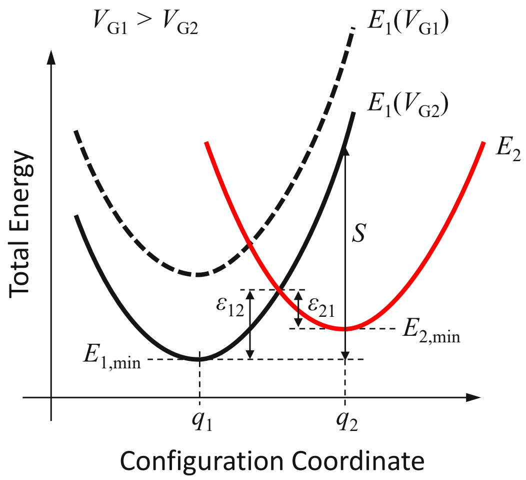

FIGURE 4.13: A schematic CC diagram of a donor-like *2-state NMP defect* with the neural state 1 and the positive state 2. The energy barriers ε_{12} and ε_{21} of the NMP process depend on the gate voltage since the parabolas are shifted according to the difference of the electrostatic potential at the defect site and at the carrier reservoir, see Eq. (3.40).

Transition Rates and Approximations

While the evaluation of the transitions rates following Eq. (4.43) and (4.44) is straightforward to implement and efficient to compute, it has to be noted that in the derivation based on Eq. (3.36) all carriers of the respective reservoir are assumed to have the same energy [GRT2]. Usually, this is chosen to be the energy of the band edges, and this approach is called *band edge approximation*, accordingly. This approximation gives good results for defects in the *strong electron-phonon coupling* regime where the intersection of the parabolas of the two charge states is between the minima of the respective states. However, the exact evaluation of the energy integral in Eq. (3.36) using Fermi-Dirac distribution functions can give substantially different results for defects in the *weak electron-phonon coupling* regime where the parabolas do *not* intersect between the minima of the two charge states. In particular, if the curvatures of the parabolas are such that there is no intersection in the weak electron-phonon coupling regime at all, the resulting rates using Eq. (4.43) and (4.44) can become zero while the exact evaluation gives substantially different results. The limiting cases for this phenomenon are shown in CC diagrams in Fig. 4.14 and the corresponding time constants are shown in Fig. 4.15. As can be seen in these figures, the band edge approximation fails to describe the time constants in certain cases. This can be improved in a computationally very efficient way by evaluating the energy barriers in the weak electron-phonon coupling regime as listed in Table 4.4 [GRJ2]. This pragmatic *FD approximation for the transition rates* simply sets ε_{12} to the difference of the energy minima ΔE_{12} given in Eq. (3.40) in the case of valence band interaction in the weak electron-phonon coupling regime where $\Delta E_{12} > 0\,\mathrm{eV}$ holds. Furthermore, ε_{12} is set to zero in the case of conduction band interaction in the weak electron-phonon coupling regime where $\Delta E_{12} < 0\,\mathrm{eV}$ holds, and for interaction with the metal gate both approximations are combined. All other cases are solved according to Eq. (3.41), see Table 4.4.

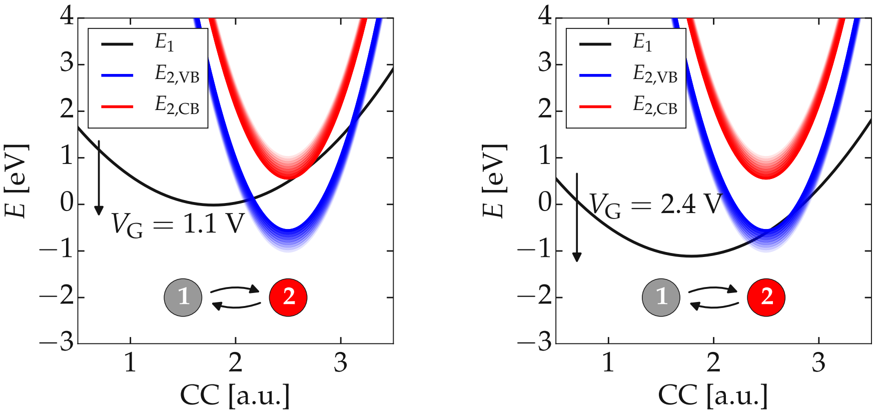

FIGURE 4.14: CC diagrams of a donor-like 2-state NMP defect ($x_\mathrm{T} = 2\,\mathrm{nm}$, $E_\mathrm{T} = 0.7\,\mathrm{eV}$, $S = 0.5\,\mathrm{eV}$, $R = 0.4$) interacting with the channel of an nMOSFET. With increasing gate voltage V_G the parabola which represents the neutral state 1 is shifted towards more negative energies. Above $V_\mathrm{G} = 1.1\,\mathrm{V}$ (left) there is no intersection for interaction with carriers at the conduction band edge (represented by red parabolas) and the total transition rate will be governed by the interaction with the valence band (represented by blue parabolas). At even larger gate voltages above $V_\mathrm{G} = 2.4\,\mathrm{V}$ (right), there is no intersection of the parabolas due to interaction with the valence band *edge*, however, excited carriers can still interact with the defect. The corresponding time constants are shown in Fig. 4.15. After [GRJ2].

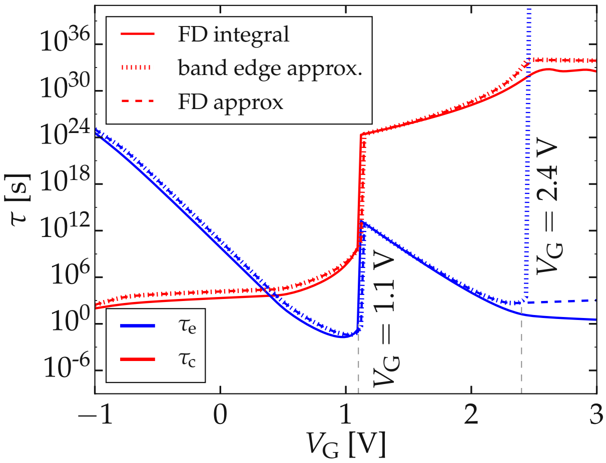

FIGURE 4.15: The time constants of the same defect as in Fig. 4.14 at $T = 300$ K with three different approximations: a) The exact solution of the energy integral in Eq. (3.36) using Fermi-Dirac distribution functions ("*FD integral*"). At negative gate voltages, the defect captures charges quickly and will be positively charged. However, with increasing gate voltages, the defect will shift below the Fermi level of the channel and will be mostly neutral above $V_G \approx 0.4$ V. Around $V_G = 1.1$ V there is a discontinuity in the time constants because carriers of the conduction band cannot interact with the defect anymore. b) The time constants are similar for the *approximation of carriers at the band edges* as used in Eq. (4.43) up to $V_G = 2.4$ V. Above this voltage, the approximation fails because the time constants are then governed by excited carriers while carriers at the valence band edge cannot interact with the defect anymore. c) With the approximation of the energy integral given in Table 4.4 ("*FD approx.*"), the discontinuity around $V_G = 2.4$ V is resolved and the resulting time constants are in the same range as of the computationally very expensive energy integral. After [GRJ2].

TABLE 4.4: Evaluation of the energy barriers in the weak electron-phonon coupling regime following the *FD approximation for the transition rates* of 2-state NMP defects [GRJ2].

ΔE_{12}	ε_{12} (val. band)	ε_{12} (cond. band)	ε_{12} (metal)
> 0 eV	ΔE_{12}	Eq. (3.41)	ΔE_{12}
< 0 eV	Eq. (3.41)	0 eV	0 eV

4.3.3 Ensembles of Defects

As discussed in Subsection 4.3.1, the *mean degradation* due to oxide defects is quantified in Comphy by the threshold voltage shift ΔV_{th} arising from $q_T(t)$ of all single oxide defects. The *mean* number of oxide defects N due to a 2-state NMP *defect band* is evaluated as

$$N = WLN_{\mathrm{OT}}\left(x_{\mathrm{T,max}} - x_{\mathrm{T,min}}\right), \tag{4.45}$$

where W and L are the effective gate oxide width and length, and N_{OT} is the constant defect concentration of this defect band located between $x_{\mathrm{T,min}}$ and $x_{\mathrm{T,max}}$ away from the channel interface. With the distributions of the parameters discussed in Subsection 4.3.1, this gives the input parameters for a *defect band in Comphy* listed in Table 4.5.

Monte Carlo Sampling of Defect Bands

In order to simulate ΔV_{th}, a set of single 2-state NMP defects has to be sampled from the defect bands described above. This can be done following a simple Monte Carlo sampling of defects from the distributions given in Table 4.5. A set of defects is depicted in the band diagram together with their CC diagrams in Fig. 4.16 and the corresponding time constants are shown in Fig. 4.17. On small devices with a limited number of defects, this approach reflects the native *variability due to oxide defects* and enables studies thereof. However, if the *mean degradation* is of interest, a large number of defects have to sampled with this approach to get an accurate result.

Defect Bands Sampled on a Grid

A more efficient way to compute the *mean degradation* due to a defect band compared to sampling a large number of defects in a Monte Carlo fashion, is to use *weighted samples on a grid*. This is illustrated in Fig. 4.18 for the three dimensions spanned by the distributed parameters of the 2-state NMP model in Comphy, see Table 4.5. In this *grid mode*, each parameter is sampled equidistantly and weighted according to the integral of the respective interval. This is done based on the definition of the grid distance which spans the space between $x_{\mathrm{T,min}}$ and $x_{\mathrm{T,max}}$ for the uniform defect concentration N_{OT}. The normally distributed parameters E_{T} and S are also sampled with a given grid distance. However, the boundaries of these grid spaces result from the probability where the tails of the normal distributions are cut off. The parameters defining the grid are summarized in Table 4.6. As an example, a device simulated in both modes, Monte Carlo sampling and sampling on a grid, see Fig. 4.19. The corresponding CC diagrams are shown in Fig. 4.20. Note that the sampling on a grid is only feasible for a limited number of distributed parameters since it scales exponentially with the number of dimensions. For example, sampling the nine distributed parameters of the 4-state NMP model (see Table 3.1) on a grid is impractical because of the huge amount of sampling points, even for sparse grids. A Monte Carlo approach has to be used there.

TABLE 4.5: Parameters of a *defect band* in the 2-state NMP model.

parameter	description	unit
$\langle E_{\mathrm{T}}\rangle \pm \sigma_{\mathrm{E_T}}$	normally distributed trap level	eV
$\langle S\rangle \pm \sigma_{\mathrm{S}}$	normally distributed relaxation energy	eV
R	constant square of the curvature ratio	1
N_{T}	uniform defect concentration	cm^{-3}
$x_{\mathrm{T,min}}, x_{\mathrm{T,max}}$	spatial location of defect band	m

TABLE 4.6: Parameters specifying the grid on which the 2-state NMP defects are sampled in the *grid mode*.

parameter	description	unit
Δx_{T}	spatial grid distance	m
ΔE_{T}	grid distance for trap levels	eV
ΔS	grid distance for relaxation energies	eV
p_{tol}	maximum cut-off probability for the tails of the normal distributions	1

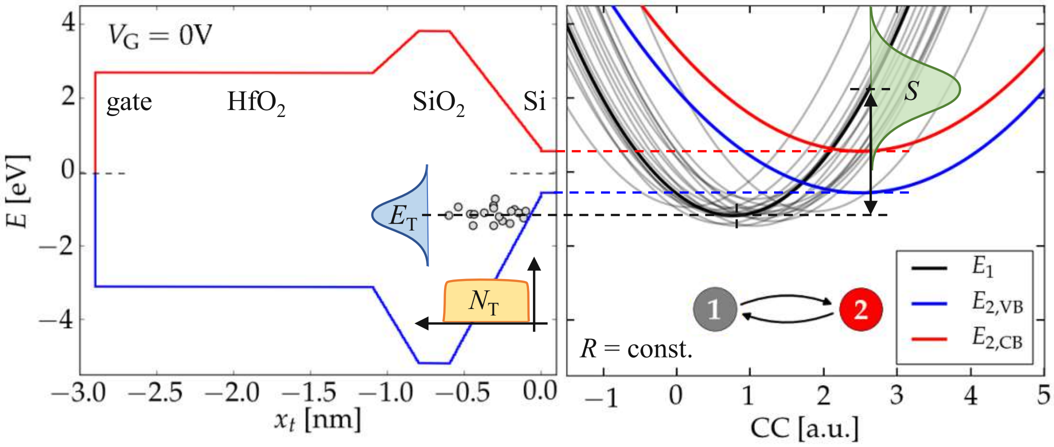

FIGURE 4.16: A band diagram (left) of a high-κ nMOSFET with donor-like 2-state NMP defects (circles) sampled in a Monte Carlo fashion based on a defect band defined by the parameters listed in Table 4.5 and the corresponding CC diagrams (right). The underlying distributions of the trap level E_T and defect concentration N_T manifest in the band diagram, while the distribution of the relaxation energy S is visible in the CC diagram. Together with the constant square of the curvature ratio R, all properties of the 2-state NMP defects are defined and their transient charge can be evaluated considering the device electrostatics introduced in Subsection 4.1.5. In the CC diagram, the mean potential energy surface of state 1 (thick black) is shown in addition to the potential energy surfaces of the single defects (gray lines) whose energy minima were shifted along the CC to better illustrate the distribution of S. The energy barriers ε_{12} and ε_{21} (not marked) are obtained from the respective energy minima to the intersection point with the parabola representing the conduction band edge (thick red) or the valence band edge (thick blue). The time constants of these defects are shown in Fig. 4.17. After [GRJ2].

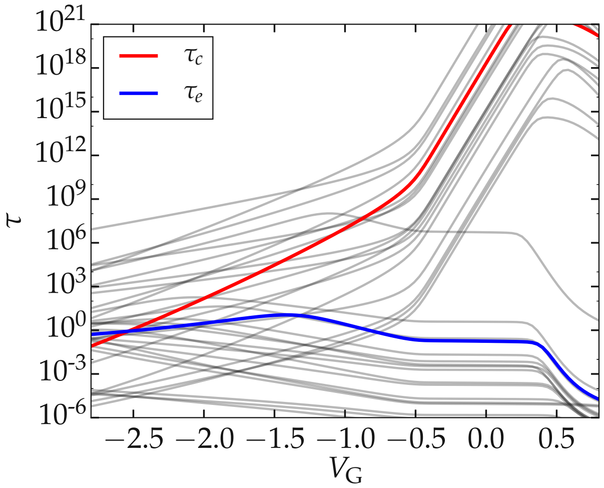

FIGURE 4.17: The capture and emission time constants of the defects shown in Fig. 4.16 at $T = 300$ K. The time constants of a defect with the mean values specified for the underlying defect band are shown in color. In accordance with experimental studies [67, 170], a broad distribution of time constants and a pronounced gate voltage dependence is observed. After [GRJ2].

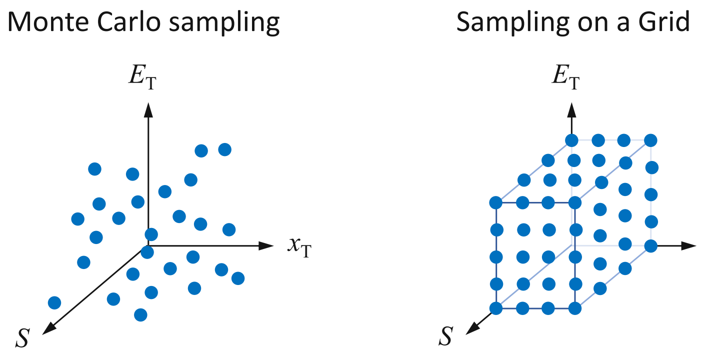

FIGURE 4.18: Schematic sampling of 2-state NMP defects for the Monte Carlo approach (left) and the sampling on a grid with weighted points where each represents a number of 2-state NMP defects according to the underlying distributions (right). The parameters of the 2-state NMP defects are listed in Table 4.3 and the parameters which specify the grid are listed in Table 4.6.

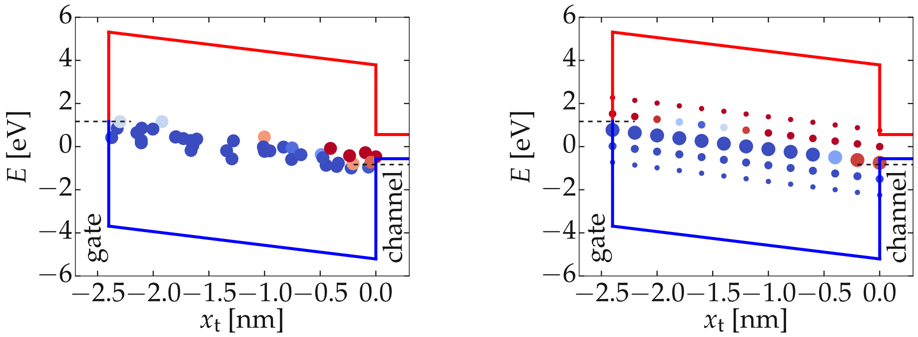

FIGURE 4.19: A pMOSFET ($V_G = -2$ V, 2.4 nm of SiO_2) with 2-state NMP defects sampled in a Monte Carlo fashion (left) and on an equidistant grid with weighted points (right). The number of 2-state NMP defects represented by the grid points is indicated by the size of the circles while the color indicates their charge state for the steady state case. A grid with $\Delta x_T = 0.2$ nm, $p_{tol} = 0.1$, $\Delta E_T = 0.5$ eV, and $\Delta S = 0.5$ eV was used (see Table 4.6). The sampling of the latter is not visible here, since defects with different S but same x_T and E_T lie on top of each other in the band diagram but it can be seen in the CC diagrams in Fig. 4.20. After [GRC2].

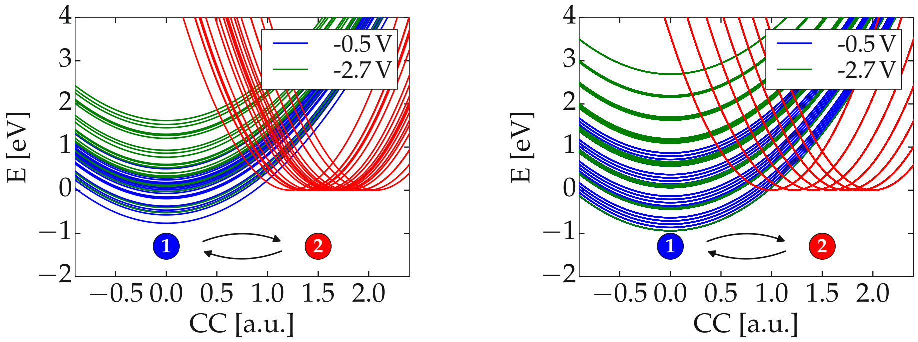

FIGURE 4.20: The CC diagrams corresponding to Fig. 4.19 for 2-state NMP defect band sampled in a Monte Carlo fashion (left) and on an equidistant grid with weighted points (right). After [GRC2].

4.3.4 Effective 3-State Frequency Dependence

Whether BTI exhibits an inherent frequency dependence[4] at high frequencies is debated with several studies reporting no frequency dependence at all [171, 172]. However, in 2016 an experimental study with on-chip measurements [173] gave strong support for a 3-state frequency dependence [142]. While 2-state defects do not show an inherent frequency dependence, charge trapping of defects with three or more states can exhibit a frequency dependence if a metastable state is involved. Assuming such a metastable state $2'$ between the neutral state 1 and the positive state 2, the capture process depends on the occupation probability $p_{2'}$ of state $2'$ and the transition rate $k_{2'2}$. If this state has a large transition rate $k_{2'1}$ at low voltages[5], $p_{2'}$ will be small for high frequencies which inhibits charge capture. However, at low frequencies, the defect can still capture charges if $k_{2'2}$ is large compared to the frequency.

This mechanism can be considered in an effective 2-state model by replacing τ_c with the *effective* capture time constant $\tau_\mathrm{c,AC} = \tau_\mathrm{c}/w$ with w being approximated as [142]

$$w \approx \begin{cases} 1 & \text{for } f < \frac{\alpha}{2\tau_{\mathrm{c}'}} \\ \frac{\alpha}{2\tau_{\mathrm{c}'} f} & \text{for } \frac{\alpha}{2\tau_{\mathrm{c}'}} < f < \frac{1-\alpha}{2\tau_{\mathrm{e}'}} \\ \frac{\tau_{\mathrm{e}'}}{\tau_{\mathrm{c}'}} \frac{\alpha}{1-\alpha} & \text{for } \frac{1-\alpha}{2\tau_{\mathrm{e}'}} < f \end{cases} \tag{4.46}$$

with the frequency f, the duty cycle α, and the capture and emission time constants $\tau_{\mathrm{c}'} = k_{12'}$ and $\tau_{\mathrm{e}'} = k_{2'1}$ of the metastable state. The values of $\tau_{\mathrm{c}'}$ and $\tau_{\mathrm{e}'}$ depend on the individual defect configurations. For a rough estimate of the frequency dependence, they can be set to typical values such as $\tau_{\mathrm{c}'} = 1\,\mathrm{ms}$ and $\tau_{\mathrm{e}'} = 1\,\mu\mathrm{s}$ for all 2-state NMP defects [142].

4.4 Double-Well Model

In the spirit of Brower's *simple thermal* model and Grasser's *field-dependent thermal transition* (see Section 3.3), we use a simple *double-well* model with a phenomenological field dependence to describe the quasi-permanent part of BTI with Comphy. This model complements the physical 2-state NMP model and covers the less understood degradation mechanisms such as generation and annealing of oxide and interface defects, possibly related to hydrogen relocation and the subsequent transformation of defect sites as described by the *gate-sided hydrogen release model*, see Subsection 3.4.3.

Similar to Eq. (3.17) and (3.18) in Brower's model for the passivation and depassivation rates, we employ a *hole capture rate* k_{12} and a *hole emission rate* k_{21} between the neutral state 1 and the positive state 2 as

$$k_{12} = k_0 \mathrm{e}^{-\beta\varepsilon_{12}}, \tag{4.47}$$

$$k_{21} = k_0 \mathrm{e}^{-\beta\varepsilon_{21}}, \tag{4.48}$$

with the transition rate for zero barrier k_0 and the activation energies ε_{12} and ε_{21}. As depicted in Fig. 4.21, the activation energy for hole capture is given by

$$\varepsilon_{12} = \varepsilon_{12,0} - \gamma E_\mathrm{ox}, \tag{4.49}$$

where γ is the phenomenological field dependence and E_ox the electric field at the interface of the oxide. In this way, the depassivation is modeled with a field dependence whereas the passivation

---

[4] An ostensible frequency dependence can always be observed due to the recoery in the last period of an AC stress signal.

[5] It is assumed that state 1 is energetically favorable at low voltages and a transition to state 2 during high voltages is inhibited if the defect relaxes from state $2'$ to 1 during the *low voltage* of each period.

does not depend on the electric field. This is in line with the qualitative observation regarding the characteristics of the recoverable and the quasi-permanent component, see Subsection 1.1.6. With these rates, the occupation probabilities of the two states can been obtained in the same way as for the 2-state NMP model following Eq. (4.40) and (4.41) which results in a net charge given in Eq. (4.38), also affecting the device electrostatics in the same way as the charge of 2-state NMP defects.

With the above description of a single double-well defect, the response of $N = WLN_\mathrm{it}$ of such defects can be obtained based on the effective gate oxide width W and length L, the defect concentration N_it, and the distributions of the model parameters. In the implementation in Comphy, we assume $\varepsilon_{12,0}$ and ε_{21} to be normally distributed while the other parameters are constant, see Table 4.7. Again, in the same way as for 2-state NMP defects, the double-well defects can be sampled in a Monte Carlo fashion or on a grid with the grid parameters listed in Table 4.8.

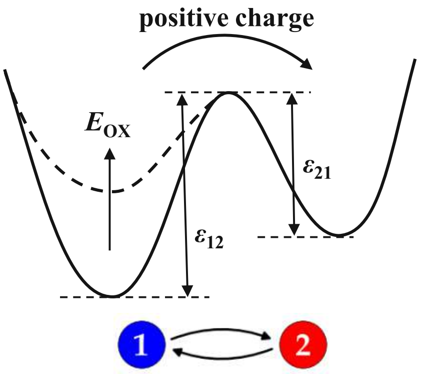

FIGURE 4.21: Schematic energy barrier of the simple double-well model used in Comphy. The activation energy for the transition from the neutral state 1 to the positive state 2 is field dependent. After [GRJ2].

TABLE 4.7: Parameters of the simple double-well model used in Comphy.

parameter	description	unit
$\langle\varepsilon_{12,0}\rangle \pm \sigma_{\varepsilon_{12,0}}$	normally distributed activation energy for depassivation	eV
$\langle\varepsilon_{21}\rangle \pm \sigma_{\varepsilon_{21}}$	normally distributed activation energy for passivation	eV
k_0	transition rate for zero activation energy	s^{-1}
γ	field dependence of depassivation	eVm/V
N_it	defect concentration	cm^{-2}

TABLE 4.8: Parameters specifying the grid on which the double-well defects are sampled in the *grid mode*.

parameter	description	unit
$\Delta\varepsilon_{12,0}$	grid distance for the activation energy of depassivation	eV
$\Delta\varepsilon_{21}$	grid distance for the activation energy of passivation	eV
p_tol	maximum cut-off probability for the tails of the normal distributions	1

4.5 Efficient Solution for AC Stress

With the framework outlined above, the degradation ΔV_{th} for arbitrary transient gate voltages $V_{\mathrm{G}}(t)$ and temperatures $T(t)$ can be calculated. The only limit to this approach are the numbers of samples in time. While the exact solution of arbitrary long constant stress can be obtained by solving Eq. (4.42) for one single time step, *each period* has to be sampled multiple times for AC stress. For the example of digital AC stress with two time samples per period, a stress signal with the frequency $f = 1\,\mathrm{MHz}$ for the stress time $t_{\mathrm{s}} = 1\,\mathrm{ks}$ requires 2×10^9 samples already with this simple approach. An efficient solution for this problem where the computational expenses do not scale with the stress time is given by GIERING *et al.* in [GRC22] and will be outlined in the following.

With the time dependent rates for carrier capture $k_{12}(t)$ and carrier emission $k_{21}(t)$ as presented for the 2-state NMP model and for the simple double-well model above, the general solution of Eq. (4.40) reads [GRC22]

$$p_2(t) = P_1(t,t_0)p_2(t_0) + P_2(t,t_0) \tag{4.50}$$

with the initial values at time t_0 and

$$P_1(t_2,t_1) = \exp\left(\int_{t_1}^{t_2} -\left(k_{12}(s) + k_{21}(s)\right)\mathrm{d}s\right), \tag{4.51}$$

$$P_2(t_2,t_1) = \int_{t_1}^{t_2} k_{12}(s)\exp\left(\int_{s}^{t_2} -(k_{12}(r) + k_{21}(r))\mathrm{d}r\right)\mathrm{d}s, \tag{4.52}$$

$$= \int_{t_1}^{t_2} k_{12}(s)P_1(t_2,s)\mathrm{d}s. \tag{4.53}$$

For a periodic stress signal with the period $t_{\mathrm{p}} = 1/f$ and the number of periods n, Eq. (4.50) evaluates to [GRC22]

$$p_2(nt_{\mathrm{p}} + t_0) = p_2(t_0)P_1(t_0 + t_{\mathrm{p}},t_0)^n + \frac{1 - P_1(t_0 + t_{\mathrm{p}},t_0)^n}{1 - P_1(t_0 + t_{\mathrm{p}},t_0)}P_2(t_0 + t_{\mathrm{p}},t_0). \tag{4.54}$$

For digital AC signals with $k_{12,\mathrm{L}}$ and $k_{21,\mathrm{L}}$ for the time t_{L} at low level and $k_{12,\mathrm{H}}$ and $k_{21,\mathrm{H}}$ for for the time t_{H} at high level (see Fig. 4.22, top), the above equation can be solved analytically by

$$P_1(t_0 + t_{\mathrm{p}},t_0) = \exp\left(-\left(k_{12,\mathrm{H}} + k_{21,\mathrm{H}}\right)t_{\mathrm{H}} - \left(k_{12,\mathrm{L}} + k_{21,\mathrm{L}}\right)t_{\mathrm{L}}\right), \tag{4.55}$$

$$\begin{aligned} P_2(t_0 + t_{\mathrm{p}},t_0) = {} & \frac{k_{12,\mathrm{H}}}{-(k_{12,\mathrm{H}} + k_{21,\mathrm{H}})}\left(\mathrm{e}^{-(k_{12,\mathrm{H}}+k_{21,\mathrm{H}})t_{\mathrm{H}}} - 1\right) \\ & + \frac{k_{12,\mathrm{L}}}{-(k_{12,\mathrm{L}} + k_{21,\mathrm{L}})}\left(\mathrm{e}^{-(k_{12,\mathrm{L}}+k_{21,\mathrm{L}})t_{\mathrm{L}}} - 1\right)\mathrm{e}^{-(k_{12,\mathrm{H}}+k_{21,\mathrm{H}})t_{\mathrm{H}}}. \end{aligned} \tag{4.56}$$

The simulation of an AC signal with the simple approach compared to the efficient solution presented in this section is shown in Fig. 4.22.

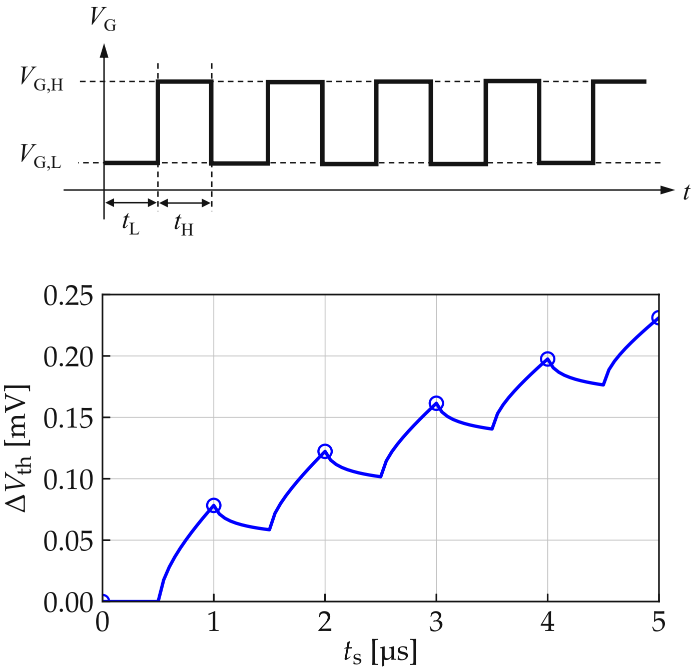

FIGURE 4.22: A digital AC stress signal with $f = 1\,\mathrm{MHz}$, $V_{G,L} = 0\,\mathrm{V}$, and $V_{G,H} = 1.8\,\mathrm{V}$ (top) is simulated on a high-κ nMOSFET with the simple approach (line in the bottom panel) and compared to the solution based on the *efficient AC mode* (circles in the bottom panel) using Eq. (4.54). Both simulations give the same result for ΔV_{th} after each period. Note that the simple approach is computed with 20 samples per period to show the continuous degradation and the same result would have been obtained with 2 samples per period. However, for longer stress times, the naive approach is not feasible because the number of samples scales with the number of periods while the computational expenses in the efficient AC mode do not scale with the number of periods.

Chapter 5

Experiments and Simulations

In this chapter, the experimental techniques presented in Chapter 2 will be applied to investigate the BTI response of various technologies. TCAD [169] and Comphy simulations [GRJ2] will be conducted to extract physical defect parameters, corroborated by dedicated experiments. Step by step, a profound understanding of BTI will be established and corroborated:

- First, the it will be analyzed how 4-state NMP defects can constitute RTN, BTI, SILC, and tunneling currents (Section 5.3).
- Next, the recoverable and the quasi-permanent components of NBTI will be studied on plain SiO_2 devices (Section 5.4).
- These insights help to analyze the recoverable component of all four cases of BTI on high-κ technologies (Section 5.5).
- Based on this, both the recoverable and the quasi-permanent component of PBTI and NBTI can be understood and described consistently for high-κ technologies (Section 5.6).
- Finally, the established framework will be used to analyze the impact of different processes of gate stacks (Section 5.7) and the AC behavior of BTI (Section 5.8).

5.1 General Material and Simulation Settings

Common to all studies in this chapter is the consistency in the approach: For each technology, *one set of oxide defects* is used to correctly describe the degradation for both NBTI and PBTI. Furthermore, *all simulations of a technology use the exact same parameters*, meaning that the eMSM, MSM, lifetime, and AC simulations for all investigated stress voltages and temperatures only differ in the applied stress signal while the device and defect parameters are the same throughout all simulations. In the following, the general simulation approach is outlined and the parameters which are common to all studies are listed.

5.1.1 Defect Parameter Extraction

The procedure for the oxide defect parameter extraction was established in [GRC15] and is the same for both TCAD and Comphy simulations: Based on the gate stack and the device characteristics ($I_D V_G$ curves and/or CV curves), the basic parameters of the investigated technology are set. This allows for physical simulation of the degradation during BTI stress using the respective oxide defect models. In the case of *TCAD simulations* [169], these are the

- 4-state NMP model (Subsection 3.4.2) to describe the recoverable component and the
- field-dependent thermal transition (Subsection 3.3.2) to describe the quasi-permanent component

and in the case of *Comphy simulations* [GRJ2], these are the

- 2-state NMP model (Section 4.3) to describe the recoverable component and the
- double-well model (Section 4.4) to describe the quasi-permanent component.

The defect parameter *distributions* of the respective models are calibrated to fit the measured degradation of eMSM experiments, conducted on devices with large active gate areas to capture the mean response of the investigated technology.

Shallow and Deep Trap Levels

In this chapter, we present two characteristic distributions of defects in SiO_2 oxides and two in HfO_2 oxides. In both materials, the mean trap level of one of the distributions is closer to the conduction band edge while the mean trap level of the other distribution is closer to the valence band edge. For simplicity, we will call the former defect bands "shallow" and the latter defect bands "deep" which refers to their mean trap level with respect to the conduction band edge.

Acceptor and Donor-Like Defects

For electrostatic reasons, a positive shift of V_{th} indicates electron capture and a negative shift indicates electron emission of oxide defects. However, the shift of V_{th} does not give direct information about the absolute charge of defects and it is difficult to determine whether a defect has donor-like or acceptor-like states. In the simulations, this defect property is only relevant if the absolute charges are considered in the Poisson equation self-consistently. In line with studies which showed that the net charge of pristine devices is usually rather low [22], we assume that the defect bands with shallow trap levels are acceptor-like and the defect bands with a deep trap level are donor-like.

5.1.2 General Comphy Settings

The following is common to *all* Comphy simulations presented in this chapter:

- The oxide layer thicknesses are listed in Table 5.4, all other oxide material parameters are listed in Table 5.1.
- The dopings N_{A} and N_{D} and the intrinsic work function difference $\Delta E_{\mathrm{W,0}}$ are listed in Table 5.4, all other channel parameters are given in Chapter 4.
- The NCP mode is used to account for the reduction of the electric field due to the oxide charges, except for the lifetime analysis in Section 5.6 where the SCP mode is used for additional accuracy.
- The grid mode is used to accurately compute the mean degradation with the parameters listed in Table 5.2. The Monte Carlo approach is used in band diagrams only to better illustrate the distributions.
- All energies refer to mid-gap of the channel material.
- The defect capture cross sections for electrons and holes are $\sigma_{0,n} = \sigma_{0,p} = 2\times10^{-19}\,\mathrm{cm}^2$.
- Following the reasoning in Subsection 4.2.1, the *transition probabilities* consider linear approximations of the band edges in the vicinity of interfaces: The band edges of SiO_2 are approximated to change from the Si values to the SiO_2 bulk values within 0.6 nm and from high-κ interfaces within 0.3 nm.

- The BTI response of SiO_2 is found to be dominated by defects with a high concentration in the near-interfacial region. Thus, we approximate all defects in SiO_2 to lie within the first 0.6 nm from the Si interface.

- Comphy 1.0 is used [174].

With the above, all Comphy simulations can be fully reproduced.

TABLE 5.1: Oxide material parameters used in the simulations with Comphy. The values are based on [175].

input quantity		SiO_2	SiON	HfO_2	Al_2O_3	unit
E_G	band gap	9.0	9.0	5.8	7.0	eV
E_{off}	valence band edge	-5.21	-5.21	-3.162	-3.6	eV
m_t	tunnel mass	0.35	0.35	0.17	0.17	1
ε_r	rel. permittivity	3.9	6.0	20	9.1	1

TABLE 5.2: Parameters specifying the grid which is used for *Comphy* simulations to obtain the *mean degradation*.

parameter	description	value
Δx_T	spacial grid distance	0.1 nm
ΔE_T	grid distance for trap levels	0.1 eV
ΔS	grid distance for relaxation energies	0.1 eV
$\Delta \varepsilon_{12,0}$	grid distance for the activation energy of depassivation	0.05 eV
$\Delta \varepsilon_{21}$	grid distance for the activation energy of passivation	0.05 eV
p_{tol}	maximum cut-off probability for the tails of the normal distributions	0.001%

5.2 List of Investigated Technologies

In this chapter, we will study four different types of Si technologies both commercial and in development. Before outlining the devices and processes in the following subsections, the main reasons to study these technologies are listed below:

- The commercial 130 nm SiON technology (*Tech. A*) serves as an excellent starting point to investigate the recoverable and quasi-permanent component of SiO_2 devices (Section 5.4) since it has a plain oxide and is well established with a large set of previously published eMSM data [176]. We complemented this data by dedicated experiments to separate the recoverable and the quasi-permanent component [GRC15] and to analyze its AC behavior [GRJ2, GRC13] (Section 5.8).

- The commercial 28 nm high-κ technology (*Tech. B*) is well suited for long-term BTI studies. We perform measurements spanning 12 decades in time [GRJ2] to verify lifetime predictions (Section 5.6).

- The 14 nm high-κ FinFET technology (*Tech. C*) is in development and not as stable as the commercial technologies above. Still, the study of pre-existing defects in these oxides gives valuable insight on the interplay of RTN, gate leakage, SILC, and BTI [GRC14] (Section 5.3) and it was used to demonstrate unified modeling of all four combinations of BTI [GRC16]. The results of the mean degradation were corroborated by studies of the variability (Section 5.5).

- The DRAM logic technology (*Tech. D*) is interesting because of its distinct gate stack and processing compared to the technologies listed above. Furthermore, the different process splits available for this technology in development help to separate the contributions of oxide layers to the total degradation [GRJ2] (Section 5.7).

5.2.1 Commercial 130 nm SiON Technology (*Tech. A*)

This technology features a poly gate process with an about 2.2 nm thick SiON oxide. PBTI is typically negligible for such technologies and we only employ pMOSFETs to study NBTI. The investigated devices have a gate width of $W = 10\,\mu\mathrm{m}$ and a length of $L = 100\,\mathrm{nm}$.

5.2.2 Commercial 28 nm High-κ Technology (*Tech. B*)

This is a planar high-κ technology with TiN metal gates. About 2.1 nm of $\mathrm{HfO_2}$ is processed on top of a rapid thermal oxidation (RTO) interfacial layer with a thickness of roughly 1 nm to obtain an equivalent oxide thickness (EOT) of about 1.41 nm. A post deposition anneal (PDA) is performed but the details of the process are confidential. In order to study NBTI and PBTI of this technology, we measure pMOSFETs and nMOSFETs where 10 identical devices are in parallel, each of which with $W = L = 1\,\mu\mathrm{m}$.

5.2.3 14 nm High-κ FinFET Technology (*Tech. C*)

This is a FinFET technology with a TiN metal gate. The high-κ stack has an about 1.6 nm thick $\mathrm{HfO_2}$ layer and an about 0.6 nm thick $\mathrm{SiO_2}$ interfacial layer, resulting in an EOT of roughly 1.2 nm. The fins have a length of about 70 nm, a height of about 30 nm, and a width of about 10 nm. Both nFinFETs and pFinFETs are investigated. Small effective gate areas of devices with 2 Fins in parallel are used to analyze the variability of this technology and large effective gate areas of devices with 220 Fins in parallel are used to analyze the mean degradation.

Process Splits

This technology is in development and was studied for two different processes:

- 14 nm high-κ FinFET technology (process 1) (*Tech. C1*)
- 14 nm high-κ FinFET technology (process 2) (*Tech. C2*)

The differences of the processes are confidential and not of particular importance for the presented studies.

5.2.4 DRAM Logic Technology (*Tech. D*)

This technology is being developed for application in the peripheral logic of dynamic random-access memory (DRAM) chips. Due to the processing of such technologies, they have a very different gate stack compared to the other technologies studied in this work: The gate stack has an in situ steam generated (ISSG) $\mathrm{SiO_2}$ layer on top of the Si channel with a thickness of $\approx 5\,\mathrm{nm}$. Further details are subject to the respective process split of this experimental technology.

Process Splits

The following four different process splits of this technology will be studied:

- The plain $\mathrm{SiO_2}$ process split of Tech. D (*Tech. D1*) comes with a poly gate on top of $\mathrm{SiO_2}$ layer.

- The $SiO_2 + HfO_2$ process split of Tech. D (*Tech. D2*) has a TiN/TaN metal gate and 20 layers of atomic layer deposition (ALD) HfO_2 on top of the SiO_2 layer.
- The $SiO_2 + HfO_2 + Al_2O_3$ process split of Tech. D (*Tech. D3*) has a TiN/TaN metal gate and in addition to the 20 cycles of ALD HfO_2 on top of the SiO_2 layer, it has 4 cycles of Al_2O_3.
- The $SiO_2 + HfO_2$ + removed Al_2O_3 process split of Tech. D (*Tech. D4*) is the same as *Tech. D3* but after a PDA, the Al_2O_3 layer is selectively removed [177].

5.3 From Noise to BTI

Historically, the NMP models, which will be used throughout this chapter, were developed based on studies of noise and single defects: After 1/f noise was identified as a response of single defects and linked to RTN [3], dedicated measurement techniques were developed to shed light on the properties of these defects (see Section 2.4). Their bias dependent capture and emission time constants were measured (see Fig. 3.11) and their role in gate leakage currents and SILC was uncovered [9]. Finally, the understanding of these defects within the NMP theory was applied to model BTI, particularly successful with the 4-state NMP model (see Section 3.4.2). In the light of all that, it comes naturally that a physical defect model can inherently describe all phenomena, from noise to BTI [GRC23]. Below, we will show that for an exemplary 4-state NMP defect which contributes to BTI of the 14 nm high-κ FinFET technology (process 1) (*Tech. C1*) *and* causes RTN, gate leakage currents, and SILC. This defect, located in the interfacial layer of this high-κ technology, was drawn in a Monte Carlo fashion from a parameter distribution which was calibrated using eMSM experiments [GRC14][1] and shows the following features:

- At low gate voltages, its large capture and emission time constants render the defect basically inactive, see Fig. 5.1.
- At moderate gate voltages, both time constants are on the same order of magnitude. The defect captures and emits holes from the channel and causes RTN, see Fig. 5.2.
- At elevated stress voltages, the defect captures holes from the channel at much higher rates compared to emission. As a consequence, the defect is positively charged most of the time and induces BTI. Furthermore, the defect has a considerable emission rate of holes to the gate and these holes, previously captured from the channel, increase the leakage current. What is more, during stress the defect will most likely transform into its puckered configuration as structural relaxations are favored in the positive charge state. In the puckered configuration, defects have altered time constants which can be observed as SILC [178, 179], see Fig. 5.3.

The features discussed above are a result of the rather involved interplay of the transition rates between the defect and the carrier reservoirs. All effective time constants for that are shown in Fig. 5.4, together with the occupancy of the exemplary defect computed with a kinetic Monte Carlo model. A striking feature of time constants is the *negative coupling*: Because of the interaction with the gate, the emission time constants can *decrease* for increasing stress. This was studied experimentally by Miki *et al.* and quantified by the *coupling factor* defined as

$$\mathrm{coupling}(\tau) \approx \log(\tau(V_{\mathrm{G},1}) - \tau(V_{\mathrm{G},2}))\frac{k_{\mathrm{B}}T}{q(V_{\mathrm{G},1} - V_{\mathrm{G},2})} \tag{5.1}$$

A comparison of the couplings computed from the 4-state NMP defects of the device calibrated for *Tech. C1* to the experimental study of Miki *et al.* is shown in Fig. 5.5.

---

[1] We omit the details of the parameter extraction here as this will be elaborated in the following sections.

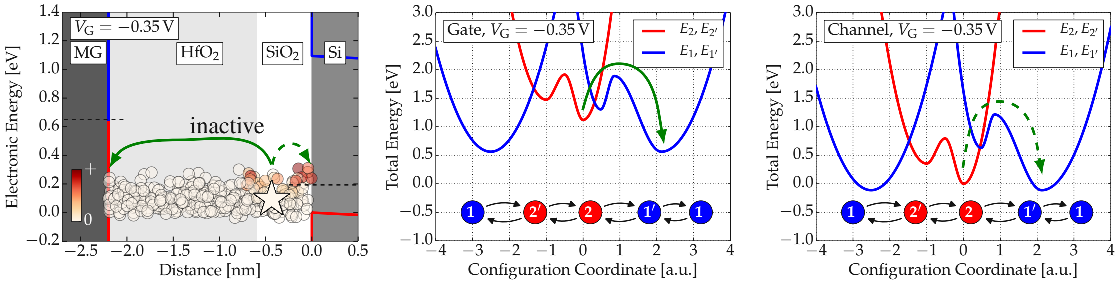

FIGURE 5.1: The band diagram (left) with oxide defects (circles, color indicates charge). The exemplary 4-state NMP defect which is studied throughout this section is marked with a star. Its CC diagrams are shown for interaction with the gate (middle, solid arrows) and with the channel (right, dashed arrows). At the low gate voltage of $V_G = 0.35$ V, the barriers for hole capture processes are large and the defect will be neutral and inactive most of the time. *Tech. C1*. After [GRC14].

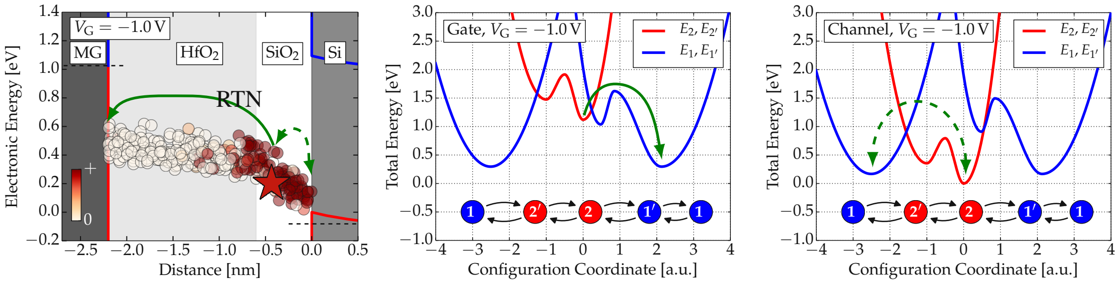

FIGURE 5.2: Same as in Fig. 5.1, but for a moderate gate voltage of $V_G = -1.0$ V. At this voltage, the exemplary defect (star) will capture and emit holes from the channel at roughly the same rates. RTN will be observed, accordingly. *Tech. C1*. After [GRC14].

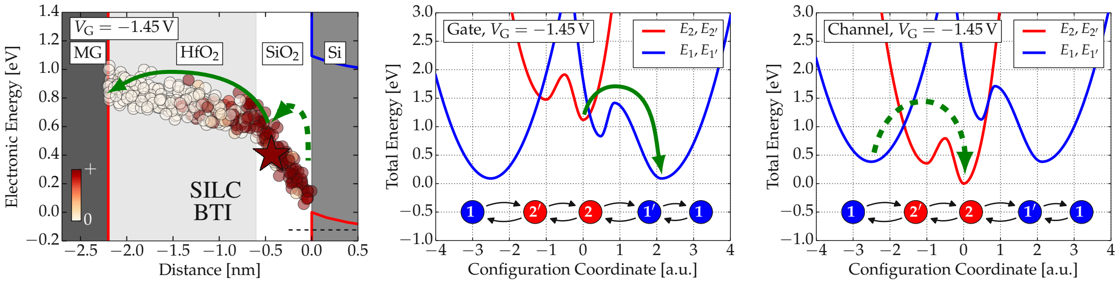

FIGURE 5.3: Same as in Fig. 5.1, but for a high stress voltage of $V_G = -1.45$ V. At this voltage, the exemplary defect (star) has a small barrier for hole capture from the gate and contributes to BTI as it is positively charged most of the time. Also the energy barrier for hole emission to the gate is small and the charges captured from the channel will be emitted to the gate frequently, increasing the gate leakage current. Finally, at these stress conditions, structural relaxation is to be expected and the defect can contribute to SILC. *Tech. C1*. After [GRC14].

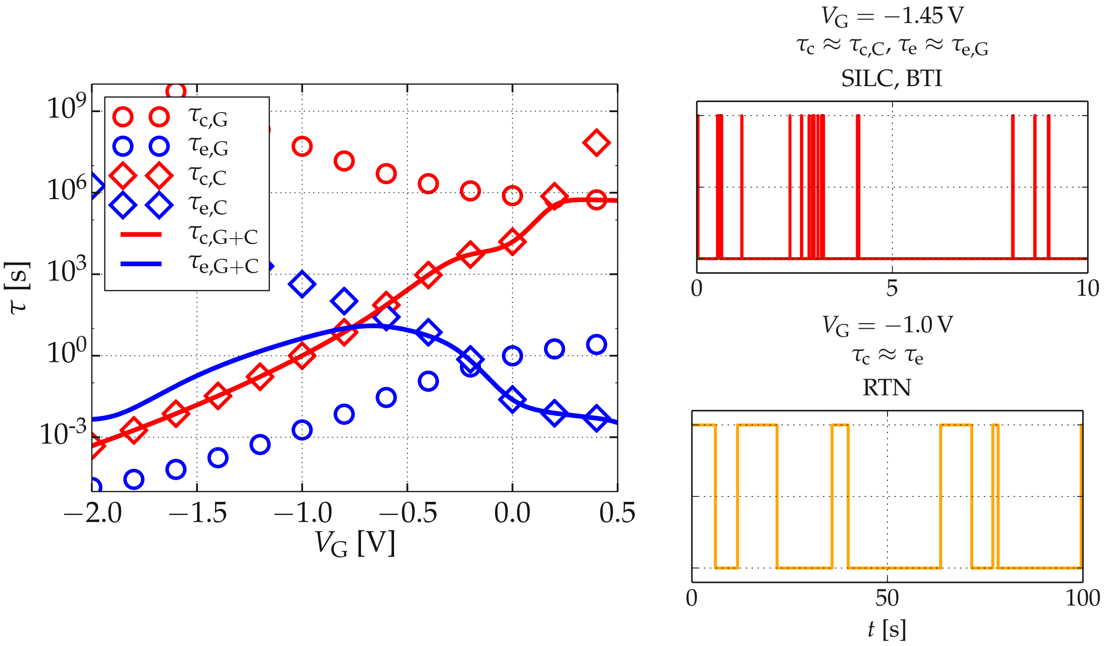

FIGURE 5.4: The time constants of the exemplary defect which is studied throughout this section (left). The time constants are also shown separately for the interaction with the gate only (denoted by "G") and with the channel only (denoted by "C"). For moderate gate voltages of $V_G = -1$ V, the effective time constants are roughly the same and the defect will produce RTN. This is apparent in the transient occupation of the defect, computed with kinetic Monte Carlo with the corresponding time constants (right bottom). At elevated stress voltages of $V_G = -1.45$ V, the defect will be mostly positive due to its fast capture time constant for holes from the channel. Additionally, it will emit these holes frequently which induces increased gate leakage current (right top). *Tech. C1*. After [GRC14].

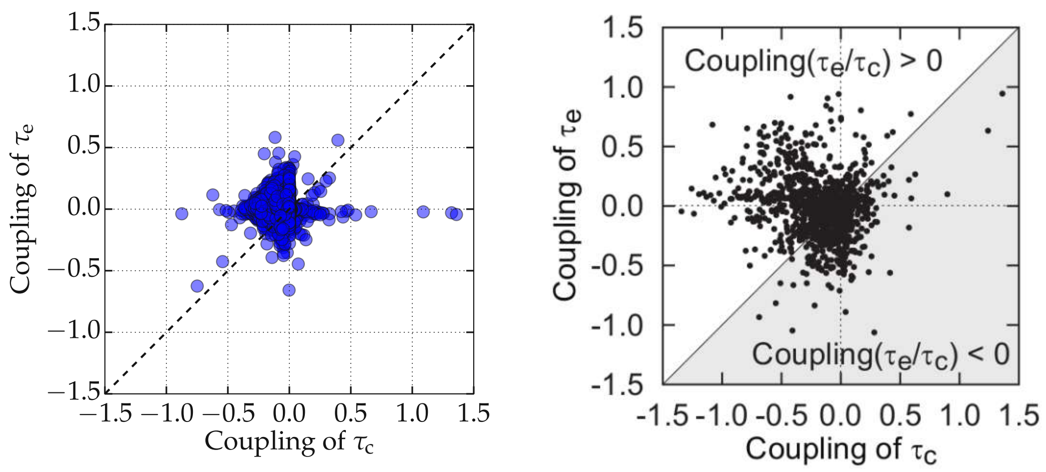

FIGURE 5.5: The coupling factors of the capture and emission rates of the 4-state NMP defects of the calibrated device of *Tech. C1* (left, after [GRC14]) and of a high-κ technology which was studied experimentally by MIKI *et al.* (right, after [170]). With the correct simulation of channel and gate interaction, all experimentally observed features are qualitatively reproduced.

5.4 Recoverable and Quasi-Permanent NBTI

While there are no rigorous definitions of the recoverable and of the quasi-permanent component of BTI, there are experimental techniques which aim at roughly splitting these two components [27], see Subsection 1.1.6. Typically, they rely on pulses into accumulation in order to quickly remove the recoverable component and subsequent measurements are expected to give a good estimate of the quasi-permanent component. These techniques are important for accurate calibration and verification of BTI models with separate descriptions of the recoverable and quasi-permanent component. In the following, we will show that for the NMP models implemented in TCAD [GRC15, GRC24] and in Comphy [GRJ2] on a commercial 130 nm SiON technology (*Tech. A*).

5.4.1 Experimental Data

For the studies in this section, we used the broad set of eMSM data (Section 2.2.1) previously obtained on pMOSFETs of *Tech. A* with different stress voltages ($-V_\mathrm{G} = 1.2$, 1.7, 2.2, 2.7, 3.2 V), temperatures ($T = 125$ and 170°C), and stress and recovery times in the range of 1 µs–100 ks [176]. These data are complemented by MSM experiments (Section 2.2) with a pulse into accumulation after the stress phases: For the pulse time t_p, the gate voltage $V_\mathrm{G} = +0.5\,\mathrm{V}$ is applied, followed by a regular recovery phase [GRC15]. Due to the distinct bias dependence of the degradation mechanisms ascribed to the recoverable and the quasi-permanent part, this pulse mainly recovers the former and the latter can be measured subsequently.

5.4.2 Modeling with TCAD

For the first studies with the *4-state NMP model* (Subsection 3.4.2) with TCAD tools [169] in 2014, we distributed the oxide defects in the first 1.2 nm of the oxide and neglected interaction of these defects with the gate, see Fig. 5.6.

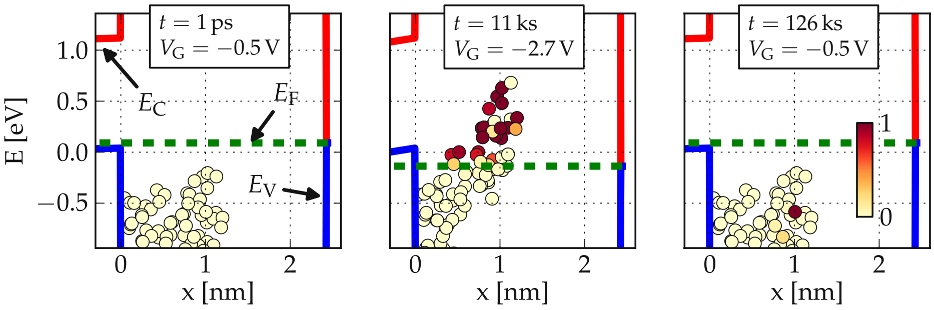

FIGURE 5.6: The band diagram of *Tech. A* with a subset of 4-state NMP defects (circles) inducing a shift of the threshold voltage ΔV_th when charged positively (red). In the initial steady-state solution (left) the occupation probability (see color bar) of the defects is determined by their trap level and the Fermi level of the channel. Since all defects are below the Fermi level, they are neutral. In the subsequent stress phase (middle), the trap levels are shifted because of the electrostatic potential at the trap positions and the occupation probabilities change depending on the transition rates of the respective states. Note that there is *no "tunneling front"* visible since the rates are mainly governed by the NMP barriers instead of the tunneling probabilities. Finally, in the recovery phase (right), the defects discharge again, approaching their initial state for infinite recovery times. *Tech. A*. After [GRC15].

The parameters which define the distributions of these defects were optimized to fit the broad set of eMSM data (see Fig. 5.7) and the MSM data with a pulse into accumulation before recovery (see Fig. 5.8). While there is certainly no unique solution for such an optimization for a subset of the experimental data, capturing *all experimental data with one and the same set of defects* is quite remarkable. This set of defects, obtained by Monte Carlo sampling of the calibrated distributions, inherently covers the features of the two components of BTI: During the stress phase, defects of both models charge, however, the subsequent pulse into accumulation mainly discharges defects of the 4-state NMP model because of their pronounced bias dependence, see

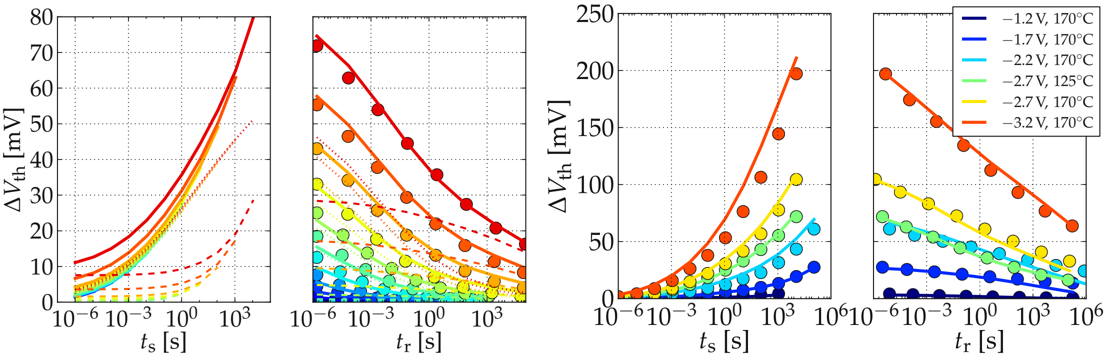

FIGURE 5.7: Shift of the threshold voltage ΔV_{th} measured (circles) with the eMSM scheme and simulated with TCAD (lines). Left: Detailed view for $V_{\mathrm{G}} = -2.7\,\mathrm{V}$ and $T = 125°\mathrm{C}$ of all consecutive stress (t_{s}) and recovery (t_{r}) phases, also the simulated contribution of the 4-state NMP model (dotted) and the field-dependent thermal transitions (dashed) are shown separately. During stress, no data is obtained with the eMSM scheme, however, the short measurement delay of 1 µs gives a good estimate of ΔV_{th} during degradation. Right: The first recovery points of each recovery phase of the eMSM experiment are compared to the simulated degradation during stress for various stress conditions. Since the data is affected by recovery even with a measurement delay of 1 µs, the experimental data during stress is below the simulation results. All recovery traces are well captured by the TCAD simulations. *Tech. A*. After [GRC15].

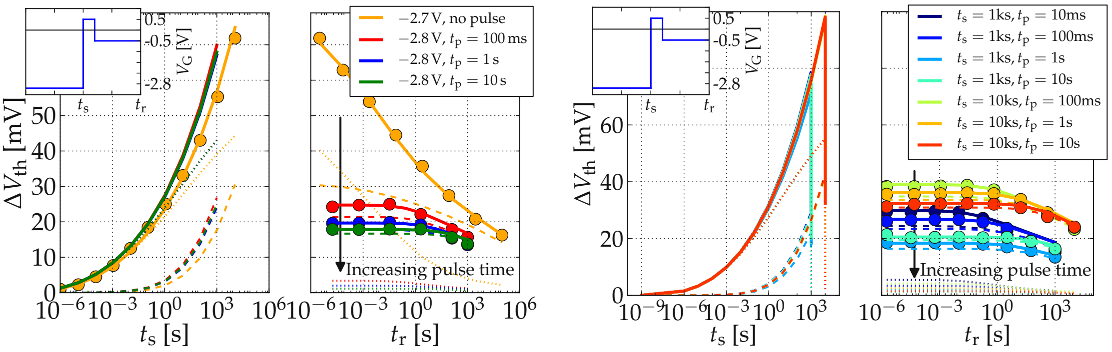

FIGURE 5.8: Similar to Fig. 5.7, measured (circles) and simulated (lines) ΔV_{th} is shown during stress and recovery phases. However, here a MSM sequence with one stress phase and one recovery phase with a short pulse into accumulation in between was applied. Left: The pulse setups with 1 ks stress are compared to similar MSM data without a pulse in between. The forced discharge of recoverable defects (dotted) is evident. Right: The same for different stress times, all experimental features are captured by the TCAD simulations. Note that the variability of the permanent component was considered by scaling the degradation of the field-dependent thermal transitions by up to ±15 %. *Tech. A*. After [GRC15].

Subsection 3.4.2. The remaining degradation is mostly due to defects modeled with the field-dependent thermal transitions (see Subsection 3.3.2), in accordance with the quasi-permanent part observed experimentally, see Fig. 5.8.

These distributions of the two models are visualized in Fig. 5.9 for the *4-state NMP defects* and in Fig. 5.10 for the defects described by the field-dependent thermal transition. Based on these distributions, single defects were obtained by sampling in a Monte Carlo fashion. On these large devices, many of these defects contribute to the degradation, resulting in smooth traces of both measured and simulated ΔV_{th}, accordingly. Due to the amorphous nature of the oxide, each defect has an individual configuration, thus, the CC diagram of each defect is different (Fig. 5.9 and 5.10, left). This leads to a broad distribution of capture and emission time constants (Fig. 5.9 and 5.10, right). From the simulations, CET maps and activation energy maps can be constructed by considering the *equilibrium occupancy difference a* of each defect defined as

$$a = p(V_{\text{G,H}}) - p(V_{\text{G,L}}) \tag{5.2}$$

with its occupation probability p given in Eq. 3.53 and its impact on V_{th}, see Eq. 3.65. The resulting densities where the defects are weighted by these two factors and plotted according to their time constants and activation energies are shown in Fig. 5.11. Note that the very broad distribution of time constants was verified by experimental studies with highly temperature accelerated tests [180]. The simulated CET map agrees well with the CET map constructed from the experimental data (see Fig. 5.12), which is a direct consequence of the agreement of the corresponding ΔV_{th} traces presented in Fig. 5.7.

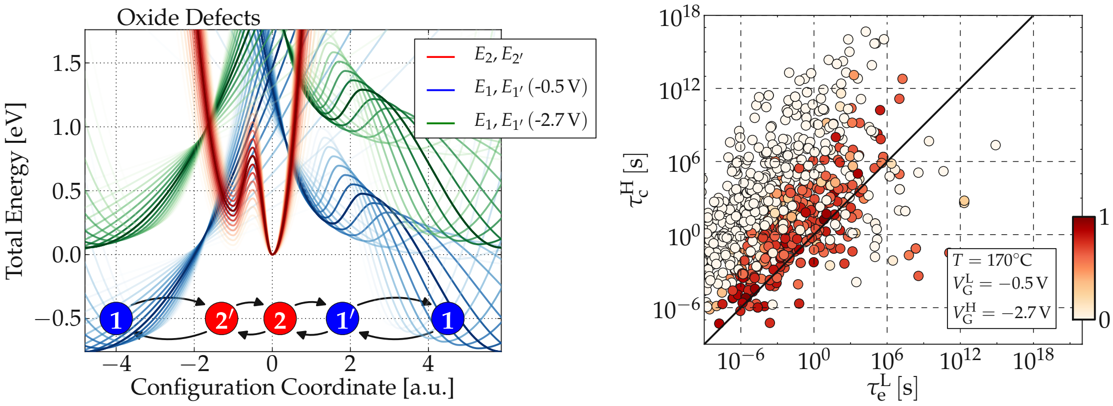

FIGURE 5.9: Left: The CC diagram of each *4-state NMP defect* depends on its parameters which were sampled in a Monte Carlo fashion from the extracted distributions. Shown here are the mean values for two different gate voltages where the fade out represents up to one σ of the distribution. Right: From the CC diagrams, the capture time constants during stress (τ_c^H) and the emission time constants during recovery (τ_e^L) can be computed for each defect (circle). The color represents the equilibrium occupancy difference *a*. *Tech. A*. After [GRC15].

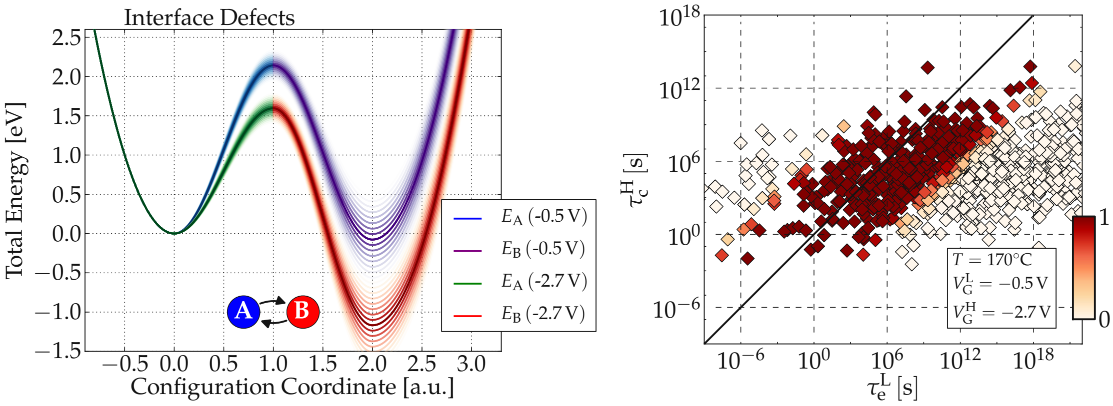

FIGURE 5.10: Similar to Fig. 5.9, the distributions of the defects modeled with the *field-dependent thermal transitions* are shown here in CC diagrams (left) and according to their time constants and equilibrium occupancy difference (right). Quite contrary to the 4-state NMP defect which represent the recoverable components, the defects here tend to long emission time constants which is characteristic for quasi-permanent defects. Still, usually there is a overlap of the widely distributed time constants, making a separation difficult. *Tech. A*. After [GRC15].

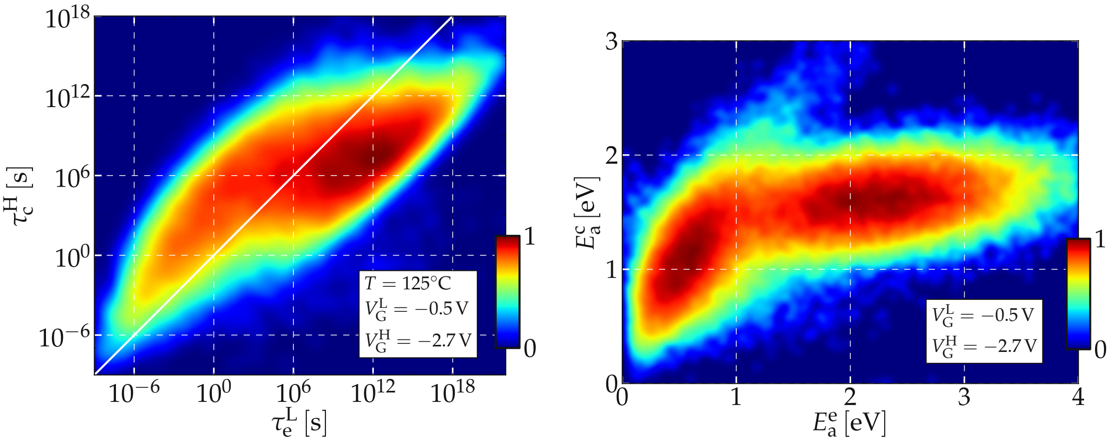

FIGURE 5.11: Combining the contributions of the simulated 4-state NMP defects (Fig. 5.9) and the defects modeled by field-dependent thermal transitions (Fig. 5.10) results in the full CET map for the respective stress conditions (left). Similarly, the defects plotted according to their activation energies for capture E_a^c and emission processes E_a^e give the corresponding activation energy map (right). *Tech. A*. Note that the densities are normalized. After [GRC15].

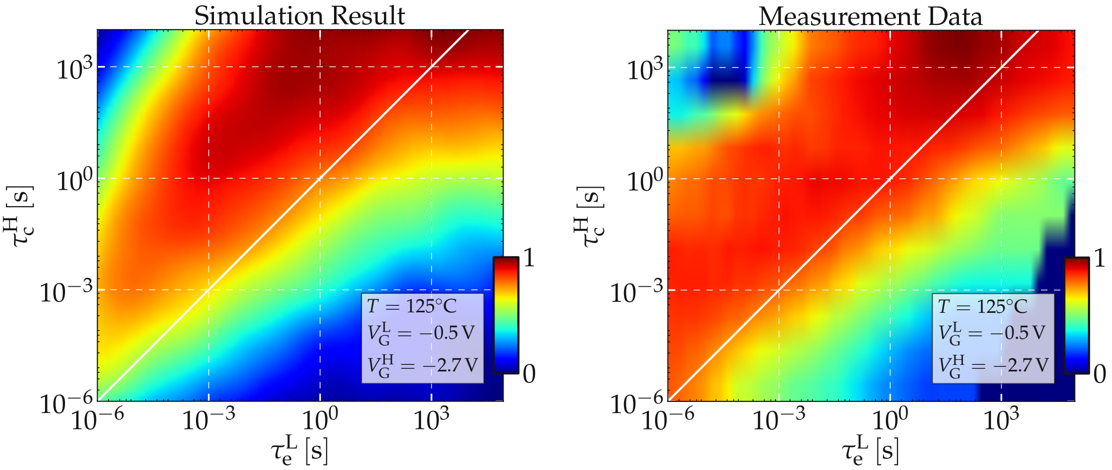

FIGURE 5.12: The simulated CET map from Fig. 5.11 (left) plotted for the range of time constants for which experimental data is available to compare to the CET map obtained directly from the experimental recovery traces (right, see Subsection 2.2.2). *Tech. A*. After [GRC15].

5.4.3 Modeling with Comphy

The full set of experimental data presented in the previous subsection was also simulated with Comphy. Similar to the TCAD approach, the recoverable component is described with an NMP model and the quasi-permanent component is described with field dependent thermal transitions. For this, the device electrostatics and the oxide parameters were adjusted in Comphy according to the technology, followed by an optimization of the defect parameters, see Fig. 5.13. Compared to the optimization of the models in TCAD, the number of parameters is much smaller which makes the optimization less complex. Despite the smaller solution space, a good fit was obtained for the full set of eMSM data, see Fig. 5.14. In order to further verify the defect properties extracted with Comphy, the MSM data set with the pulse into accumulation was simulated as well, see Fig. 5.15. Small deviations are visible for the quasi-permanent component because of the *variability in the experimental data* [GRC15]. Note that this could be easily accounted for in the Comphy simulations as it was done in the TCAD simulations to get a better agreement. That said, the simulation results with Comphy are very convincing throughout all stress conditions and recovery times, indicating that the gist of the degradation mechanisms is well described with the limited number of model parameters, see Table 5.5.

In the same way as for the TCAD simulations, the CET map can be computed based on the calibrate Comphy device. This is done for the same stress conditions as for the TCAD device (see Fig. 5.11), and in accordance with the good fit to the ΔV_{th} data in the stress and recovery traces, the maps are very similar as well (see Fig. 5.16).

With an accurate physical description, the degradation for various stress scenarios can be accurately predicted. In Fig. 5.16, we explore the degradation of *Tech. A* for stress times up to 1×10^{10} s. In line with the experimental data, the technology does not fulfill the lifetime criterion of 30 mV after 10 years at elevated temperatures. However, at room temperature, this criterion is easily met. A very interesting feature in this data is the increase of the slope around $t_{\mathrm{s}} = 1 \times 10^{4}$ s for particular stress conditions. For example, this behavior is visible in the experimental data for stress with $V_{\mathrm{G}} = -1.7$ V and $T = 170$°C. At these stress voltages, the contribution of the recoverable component is rather weak, however, accelerated temperatures strongly activate the quasi-permanent component[2]. This is well reproduced by the Comphy simulations using the 2-state NMP model and the double-well model.

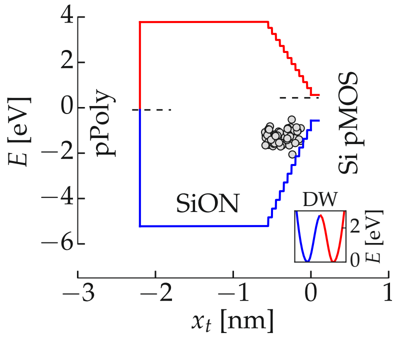

FIGURE 5.13: The band diagram of the pMOSFET at flat band conditions, calibrated with Comphy. The 2-state NMP defects (circles) are distributed slightly below the valence band edge of the Si channel. The CC diagram with the mean parameters of the double-well model is shown in the inset. *Tech. A*. After [GRJ2].

---

[2] This is in line with the observations and models presented by JEPPSON and SVENSSON already in 1977 [53].

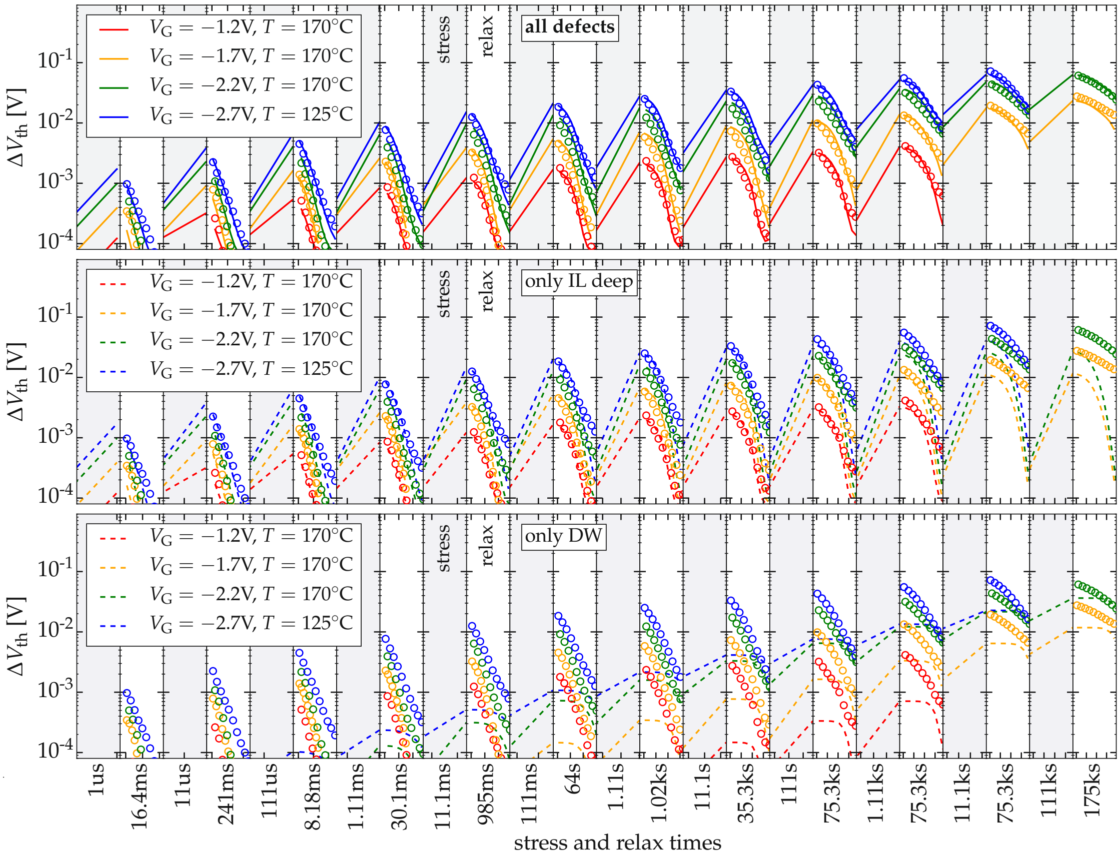

FIGURE 5.14: The degradation during all stress and recovery phases of an eMSM experiment (circles) on a log-log plot to properly show all features of ΔV_{th} for various NBTI conditions. Each phase is shown from 0.1 µs up to the duration given below. In addition to the total degradation (top), the simulation results of the 2-state NMP (middle) and the double-well (bottom) are also shown, representing the recoverable and the quasi-permanent part, respectively. *Tech. A.* After [GRJ2].

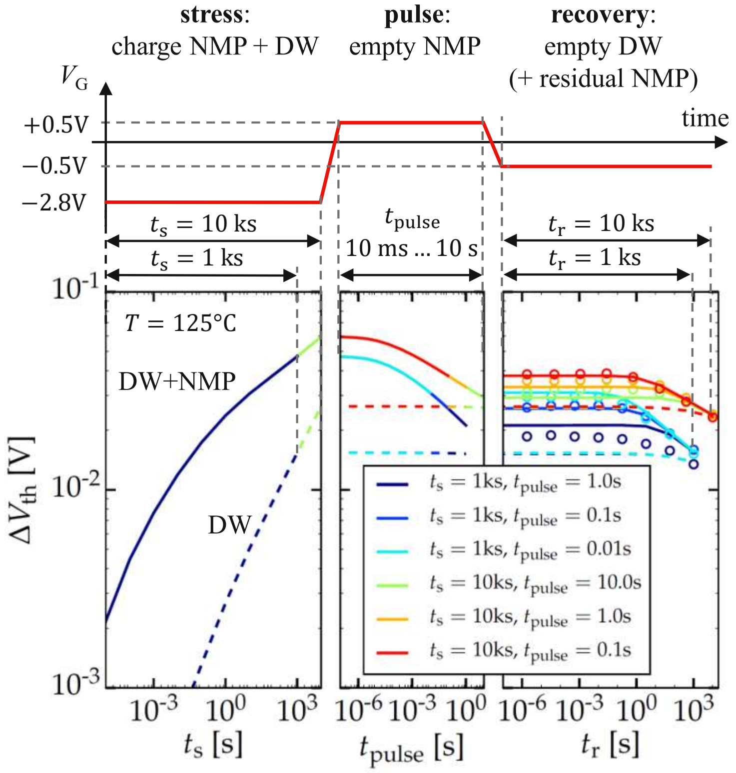

Figure 5.15: To verify the contribution of the quasi-permanent component, the measured recovery trace (circles) after a stress phase followed by a short pulse into accumulation was simulated with the calibrated Comphy device (lines). For all combinations of stress times and pulse times, good agreement is obtained, verifying the contribution of the double-well model (dashed lines) which represents the quasi-recoverable component. Note that there is some variability in the experimental which causes small deviations for some stress conditions [GRC15]. *Tech. A*. After [GRJ2].

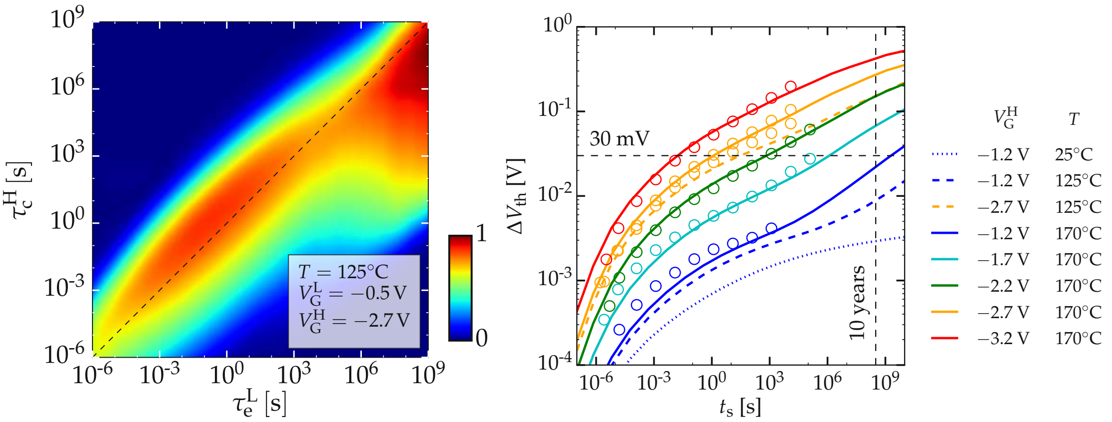

Figure 5.16: Left: The CET map computed from the calibrated Comphy device with defects sampled on a grid for smooth curves. The shape is similar to the CET map from TCAD simulations, see Fig. 5.11. Right: The first measured recovery point of each trace (circles) gives a good estimate of the degradation directly at stress conditions because of the short measurement delay of 1 µs. The simulations with the calibrated Comphy device (lines) are in good agreement with the data and allow for a reliable extrapolation of the lifetime of the technology. *Tech. A*. After [GRJ2].

5.5 Recoverable BTI of High-κ Devices

The separation of the two components of BTI was discussed in the previous section for a technology with a simple single-layer technology (commercial 130 nm SiON technology (*Tech. A*)). Next, the instabilities of a 14 nm high-κ FinFET technology (process 2) (*Tech. C2*) will be investigated. In general, high-κ technologies show pronounced degradation for positive stress voltages as opposed to plain SiO_2 technologies which typically barely degrade at these conditions [181]. Thus, high-κ technologies are suitable to verify the following:

Assuming that pre-existing oxide defects are the common underlying cause of the recoverable component of both NBTI and PBTI, it must be possible to describe the degradation of pMOSFETs and nMOSFETs of the same technology consistently by the same physical defect parameters for both stress polarities.

Using a dedicated measurement technique to obtain the recoverable component of PBTI and NBTI, we will show that this assumption holds for the 4-state NMP model by simulating all four combinations of N/PBTI on n/pMOSFETs with *one and the same set of oxide defects*, see Fig. 5.17 [GRC16].

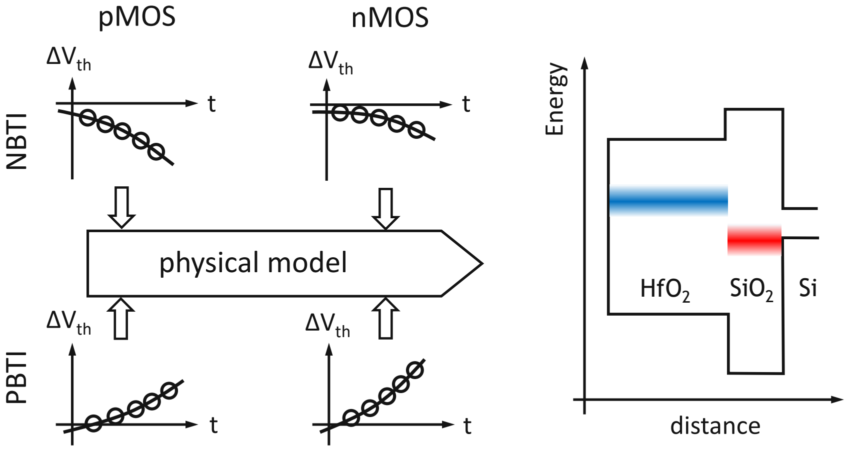

FIGURE 5.17: Concept of unified modeling of BTI: The simulation of the recoverable component of all four cases (P/NBTI on p/nMOSFETs) with a single consistent set of pre-existing oxide defects provides accurate calibration of the physical model parameters and corroborates its validity.

5.5.1 Experimental Data

Similar to the pulse into accumulation after stress (see Subsection 5.4.1) we utilize the distinct bias dependence of the two degradation mechanisms to separate the recoverable and the quasi-permanent component of BTI. The schematic measurement procedure is depicted in Fig. 5.18: While there is a drift of the quasi-permanent component, the recoverable component can be reproduced by subsequent measurements on the same device. This is shown in Fig. 5.19 where the recoverable component after a stress phase at $V_G = -1.25\,\mathrm{V}$ is measured multiple times on the same device. Despite a change in the permanent component, the recoverable component is very similar throughout this experiment and only increases slightly after an additional stress phase at pronounced PBTI conditions.

Following the scheme presented in Fig. 5.18, a broad set of MSM data was obtained on *Tech. C2* with gate voltages between -1.5 and $+1.5$ V on both p and nFinFETs for various stress times. Note that the experiments were conducted on 220 devices in parallel to obtain the mean BTI response of this technology.

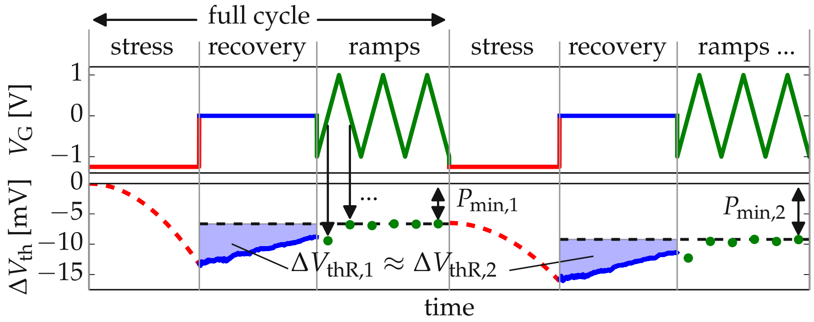

FIGURE 5.18: One measurement cycle to determine the recoverable component after BTI stress consists of a regular stress/recovery phase, followed by a series of $I_D V_G$ sweeps. These sweeps discharge the bias dependent defects which constitute the recoverable component, see Subsection 1.1.6. The remaining degradation P_{min} can be subtracted from the total ΔV_{th} to obtain the recoverable component $\Delta V_{th,R}$, accordingly. After [GRC16].

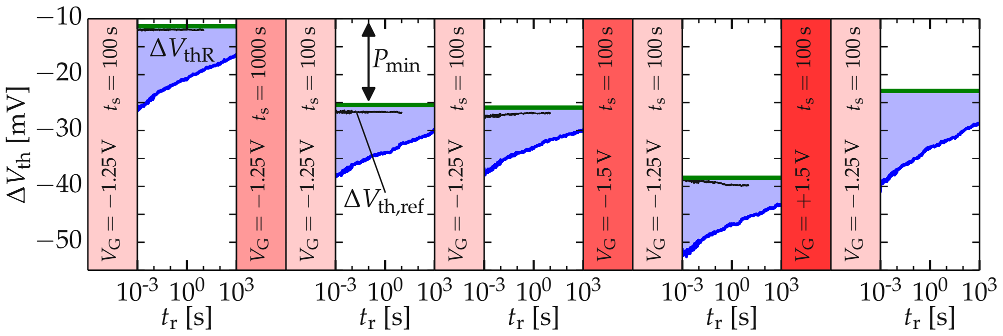

FIGURE 5.19: An example for measurements obtained following the scheme presented in Fig. 5.18. The recoverable component (blue, obtained after subtracting the quasi-permanent component P_{min}) stays constant for subsequent measurements on the same device, independent of intermediate stress phases with various stress times t_s and gate voltages of both polarities (sections marked with red background). *Tech. C2*. After [GRC16].

5.5.2 Unified TCAD Simulations

For accurate simulation of oxide defects, the FinFET devices were calibrated with 3D TCAD simulations based on the doping and the gate stack parameters. A good fit was obtained for the experimental $I_D V_G$ curves, see Fig. 5.20.

Following the scheme presented in Subsection 3.4.2, the distribution of the 4-state NMP model parameters was extracted by simultaneous optimization of all four cases of BTI, see Fig. 5.17. For this extraction, constant defect densities were assumed in the HfO_2 and in the SiO_2 layers, respectively, each with an independent set of defect parameters. Note that some studies indicate that there are more than this one distribution of defects in each of these oxide materials:

- In HfO_2, defects with a deep trap level have been reported. However, these defects barely contribute at the investigated stress conditions [GRJ2].
- In SiO_2, defects with a shallow trap level are inferred from RTN studies [100] and from MSM experiments on particular technologies [181]. However, typically they have very low defect densities and their contribution is overshadowed by defects in the HfO_2 [GRJ2].

Thus, the degradation due to pre-existing oxide defects of *Tech. C2* can be well captured with one dominant defect distributions in each material, depicted in Fig. 5.21 for pFinFETs and in Fig. 5.22 for nFinFETs.

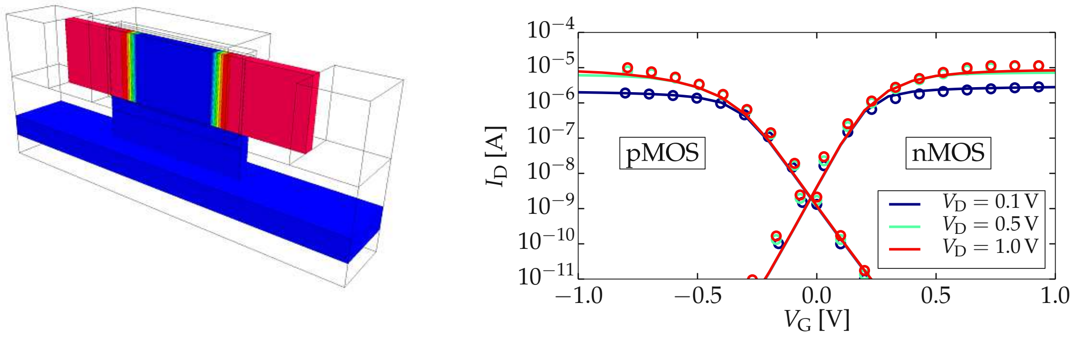

FIGURE 5.20: The FinFET device simulted with TCAD tools, the geometries are given in Subsection 5.2.3 (left) and the corresponding $I_D V_G$ curves on both n and pFinFETs (right). A good fit of the simulated electrostatics (lines) to the experimental data (circles) is a necessary prerequisite for accurate physical defect modeling. *Tech. C2*.

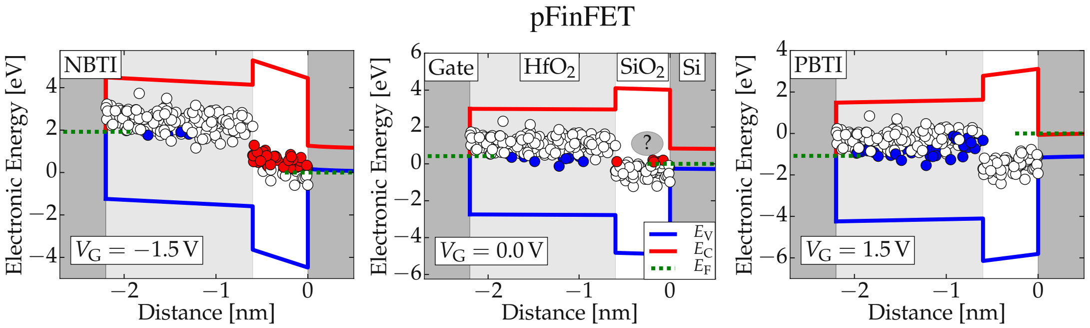

FIGURE 5.21: The band diagrams of the *pFinFET* devices for three different gate voltages. The oxide defects (circles) are depicted according to their charge at the respective steady-state condition. The acceptor-like defects in HfO_2 are either neutral (white) or negative (blue) while the donor-like defects in the SiO_2 are either neutral or positive (red). The neglected defects in the SiO_2 with a shallow trap level are denoted by a question mark. *Tech. C2*. After [GRC16].

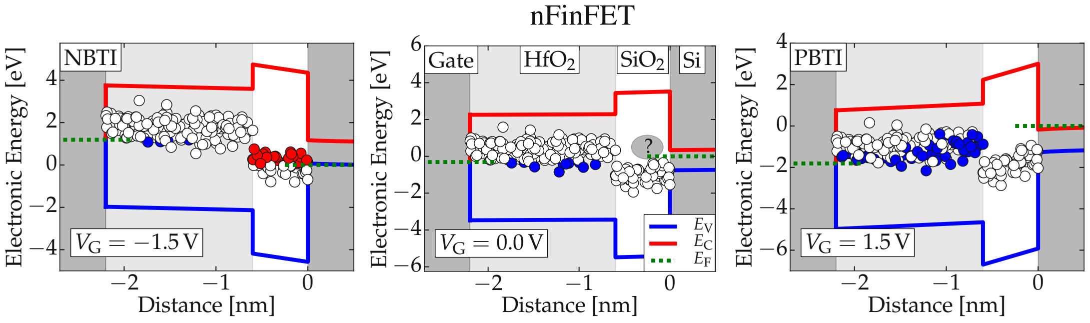

FIGURE 5.22: The same as in Fig. 5.21, but for *nFinFET* devices. *Tech. C2*. After [GRC16].

The extracted defect levels and concentrations in the HfO_2 and SiO_2 layer are listed in Table 5.3. Note that the defect concentrations in both materials agree very well with the values obtained from Comphy simulations of various technologies (see Table 5.1). Also the distribution of the trap level in HfO_2 is in line with typical values [GRC2, GRJ2]. Only the trap level of defects extracted in SiO_2 is slightly higher compared those studies. This might be related to the processing of this very thin interfacial layer with low thermal budget [GRJ2].

TABLE 5.3: Distribution of the trap level and the defect concentration in the HfO_2 and SiO_2 oxide determined for *Tech. C2* [GRC16].

	$\langle E_T \rangle$	σ_{E_T}	N_{OT}
SiO_2	−0.78 eV	0.35 eV	$0.9 \times 10^{20}\,\mathrm{cm}^{-3}$
HfO_2	0.66 eV	0.43 eV	$2.9 \times 10^{20}\,\mathrm{cm}^{-3}$

The resulting degradation obtained with the extracted distributions are in good agreement for various stress times (see Fig. 5.23) and gate voltages (see Fig. 5.24). While there are some minor deviations to the experimental data at short stress times, the capability of the 4-state NMP model to capture the essence of the recoverable component consistently and in a unified manner for all cases of BTI demonstrates its capability to describe the degradation of pre-existing oxide defects.

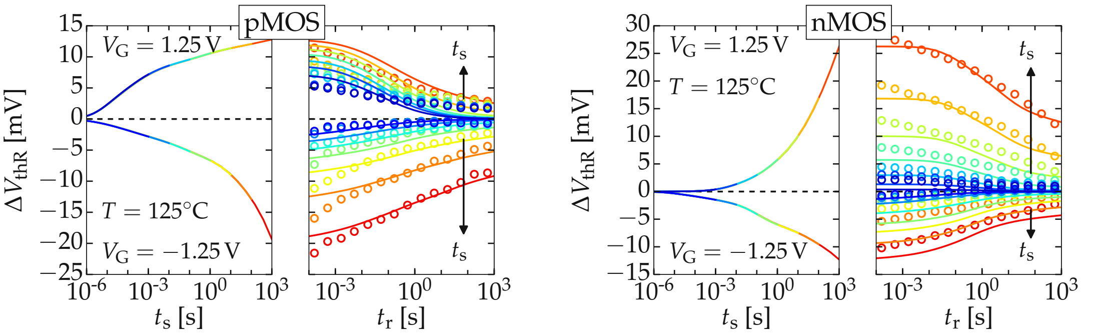

FIGURE 5.23: The measured (circles) and simulated (lines) recoverable component ΔV_{thR} after BTI stress with $V_G = +1.25\,V$ and −1.25 V and $T = 125$°C for stress times in the range of $t_s = 1$ ms up to 1 ks. The degradation of *pFinFETs* (left) is more pronounced for negative gate voltages while the degradation of *nFinFETs* (right) is more pronounced at positive gate voltages. *Tech. C2*.

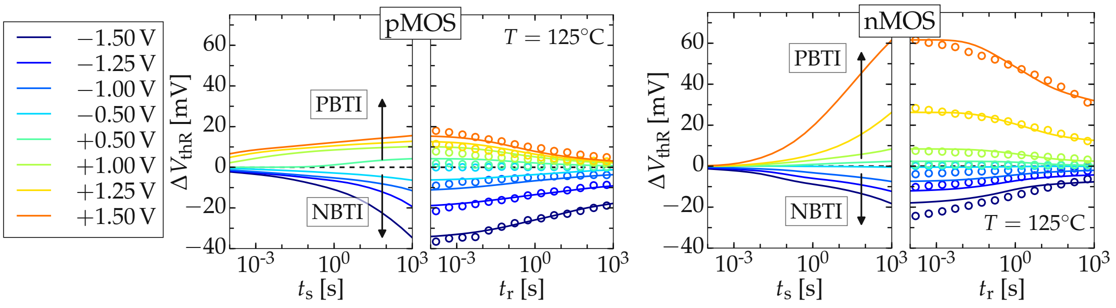

FIGURE 5.24: Similar to Fig. 5.23, the degradation of the recoverable component of BTI is shown for pFinFETs (left) and nFinFETs (right). All voltages between $V_G = +1.5$ V and −1.5 V are shown for a stress time of 1 ks. *Tech. C2*. After [GRC16].

5.5.3 Contributions of Shallow HfO_2 and Deep SiO_2 Defects

The results presented in the previous subsection show that the recoverable component of BTI can be described consistently for *Tech. C2* considering defects in HfO_2 with shallow trap levels complemented by defects in SiO_2 with deep trap levels. However, experimentally only the total degradation was obtained, raising the question whether the simulations correctly reproduce the respective contributions of the two oxide materials to the total ΔV_{th}. The total recoverable component for BTI conditions and the respective contributions of the two oxide layers is shown in Fig. 5.25, simulated with the calibrated 4-state NMP defects. This graph shows that PBTI of pFinFETs is dominated by defects in the SiO_2 while it is dominated by defects in HfO_2 in nFinFETs. This striking feature will be investigated and verified by experiments in the following.

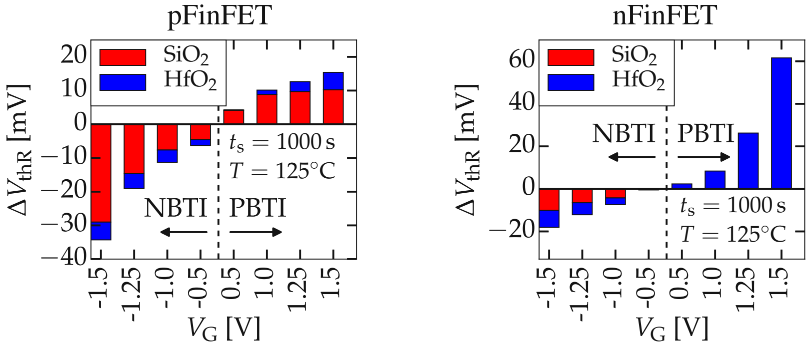

FIGURE 5.25: The recoverable component of BTI simulated with the calibrated 4-state NMP model with contributions from defects in HfO_2 (blue) and SiO_2 (red) for *pFinFETs* (left) and *nFinFETs* (right). Consistent with the very weak degradation of plain SiO_2 technologies, PBTI on nFinFETs is governed by defects in HfO_2. The degradation of pFinFETs at NBTI, on the other hand, origins from defects in SiO_2. *Tech. C2*. After [GRC16].

Experimentally, two differences are to be expected between defects in the HfO_2 layer and in the interfacial SiO_2 layer:

- *Difference in time constants*: The minimal capture time constants of defects will be shorter for defects in SiO_2 because of the higher tunneling probability, compare Eq. (3.45).
- *Difference in step heights*: On average, the impact of charges on V_{th} will be larger for defects in the SiO_2 layer of *Tech. C2* for electrostatic reasons, compare Eq. (3.65).

Difference in Time Constants

The abovementioned peculiarity is in line with the calibrated 4-state NMP defects as shown in Fig. 5.26: Experiments as well as simulations show that PBTI is more pronounced on pFinFETs compared to nFinFETs for short stress times while the opposite is the case for long stress times. The simulations show that this peculiarity is due to fast defects in SiO_2 which barely contribute on nFinFETs where most of these defects are already neutral before the stress experiment. This is evident in the band diagrams of the pFinFETs (Fig. 5.21) and nFinFETs (Fig. 5.22): Initially, the defects are charged roughly according to the steady-state case with $V_G = 0\,\mathrm{V}$. Because of the difference in the Fermi level, this means that some of the defects in SiO_2 are positively charged on pFinFETs while nearly all these defects will be neutral on nFinFETs. During PBTI stress the positive defects in SiO_2 can be neutralized causing the recoverable degradation on pFinFETs. This mechanism is negligible on nFinFETs which are dominated by the defects in the HfO_2 with larger time constants.

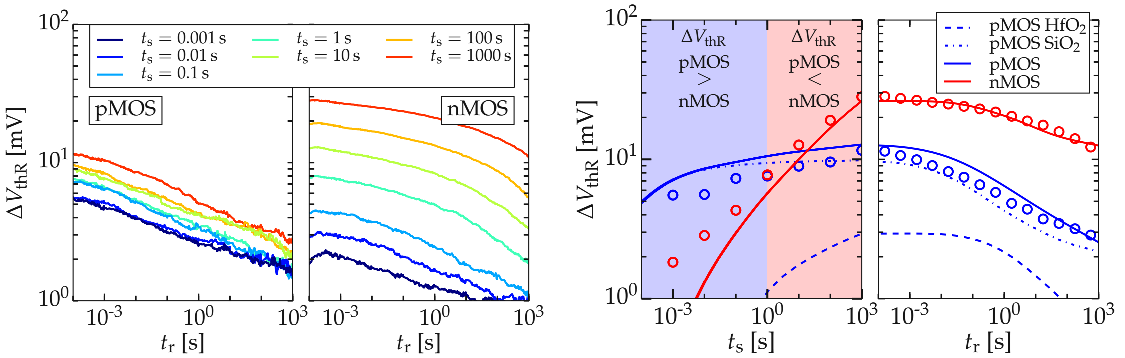

FIGURE 5.26: Analysis of PBTI stress with $V_G = 1.25$ V and $T = 125$°C. Left: The recoverable component of PBTI recorded on pFinFETS and nFinFETs after varying stress times t_s. Right: The same data but only the first recovery point of each trace to estimate of the degradation during stress (circles in the left panel) and the recovery after $t_s = 1$ ks (circles in the right panel). The peculiar crossing point around $t_s \approx 1$ s where the degradation of the pFinFETs exceeds the degradation of nFinFETs can be understood based on the simulations (lines): Due to the contribution of the tunneling probability, the minimum capture time constants of defects in the interfacial SiO$_2$ layer (dash-dotted) are on average smaller compared to the time constants of defects in the HfO$_2$ layer. Therefore, pFinFETs (governed by defects in SiO$_2$) degrade quickly while the degradation of nFinFETs (governed by defects in HfO$_2$) is delayed. *Tech. C2*.

Difference in Step Heights

The differences in the average impact of defects in the HfO$_2$ and SiO$_2$ layer are studied based on the variability. To obtain the mean step height η and the number of active defects N after BTI stress, we measured more than 1100 small devices[3], again for all four combinations of BTI, and applied the *defect centric* analysis (see Section 3.2). All predictions[4] of the simulations with the 4-state NMP model agree with the experimental observations:

- In the *simulations*, PBTI is governed by defects in HfO$_2$ on nFinFETs and by defects in SiO$_2$ on pFinFETs, see Fig. 5.25. *Experimentally*, η of nFinFETs is smaller compared to pFinFETs for all cases of PBTI stress, see Fig. 5.27 and 5.28. This is a consequence of the smaller step height of defects in HfO$_2$ because their electrostatic impact is scaled by the distance to the channel interface.

- In the *simulations*, some defects in the HfO$_2$ of pFinFETs capture charges at PBTI conditions with time constants roughly above 1 s which is not the case for nFinFETs, see Fig. 5.26. *Experimentally*, η *decreases* from 1.34 mV ($t_s = 1$ s) to 1.22 mV ($t_s = 100$ s) on pFinFETs while it *increases* from 0.75 mV ($t_s = 1$ s) to 0.88 mV ($t_s = 100$ s) on nFinFETs, see Fig. 5.27 and 5.28. In perfect agreement, defects with small step heights (in HfO$_2$) are charged in this interval on pFinFETs, thus, the average step height of these devices converges towards the average step height of nFinFETs which were governed by defects in HfO$_2$ for all stress times.

- In the *simulations*, NBTI of pFinFETs is dominated by defects in SiO$_2$ while on nFinFETs defects in the HfO$_2$ and SiO$_2$ contribute in a roughly similar manner, see Fig. 5.25. The largest value of η of all *experiments* is obtained from NBTI on pFinFETs while η of nFinFETs after NBTI stress is well in the middle of all values, see Fig. 5.29.

---

[3] Devices of *Tech. C2* with 2 FinFETs in parallel as opposed to 220 FinFETs in parallel to study the means.

[4] Note that such experimental data was not available at the time of publication of [GRC16].

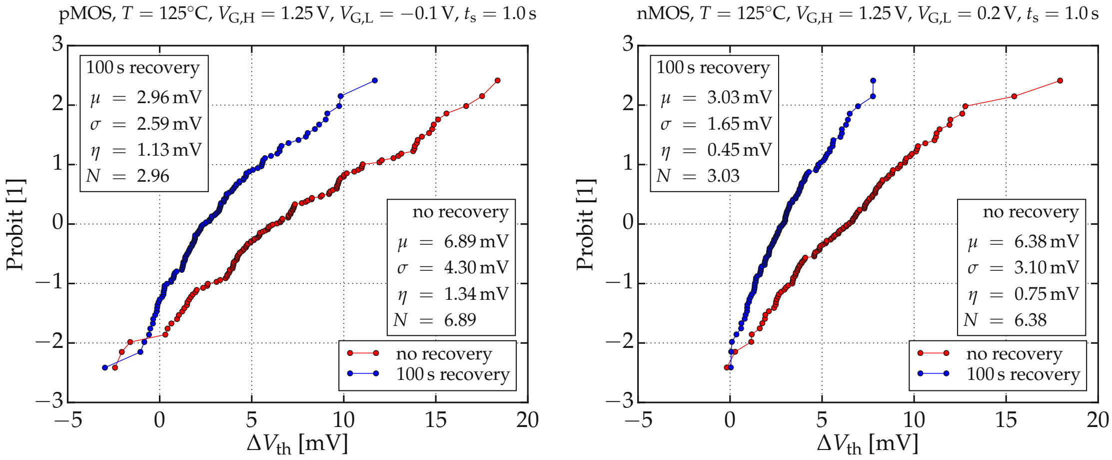

FIGURE 5.27: Probit plot showing the distribution (mean μ, standard deviation σ) of the threshold voltage shifts ΔV_{th} of 126 pFinFETs (left) and 125 nFinFETs (right) after 1 s of PBTI stress ($V_{\mathrm{G}} = 1.25$ V and $T = 125$°C). The distribution is shown without recovery (red, measurement delay of 50 µs) and after 100 s recovery (blue). The mean step height η and the number of active defects N are deduced from these distributions using the defect centric analysis [109]. A smaller η is obtained for nFinFETs which confirms that they are governed by defects in HfO_2, opposed pFinFETs which are governed by defects in SiO_2 at these stress conditions, see Fig. 5.25. *Tech. C2*.

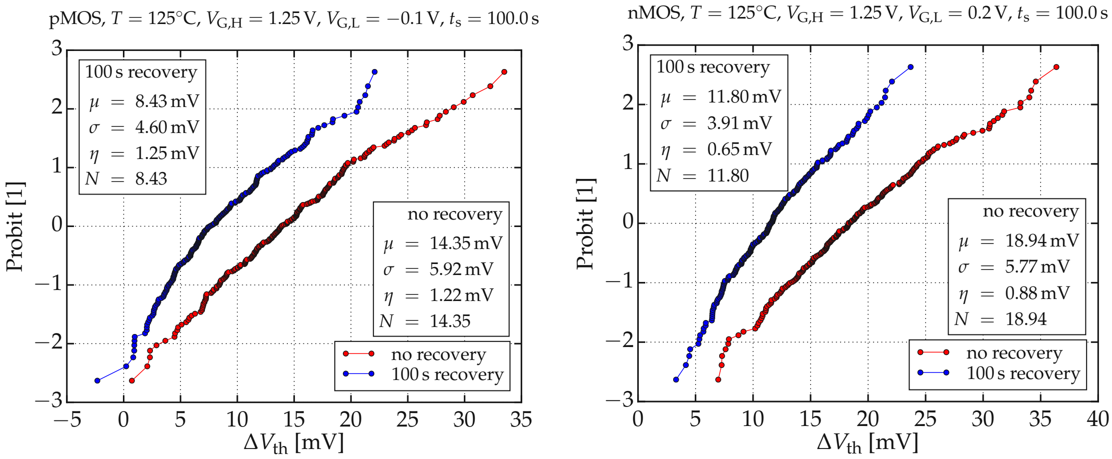

FIGURE 5.28: The same as in Fig. 5.27 but for 234 pFinFETs (left) and 234 nFinFETs (right) after 100 s of PBTI stress ($V_{\mathrm{G}} = 1.25$ V and $T = 125$°C). Compared to the result after 1 s stress in Fig. 5.27, η of pFinFETs is slightly smaller because of slow defects capturing charges in HfO_2. This is not the case for nFinFETs, in line with the simulations, see Fig. 5.26. *Tech. C2*.

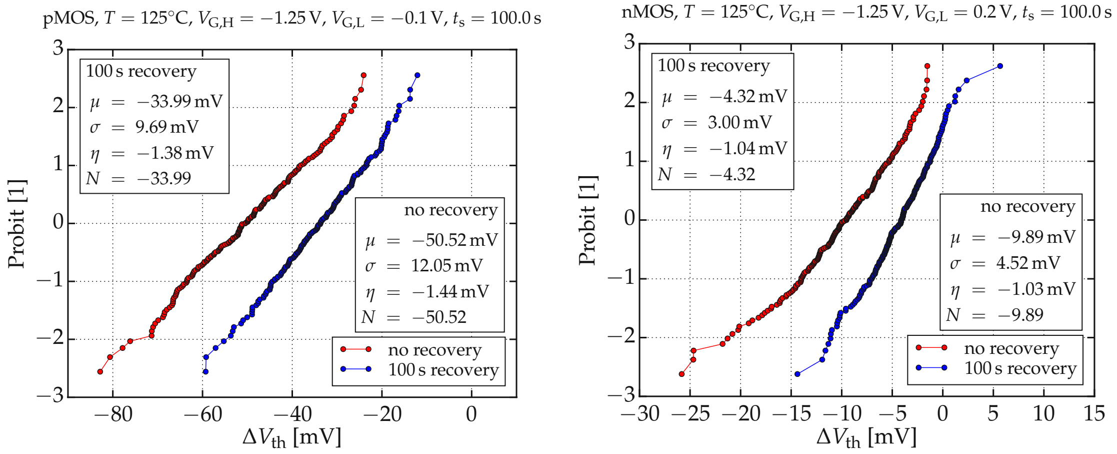

FIGURE 5.29: The same as in Fig. 5.27 but for 189 pFinFETs (left) and 227 nFinFETs (right) after 100 s of NBTI stress ($V_G = -1.25\,V$ and $T = 125°C$). At these stress conditions, the degradation of pFinFETs is dominated by defects in SiO_2. The largest values for η are obtained, in agreement with the simulations, see Fig. 5.25. *Tech. C2*.

5.6 Full BTI of High-κ Devices

After understanding the contributions of the recoverable and the quasi-permanent component on plain SiO_2 devices (see Section 5.4) and verifying the origin of the recoverable component in high-κ devices (see Section 5.5) we will now investigate the total degradation of high-κ devices. For this, the NBTI and PBTI responses of a commercial 28 nm high-κ technology (*Tech. B*) will be studied, the defect distributions will be extracted with Comphy, and the lifetime projections will be compared to power law extrapolations.

5.6.1 Experimental Data

For the extraction of the parameters of *Tech. B* with Comphy, conventional eMSM measurements were conducted: On pMOSFETs, the NBTI response was recorded for two stress voltages and two temperatures with a measurement delay of 10 ms, stress times between 0.1 s and 6.3 ks, and recovery times of up to 5 ks. Similarly, on nMOSFETs, the PBTI response was recorded, but with three stress voltages and with extended stress and recovery times up to ≈ 100 ks. In order to verify the lifetime projection with Comphy, further experiments were conducted at PBTI conditions with $V_G = 1.8\,V$ and $T = 25°C$, complementing the eMSM data:

- MSM experiments with ultra fast $I_D V_G$ measurements after the stress phase with stress times starting from 10 µs and a measurement delay of 1 µs.
- To extend the eMSM data for longer stress times, an nMOSFET was measured for three months of stress, interrupted by short $I_D V_G$ measurements to monitor V_{th}.

5.6.2 Parameter Extraction with Comphy

Similar to the optimization described in Section 5.4, Comphy was calibrated to the eMSM data for PBTI and NBTI. This was done for pMOSFETs and nMOSFETs simultaneously with the *same* defect parameters to ensure unified modeling of BTI: Since the processing of the oxide for p and nMOSFETs is similar for *Tech. B*, physical defects with the same properties must explain BTI in both types of devices consistently. In line with the study presented in Section 5.5, the defects which constitute NBTI on pMOSFETs were found to be inactive at PBTI conditions on nMOSFETs. Vice versa, the defects extracted on nMOSFETs of *Tech. B* were found to not contribute to NBTI on pMOSFETs. Note that the latter depends on the exact alignment of the trap levels to Fermi energies, hence, there can be a minor interplay for some technologies at elevated stress conditions, see Section 5.5.

In summary NBTI on pMOSFETs was found to be governed by

- defects in SiO_2 with a deep trap level (dominant),
- defects in HfO_2 with a deep trap level (minor), and
- quasi-permanent degradation

PBTI on nMOSFETs was found to be governed by

- defects in SiO_2 with a shallow trap level (minor) and
- defects in HfO_2 with a shallow trap level (dominant)

In Comphy simulations of this technology, the oxide is considered to be the same for n and pMOSFETs and all five types of defects were considered at all times, accordingly. The band diagrams in Fig. 5.30, left, show the dominant defect types for the respective devices.

The eMSM data, together with the Comphy simulations considering all five types of defects is shown in Fig. 5.30, right. For small ΔV_{th} the log-log plots bring out minor deviations after PBTI stress. This is probably related to deviations of the capture cross sections, tunneling mass, and other oxide material parameters of *Tech. B* which, for simplicity and consistency of the presented Comphy studies, were assumed to be the same across *all technologies* (see Section 5.1).

5.6.3 Lifetime Extrapolation

In this subsection, the lifetime simulated with Comphy is compared to simple power law extrapolations. Despite the quantitative difference of these two approaches, which will be discussed in the following, it should be noted that the power law description is a very useful tool as such: Despite its simplicity, it often gives reasonable estimates for the lifetime of devices. However, it will be elaborated that an unambiguous extraction of the power law time dependence n does not exist, making lifetime extrapolations vague. Throughout the discussion of these details one should keep in mind the substantial difference between simulations with Comphy and the power law extrapolations: Physical simulations with Comphy allow for exploration, which is not only limited to arbitrary AC and DC stress signals in both temperature and voltage; Even impacts of processes and gate stack engineering is inherently captured with this approach [GRJ2].

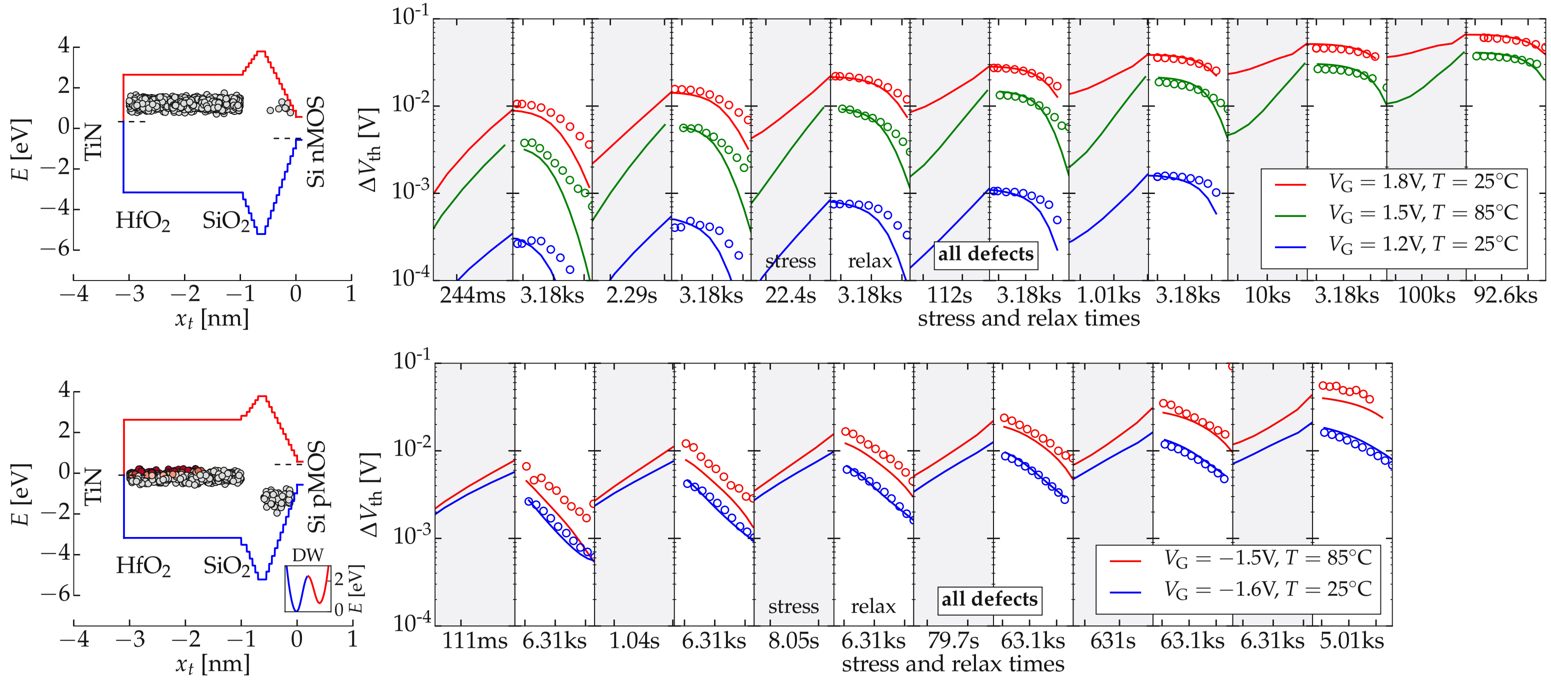

FIGURE 5.30: The PBTI response of nMOSFETs (top right) and the NBTI response of pMOSFETs (bottom right) of the commercial 28 nm high-κ technology (*Tech. B*). All simulations considered the same five distributions of defects. The dominant contributors at the respective stress conditions are depicted in the band diagrams, shown for flat band conditions (left). While PBTI is governed by defects in the HfO$_2$ layer with a shallow trap level, NBTI is governed by defects in the SiO$_2$ with deep trap levels and the quasi-permanent component which is described with the double-well model (inset showing CC diagram with the mean parameters). The degradation (right) is presented on log-log plots where each phase is shown from 10 ms up to the duration given below. After [GRJ2].

PBTI Lifetime

The p and nMOSFETs of *Tech. B*, calibrated with the eMSM data as described above, are now used to simulate PBTI and NBTI for stress times from µs up to 10 years. First, PBTI will be investigated. Here we have recorded additional measurement data to complement the eMSM experiment, see Subsection 5.6.1. The resulting measurement data spans 12 decades in time and is in good agreement with the Comphy simulations, see Fig. 5.31. Furthermore, PBTI for the other temperatures and stress voltages is captured well with the *same set of oxide defects*. For these simulations, it is important to account for the reduction of the electric field due to the oxide charges in a self-consistent manner, see Subsection 4.1.5. Thus, the SCP mode is used in the Comphy simulations. For NBTI as well as for PBTI a power law time dependence of $n = 0.16$ is frequently suggested [182]. As shown in Fig. 5.31, left, such a power law extrapolation describes the experimental data very well for stress times between 1 s and 1 ks, however, fails to describe the experimental data for shorter and longer stress times [GRJ2]. One could argue that the data for long stress times can be described with a smaller n, and in fact, the Comphy simulations may slightly overestimate the saturation for very long stress times. However, again, this is rather an issue of slight deviations of the general oxide material parameters for *Tech. B* (see Section 5.1), and even the data for very long stress times exhibits some saturation (see Fig. 5.31, left). In order to quantify the deviations in the lifetime extrapolation of these two approaches, a 30 mV lifetime criterion is applied for both, Comphy simulations and power law extrapolations, see Fig. 5.31, right. For this, the calibrated nMOSFET was simulated in Comphy for various stress voltages. On this data, the power law was fitted between $t_s = 0.1$ s and 100 s which yields roughly $n = 0.16$, see Fig. 5.31, left. In general, the extrapolation with the power-law underestimates the lifetime, compared to the prediction with Comphy.

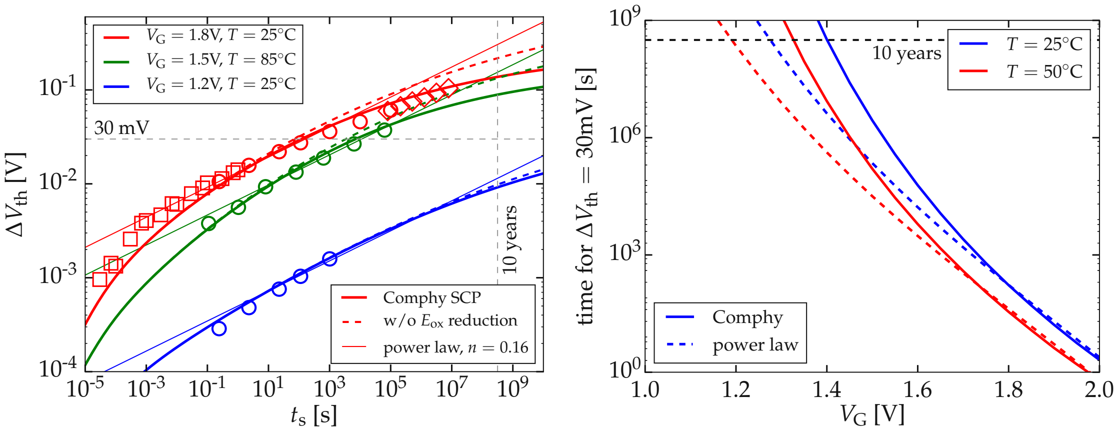

FIGURE 5.31: PBTI lifetime analysis of high-κ nMOSFETs. Left: The first recovery points of the eMSM traces (circles) presented in Fig. 5.30, top, are plotted as a function of the stress t_s together with the data from fast MSM measurements (squares, measurement delay of 1 µs) and a three months stress study (diamonds). The Comphy simulations, considering the reduction of the electric field self-consistently in the SCP mode (thick lines), reproduce the data for all 12 decades in time and for different temperatures and stress voltages with the *exactly same model parameters*. The power law extrapolation is plotted as a reference with the frequently suggested $n = 0.16$ [182] which describes the data well for moderate stress times but fails to describe the data for short and long stress times. Right: The lifetime with a 30 mV criterion as a function of the gate voltage for two temperatures, reflecting the deviation of the power law extrapolation (dashed lines) from to the Comphy simulations (solid lines) due to the non-linear increase of ΔV_{th} on log-log plots for long stress times. *Tech. B*. After [GRJ2].

NBTI Lifetime

Similar to the analysis of PBTI above, we will now investigate the lifetime predictions of Comphy for NBTI stress on the previously calibrated pMOSFET devices of *Tech. B* and compare it to estimates with the power law description. One major difference between NBTI and PBTI on high-κ technologies lies in the recovery behavior, visible in Fig. 5.30: PBTI is governed by defects in the HfO_2 whose minimal time constants are larger compared to defects in SiO_2 which are mainly responsible for NBTI. As a consequence, there is no substantial recovery immediately after PBTI stress, while NBTI is known to recovery already after nanoseconds [76]. Accordingly, the simple estimate of the degradation during stress by taking the first recovery point of eMSM measurements as done for PBTI (see Fig. 5.31) is not possible for NBTI. Conveniently, the full eMSM measurement procedure can be simulated with Comphy, including the recovery phases and the measurement delay. This allows reconstructing the degradation during NBTI stress from the data as shown in Fig. 5.32, left. The ambiguity of the extracted power law time dependence n can be demonstrated based on these observations: While the real degradation at NBTI stress can never be measured directly with these techniques [76], the n obtained from MSM data strongly depends on the measurement delay, see Fig. 5.32, right. This was experimentally verified in the literature [24, 25].

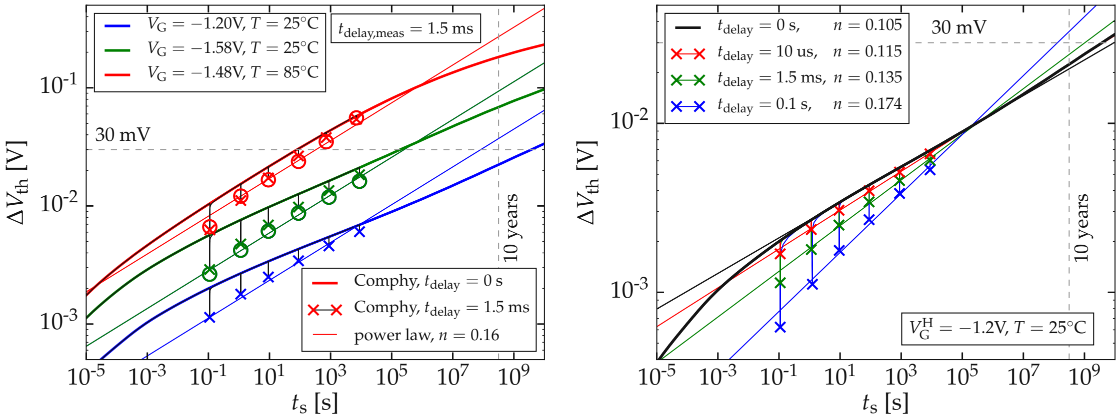

FIGURE 5.32: NBTI lifetime analysis of high-κ pMOSFETs. Left: Due to the fast recovery after NBTI stress with an onset in the sub nanoseconds regime [76], the eMSM data (circles) is not a valid estimate of the degradation during stress. However, the simulation of the full measurement procedure with Comphy including the measurement delay (crosses) enables a reconstruction of the degradation during stress (thick lines) based on eMSM data. While a simple power law extrapolation with $n = 0.16$ [182] would have been obtained from the data with the measurement delay, this is obviously not the *real* power law time dependence of the device. Right: The dependence of the extracted n on the measurement delay is demonstrated based on NBTI simulations. The extracted power law time dependence varies between $n \approx 0.1$ for zero measurement delay and $n \approx 0.17$ if measured with a delay of 0.1 s. *Tech. B*. After [GRJ2].

Same as for PBTI we now can apply a 30 mV lifetime criterion to compare the results from Comphy simulations with the estimations from power law extrapolations. The latter is again obtained by fitting to the simulated data for stress times between 0.1 s and 100 s. This gives roughly $n = 0.16$ for a measurement delay of 1 ms and, coincidentally, in a very good agreement with Comphy simulations, see Fig. 5.33.

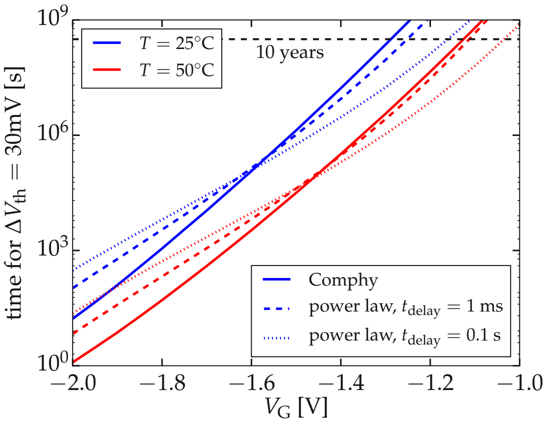

FIGURE 5.33: The NBTI lifetime of high-κ pMOSFETs with a 30 mV criterion as a function of the gate voltage for two temperatures. The results from simulations with Comphy (solid lines) are compared to power law extrapolations based on data with 0.1 s (dotted lines) and 1 ms recovery (dashed lines). The latter corresponds roughly to $n = 0.16$ and is in good agreement with the Comphy simulations. However, extrapolations based on data with longer measurement delay gives pessimistic lifetime estimations. *Tech. B*. After [GRJ2].

5.7 Gate Stack Engineering and Anomalous BTI

With the Comphy framework fully established and verified above, we now will investigate different process splits of *Tech. D*. This technology targets the peripheral logic in DRAM chips and is quite different compared to the usual logic technologies because of the distinct DRAM processing flows with a thick ISSG SiO_2 oxide. The study of *Tech. D* is interesting for two reasons: First, we will verify that the physical modeling approach presented in the previous sections can be applied to this kind of devices and we will investigate the differences of the extracted physical properties. Secondly, the direct comparison between the process splits of this technology (see Subsection 5.2.4) allows for a constrained analysis of the impact of the individual oxide layers on the degradation. In short, *Tech. D1* has a plain SiO_2 oxide, *Tech. D2* has a HfO_2 layer on top of the SiO_2 layer, *Tech. D3* has the same high-κ stack with an additional Al_2O_3 layer on top, and in *Tech. D4* the Al_2O_3 layer was selectively removed.

5.7.1 Experimental Data

The extraction of all defects parameters with Comphy will again be based on eMSM data. On *each* process split, we conduct efficient measurements for both, NBTI on pMOSFETs and PBTI on nMOSFETs: 12 cycles of eMSM with stress times ranging from $t_\mathrm{s} \approx 2.3$ s up to 1.3 ks and recovery times up to 100 s. About four different stress voltages are studied for each device with electric fields between 5 MV/cm and 10 MV/cm, all at $T = 125°\mathrm{C}$.

5.7.2 Investigation of PBTI

The defects parameters are extracted with Comphy for all devices as described in Subsection 5.1.1. First, we will study the properties of the plain SiO_2 process split of Tech. D (*Tech. D1*) to isolate the impact of the SiO_2 layer. In accordance with the study of SiO_2 at PBTI stress in Section 5.6, the degradation is found to be governed by pre-existing oxide defects with shallow trap levels. Since these defects have a low defect concentration, the degradation is quite small. Still, they have been already deduced from RTN [100] and BTI studies [181]. The corresponding measurement data and the simulations results for *Tech. D1* are shown in the top panel of Fig. 5.34.

The extraction of the defects in the SiO_2 oxide of the *Tech. D1* now allows analyzing the impact of the HfO_2 layer of the SiO_2 + HfO_2 process split of Tech. D (*Tech. D2*) more accurately because the additional low temperature ALD HfO_2 process of *Tech. D2* most probably barely affects the defects in SiO_2 with the shallow trap level. In line with the study of HfO_2 in Section 5.6, the additional HfO_2 layer *Tech. D2* substantially changes the PBTI response: A pronounced degradation is now observed which overshadows the impact of defects in SiO_2 and barely recovers, see Fig. 5.34. In fact, a slight *degradation* after long recovery can be observed. This phenomenon is more pronounced in *Tech. D3* and will be investigated in the following.

Three possible ways in which the very thin additional Al_2O_3 layer in *Tech. D3* can affect its PBTI behavior are discussed below:

- The Al_2O_3 layer itself is certainly not defect-free and, in general, charging of these defects will considerably contribute to PBTI. However, *Tech. D3* has a thick oxide and the electrostatic impact of the defects in the thin Al_2O_3 layer next to the gate is very small and, thus, will be neglected, see Eq. (3.65).
- The processing of the ALD Al_2O_3 layer could affect the defects in the rest of the oxide because of thermal activation and of diffusion of Al. This impact will be analyzed by comparing to *Tech. D4* were the Al_2O_3 layer is selectively removed and, in fact, minor deviations to *Tech. D3* are observed.
- The additional oxide layer inherently changes the device electrostatics and, most importantly, acts as a lever, *enhancing the difference between the trap level of defects in the* HfO_2 *and the Fermi level* of the gate for elevated stress voltages. For this, the permittivity of the Al_2O_3 layer between the gate and the HfO_2 is crucial.

The last point is completely inherent and consistently covered in Comphy and its impact can be simulated straightforward. As shown in Fig. 5.35, the change of the alignment of trap levels and Fermi energy enhances *hole capture from the gate* during stress, in addition to the usually observed *electron capture from the channel* during PBTI stress. These holes are released in subsequent recovery phases, causing an anomalous positive shift of ΔV_{th}. This observation is in perfect agreement with the work of TOLEDANO-LUQUE *et al.* which found *anomalous PBTI* (see Subsection 1.1.6) to be “due to charge exchange between the high-k layer and the metal gate” [32].

5.7.3 Investigation of NBTI

In the same way as for PBTI in the previous subsection, we will now extract and investigate the defects which constitute *NBTI* on pMOSFETs of the process splits of *Tech. D*.

For plain SiO_2 process split of Tech. D (*Tech. D1*), this extraction is straightforward, given the detailed study of NBTI of plain SiO_2 devices in Section 5.4. The resulting degradation with deep level defects, corresponding to the recoverable component due to pre-existing defects, and with double-well defects for the quasi-permanent component is presented in Fig. 5.36.

Following the same reasoning as in the previous subsection, also for NBTI the additional layer in the *Tech. D2* is considered to give a roughly independent additional component to the total degradation. However, the defects in HfO_2 barely affect the degradation of *Tech. D2*, except from a very small *positive* shift of V_{th} during NBTI stress.

Finally, also the observations of NBTI on SiO_2 + HfO_2 + Al_2O_3 process split of Tech. D (*Tech. D3*) are consistent with the PBTI study: The additional Al_2O_3 layer enhances the effect of the *positive* shift of V_{th} during NBTI stress. Here, this effect is mostly overshadowed by the degradation of defects in SiO_2, however, subtle degradation reversal is observed in the experimental data, see Fig. 5.38. This anomalous NBTI is due to *electron capture from the gate*.

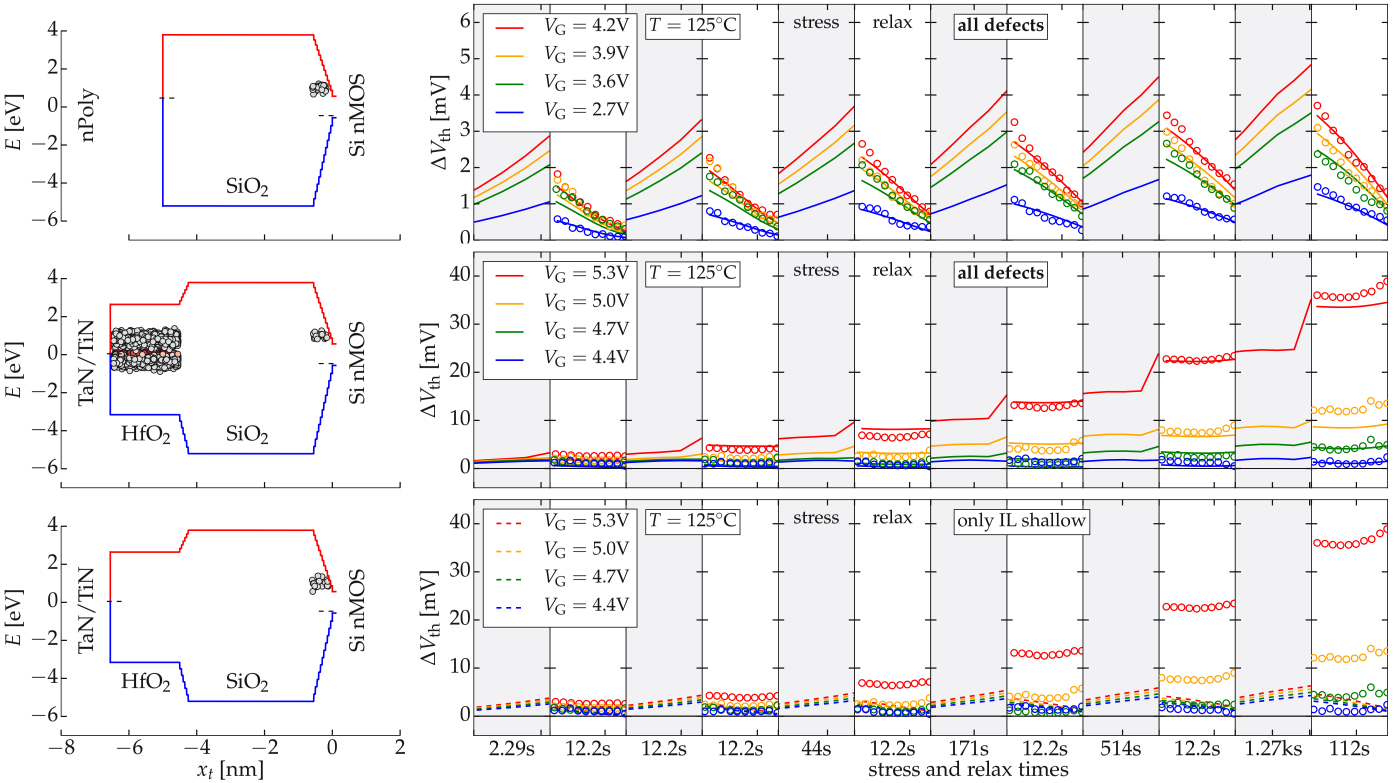

FIGURE 5.34: The PBTI response (right) of nMOSFETs of the plain SiO$_2$ process split of Tech. D (*Tech. D1*) (top panel) and the SiO$_2$ + HfO$_2$ process split of Tech. D (*Tech. D2*) (middle panel with all defects and bottom panel only with SiO$_2$ defects). The corresponding band diagrams are shown for flat band conditions (left). The defects in SiO$_2$ with shallow trap levels have a low defect concentration and give weak PBTI response on both, *Tech. D1* and *Tech. D2*. The high concentration of defects in HfO$_2$, on the other hand, amounts to considerable degradation which barely recovers, compare Section 5.6. The degradation (right) is presented on log-log plots where each phase is shown from 1 ms up to the duration given below. After [GRJ2].

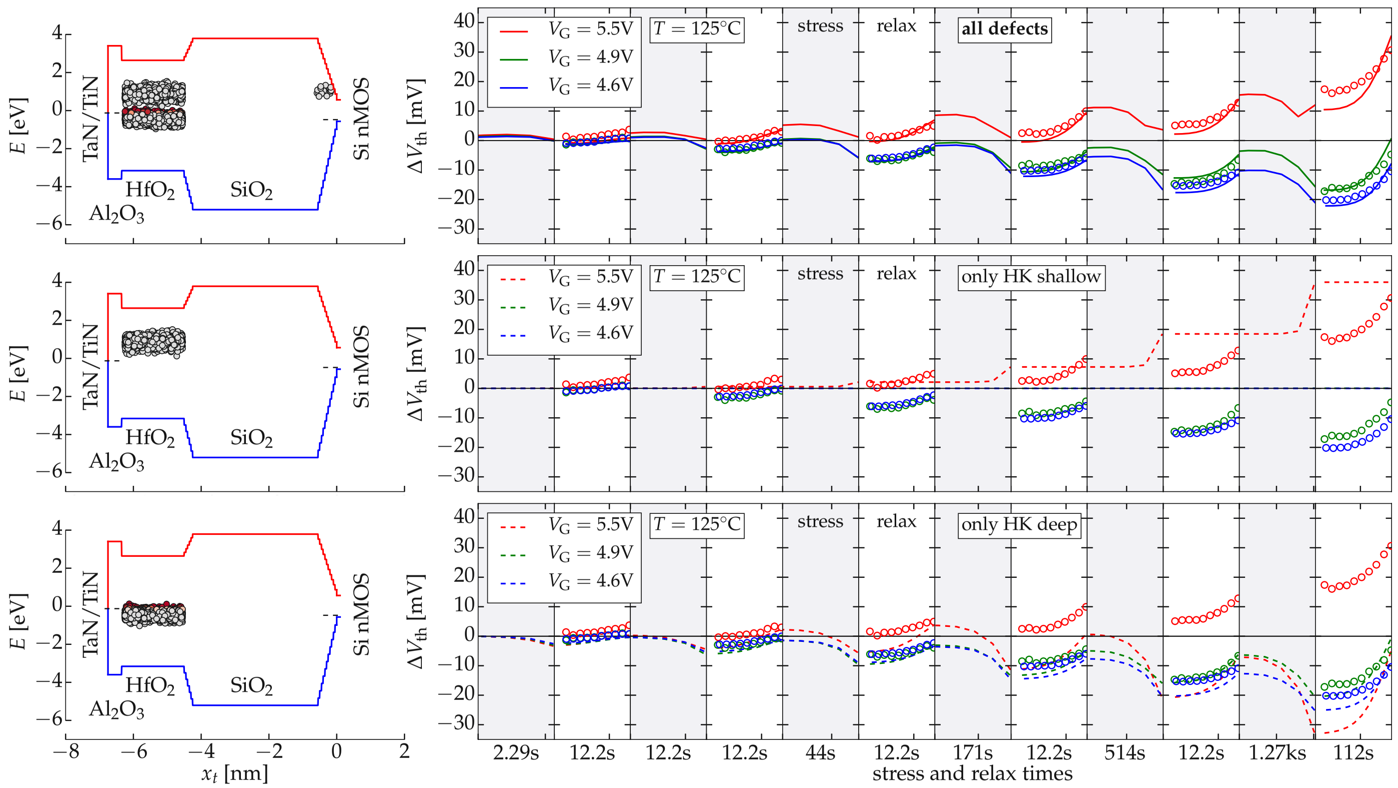

FIGURE 5.35: The PBTI response (right) of nMOSFETs of the SiO$_2$ + HfO$_2$ + Al$_2$O$_3$ process split of Tech. D (*Tech. D3*). The two dominant contributions to the the total degradation (top panel) come from defects in HfO$_2$ and cause *anomalous PBTI* at moderate stress voltages: Defects with shallow trap levels (middle panel) induce a regular positive shift of V_{th} due to electron trapping from the channel at elevated stress voltages. Vice versa, defects with deep trap levels induce a negative shift because of hole capture from the gate during PBTI stress. The corresponding band diagrams are shown for flat band conditions (left). The degradation (right) is presented on log-log plots where each phase is shown from 1 ms up to the duration given below. After [GRJ2].

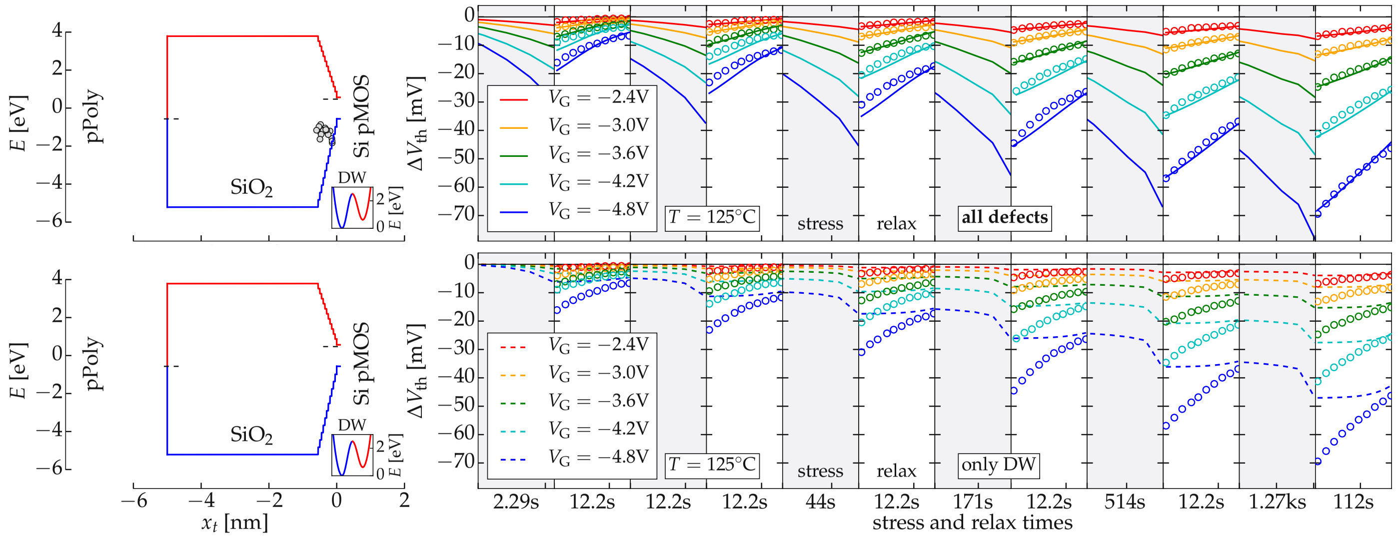

FIGURE 5.36: The NBTI response (right) of pMOSFETs of the plain SiO$_2$ process split of Tech. D (*Tech. D1*). The total degradation (top panel) comprises contributions from defects with deep trap levels, usually associated with the recoverable component of NBTI, complemented by the quasi-permanent part described by the double-well model (lower panel). The corresponding band diagrams are shown for flat band conditions (left) with the CC diagram representing the mean parameters of the double-well model in the inset. After [GRJ2].

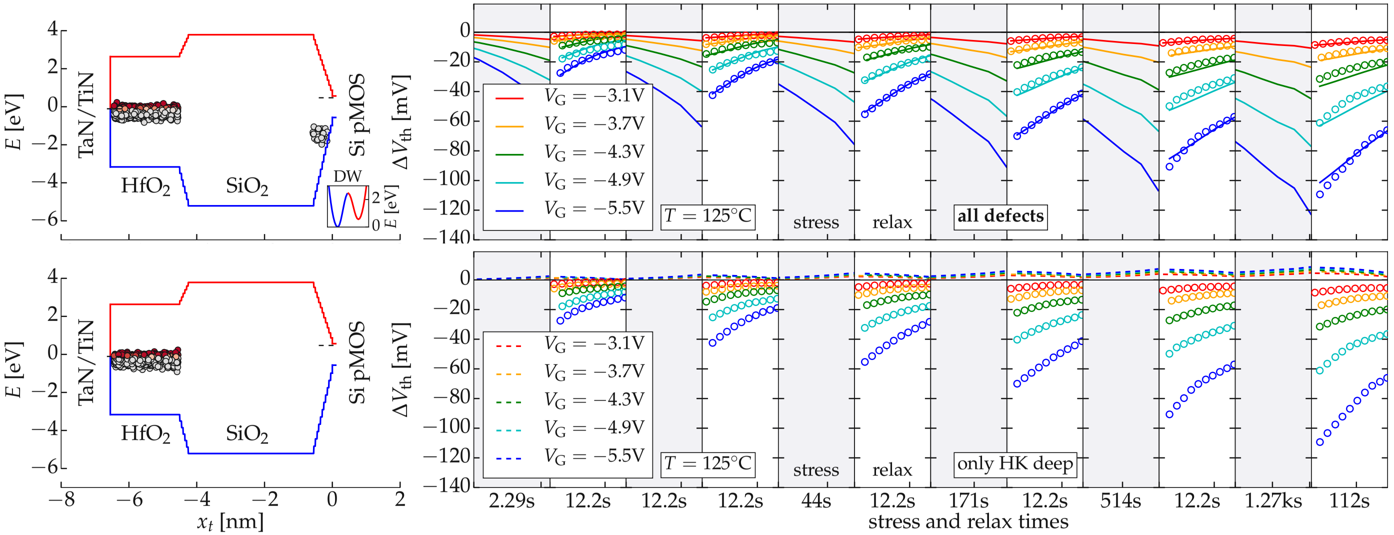

FIGURE 5.37: The NBTI response (right) of pMOSFETs of the SiO$_2$ + HfO$_2$ process split of Tech. D (*Tech. D2*). In addition to the degradation due to defects in SiO$_2$ (see Fig. 5.36), the total degradation (top panel) comprises a *positive* shift during NBTI stress because of defects in HfO$_2$ (bottom panel). This abnormal degradation is due to the interaction of these defects with the gate. The corresponding band diagrams are shown for flat band conditions (left) with the CC diagram representing the mean parameters of the double-well model in the inset. After [GRJ2].

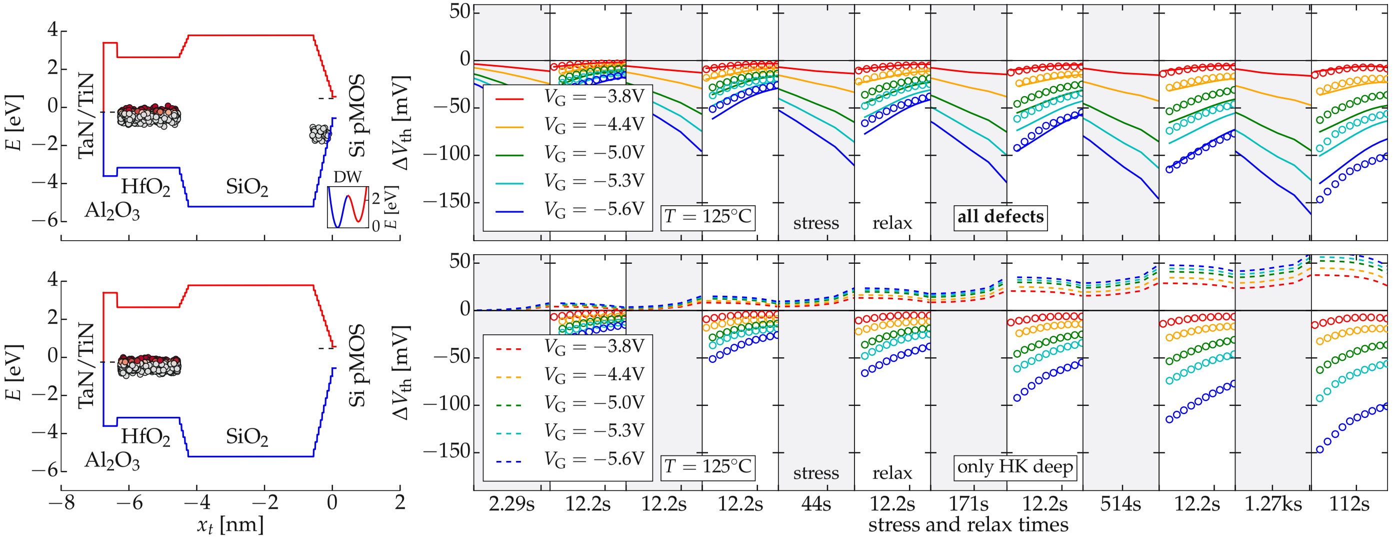

FIGURE 5.38: The NBTI response (right) of pMOSFETs of the SiO_2 + HfO_2 + Al_2O_3 process split of Tech. D (*Tech. D3*). The total degradation is shown (top panel) as well as the contribution of defects in HfO_2 (bottom panel). Compared to *Tech. D2*, the additional Al_2O_3 layer acts as a lever in the same way as for PBTI: it enhances the difference of the trap level of the defects in HfO_2 to the Fermi level of the gate. Thus, these defects can capture electrons during NBTI stress, causing an abnormal shift of V_{th} towards positive voltages. Note the subtle *anomalous NBTI* in the experimental data in the last recovery trace at $V_G = -3.8$ V. The corresponding band diagrams are shown for flat band conditions (left) with the CC diagram representing the mean parameters of the double-well model in the inset. After [GRJ2].

5.7.4 Summary and Lifetime

In this section, it was elaborated that the pronounced anomalous BTI seen in *Tech. D3* is due to the favorable alignment of the trap levels to the Fermi level of the gate, induced by the Al_2O_3 layer rather than due to diffusion of aluminum in the oxide. In line with the discussion in Subsection 5.7.2, the experimental data of the *Tech. D4* corroborates the favorable alignment in energy as the underlying cause: After selective removal of the Al_2O_3 layer, the anomalous BTI is reverted, see Fig. 5.39. This is in perfect agreement with the Comphy simulations with consistent defect parameters across all splits of *Tech. D*, see Section 5.1 and Tables 5.4 and 5.5. Note that the impact of charges in the Al_2O_3 itself as the responsible mechanism was excluded for electrostatic reasons, see Subsection 5.7.2.

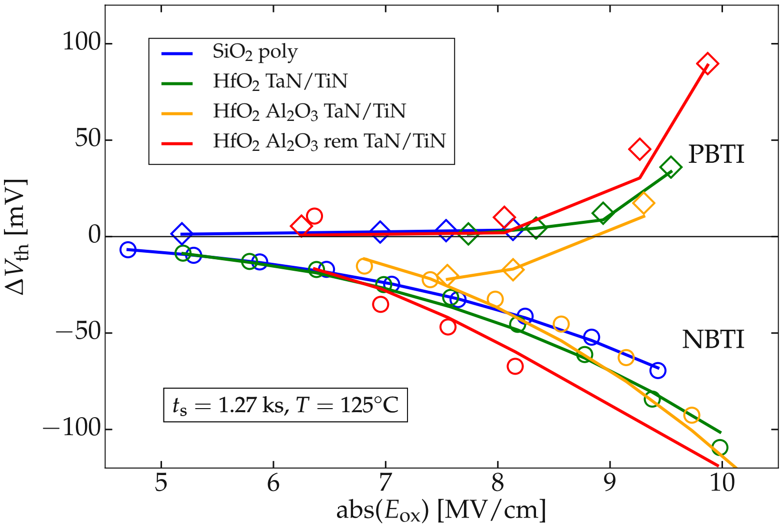

FIGURE 5.39: The measured (symbols) and simulated (lines) degradation after NBTI (circles) and PBTI (diamonds) stress. PBTI is typically negligible for plain SiO_2 technologies such as *Tech. D1* (blue). For the investigated high-κ technologies *Tech. D2* (green), *Tech. D3* (orange), and *Tech. D4* (red), PBTI is weak up to elevated oxide fields of ≈ 9 MV/cm which facilitate electron capture of HfO_2 defects in the Fowler-Nordheim tunneling regime. *Anomalous BTI* is apparent as *Tech. D3* shows the smallest degradation for oxide fields of around 8 MV/cm and in the case of PBTI even becomes negative. After the selective removal of Al_2O_3 in *Tech. D4*, this behavior is reverted. After [GRJ2].

Finally, the lifetimes are simulated with the calibrated Comphy devices of *Tech. D* in the same way as presented in Section 5.6. A peculiar feature here is that *Tech. D3* shows good NBTI lifetime performance because some regular degradation is compensated by the anomalous electron trapping from the gate, see Fig. 5.40.

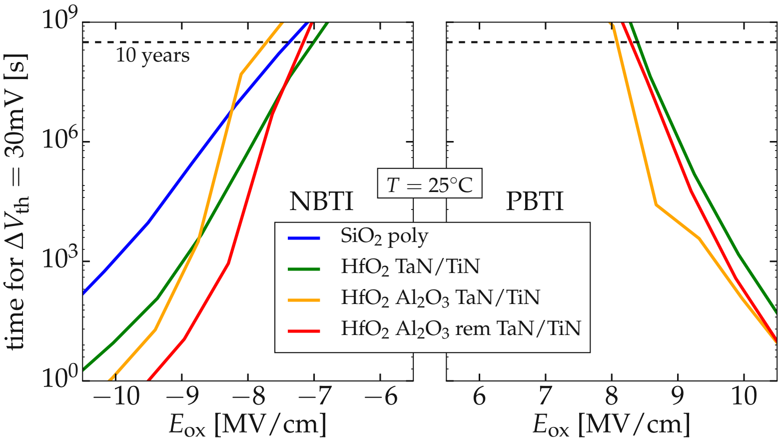

FIGURE 5.40: All splits of *Tech. D* meet the reliability target of 30 mV degradation after 10 years for oxide fields up to ≈ 7 MV/cm. For larger oxide fields, *Tech. D2* (green) and *Tech. D4* (red) show similar lifetimes. The lifetime of *Tech. D1* (blue) is beyond this scale for PBTI. Interestingly, *Tech. D3* shows the best NBTI lifetime because some hole trapping from the channel is compensated by electron trapping from the gate. After [GRJ2].

5.8 AC and Frequency Dependence

The simulations of arbitrary stress signals with Comphy is demonstrated here for a sawtooth signal which was measured on the commercial 130 nm SiON technology (*Tech. A*) and calibrated in in Section 5.4. As shown in Fig. 5.41, the measured degradation is well reproduced.

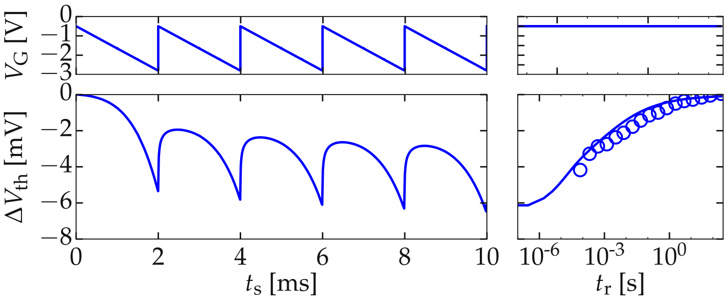

FIGURE 5.41: A sawtooth stress signal with a frequency of 500 Hz is applied on a pMOSFET of *Tech. A* for $t_s = 10$ ms (left) and the subsequent recovery (right) is measured (circles) and simulated (lines). After [GRJ2].

5.8.1 2-State Frequency Dependence

For periodic signals, a very efficient computation methodology was presented in Section 4.5 which allows to accurately simulate long-term BTI degradation with high-frequency AC stress. In Fig. 5.42, the stress data measured on pMOSFETs of *Tech. A* for frequencies in the range of 0.02 Hz up to 2 MHz is compared to the Comphy simulations. The trend for frequencies up to 2 kHz is well reproduced. In this range, the frequency dependence is dominated by charge trapping of the last stress period: For digital AC stress with the frequency f and a duty cycle of 0.5, the last stress phase is applied for $t_s = 1/(2f)$ before the measurement of ΔV_{th}. Thus, all defects with a capture time constant smaller than $\approx 1/(2f)$ will be charged which can constitute a considerable degradation in particular for NBTI with its fast capture and emission time constants.

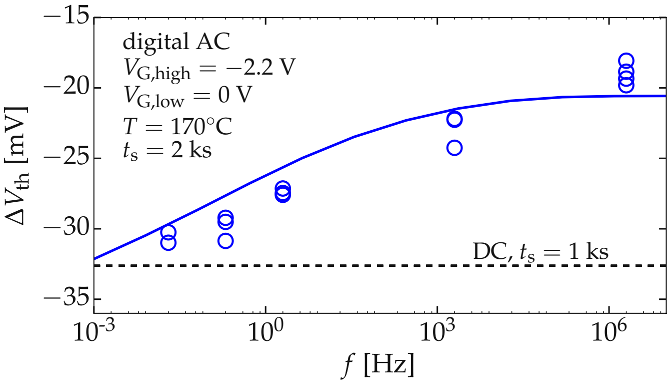

FIGURE 5.42: The frequency dependence of digital AC stress (first half period low, second half period high) measured on multiple pMOSFETs of *Tech. A* for each frequency f to reduce uncertainty due to device-to-device variability (circles). The Comphy simulations with the simple 2-state NMP model (line) reproduce the frequency dependence up to $f \approx 2\,\mathrm{kHz}$ well, but saturates above that. This indicates the additional frequency dependence due to metastable states which can be considered effectively in 2-state models. The degradation after DC stress is simulated and plotted as a reference (dashed line) with the same net stress time as for the AC experiments.

5.8.2 Effective 3-State Frequency Dependence

The observation of the frequency dependence for high frequencies in Fig. 5.42 is in line with other studies which support the mechanism of an inherent frequency dependence due to metastable states [173]. This mechanism is also important for correct modeling of the duty cycle dependence with its frequently reported “S-shape” [87, 90, 142]. The Comphy simulations of the pMOSFET device previously calibrated for *Tech. A*, now with the effective 3-state frequency dependence (see Subsection 4.3.4) using $\tau_{\mathrm{c}'} = 1\,\mathrm{ms}$ and $\tau_{\mathrm{e}'} = 1\,\mu\mathrm{s}$, gives a good agreement to the experimental duty cycle dependence of *Tech. A*, see Fig. 5.43.

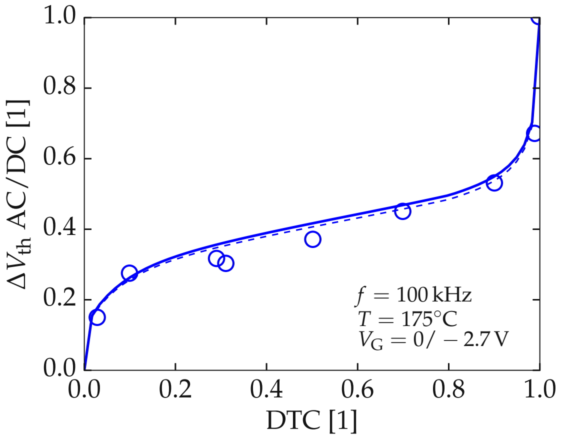

FIGURE 5.43: The relative degradation during NBTI AC stress as a function of the duty cycle DTC is simulated with the calibrated Comphy pMOSFETs (*Tech. A*) using the effective 3-state frequency dependence (lines) and compared to experimental data of the same technology [90]. The frequently reported “S-shape” is reproduced. Both, the degradation directly after stress (solid line) and the degradation considering the measurement delay of 1 µs (dashed line) are simulated. After [GRJ2].

5.9 Summary of the Results

The key findings of the studies presented in this chapter will be reviewed in the following. All defect distributions extracted with Comphy simulations are depicted in Fig. 5.44. The corresponding technology details and parameters which define the electrostatics are listed in Table 5.4. Finally, the full list of defect model parameters is presented in Table 5.5.

5.9.1 Defects Responsible for BTI

In total, five characteristic defect distributions were extracted, two of which in HfO_2 materials, two in SiO_2 materials, and one is ascribed to defects in the interfacial region of Si/SiO_2:

- In SiO_2, the dominant defects have deep trap levels.
- In addition, defects in SiO_2 with a shallow trap level and a low effective defect concentration were verified.
- In HfO_2, the dominant defects have shallow trap levels.
- In addition, defects in HfO_2 with a deep trap level were extracted. Due to their energy alignment, on Si technologies they only contribute to the degradation at particular conditions.
- More phenomenologically, a distribution of thermal transitions was determined and modeled with a field dependent double-well. This degradation is typically referred to as quasi-permanent and ascribed to defect generation, interface state depassivation, or defect transformation and is probably related to the relocation of hydrogen.

PBTI on Plain SiO_2 Technologies

Historically, less attention was paid to PBTI because of its negligible impact on plain SiO_2 technologies. Still, it was deduced from RTN studies [100] and reported at high stress fields [181]. Our calibrations show that the defects responsible for PBTI in SiO_2 layers have a shallow trap level which lies about 1 eV above the mid-gap of the Si channel. Its impact was clearly observed on *Tech. D1* because of the thick SiO_2 layer but mostly overshadowed by defects on HfO_2 on high-κ technologies.

NBTI on Plain SiO_2 Technologies

This phenomenon was already observed in 1967 [22] and intensively studied around the year 2000 where it became a severe reliability concern in scaled SiO_2 technologies. In line with earlier studies [GRC21], the responsible defects were identified with a defect level of about $-1.4\,\text{eV}$ with respect to the mid-gap of the Si channel. While these defects constitute the recoverable component of BTI, a pronounced quasi-permanent degradation is observed at NBTI conditions. Its contribution is captured well with simple thermal transitions with an empiric field dependence of the activation energies.

PBTI on High-κ Technologies

As opposed to plain SiO_2 technologies, the degradation at positive stress voltages can be more dominant on high-κ technologies compared to the degradation at negative stress voltages. The responsible defects are situated in the HfO_2 layer with defect levels of about 1 eV with respect to the mid-gap of the channel. The shallow defects in the interfacial SiO_2 layer of high-κ technologies barely contribute.

NBTI on High-κ Technologies

Same as for NBTI on plain SiO_2 technologies, defects in the SiO_2 layer with a deep trap level and the quasi-permanent component typically govern NBTI of high-κ technologies. Defects in the HfO_2 layer with a deep trap level can contribute, as discussed in the next subsection.

5.9.2 Anomalous BTI

An additional thin oxide layer which is adjacent to the gate and which has a lower permittivity compared to HfO_2 can enhance charge capture of defects in the HfO_2 layer. This is because of its effect on the energetic alignment of the Fermi level of the gate to the defects in the HfO_2 layer (see Subsection 1.1.6). The simulations with Comphy consistently describe this phenomenon as charge trapping of defects in HfO_2 with a deep trap level from the gate, see Section 5.7.

5.9.3 Lifetime Extrapolation

Simple lifetime assessments by linear extrapolation of degradation data on log-log plots may give reasonable estimates for particular technologies and stress conditions. However, such power law descriptions are prone to inaccurate determination of the time dependence n, in particular for NBTI, see Subsection 5.6.3 and cannot predict the lifetime of more involved technologies such as *Tech. D* where anomalous BTI is observed (see Subsection 5.7.4). Furthermore, this is an agnostic method while lifetime estimations in the design of more stable technologies require physical models.

5.9.4 Thermal Budget and Anneals

The impact of the thermal budget on the device properties can be manifold and is difficult to grasp precisely. For example, thermal anneals of oxide stacks were found to induce scavenging of the interfacial layer, strongly depending on the gate material during the anneal [183]. Still, some trends are apparent in the extracted defect bands as presented below.

Impact on Defects in HfO_2

In general, thermal anneals of high-κ stacks induce a positive shift of the effective trap level of defects in the HfO_2 layer [GRC2]. Consistently, the mean trap level of the shallow defects in HfO_2 of *Tech. B* and *Tech. D4* is about 0.35 eV higher compared to the technologies without a PDA, see Table 5.5.

Impact on Defects in SiO_2

Quite the opposite to HfO_2, the thermal anneal does have an impact on the defect concentration of the pre-existing defects in SiO_2 but does not substantially change their trap level. The technologies with an ISSG SiO_2 layer (*Tech. D*) have a very low concentration of defects with deep trap levels which is increased after the PDA (*Tech. D4*), approaching the high values obtained for technologies with annealed RTO oxides. The role of hydrogen remains speculative at this point and has to be elaborated.

5.9.5 Diffusion of Aluminum

The diffusion of Al into the HfO_2 layer during an anneal was demonstrated for a technology very similar to *Tech. D* [177]. The comparison of *Tech. B* and *Tech. D4* indicates that the Al, which remains in the HfO_2 layer of *Tech. D4* after the selective removal, induces a decrease of defects densities with a shallow trap level and an increase of defects densities with a deep trap level.

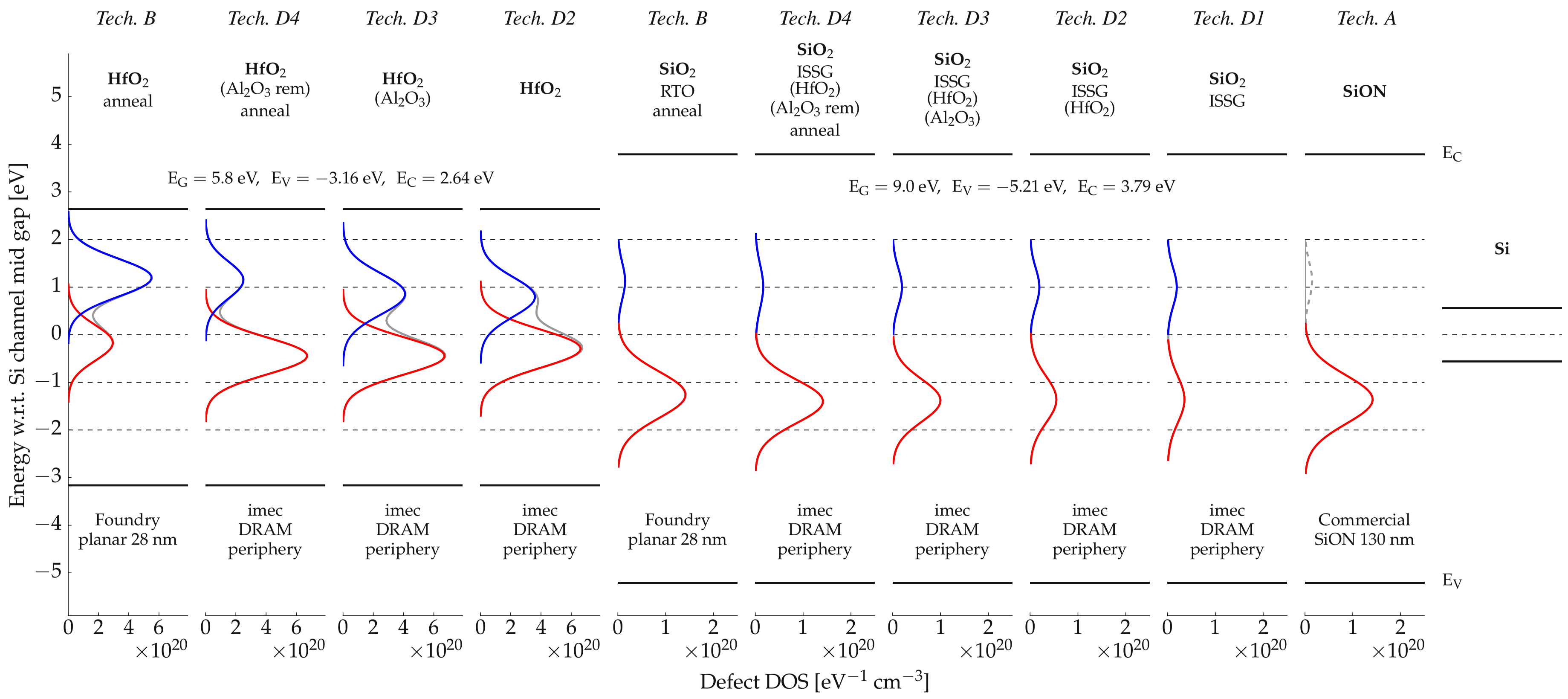

FIGURE 5.44: Four characteristic oxide defect distributions have been extracted in this chapter, two in HfO$_2$ and two in SiO$_2$. Typically, NBTI is governed by the defects in SiO$_2$ with deep trap levels and PBTI is governed by defects in HfO$_2$ with shallow trap levels. Considering all four defect distributions in physical simulations allows to understand, accurately reproduce, and predict the degradation of MOS devices for various stress conditions. After [GRJ2].

TABLE 5.4: Technologies simulated with Comphy and the parameters used to describe their *electrostatics* [GRJ2].

			Tech. A Commercial SiON 130 nm	*Tech. D1* imec DRAM periphery	*Tech. D2* imec DRAM periphery	*Tech. D3* imec DRAM periphery	*Tech. D4* imec DRAM periphery	*Tech. B* Foundry planar 28 nm
technology details	SiO_2		SiON	ISSG	ISSG	ISSG	ISSG	RTO
	HfO_2		-	-	✓	✓	✓	✓
	Al_2O_3		-	-	-	✓	removed	-
	PDA		-	-	-	-	✓	✓
	gate		poly	poly	TaN/TiN	TaN/TiN	TaN/TiN	TiN
	EOT	nm	1.43	5	4.94	5.07	4.9	1.41
	$V_{\mathrm{th},0}$ nMOS	V	-	0.375	0.952	1.25	1.11	0.438
	$V_{\mathrm{th},0}$ pMOS	V	-0.431	-0.469	-0.929	-0.759	-0.755	-0.404
	V_{fb} nMOS	V	-	-0.921	-0.516	-0.35	-0.464	-0.826
	V_{fb} pMOS	V	0.532	1.04	0.579	0.716	0.705	0.523
input parameters	N_{A} nMOS	cm^{-3}	-	2.8×10^{17}	5×10^{17}	6.77×10^{17}	6.77×10^{17}	1.59×10^{18}
	N_{D} pMOS	cm^{-3}	2×10^{17}	5.5×10^{17}	5.6×10^{17}	4.9×10^{17}	4.9×10^{17}	1.4×10^{17}
	$\Delta E_{\mathrm{W},0}$ nMOS	eV	-	-0.48	-0.06	0.114	0	-0.34
	$\Delta E_{\mathrm{W},0}$ pMOS	eV	0.1	0.581	0.12	0.261	0.25	0.1
	$x_{\mathrm{SiO_2}}$	nm	2.2	5	4.55	4.55	4.55	1
	$x_{\mathrm{HfO_2}}$	nm	-	-	2	1.8	1.8	2.1
	$x_{\mathrm{Al_2O_3}}$	nm	-	-	-	0.4	-	-

TABLE 5.5: Technologies simulated with Comphy and the parameters used to describe their *oxide degradation* [GRJ2].

			Tech. A Commercial SiON 130 nm	*Tech. D1* imec DRAM periphery	*Tech. D2* imec DRAM periphery	*Tech. D3* imec DRAM periphery	*Tech. D4* imec DRAM periphery	*Tech. B* Foundry planar 28 nm
shallow SiO_2	N_T	cm^{-3}	-	1.93×10^{19}	1.93×10^{19}	1.93×10^{19}	1.65×10^{19}	1.5×10^{19}
	$\langle E_T\rangle \pm \sigma_{E_T}$	eV	-	0.998 ± 0.162	0.998 ± 0.162	0.998 ± 0.162	1.01 ± 0.218	1.13 ± 0.15
	$\langle S\rangle \pm \sigma_S$	eV	-	4.93 ± 1.99	4.93 ± 1.99	4.93 ± 1.99	3.82 ± 1.36	3.82 ± 1.36
	R	1	-	0.437	0.437	0.437	0.407	0.407
deep SiO_2	N_T	cm^{-3}	1.42×10^{20}	3.54×10^{19}	5.5×10^{19}	1×10^{20}	1.42×10^{20}	1.42×10^{20}
	$\langle E_T\rangle \pm \sigma_{E_T}$	eV	-1.36 ± 0.26	-1.36 ± 0.24	-1.36 ± 0.24	-1.38 ± 0.2	-1.4 ± 0.21	-1.26 ± 0.24
	$\langle S\rangle \pm \sigma_S$	eV	7.95 ± 3.5	5.63 ± 2.67	5.63 ± 2.67	5.63 ± 2.67	5.63 ± 2.67	5.63 ± 2.67
	R	1	2.59	2.25	2.25	2.25	2.25	1.8
shallow HfO_2	N_T	cm^{-3}	-	-	3.61×10^{20}	4.11×10^{20}	2.5×10^{20}	5.52×10^{20}
	$\langle E_T\rangle \pm \sigma_{E_T}$	eV	-	-	0.794 ± 0.169	0.857 ± 0.189	1.15 ± 0.15	1.2 ± 0.156
	$\langle S\rangle \pm \sigma_S$	eV	-	-	6.98 ± 0.511	6.45 ± 0.34	6 ± 0.6	3.19 ± 0.77
	R	1	-	-	0.692	0.659	0.61	0.587
deep HfO_2	N_T	cm^{-3}	-	-	6.63×10^{20}	6.72×10^{20}	6.72×10^{20}	2.95×10^{20}
	$\langle E_T\rangle \pm \sigma_{E_T}$	eV	-	-	-0.292 ± 0.158	-0.444 ± 0.15	-0.444 ± 0.15	-0.17 ± 0.14
	$\langle S\rangle \pm \sigma_S$	eV	-	-	5.81 ± 1.74	3.55 ± 0.741	3.55 ± 0.741	6.5 ± 1.99
	R	1	-	-	1	1	1	0.514
double well	N_T	cm^{-2}	6.5×10^{13}	4.5×10^{13}	4.5×10^{13}	4.5×10^{13}	4.5×10^{13}	4.5×10^{13}
	$\langle \varepsilon_1\rangle \pm \sigma_{\varepsilon_1}$	eV	2.73 ± 0.43	2.51 ± 0.376	2.46 ± 0.376	2.34 ± 0.395	2.33 ± 0.376	2.32 ± 0.376
	$\langle \varepsilon_2\rangle \pm \sigma_{\varepsilon_2}$	eV	2.75 ± 0.7	1.9 ± 0.5	1.9 ± 0.5	1.9 ± 0.5	1.9 ± 0.5	1.77 ± 0.5
	k_0	s^{-1}	1×10^{13}	1×10^{13}	1×10^{13}	1×10^{13}	1×10^{13}	1×10^{13}
	γ	eV m/V	7×10^{-10}	4.8×10^{-10}	4.8×10^{-10}	4.5×10^{-10}	4.5×10^{-10}	6.8×10^{-10}

Chapter 6

Conclusions and Outlook

6.1 Conclusions

This thesis investigated recoverable BTI of MOS devices as a reaction-limited oxide charge trapping process within the NMP theory and employed a phenomenological model to describe the quasi-permanent component of BTI in two different frameworks:

- The full 4-state NMP model was implemented in a commercial TCAD software and complemented by field-dependent thermal transitions.
- The 2-state NMP model was implemented in a concise Python modeling framework called Comphy, short for "compact-physics" together with a simple double-well model.

While the former enabled the study of all details of charge trapping such as RTN and SILC, the latter is much more efficient and, thus, enabled the study of the physical defect properties of a broad range of technologies. In summary, with these two modeling frameworks we have achieved the following:

- RTN, SILC, and tunneling currents were verified to be consistent with BTI as they are all governed by charge trapping at oxide defects.
- We have extracted the characteristic oxide defect distributions in HfO_2 and SiO_2 oxides for several different processes and listed *all* parameters used in the Comphy simulations.
- *Unified* modeling of all four combinations of PBTI and NBTI on pMOS and nMOS devices was demonstrated.
- We have corroborated the correct lifetime prediction by experimental studies of commercial high-κ technologies which span 12 decades in stress time.
- Efficient implementations of AC simulations with arbitrary signals were discussed and demonstrated.
- We have verified and consistently modeled anomalous BTI due to charge trapping of oxide defects which interact with carriers in the gate of MOS devices.

Thus, this thesis contributes to a better understanding and a more efficient modeling of BTI. This can aid improvement of existing and development of future MOS technologies.

6.2 Outlook

A profound understanding of BTI was established in this work for devices with Si channels and SiO_2 and HfO_2 oxides. This physical foundation enables various studies in the still very complex field of BTI research.

6.2.1 Extensions of the Comphy Framework

The Comphy framework and the accurately verified physical parameters enable detailed modeling of the mean degradation during BTI stress. Extensions of this physical framework are straightforward to make it more versatile.

Physical Modeling of Quasi-Permanent BTI

In particular, the gate-sided hydrogen release model improved the physical understanding of the quasi-permanent component. Still, the defect creation, the depassivation of dangling bonds, and the transformation of oxide defects is not fully understood and Comphy uses a simple double-well model to capture these quasi-permanent contributions. Future studies should further elaborate the mechanisms which contribute to the quasi-permanent component of BTI in order to improve or replace the double-well model.

Modeling of CV Curves

CV curves comprise detailed information on defects and their time constants, in particular if they are recorded for various measurement frequencies. Modeling the capacitance of MOS devices and its distortion by defects is straightforward and should be implemented in Comphy.

Variability

A lot of work was done to understand the initial and the time-dependent variability of MOS devices with small effective gate areas. Both the device-to-device variability as well as the process dependent across-wafer variability is investigated in the literature. The modeling of single defects sampled in a Monte Carlo fashion enables Comphy to deal with variability. This should be elaborated in future studies.

Hot-Carrier Degradation

In actual circuits, a mixture of BTI and HCD is observed and their interplay is still controversial. Once the physical mechanisms which are responsible for HCD are fully established, the description could be incorporated into the Comphy framework to model the degradation for various drain voltages of MOSFETs.

6.2.2 Studies of Novel Materials and Structures

Novel technologies with 2D channel and oxide materials such as BP, MoS_2, or hexagonal boron nitride (h-BN) as well as devices with novel geometries such as nanowires suffer from severe charge trapping. On the other hand, several technologies are designed to exploit these degradation mechanisms, for example, resistive random-access memories (RRAMs) and physical unclonable functions (PUFs). The results presented in this thesis may contribute to a successful transfer of the knowledge gathered on Si technologies to these new applications.

Bibliography

[1] W. Schottky. “Small-Shot Effect and Flicker Effect”. In: *Physical Review* 28.1 (1926), pp. 74–103.

[2] R.L. Petritz. “On the Theory of Noise in P-N Junctions and Related Devices”. In: *Proceedings of the IRE* 40.11 (1952), pp. 1440–1456.

[3] M.J. Uren, D.J. Day, and M.J. Kirton. “1/F and Random Telegraph Noise in Silicon Metal-Oxide-Semiconductor Field-Effect Transistors”. In: *Appl.Phys.Lett.* 47.11 (1985), pp. 1195–1197.

[4] M.J. Uren, M.J. Kirton, and S. Collins. “Anomalous Telegraph Noise in Small-Area Silicon Metal-Oxide-Semiconductor Field-Effect Transistors”. In: *Physical Review B* 37.14 (1988), pp. 8346–8350.

[5] M.E. Welland and R.H. Koch. “Spatial Location of Electron Trapping Defects on Silicon by Scanning Tunneling Microscopy”. In: *Appl.Phys.Lett.* 48.11 (1986), pp. 724–726.

[6] M.O. Andersson, Z. Xiao, S. Norrman, and O. Engström. “Model Based on Trap-Assisted Tunneling for Two-Level Current Fluctuations in Submicrometer Metal — Silicon-Dioxide — Silicon Diodes”. In: *Physical Review B* 41.14 (1990), pp. 9836–9842.

[7] C.M. Osburn and N.J. Chou. “Accelerated Dielectric Breakdown of Silicon Dioxide Films”. In: *J.Electrochem.Soc.* 120.10 (1973), pp. 1377–1384.

[8] R. Degraeve, G. Groeseneken, R. Bellens, M. Depas, and H.E. Maes. “A Consistent Model for the Thickness Dependence of Intrinsic Breakdown in Ultra-Thin Oxides”. In: *Proc. Intl.Electron Devices Meeting (IEDM)*. 1995, pp. 863–866.

[9] P. Olivo, T.N. Nguyen, and B. Riccó. “High-Field-Induced Degradation in Ultra-Thin SiO_2 Films”. In: *IEEE Trans.Electron Devices* 35.12 (1988), pp. 2259–2267.

[10] F. Crupi, R. Degraeve, A. Kerber, D.H. Kwak, and G. Groeseneken. “Correlation between Stress-Induced Leakage Current (SILC) and the HfO_2 Bulk Trap Density in a SiO_2/HfO_2 Stack”. In: *Proc. Intl.Rel.Phys.Symp. (IRPS)*. 2004, pp. 181–187.

[11] E. Cartier and A. Kerber. “Stress-Induced Leakage Current and Defect Generation in nFETs with HfO_2/TiN Gate Stacks During Positive-Bias Temperature Stress”. In: *Proc. Intl.Rel.Phys.Symp. (IRPS)*. 2009, pp. 486–492.

[12] D. Veksler, G. Bersuker, H. Park, C. Young, K. Y. Lim, W. Taylor, S. Lee, and H. Shin. “The Critical Role of the Defect Structural Relaxation for Interpretation of Noise Measurements in MOSFETs”. In: *Proc. Intl.Integrated Reliability Workshop*. 2009, pp. 102–105.

[13] L. Larcher, A. Paccagnella, and G. Ghidini. “A Model of the Stress Induced Leakage Current in Gate Oxides”. In: *IEEE Trans.Electron Devices* 48.2 (2001), pp. 285–288.

[14] S.A. Abbas and R.C. Dockerty. “Hot-Carrier Instability in IGFET’s”. In: *Appl.Phys.Lett.* 27.3 (1975), pp. 147–148.

[15] T.H. Ning, P.W. Cook, R.H. Denard, C.M. Osburn, S.E. Schuster, and H.N. Yu. “1 µm MOSFET VLSl Technology: Part IV - Hot-Electron Design Constraints”. In: *IEEE Trans.Electron Devices* ED-26.4 (1979).

[16] C. Hu, S.C. Tam, F.C. Hsu, P.K. Ko, T.Y. Chan, and K.W. Terrill. “Hot-Electron-Induced MOSFET Degradation—Model, Monitor, and Improvement”. In: *IEEE Trans.Electron Devices* 32.2 (1985), pp. 375–385.

[17] S. Tyaginov and T. Grasser. “Modeling of Hot-Carrier Degradation: Physics and Controversial Issues”. In: *Proc. Intl.Integrated Reliability Workshop* (2012), pp. 206–215.

[18] A. Coblenz and H.L. Owens. “Variation of Transistor Parameters with Temperature”. In: *Proceedings of the IRE* 40.11 (1952), pp. 1472–1476.

[19] G.G. Harman and R.L. Raybold. “Direct Observation of Charge Storage in the Surface States of Silicon”. In: 34.2 (1963), pp. 380–383.

[20] J.E. Thomas and D.R. Young. “Space-Charge Model for Surface Potential Shifts in Silicon Passivated with Thin Insulating Layers”. In: *IBM Journal of Research and Development* 8.4 (Sept. 1964), pp. 368–375.

[21] Y. Miura and Y. Matukura. “Investigation of Silicon-Silicon Dioxide Interface Using MOS Structure”. In: *Jap.J.Appl.Phys.* 5 (1966), p. 180.

[22] B.E. Deal, M. Sklar, A. S. Grove, and E. H. Snow. “Characteristics of the Surface-State Charge (Qss) of Thermally Oxidized Silicon”. In: *J.Electrochem.Soc.* 114.3 (1967), p. 266.

[23] X. Federspiel, M. Rafik, D. Angot, F. Cacho, and D. Roy. “Interaction Between BTI and HCI Degradation in high-κ Devices”. In: *Proc. Intl.Rel.Phys.Symp. (IRPS)* (2013), pp. 1–4.

[24] M. Ershov, R. Lindley, S. Saxena, A. Shibkov, S. Minehane, J. Babcock, S. Winters, H. Karbasi, T.Yamashita, P. Clifton, and M. Redford. “Transient Effects and Characterization Methodology of Negative Bias Temperature Instability in pMOS Transistors”. In: *Proc. Intl.Rel.Phys.Symp. (IRPS)*. 2003, pp. 606–607.

[25] D.K. Schroder. “Negative Bias Temperature Instability: What Do We Understand?” In: *Microelectronics Reliability* 47.6 (2007), pp. 841–852.

[26] V. Huard. “Two Independent Components Modeling for Negative Bias Temperature Instability”. In: *Proc. Intl.Rel.Phys.Symp. (IRPS)*. May 2010, pp. 33–42.

[27] T. Grasser, Th. Aichinger, H. Reisinger, J. Franco, P.-J. Wagner, M. Nelhiebel, C. Ortolland, and B. Kaczer. “On the ‘Permanent’ Component of NBTI”. In: *Proc. Intl.Integrated Reliability Workshop*. Oct. 2010.

[28] J.F. Zhang, C.Z. Zhao, A.H. Chen, G. Groeseneken, and R. Degraeve. “Hole Traps in Silicon Dioxides - Part I: Properties”. In: *IEEE Trans.Electron Devices* 51.8 (2004), pp. 1267–1273.

[29] V. Huard, M. Denais, and C. Parthasarathy. “NBTI Degradation: From Physical Mechanisms to Modelling”. In: *Microelectronics Reliability* 46.1 (2006), pp. 1–23.

[30] S.C. Chen, C.H. Chien, and J.C. Lou. “Impact of Charge Trapping Effect on Negative Bias Temperature Instability in P-MOSFETs with HfO_2/SiON Gate Stack”. In: *Journal of Physics: Conference Series* 100.4 (2008), p. 042045.

[31] R. O’Connor, V.S. Chang, L. Pantisano, L.Å. Ragnarsson, M. Aoulaiche, B. O’Sullivan, and G. Groeseneken. “Anomalous Positive-Bias Temperature Instability of High-κ/Metal Gate Devices with Dy_2O_3 Capping”. In: *Applied Physics Letters* 93.5 (2008), p. 053506.

[32] M. Toledano-Luque, B. Kaczer, M. Aoulaiche, A. Spessot, Ph J. Roussel, R. Ritzenthaler, T. Schram, A. Thean, and G. Groeseneken. "Analytical Model for Anomalous Positive Bias Temperature Instability in La-based HfO_2 nFETs Based on Independent Characterization of Charging Components". In: *Microelectronic Engineering* 109 (2013), pp. 314–317.

[33] A. Stesmans and V.V. Afanas'ev. *ESR of Interfaces and Nanolayers in Semiconductor Heterostructures*. Elsevier B.V., 2008, pp. 435–482.

[34] M.A. Jupina and P.M. Lenahan. "A Spin Dependent Recombination Study of Radiation Induced Defects at and Near the Si/SiO_2 Interface". In: *IEEE Trans.Nucl.Sci.* 36.6 (1989), pp. 1800–1807.

[35] S. Fujieda, M. Terai, M. Saitoh, A. Toda, Y. Miura, Z. Liu, Y. Teraoka, A. Yoshigoe, M. Wilde, and K. Fukutani. "Bias Temperature Instability Characterization of Advanced Gate Stacks". In: *ECS Trans.* 6.3 (2007), pp. 185–202.

[36] D.B. Williams and C.B. Carter. *Transmission Electron Microscopy*. Vol. 5. 1999, pp. 452–453.

[37] G. Binnig, H. Fuchs, C. Gerber, H. Rohrer, E. Stoll, and E. Tosatti. "Energy-Dependent State-Density Corrugation of a Graphite Surface as Seen by Scanning Tunneling Microscopy". In: *EPL (Europhysics Letters)* 1.1 (1986), p. 31.

[38] R.F.K. Herzog and F.P. Viehböck. "Ion Source for Mass Spectrography". In: *Physical Review* 76.6 (1949), pp. 855–856.

[39] G. Groeseneken, H.E. Maes, N. Beltran, and R.F. de Keersmaecker. "A Reliable Approach to Charge-Pumping Measurements in MOS Transistors". In: *IEEE Trans.Electron Devices* 31.1 (1984), pp. 42–53.

[40] D.J. Fitzgerald and A.S. Grove. "Surface Recombination in Semiconductors". In: *Surf.Sci.* 9.July (1968), pp. 347–369.

[41] A. Neugroschel, C.-T. Sah, K.M. Han, M.S. Carroll, T. Nishida, J.T. Kavalieros, and Y. Lu. "Direct-Current Measurements of Oxide and Interface Traps on Oxidized Silicon". In: *IEEE Trans.Electron Devices* 42.9 (1995), pp. 1657–1662.

[42] E.H. Nicollian and A. Goetzberger. "MOS Conductance Technique for Measuring Surface State Parameters". In: *Appl.Phys.Lett.* 7.8 (1965), pp. 216–219.

[43] P.V. Gray and D.M. Brown. "Densitiy of SiO_2-Si Interface States". In: *Appl.Phys.Lett.* 8.2 (1966), pp. 31–33.

[44] F. Schanovsky, W. Goes, and T. Grasser. "An Advanced Description of Oxide Traps in MOS Transistors and its Relation to DFT". In: *J.Comp.Elec.* 9.3-4 (2010), pp. 135–140.

[45] B. Tuttle and C.G. Van de Walle. "Structure, Energetics, and Vibrational Properties of Si-H Bond Dissociation in Silicon". In: *Physical Review B* 59.20 (1999), pp. 12884–12889.

[46] A. Stesmans. "Dissociation Kinetics of Hydrogen-Passivated P_b Defects at the $(111)Si/SiO_2$ Interface". In: *Physical Review B* 61.12 (2000), pp. 8393–8403.

[47] C.G. Van de Walle and B.R. Tuttle. "Microscopic Theory of Hydrogen in Silicon Devices". In: *IEEE Trans.Electron Devices* 47.10 (2000), pp. 1779–1786.

[48] E.H. Poindexter, G.J. Gerardi, M.-E. Rueckel, P.J. Caplan, N.M. Johnson, and D.K. Biegelsen. "Electronic Traps and P_b Centers at the Si/SiO_2Interface: Band-Gap Energy Distribution". In: *J.Appl.Phys.* 56.10 (1984), pp. 2844–2849.

[49] P.M. Lenahan and J.F. Conley Jr. “What Can Electron Paramagnetic Resonance Tell Us about the Si/SiO$_2$ System?” In: *J.Vac.Sci.Technol.B* 16.4 (1998), pp. 2134–2153.

[50] P.M. Lenahan and P.V. Dressendorfer. “Hole Traps and Trivalent Silicon Centers in Metal/Oxide/Silicon Devices”. In: *J.Appl.Phys.* 55.10 (1984), pp. 3495–3499.

[51] P.E. Blöchl and J.H. Stathis. “Aspects of Defects in Silica Related to Dielectric Breakdown of Gate Oxides in MOSFETs”. In: *Physica B* 273-274 (1999), pp. 1022–1026.

[52] A.M. El-Sayed, M.B. Watkins, T. Grasser, V.V. Afanas’ev, and A.L. Shluger. “Hydrogen Induced Rupture of Strained Si-O Bonds in Amorphous Silicon Dioxide”. In: *Physical Review Letters* 114.11 (2015), pp. 115503.1–115503.5.

[53] K.O. Jeppson and C.M. Svensson. “Negative Bias Stress of MOS Devices at High Electric Fields and Degradation of MNOS Devices”. In: *J.Appl.Phys.* 48.5 (1977), pp. 2004–2014.

[54] J.H. Stathis, S. Mahapatra, and T. Grasser. “Controversial Issues in Negative Bias Temperature Instability”. In: *Microelectronics Reliability* 81 (2018), pp. 244–251.

[55] S. Chakravarthi, A.T. Krishnan, V. Reddy, C.F. Machala, and S. Krishnan. “A Comprehensive Framework for Predictive Modeling of Negative Bias Temperature Instability”. In: *Proc. Intl.Rel.Phys.Symp. (IRPS)*. 2004, pp. 273–282.

[56] S. Mahapatra, P.B. Kumar, and M.A. Alam. “Investigation and Modeling of Interface and Bulk Trap Generation During Negative Bias Temperature Instability of p-MOSFETs”. In: *IEEE Trans.Electron Devices* 51.9 (2004), pp. 1371–1379.

[57] S. Mahapatra, M.A. Alam, P.B. Kumar, T.R. Dalei, D. Varghese, and D. Saha. “Negative Bias Temperature Instability in CMOS Devices”. In: *Microelectronic Engineering* 80.Suppl. (2005), pp. 114–121.

[58] A.T. Krishnan, S. Chakravarthi, P. Nicollian, V. Reddy, and S. Krishnan. “Negative Bias Temperature Instability Mechanism: The Role of Molecular Hydrogen”. In: *Appl.Phys.Lett.* 88.15 (2006), pp. 1–3.

[59] D.S. Ang and S. Wang. “Recovery of the NBTI-Stressed Ultrathin Gate p-MOSFET: The Role of Deep-Level Hole Traps”. In: *IEEE Electron Device Lett.* 27.11 (2006), pp. 914–916.

[60] T. Grasser, B. Kaczer, and W. Goes. “An Energy-Level Perspective of Bias Temperature Instability”. In: *Proc. Intl.Rel.Phys.Symp. (IRPS)*. 2008, pp. 28–38.

[61] T. Grasser, B. Kaczer, W. Goes, Th. Aichinger, Ph. Hehenberger, and M. Nelhiebel. “A Two-Stage Model for Negative Bias Temperature Instability”. In: *Proc. Intl.Rel.Phys.Symp. (IRPS)*. 2009, pp. 33–44.

[62] S. Mahapatra, K. Ahmed, D. Varghese, A. E. Islam, G. Gupta, L. Madhav, D. Saha, and M. A. Alam. “On the Physical Mechanism of NBTI in Silicon Oxynitride p-MOSFETs: Can Differences in Insulator Processing Conditions Resolve the Interface Trap Generation versus Hole Trapping Controversy?” In: *Proc. Intl.Rel.Phys.Symp. (IRPS)*. 2007, pp. 1–9.

[63] S. Mahapatra, N. Goel, S. Desai, S. Gupta, B. Jose, S. Mukhopadhyay, K. Joshi, A. Jain, A.E. Islam, and M.A. Alam. “A Comparative Study of Different Physics-Based NBTI Models”. In: *IEEE Trans.Electron Devices* 60.3 (2013), pp. 901–916.

[64] J.H. Stathis and S. Zafar. “The Negative Bias Temperature Instability in MOS Devices: A Review”. In: *Microelectronics Reliability* 46.2-4 (2006), pp. 270–286.

[65] S. Mahapatra, N. Goel, S. Desai, S. Gupta, B. Jose, S. Mukhopadhyay, K. Joshi, A. Jain, A.E. Islam, and M.A. Alam. “A Comparative Study of Different Physics-Based NBTI Models”. In: *IEEE Trans.Electron Devices* 60.3 (2013), pp. 901–916.

[66] https://scholar.google.com. Search phrase: “Bias Temperature Instability” OR “Bias Temperature Stress”.

[67] T. Grasser. “Stochastic Charge Trapping in Oxides: From Random Telegraph Noise to Bias Temperature Instabilities”. In: *Microelectronics Reliability* 52 (2012), pp. 39–70.

[68] K. Chatty, S. Banerjee, T.P. Chow, and Gutmann R.J. “Hysteresis in Transfer Characteristics in 4H – SiC Depletion / Accumulation-Mode MOSFETs”. In: *IEEE Electron Device Lett.* 23.6 (2002), pp. 330–332.

[69] H. Reisinger, O. Blank, W. Heinrigs, A. Mühlhoff, W. Gustin, and C. Schlünder. “Analysis of NBTI Degradation- and Recovery-Behavior Based on Ultra Fast V_{th}-Measurements”. In: *Proc. Intl.Rel.Phys.Symp. (IRPS)*. 2006, pp. 448–453.

[70] C.T. Sah, T.H. Ning, and L.L. Tschopp. “The Scattering of Electrons by Surface Oxide Charges and by Lattice Vibrations at the Silicon-Silicon Dioxide Interface”. In: *Surface Science* 32.3 (1972), pp. 561–575.

[71] A.T. Dejenfelt and O. Engström. “MOSFET Mobility Degradation due to Interface-States, Generated by Fowler-Nordheim Electron Injection”. In: *Microelectronic Engineering* 15 (1991), pp. 461–464.

[72] D.K. Schroder and J.A. Babcock. “Negative Bias Temperature Instability: Road to Cross in Deep Submicron Silicon Semiconductor Manufacturing”. In: *J.Appl.Phys.* 94.1 (2003), pp. 1–18.

[73] A. Ortiz-Conde, J. Rodrguez, F.J. Garca Sánchez, and J.J. Liou. “An Improved Definition for Modeling the Threshold Voltage of MOSFETs”. In: *Solid-State Electron.* 42.9 (1998), pp. 1743–1746.

[74] K. Terada, K. Nishiyama, and K.I. Hatanaka. “Comparison of MOSFET-Threshold-Voltage Extraction Methods”. In: *Solid-State Electron.* 45.1 (2001), pp. 35–40.

[75] A. Ortiz-Conde, F.J. García Sánchez, J.J. Liou, A. Cerdeira, M. Estrada, and Y. Yue. “A Review of Recent MOSFET Threshold Voltage Extraction Methods”. In: *Microelectronics Reliability* 42.4-5 (2002), pp. 583–596.

[76] X. Yu, R. Cheng, W. Liu, Y. Qu, J. Han, B. Chen, J. Lu, and Y. Zhao. “A Fast Vth Measurement (FVM) Technique for NBTI Behavior Characterization”. In: *IEEE Electron Device Lett.* 39.2 (2018), pp. 172–175.

[77] S.C. Sun and J. D. Plummer. “Electron and Hole Mobilities in Inversion Layers on Thermally Oxidized Silicon Surfaces”. In: *IEEE Trans.Electron Devices* ED-27.8 (1980), pp. 1497–1508.

[78] K. Aoyama. “A Method for Extracting the Threshold Voltage of MOSFETs Based on Current Components”. In: *Proc. Simulation of Semiconductor Devices and Processes*. Vol. 6. September. 1995, pp. 118–121.

[79] S.M. Sze. *Physics of Semiconductor Devices*. Third. New York: Wiley, 1981.

[80] J.S. Lyu, K.S. Nam, and C. Lee. “Determination of the Interface Trap Density in Metal Oxide Semiconductor Field-Effect Transistor through Subthreshold Slope Measurement”. In: *J.Appl.Phys.* 32.10 (1993), pp. 4393–4397.

[81] S.A. Imam, S. Sabri, and T. Szkopek. “Low-Frequency Noise and Hysteresis in Graphene Field-Effect Transistors on Oxide”. In: *Nano Letters* 5.1 (2010), p. 37.

[82] G. Bersuker, J.H. Sim, C.D. Young, R. Choi, P.M. Zeitzoff, G.A. Brown, B.H. Lee, and R.W. Murto. “Effect of Pre-Existing Defects on Reliability Assessment of High-K Gate Dielectrics”. In: *Microelectronics Reliability* 44 (2004), pp. 1509–1512.

[83] J. Franco, B. Kaczer, J. Roussel, M. Cho, T. Grasser, J. Mitard, H. Arimura, L. Witters, D. Cott, N. Waldron, D. Zhou, A. Vais, D. Lin, A. Alian, M. A. Pourghaderi, K. Martens, S. Sioncke, N. Collaert, A. Thean, M. Heyns, and G. Groeseneken. “BTI Reliability of High-Mobility Channel Devices: SiGe, Ge and InGaAs”. In: *Proc. Intl.Integrated Reliability Workshop*. 2014.

[84] D.J. Breed. “A New Model for the Negative Bias Temperature Instability”. In: *Appl.Phys.Lett.* 26.3 (1975), pp. 116–118.

[85] M. Ershov, S. Saxena, H. Karbasi, S. Winters, S. Minehane, J. Babcock, R. Lindley, P. Clifton, M.Redford, and A. Shibkov. “Dynamic Recovery of Negative Bias Temperature Instability in p-type Metal-Oxide-Semiconductor Field-Effect Transistors”. In: *Appl.Phys.Lett.* 83.8 (2003), pp. 1647–1649.

[86] S. Rangan, N. Mielke, and E.C.C. Yeh. “Universal Recovery Behavior of Negative Bias Temperature Instability”. In: *Proc. Intl.Electron Devices Meeting (IEDM)*. 2003, pp. 341–344.

[87] B. Kaczer, T. Grasser, Ph.J. Roussel, J. Martin-Martinez, R. O’Connor, B.J. O’Sullivan, and G. Groeseneken. “Ubiquitous Relaxation in BTI Stressing – New Evaluation and Insights”. In: *Proc. Intl.Rel.Phys.Symp. (IRPS)*. 2008, pp. 20–27.

[88] T. Grasser and B. Kaczer. “Evidence that Two Tightly Coupled Mechanism are Responsible for Negative Bias Temperature Instability in Oxynitride MOSFETs”. In: *IEEE Trans.Electron Devices* 56.5 (2009), pp. 1056–1062.

[89] H. Reisinger, T. Grasser, W. Gustin, and C. Schlünder. “The Statistical Analysis of Individual Defects Constituting NBTI and its Implications for Modeling DC- and AC-Stress”. In: *Proc. Intl.Rel.Phys.Symp. (IRPS)*. May 2010, pp. 7–15.

[90] H. Reisinger, T. Grasser, K. Ermisch, H. Nielen, W. Gustin, and Ch. Schlünder. “Understanding and Modeling AC BTI”. In: *Proc. Intl.Rel.Phys.Symp. (IRPS)*. Apr. 2011, pp. 597–604.

[91] M. Denais, A. Bravaix, V. Huard, C. Parthasarathy, G. Ribes, F. Perrier, Y. Rey-Tauriac, and N. Revil. “On-the-fly Characterization of NBTI in Ultra-Thin Gate Oxide pMOSFET’s”. In: *Proc. Intl.Electron Devices Meeting (IEDM)*. 2004, pp. 109–112.

[92] T. Grasser, P.-J. Wagner, Ph. Hehenberger, W. Goes, and B. Kaczer. “A Rigorous Study of Measurement Techniques for Negative Bias Temperature Instability”. In: *Proc. Intl.Integrated Reliability Workshop*. 2007, pp. 6–11.

[93] S. Machlup. “Noise in Semiconductors: Spectrum of a Two-Parameter Random Signal”. In: *J.Appl.Phys.* 25.3 (1954), pp. 341–343.

[94] A.L. McWhorter. “1/f Noise and Germanium Surface Properties”. In: *Sem.Surf.Phys* (1957), pp. 207–228.

[95] H. Mikoshiba. “1/f Noise in n-Channel Silicon-Gate MOS Transistors”. In: *IEEE Trans.Electron Devices* 29.6 (1982), pp. 965–970.

[96] K.S. Ralls, W.J. Skocpol, L.D. Jackel, R.E. Howard, L.A. Fetter, R.W. Epworth, and D.M. Tennant. “Discrete Resistance Switching in Submicrometer Silicon Inversion Layers: Individual Interface Traps and Low-Frequency ($1/f$?) Noise”. In: *Physical Review Letters* 52.3 (1984), pp. 228–231.

[97] K. Kandiah, M.O. Deighon, and F.B. Whiting. “A Physical Model for Random Telegraph Signal Currents in Semiconductor Devices”. In: *J.Appl.Phys.* 66.2 (1989), pp. 937–948.

[98] N.V. Amarasinghe and C.B. Zeynep. “Complex Random Telegraph Signals in 0.06 μm^2 MDD n-MOSFETs”. In: *Solid State Electronics* 44 (2000), pp. 1013–1019.

[99] A. Avellán, D. Schroeder, and W. Krautschneider. “Modeling Random Telegraph Signals in the Gate Current of Metal-Oxide-Semiconductor Field Effect Transistors after Oxide Breakdown”. In: *J.Appl.Phys.* 94.1 (2003), pp. 703–708.

[100] T. Nagumo, K. Takeuchi, T. Hase, and Y. Hayashi. “Statistical Characterization of Trap Position, Energy, Amplitude and Time Constants by RTN Measurement of Multiple Individual Traps”. In: *Proc. Intl.Electron Devices Meeting (IEDM)*. 2010, pp. 628–631.

[101] T. Grasser, B. Kaczer, W. Goes, Th. Aichinger, Ph. Hehenberger, and M. Nelhiebel. “Understanding Negative Bias Temperature Instability in the Context of Hole Trapping”. In: *Microelectronic Engineering* 86.7-9 (2009), pp. 1876–1882.

[102] S. Guo, R. Wang, D. Mao, Y. Wang, and R. Huang. “Anomalous Random Telegraph Noise in Nanoscale Transistors as Direct Evidence of Two Metastable States of Oxide Traps”. In: *Scientific Reports* 7.1 (2017), pp. 1–6.

[103] C.Y. Chen, Q. Ran, H.J. Cho, A. Kerber, Y. Liu, M.R. Lin, and R.W. Dutton. “Correlation of I_d- and I_g-Random Telegraph Noise to Positive Bias Temperature Instability in Scaled High-κ/Metal Gate n-Type MOSFETs”. In: *Proc. Intl.Rel.Phys.Symp. (IRPS)*. 2011, 3A.2.1–3A.2.6.

[104] M. Toledano-Luque, B. Kaczer, E. Simoen, R. Degraeve, J. Franco, P.J. Roussel, T. Grasser, and G. Groeseneken. “Correlation of Single Trapping and Detrapping Effects in Drain and Gate Currents of Nanoscaled nFETs and pFETs”. In: *Proc. Intl.Rel.Phys.Symp. (IRPS)*. 2012, XT.5.1–XT.5.6.

[105] D.V. Lang. “Deep-Level Transient Spectroscopy: A New Method to Characterize Traps in Semiconductors”. In: *J.Appl.Phys.* 45.7 (1974), pp. 3023–3032.

[106] A. Karwath and M. Schulz. “Deep Level Transient Spectroscopy on Single, Isolated Interface Traps in Field-Effect Transistors”. In: *Appl.Phys.Lett.* 52.8 (1988), pp. 634–636.

[107] T. Grasser, H. Reisinger, P.-J. Wagner, W. Goes, F. Schanovsky, and B. Kaczer. “The Time Dependent Defect Spectroscopy (TDDS) for the Characterization of the Bias Temperature Instability”. In: *Proc. Intl.Rel.Phys.Symp. (IRPS)*. May 2010, pp. 16–25.

[108] A.K. Sinha and T.E. Smith. “Kinetics of the Slow-Trapping Instability at the Si/SiO_2 Interface”. In: *J.Electrochem.Soc.* 125 (1978), pp. 743–746.

[109] B. Kaczer, Ph. Roussel, T. Grasser, and G. Groeseneken. “Statistics of Multiple Trapped Charges in the Gate Oxide of Deeply Scaled MOSFET Devices-Application to NBTI”. In: *IEEE Electron Device Lett.* 31.5 (2010), pp. 411–413.

[110] B. Kaczer, T. Grasser, Ph.J. Roussel, J. Franco, R. Degraeve, L.A. Ragnarsson, E. Simoen, G. Groeseneken, and H. Reisinger. “Origin of NBTI Variability in Deeply Scaled PFETs”. In: *Proc. Intl.Rel.Phys.Symp. (IRPS)*. 2010, pp. 26–32.

[111] O. Roux dit Buisson, G. Ghibaudo, and J. Brini. “Model for Drain Current RTS Amplitude in Small-Area MOS Transistors”. In: *Solid-State Electron.* 35.9 (1992), pp. 1273–1276.

[112] A. Asenov, R. Balasubramaniam, A.R. Brown, and J.H. Davies. “RTS Amplitudes in Decananometer MOSFETs: 3-D Simulation Study”. In: *IEEE Trans.Electron Devices* 50.3 (2003), pp. 839–845.

[113] A. Ghetti, C. Monzio Compagnoni, F. Biancardi, A.L. Lacaita, S. Beltrami, L. Chiavarone, A.S. Spinelli, and A. Visconti. “Scaling Trends for Random Telegraph Noise in Deca-Nanometer Flash Memories”. In: *Proc. Intl.Electron Devices Meeting (IEDM)* (2008).

[114] K. Sonoda, K. Ishikawa, T. Eimori, and O. Tsuchiya. “Discrete Dopant Effects on Statistical Variation of Random Telegraph Signal Magnitude”. In: *IEEE Trans.Electron Devices* 54.8 (2007), pp. 1918–1925.

[115] N. Tega, H. Miki, F. Pagette, D.J. Frank, A. Ray, M.J. Rooks, W. Haensch, and K. Torii. “Increasing Threshold Voltage Variation due to Random Telegraph Noise in FETs as Gate Lengths Scale to 20 nm”. In: *IEEE Symposium on VLSI Technology Digest of Technical Papers* (2009), pp. 50–51.

[116] S. Realov and K.L. Shepard. “Analysis of Random Telegraph Noise in 45-nm CMOS Using On-Chip Characterization System”. In: *IEEE Trans.Electron Devices* 60.5 (2013), pp. 1716–1722.

[117] S.E. Rauch. “Review and Reexamination of Reliability Effects Related to NBTI-Induced Statistical Variations”. In: *IEEE Trans.Dev.Mat.Rel.* 7.4 (2007), pp. 524–530.

[118] K. L. Brower. “Passivation of Paramagnetic Si/SiO$_2$ Interface States with Molecular Hydrogen”. In: *Appl.Phys.Lett.* 53.6 (1988), pp. 508–510.

[119] K.L. Brower. “Kinetics of H$_2$ Passivation of P$_b$ Centers at the (111) Si-SiO$_2$ Interface”. In: *Physical Review B* 38.14 (1988), pp. 9657–9666.

[120] K.L. Brower and S.M. Myers. “Chemical Kinetics of Hydrogen and (111) Si-SiO$_2$ Interface Defects”. In: *Appl.Phys.Lett.* 57.2 (1990), pp. 162–164.

[121] K.L. Brower. “Dissociation Kinetics of Hydrogen-Passivated (111) Si-Si0$_2$ Interface Defects”. In: *Physical Review B* 42.6 (1990), pp. 3444–3454.

[122] C.H. Henry and D.V. Lang. “Nonradiative Capture and Recombination by Multiphonon Emission in GaAs and GaP”. In: *Physical Review B* 15.2 (1977), pp. 989–1016.

[123] J.P. Campbell, J. Qin, K.P. Cheung, L.C. Yu, J.S. Suehle, A. Oates, and K. Sheng. “Random Telegraph Noise in Highly Scales nMOSFETs”. In: *Proc. Intl.Rel.Phys.Symp. (IRPS)*. 2009, pp. 382–388.

[124] M.B. Weissman. “$1/f$ Noise and other Slow, Nonexponential Kinetics in Condensed Matter”. In: *Rev.Mod.Phys* 60.2 (1988), pp. 537–571.

[125] M. Born and R. Oppenheimer. “Zur Quantentheorie der Molekeln”. In: *Annalen der Physik* 389.20 (1927), pp. 457–484.

[126] K. Huang and A. Rhys. “Theory of Light Absorption and Non-Radiative Transitions in F-Centres”. In: *Proc.R.Soc.A* 204 (1950), pp. 406–423.

[127] M.J. Kirton and M.J. Uren. “Noise in Solid-State Microstructures: A New Perspective on Individual Defects, Interface States and Low-Frequency (1/f) Noise”. In: *Adv.Phys.* 38.4 (1989), pp. 367–486.

[128] E. Condon. “A Theory of Intensity Distribution in Band Systems”. In: *Physical Review* 28.6 (1926), pp. 1182–1201.

[129] D.V. Lang and C.H. Henry. “Nonradiative Recombination at Deep Levels in GaAs and GaP by Lattice-Relaxation Multiphonon Emission”. In: *Physical Review Letters* 35.22 (1975), pp. 1525–1528.

[130] A.M. Stoneham. “Non-radiative Transitions in Semiconductors”. In: *Rep.Prog.Phys.* 44 (1981), pp. 1251–1295.

[131] S. Makram-Ebeid and M. Lannoo. “Quantum Model for Phonon-Assisted Tunnel Ionization of Deep Levels in a Semiconductor”. In: *Physical Review B* 25.10 (1982), pp. 6406–6424.

[132] M.J. Kirton and M.J. Uren. “Capture and Emission Kinetics of Individual Si:SiO2 Interface States”. In: *Appl.Phys.Lett.* 48.19 (1986), pp. 1270–1272.

[133] M.J. Kirton, M.J. Uren, and S. Collins. “Individual Interface States and their Implications for Low-Frequency Noise in MOSFETs”. In: *Applied Surface Science* 30 (1987), pp. 148–152.

[134] M. Schulz and A. Karmann. “Single, Individual Traps in MOSFETs”. In: *Physica Scripta* T35 (1991), pp. 273–280.

[135] T.L. Tewksbury. “Relaxation Effects in MOS Devices due to Tunnel Exchange with Near-Interface Oxide Traps”. Ph.D. Thesis. MIT, 1992.

[136] T.L. Tewksbury and H.-S. Lee. “Characterization, Modeling, and Minimization of Transient Threshold Voltage Shifts in MOSFETs”. In: *IEEE J.Solid-State Circuits* 29.3 (1994), pp. 239–252.

[137] A. Schenk. “A Model for the Field and Temperature Dependence of Shockley-Read-Hall Lifetimes in Silicon”. In: *Solid-State Electron.* 35.11 (1992), pp. 1585–1596.

[138] S. Takagi, N. Yasuda, and A. Toriumi. “Experimental Evidence of Inelastic Tunneling and New I-V Model for Stress-induced Leakage Current”. In: *Proc. Intl.Electron Devices Meeting (IEDM)* (1996), pp. 323–326.

[139] K. Sakakibara, N. Ajika, K. Eikyu, K. Ishikawa, and H. Miyoshi. “A Quantitative Analysis of Time-Decay Reproducible Stress-Induced Leakage Current in SiO Films”. In: *IEEE Trans.Electron Devices* 44.6 (1997), pp. 1002–1008.

[140] A.J. Lelis, H.E. Boesch, T.R. Oldham, and F.B. McLean. “Reversibility of Trapped Hole Annealing”. In: *IEEE Trans.Nucl.Sci.* 35.6 (1988), pp. 1186–1191.

[141] A.J. Lelis and T.R. Oldham. “Time Dependence of Switching Oxide Traps”. In: *IEEE Trans.Nucl.Sci.* 41.6 (Dec. 1994), pp. 1835–1843.

[142] T. Grasser, B. Kaczer, H. Reisinger, P.-J. Wagner, and M. Toledano-Luque. “On the Frequency Dependence of the Bias Temperature Instability”. In: *Proc. Intl.Rel.Phys.Symp. (IRPS)*. Apr. 2012, XT.8.1–XT.8.7.

[143] E.H. Poindexter and W.L. Warren. “Paramagnetic Point Defects in Amorphous Thin Films of SiO_2 and Si_3N_4: Updates and Additions”. In: *J.Electrochem.Soc.* 142.7 (1995), pp. 2508–2516.

[144] J.M.M. de Nijs, K.G. Druijf, V.V. Afanas’ev, E. van der Drift, and P. Balk. “Hydrogen Induced Donor-Type Si/SiO_2 Interface States”. In: *Appl.Phys.Lett.* 65.19 (1994), pp. 2428–2430.

[145] J.F. Zhang, H.K. Sii, R. Degraeve, and G. Groeseneken. “Mechanism for the Generation of Interface State Precursors”. In: *J.Appl.Phys.* 87.6 (2000), pp. 2967–2977.

[146] E. Cartier and J.H. Stathis. “Atomic Hydrogen-Induced Degradation of the Si/SiO_2 Structure”. In: *Microelectronic Engineering* 28.1-4 (1995), pp. 3–10.

[147] E. Cartier and J.H. Stathis. “Hot-Electron Induced Passivation of Silicon Dangling Bonds at the Si(111)/SiO_2 Interface”. In: *Appl.Phys.Lett.* 69.1 (1996), pp. 103–105.

[148] J.P. Campbell, P.M. Lenahan, A.T. Krishnan, and S. Krishnan. “Direct Observation of the Structure of Defect Centers Involved in the Negative Bias Temperature Instability”. In: *Appl.Phys.Lett.* 87.20 (2005), pp. 1–3.

[149] V. Huard, C. Parthasarathy, N. Rallet, C. Guerin, M. Mammase, D. Barge, and C. Ouvrard. “New Characterization and Modeling Approach for NBTI Degradation from Transistor to Product Level”. In: *Proc. Intl.Electron Devices Meeting (IEDM)*. 2007, pp. 797–800.

[150] M. Houssa, V.V. Afanas’ev, A. Stesmans, M. Aoulaiche, G. Groeseneken, and M.M. Heyns. “Insights on the Physical Mechanism behind Negative Bias Temperature Instabilities”. In: *Appl.Phys.Lett.* 90.4 (2007), p. 043505.

[151] T. Grasser, K. Rott, H. Reisinger, M. Waltl, P. Wagner, F. Schanovsky, W. Goes, G. Pobegen, and B. Kaczer. “Hydrogen-Related Volatile Defects as the Possible Cause for the Recoverable Component of NBTI”. In: *Proc. Intl.Electron Devices Meeting (IEDM)*. Dec. 2013.

[152] D.L. Griscom. “Diffusion of Radiolytic Molecular Hydrogen as a Mechanism for the Post-Irradiation Buildup of Interface States in SiO_2-on-Si Structures”. In: *J.Appl.Phys.* 58.7 (1985), pp. 2524–2533.

[153] M.A. Green. “Intrinsic Concentration, Effective Densities of States, and Effective Mass in Silicon”. In: *J.Appl.Phys.* 67.6 (1990), pp. 2944–2954.

[154] W. Bludau, A. Onton, and W. Heinke. “Temperature Dependence of the Band Gap of Silicon”. In: *J.Appl.Phys.* 45.4 (1974), pp. 1846–1848.

[155] G.G. Macfarlane, T.P. McLean, J.E. Quarrington, and V. Roberts. “Fine Structure in the Absorption-Edge Spectrum of Si”. In: *Physical Review* 111.5 (1958), pp. 1245–1254.

[156] K.L. Shaklee and R.E. Nahory. “Valley-Orbit Splitting of Free Excitons? The Absorption Edge of Si”. In: *Physical Review Letters* 24.17 (1970), pp. 942–945.

[157] H.D. Barber. “Effective Mass and Intrinsic Concentration in Silicon”. In: *Solid-State Electron.* 10.11 (1967), pp. 1039–1051.

[158] F.L. Madarasz, J.E. Lang, and P.M. Hemeger. “Effective Masses for Nonparabolic Bands in p-Type Silicon”. In: *J.Appl.Phys.* 52.7 (1981), pp. 4646–4648.

[159] J.E. Lang, F.L. Madarasz, and P.M. Hemenger. “Temperature Dependent Density of States Effective Mass in Nonparabolic p-Type Silicon”. In: *J.Appl.Phys.* 54.6 (1983), p. 3612.

[160] W.B. Joyce and R.W. Dixon. “Analytic Approximations for the Fermi Energy of an Ideal Fermi Gas”. In: *Appl.Phys.Lett.* 31.5 (1977), pp. 354–356.

[161] *J.R. Hauser, CVC version 5.0 (www.ece.ncsu.edu/research/tools).*

[162] L.D. Landau and E.M. Lifshitz. *Quantum Mechanics*. Reading, Mass: Addison-Wesley, 1958.

[163] R.H. Fowler and L. Nordheim. “Electron Emission in Intense Electric Fields”. In: *Proc.Roy.Soc.A* 119 (1928), pp. 173–181.

[164] C. Kaneta, T. Yamasaki, T. Uchiyama, T. Uda, and K. Terakura. “Structure and Electronic Property of Si(100)/SiO_2 Interface”. In: *Microelectronic Engineering* 48 (1999), pp. 117–20.

[165] Y. Yamashita, S. Yamamoto, K. Mukai, J. Yoshinobu, Y. Harada, T. Tokushima, T. Takeuchi, Y. Takata, S. Shin, K. Akagi, and S. Tsuneyuki. “Direct Observation of Site-Specific Valence Electronic Structure at the SiO_2/Si Interface”. In: *Physical Review B* 73.4 (2006), p. 045336.

[166] O. Sharia, A.A. Demkov, G. Bersuker, and B.H. Lee. “Theoretical Study of the Insulator/Insulator Interface: Band SiO_2/HfO_2 Junction”. In: *Physical Review B* 75.3 (2007), p. 035306.

[167] Z. Huiwen, L. Yongsong, M. Lingfeng, S. Jingqin, Z. Zhiyan, and T. Weihua. “Theoretical Study of the SiO_2/Si Interface and its Effect on Energy Band Profile and MOSFET Gate Tunneling Current”. In: *Journal of Semiconductors* 31.8 (2010), p. 082003.

[168] L. Gerrer, S. Ling, S.M. Amoroso, P. Asenov, A.L. Shluger, and A. Asenov. “From Atoms to Product Reliability: Toward a Generalized Multiscale Simulation Approach”. In: *Journal of Computational Electronics* 12.4 (2013), pp. 638–650.

[169] *Minimos-NT (www.globaltcad.com)*.

[170] H. Miki, N. Tega, M. Yamaoka, D. J. Frank, A. Bansal, M. Kobayashi, K. Cheng, C.P. D’Emic, Z. Ren, S. Wu, J-B. Yau, Y. Zhu, M. A. Guillorn, D.-G. Park, W. Haensch, E. Leobandung, and K. Torii. “Statistical Measurement of Random Telegraph Noise and Its Impact in Scaled-down High-κ/Metal-gate MOSFETs”. In: *Proc. Intl.Electron Devices Meeting (IEDM)*. 2012, pp. 450–453.

[171] R. Fernández, B. Kaczer, A. Nackaerts, S. Demuynck, R. Rodriguez, M. Nafria, and G. Groeseneken. “AC NBTI Studied in the 1 Hz - 2 GHz Range on Dedicated On-Chip CMOS Circuits”. In: *Proc. Intl.Electron Devices Meeting (IEDM)*. 2006, pp. 337–340.

[172] A. Kerber and T. Nigam. “Application of CVS and VRS Method for Correlation of Logic CMOS Wear Out to Discrete Device Degradation Based on Ring Oscillator Circuits”. In: *VLSI Tchnology*. 2016, pp. 44–45.

[173] L. Heiß, A. Lachmann, R. Schwab, G. Panagopoulos, P. Baumgartner, M.Y. Virupakshappaa, and D. Schmitt-Landsiedel. “New Methodology for On-Chip RF Reliability Assessment”. In: *Proc. Intl.Rel.Phys.Symp. (IRPS)*. 2016, pp. 4C51–4C57.

[174] *Comphy version 1.0 (www.comphy.eu), Institute for Microelectronics / TU Wien and imec, 2018.*

[175] E. Bersch, S. Rangan, R.A. Bartynski, E. Garfunkel, and E. Vescovo. “Band Offsets of Ultrathin High-κ Oxide Films with Si”. In: *Physical Review B* 78.8 (2008), pp. 1–10.

[176] T. Grasser, P.-J. Wagner, H. Reisinger, Th. Aichinger, G. Pobegen, M. Nelhiebel, and B. Kaczer. “Analytic Modeling of the Bias Temperature Instability Using Capture/Emission Time Maps”. In: *Proc. Intl.Electron Devices Meeting (IEDM)*. Dec. 2011, pp. 27.4.1–27.4.4.

[177] R. Ritzenthaler, T. Schram, A. Spessot, C. Caillat, M. Cho, E. Simoen, M. Aoulaiche, J. Albert, S.A. Chew, K.B. Noh, Y. Son, P. Fazan, N. Horiguchi, and A. Thean. “A New high-κ/ Metal Gate CMOS Integration Scheme (Diffusion and Gate Replacement) Suppressing Gate Height Asymmetry and Compatible with High-Thermal Budget Memory Technologies”. In: *Proc. Intl.Electron Devices Meeting (IEDM)*. 2014, pp. 772–775.

[178] B. Kaczer, M. Toledano-Luque, W. Goes, T. Grasser, and Groeseneken G. “Gate Current Random Telegraph Noise and Single Defect Conduction”. In: *Microelectronic Engineering* 109.7 (2013), pp. 123–125.

[179] W. Goes, M. Toledano-Luque, O. Baumgartner, M. Bina, F. Schanovsky, B. Kaczer, and T. Grasser. “Understanding Correlated Drain and Gate Current Fluctuations”. In: *Proc. Intl.Symp. on Physical and Failure Analysis of Integrated Circuits*. 2013, pp. 51–56.

[180] G. Pobegen and T. Grasser. “On the Distribution of NBTI Time Constants on a Long, Temperature-Accelerated Time Scale”. In: *IEEE Trans.Electron Devices* 60.7 (2013), pp. 2148–2155.

[181] E. Cartier, A. Kerber, T. Ando, M.M. Frank, K. Choi, S. Krishnan, B. Linder, K. Zhao, F. Monsieur, J. Stathis, and V. Narayanan. “Fundamental Aspects of HfO_2-based High-κ Metal Gate Stack Reliability and Implications on t_{inv}-scaling”. In: *Proc. Intl.Electron Devices Meeting (IEDM)* (2011), pp. 18.4.1–18.4.4.

[182] S. Mukhopadhyay and S. Mahapatra. “An Experimental Perspective of Trap Generation Under BTI Stress”. In: *IEEE Trans.Electron Devices* 62.7 (2015), pp. 2092–2097.

[183] L.Å. Ragnarsson, Z. Li, J. Tseng, T. Schram, E. Rohr, M.J. Cho, T. Kauerauf, T. Conard, Y. Okuno, B. Parvais, P. Absil, S. Biesemans, and T.Y. Hoffmann. “Ultra Low-EOT (5 Å) Gate-First and Gate-Last High Performance CMOS Achieved by Gate-Electrode Optimization”. In: *Proc. Intl.Electron Devices Meeting (IEDM)*. 2009, pp. 663–666.

List of Publications

Scientific Journals

[GRJ1] B. Kaczer, J. Franco, S. Tyaginov, M. Jech, **G. Rzepa**, T. Grasser, B.J. O'Sullivan, R. Ritzenhaler, T. Schram, A. Spessot, D. Linten, and N. Horiguchi. "Mapping of CMOS FET Degradation in Bias Space—Application to DRAM Peripheral Devices". In: *J.Vac.Sci.Technol.B* 35.1 (2017), 01A109.

[GRJ2] **G. Rzepa**, J. Franco, B. O'Sullivan, A. Subirats, M. Simicic, G. Hellings, P. Weckx, M. Jech, T. Knobloch, M. Waltl, P.J. Roussel, D. Linten, B. Kaczer, and T. Grasser. "Comphy — A Compact-Physics Framework for Unified Modeling of BTI". In: *Microelectronics Reliability* 85 (2018), pp. 49–65.

[GRJ3] M. Waltl, **G. Rzepa**, A. Grill, W. Goes, J. Franco, B. Kaczer, L. Witters, J. Mitard, N. Horiguchi, and T. Grasser. "Superior NBTI in High-κ SiGe Transistors-Part I: Experimental". In: *IEEE Trans.Electron Devices* 64.5 (2017), pp. 2092–2098.

[GRJ4] M. Waltl, **G. Rzepa**, A. Grill, W. Goes, J. Franco, B. Kaczer, L. Witters, J. Mitard, N. Horiguchi, and T. Grasser. "Superior NBTI in High-κ SiGe Transistors-Part II: Theory". In: *IEEE Trans.Electron Devices* 64.5 (2017), pp. 2099–2105.

[GRJ5] Y.Y. Illarionov, M. Waltl, **G. Rzepa**, J.S. Kim, S. Kim, A. Dodabalapur, D. Akinwande, and T. Grasser. "Long-Term Stability and Reliability of Black Phosphorus Field-Effect Transistors". In: *ACS Nano* (2016), pp. 9543–9549.

[GRJ6] Y.Y. Illarionov, M. Waltl, **G. Rzepa**, T. Knobloch, J.S. Kim, D. Akinwande, and T. Grasser. "Highly-Stable Black Phosphorus Field-Effect Transistors with Low Density of Oxide Traps". In: *npj 2D Materials and Applications* 1.1 (2017), p. 23.

[GRJ7] Y.Y. Illarionov, T. Knobloch, M. Waltl, **G. Rzepa**, A. Pospischil, D.K. Polyushkin, M.M. Furchi, T. Mueller, and T. Grasser. "Energetic Mapping of Oxide Traps in MoS_2 Field-Effect Transistors". In: *2D Materials* 4.2 (2017).

[GRJ8] T. Knobloch, **G. Rzepa**, Y.Y. Illarionov, M. Waltl, D. Polyushkin, A. Pospischil, M. Furchi, T. Mueller, and T. Grasser. "Impact of Gate Dielectrics on the Threshold Voltage in MoS_2 Transistors". In: *ECS Trans.* 80.1 (2017), pp. 203–217.

[GRJ9] B. Kaczer, J. Franco, P. Weckx, P.J. Roussel, V. Putcha, E. Bury, M. Simicic, A. Chasin, D. Linten, B. Parvais, F. Catthoor, **G. Rzepa**, M. Waltl, and T. Grasser. "A Brief Overview of Gate Oxide Defect Properties and their Relation to MOSFET Instabilities and Device and Circuit Time-Dependent Variability". In: *Microelectronics Reliability* 81 (2018), pp. 186–194.

[GRJ10] W. Goes, Y. Wimmer, A.M. El-Sayed, **G. Rzepa**, M. Jech, A.M. Shluger, and T. Grasser. "Identification of Oxide Defects in Semiconductor Devices: A Systematic Approach Linking DFT to Rate Equations and Experimental Evidence". In: *Microelectronics Reliability* (2018).

Conference Proceedings

[GRC1] T. Grasser, M. Waltl, **G. Rzepa**, W. Goes, Y. Wimmer, A.M. El-Sayed, A.L. Shluger, H. Reisinger, and B. Kaczer. “The “Permanent” Component of NBTI Revisited: Saturation, Degradation-Reversal, and Annealing”. In: *Proc. Intl.Rel.Phys.Symp. (IRPS)*. June 2016.

[GRC2] **G. Rzepa**, J. Franco, A. Subirats, M. Jech, A. Chasin, A. Grill, M. Waltl, T. Knobloch, D. Linten, B. Kaczer, and T. Grasser. “Efficient Physical Defect Model Applied to PBTI in High-κ Stacks”. In: *Proc. Intl.Rel.Phys.Symp. (IRPS)*. 2017, XT–11.1–XT–11.6.

[GRC3] T. Grasser, B. Stampfer, M. Waltl, **G. Rzepa**, K. Rupp, F. Schanovsky, G. Pobegen, K. Puschkarsky, H. Reisinger, B.J. O’Sullivan, and B. Kaczer. “Characterization and Physical Modeling of the Temporal Evolution of Near-Interfacial States Resulting from NBTI / PBTI Stress in nMOS / pMOS Transistors”. In: *Proc. Intl.Rel.Phys.Symp. (IRPS)*. 2018.

[GRC4] M. Waltl, A. Grill, **G. Rzepa**, W. Goes, J. Franco, B. Kaczer, J. Mitard, and T. Grasser. “Nanoscale Evidence for the Superior Reliability of SiGe High-k pMOSFETs”. In: *Proc. Intl.Rel.Phys.Symp. (IRPS)*. 2016.

[GRC5] A. Grill, **G. Rzepa**, P. Lagger, C. Ostermaier, H. Ceric, and T. Grasser. “Charge Feedback Mechanisms at Forward Threshold Voltage Stress in GaN / AlGaN HEMTs”. In: 2015.

[GRC6] J. Franco, V. Putcha, A. Vais, S. Sioncke, N. Waldron, D. Zhou, **G. Rzepa**, Ph J. Roussel, G. Groeseneken, M. Heyns, N. Collaert, D. Linten, T. Grasser, and B. Kaczer. “Characterization of Oxide Defects in InGaAs MOS Gate Stacks for High-Mobility n-Channel MOSFETs”. In: *Proc. Intl.Electron Devices Meeting (IEDM)*. 2017, pp. 7.5.1–7.5.4.

[GRC7] M. Karner, O. Baumgartner, Z. Stanojevic, F. Schanovsky, G. Strof, C. Kernstock, H.W. Karner, **G. Rzepa**, and T. Grasser. “Vertically Stacked Nanowire MOSFETs for Sub-10 nm Nodes: Advanced Topography, Device, Variability, and Reliability Simulations”. In: *Proc. Intl.Electron Devices Meeting (IEDM)*. 2016, pp. 762–765.

[GRC8] H. Demel, Z. Stanojevic, M. Karner, **G. Rzepa**, and T. Grasser. “Expanding TCAD Simulations from Grid to Cloud”. In: *Proc. Simulation of Semiconductor Processes and Devices*. 2015, pp. 186–189.

[GRC9] A. Chasin, J. Franco, B. Kaczer, V. Putcha, P. Weckx, R. Ritzenthaler, H. Mertens, N. Horiguchi, D. Linten, and **G. Rzepa**. “BTI Reliability and Time-Dependent Variability of Stacked Gate-All-Around Si Nanowire Transistors”. In: *Proc. Intl.Rel.Phys.Symp. (IRPS)*. 2017.

[GRC10] B. Kaczer, **G. Rzepa**, J. Franco, P. Weckx, A. Chasin, V. Putcha, E. Bury, M. Simicic, P. Roussel, G. Hellings, A. Veloso, P. Matagne, T. Grasser, and D. Linten. “Benchmarking Time-Dependent Variability of Junctionless Nanowire FETs”. In: *Proc. Intl.Rel.Phys.Symp. (IRPS)*. 2017, pp. 2D–6.1–7.

[GRC11] T. Knobloch, **G. Rzepa**, Y.Y. Illarionov, M. Waltl, F. Schanovsky, M. Jech, B. Stampfer, M.M. Furchi, T. Muller, and T. Grasser. “Physical Modeling of the Hysteresis in MoS_2 Transistors”. In: *Proc. ESSDERC*. 2017.

[GRC12] T. Knobloch, **G. Rzepa**, Y.Y. Illarionov, M. Waltl, D. Polyushkin, A. Pospischil, M. Furchi, T. Mueller, and T. Grasser. “Impact of Gate Dielectrics on the Threshold Voltage in MoS_2 Transistors”. In: vol. 80. 1. 2017, pp. 203–217.

[GRC13] K.-U. Giering, G. Rott, **G. Rzepa**, H. Reisinger, A.K. Puppala, T. Reich, W. Gustin, T. Grasser, and R. Jancke. “Analog-Circuit NBTI Degradation and Time-Dependent NBTI Variability: An Efficient Physics-Based Compact Model”. In: *Proc. Intl.Rel.Phys.Symp. (IRPS)*. 2016.

[GRC14] **G. Rzepa**, M. Waltl, W. Goes, B. Kaczer, and T. Grasser. “Microscopic Oxide Defects Causing BTI, RTN, and SILC on High-κ FinFETs”. In: *Proc. Simulation of Semiconductor Processes and Devices*. 2015, pp. 144–147.

[GRC15] **G. Rzepa**, W. Goes, G. Rott, K. Rott, M. Karner, C. Kernstock, B. Kaczer, H. Reisinger, and T. Grasser. “Physical Modeling of NBTI: From Individual Defects to Devices”. In: *Proc. Simulation of Semiconductor Processes and Devices*. 2014, pp. 81–84.

[GRC16] **G. Rzepa**, M. Waltl, W. Goes, B. Kaczer, J. Franco, T. Chiarella, N. Horiguchi, and T. Grasser. “Complete Extraction of Defect Bands Responsible for Instabilities in n and pFinFETs”. In: *IEEE Symposium on VLSI Technology Digest of Technical Papers*. 2016, pp. 208–209.

[GRC17] Y.Y. Illarionov, **G. Rzepa**, M. Waltl, T. Knobloch, J.-S. Kim, D. Akinwande, and T. Grasser. “Accurate Mapping of Oxide Traps in Highly-Stable Black Phosphorus FETs”. In: *Proc. Intl.Conf. on Electron Devices Technology and Manufacturing*. 2017.

[GRC18] B. Kaczer, S.M. Amoroso, R. Hussin, A. Asenov, J. Franco, P. Weckx, P.J. Roussel, **G. Rzepa**, T. Grasser, and N. Horiguchi. “On the Distribution of the FET Threshold Voltage Shifts due to Individual Charged Gate Oxide Defects”. In: *Proc. Intl.Integrated Reliability Workshop*. 2016, pp. 18–20.

[GRC19] B. Kaczer, J. Franco, P. Weckx, Ph.J. Roussel, E. Bury, M. Cho, R. Degraeve, D. Linten, G. Groeseneken, H. Kukner, P. Raghavan, F. Catthoor, **G. Rzepa**, W. Goes, and T. Grasser. “The Defect-Centric Perspective of Device and Circuit Reliability — From Individual Defects to Circuits”. In: *Proc. ESSDERC*. 2015, pp. 218–225.

[GRC20] T. Grasser, M. Waltl, Y. Wimmer, W. Goes, R. Kosik, **G. Rzepa**, H. Reisinger, G. Pobegen, A.M. El-Sayed, A.L. Shluger, and B. Kaczer. “Gate-Sided Hydrogen Release as the Origin of “Permanent” NBTI Degradation: From Single Defects to Lifetimes”. In: *Proc. Intl.Electron Devices Meeting (IEDM)*. Dec. 2015.

[GRC21] T. Grasser, W. Goes, Y. Wimmer, F. Schanovsky, **G. Rzepa**, M. Waltl, K. Rott, H. Reisinger, V.V. Afanas’ev, A. Stesmans, A.M. El-Sayed, and A.L. Shluger. “On the Microscopic Structure of Hole Traps in pMOSFETs”. In: *Proc. Intl.Electron Devices Meeting (IEDM)*. Dec. 2014.

[GRC22] K.-U. Giering, C. Sohrmann, **G. Rzepa**, L. Heiß, T. Grasser, and R. Jancke. “NBTI Modeling in Analog Circuits and its Application to Long-Term Aging Simulations”. In: *Proc. Intl.Integrated Reliability Workshop*. 2014, pp. 29–34.

[GRC23] W. Goes, M. Waltl, Y. Wimmer, **G. Rzepa**, and T. Grasser. “Advanced Modeling of Charge Trapping: RTN, 1/f noise, SILC, and BTI”. In: *Proc. Simulation of Semiconductor Processes and Devices*. 2014, pp. 77–80.

[GRC24] **G. Rzepa**, W. Goes, B. Kaczer, and T. Grasser. “Characterization and Modeling of Reliability Issues in Nanoscale Devices”. In: *Proc. Intl.Symp.on Circuits and Systems (ISCAS)*. 2015, pp. 2445–2448.

Master Theses

[GRT1] T. Knobloch (supervised by **G. Rzepa** and T. Grasser). “Characterization and Physical Modeling of Degradation in MoS_2 Transistors”. Master Thesis. TU Wien, 2016.

[GRT2] **G. Rzepa** (supervised by W. Goes, M. Karner, and T. Grasser). “Microscopic Modeling of NBTI in MOS Transistors”. Master Thesis. TU Wien, 2013.

Curriculum Vitae

Gerhard Rzepa

Assistant Professor
Institute for Microelectronics
TU Wien, Austria

Born: June 24th, 1985 – Kasten, Austria

Education

2005	**High school graduation** Secondary Technical School, St. Pölten, *distinction*
2006 – 2010	**Bachelor of Science** Electrical Engineering and Information Technology, TU Wien
2010 – 2013	Diplom-Ingenieur, equivalent to **Master of Science** Microelectronics, TU Wien, *distinction*
since 2013	**Doctoral (PhD) programme** in Engineering Sciences Institute for Microelectronics, TU Wien
August 2014	Sixth Sinano **Summer School** on Reliability and Variability of Electronic Devices, Bertinoro, Italy

Experience

2007 – 2011	**Graphic Designer** NÖ Pressehaus GmbH, St. Pölten, Austria
2012 – 2013	**TCAD Software Developer** Global TCAD Solutions GmbH, Vienna, Austria
2013 – 2014	**Scientific Assistant** Institute for Microelectronics, TU Wien
since 2014	**Assistant Professor** Institute for Microelectronics, TU Wien
June – September 2016	**International Scholar** KU Leuven, imec, Belgium
February – March 2017	**Visiting Scholar** KU Leuven, imec, Belgium
July – September 2017	**Visiting Scholar** KU Leuven, imec, Belgium